

2001

Ultrasonographic measurement of periodontal attachment levels

John Edward Lynch

College of William & Mary - Arts & Sciences

Follow this and additional works at: <https://scholarworks.wm.edu/etd>



Part of the [Biomedical Engineering and Bioengineering Commons](#), [Dentistry Commons](#), and the [Investigative Techniques Commons](#)

Recommended Citation

Lynch, John Edward, "Ultrasonographic measurement of periodontal attachment levels" (2001). *Dissertations, Theses, and Masters Projects*. Paper 1539623384. <https://dx.doi.org/doi:10.21220/s2-24hz-5v29>

This Dissertation is brought to you for free and open access by the Theses, Dissertations, & Master Projects at W&M ScholarWorks. It has been accepted for inclusion in Dissertations, Theses, and Masters Projects by an authorized administrator of W&M ScholarWorks. For more information, please contact scholarworks@wm.edu.

**ULTRASONOGRAPHIC MEASUREMENT
OF PERIODONTAL ATTACHMENT
LEVELS**

A Dissertation

Presented to

The Faculty of the Department of Applied Science

The College of William and Mary in Virginia

In Partial Fulfillment

Of the Requirements for the Degree of

Doctor of Philosophy

By

John E. Lynch

2001

UMI Number: 3026407

UMI[®]

UMI Microform 3026407

Copyright 2001 by Bell & Howell Information and Learning Company.

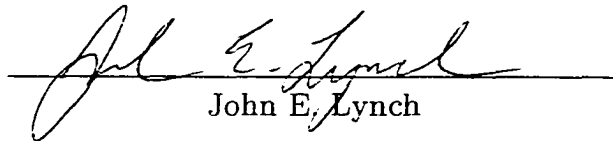
All rights reserved. This microform edition is protected against
unauthorized copying under Title 17, United States Code.

Bell & Howell Information and Learning Company
300 North Zeeb Road
P.O. Box 1346
Ann Arbor, MI 48106-1346


APPROVAL SHEET

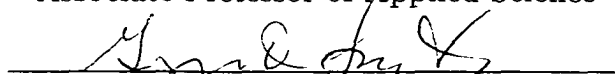
This dissertation is submitted in partial fulfillment of
the requirements for the degree of

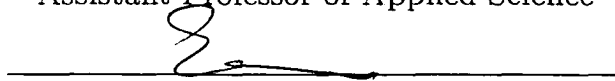
Doctor of Philosophy

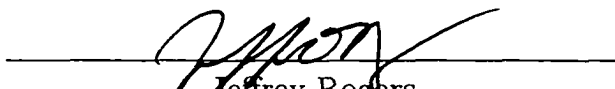

John E. Lynch

Approved, June 2001


Mark K. Hinders
Associate Professor of Applied Science


Gregory Smith
Assistant Professor of Applied Science


Eric Madaras
NASA Langley Research Center


Jeffrey Rogers
Medical College of Virginia

**ULTRASONOGRAPHIC MEASUREMENT OF
PERIODONTAL ATTACHMENT LEVELS**

Copyright

by

John E. Lynch

2001

Dedication

To Mary and Evan. Also, to my father, who's now forgiven for all those bad statistician jokes.

Contents

Acknowledgements	viii
List of Tables	ix
List of Figures	xv
1 Introduction	1
1.1 Periodontal Disease	1
1.2 Current Diagnostic Techniques	7
1.3 New Diagnostic Tests	13
2 Introduction to Ultrasonography	19
2.1 The Physics of Ultrasound	19
2.2 Imaging with Ultrasound	23
2.3 History of Ultrasound in Medicine and Dentistry	28
3 Optimization of Probe Tip Geometry	31
3.1 The Cylindrical Acoustic Finite Integration Technique	31

3.2	Parameter Testing	36
3.3	Shape Comparisons	54
4	Development of the Probe	58
4.1	Probe System Setup	58
4.2	Determination of Optimal Water Flow	60
4.3	Experimental Validation of the Tip Shape Simulation	67
4.4	Transducer Testing	82
5	Development of Signal Processing Algorithms	90
5.1	Preliminary Tests	90
5.2	Signal Processing	103
6	Clinical Trials	113
6.1	The Study Protocol	113
6.2	Data Processing Techniques	119
6.3	Statistical Analysis of the Probing Depth Measurements	129
7	Elastodynamic Simulation of the Periodontium	148
7.1	Simulation Development	148
7.2	Simulation Testing	153
7.3	Simulation Results	160
8	Conclusion and Recommendations for Future Work	170

8.1	Engineering of the Probe	170
8.2	Signal Processing	173
8.3	Clinical Trials	174
	Bibliography	179

Acknowledgements

This effort was made possible by the assistance of many people. First I would like to thank Dr. Hinders and the other members of my committee for their support and helpful suggestions in preparing the manuscript. I would also like to thank Jonathan Stevens for constructing much of the instrumentation used in this work, Gayle McCombs of Old Dominion University for her assistance in organizing the clinical trials, and my father, John K. Lynch, for his assistance with the statistical analysis of the clinical trials data. I would also like to acknowledge the support of my colleagues at the National Technology Transfer Center, who gave me the freedom to remain in Williamsburg while pursuing this work.

List of Tables

4.1	Water flow and velocity versus pressure values	64
4.2	Hole depths in the plexiglas phantom	76
5.1	Pocket depths in cadaver jaw specimens	100
6.1	Feature depths for three different algorithms	127

List of Figures

1.1	U.S. periodontal disease infection rate	2
1.2	The periodontal anatomy	4
1.3	Stages of periodontal disease	6
1.4	Diagnostic tests for periodontal disease	8
1.5	Manual periodontal probe	9
1.6	Ultrasonic periodontal probe position	14
1.7	Periodontal probe described by Hinders and Companion.	16
2.1	The compressions and rarefactions of a sound wave	20
2.2	Reflection and transmission of a sound wave	23
2.3	Transmission of an elastodynamic wave	24
2.4	A pulse-echo setup used in ultrasonic imaging	25
2.5	Representative A-scan image	26
2.6	Representative B-scan image	27
3.1	The staggered grid of the CAFIT algorithm	34

3.2	Simulation results for $\Delta r = 0.05$ r.u.	37
3.3	Wavefront at $t = 10$ r.u. for $\Delta r = 0.05$ r.u.	38
3.4	Simulation results for $\Delta r = 0.01$ r.u.	39
3.5	Wavefront at $t = 10$ r.u. for $\Delta r = 0.01$ r.u.	40
3.6	Simulation results for $\Delta r = 0.005$ r.u.	41
3.7	Wavefront at $t = 10$ r.u. for $\Delta r = 0.005$ r.u.	42
3.8	Simulation results for $\Delta r = 0.003$ r.u.	43
3.9	Wavefront at $t = 10$ r.u. for $\Delta r = 0.003$ r.u.	44
3.10	Frequency and return signal quality	45
3.11	Step size and return signal quality	46
3.12	Tip shape as the wall angle varies	47
3.13	Results for varying wall angles	48
3.14	Tip shape as the angle varies (distance to reflector constant)	49
3.15	Results for varying wall angles (distance to reflector constant)	50
3.16	Tip shape as the tip diameter at the top varies	51
3.17	Results for varying the tip diameter	52
3.18	The effect of aiming the tip into a bath of water	53
3.19	Return signal for the linear tip	55
3.20	Return signal for the exponential tip	55
3.21	Return signal for the parabolic tip	56
3.22	Return signal for the ellipsoid tip	56

4.1	Design drawings for prototype probe	59
4.2	Rackmount computer system	61
4.3	Signal at different flow states	63
4.4	Signal at different pressure settings	66
4.5	Shapes of the machined tips.	68
4.6	Simulated and experimental results for linear tip	69
4.7	Simulated and experimental results for exponential tip	70
4.8	Simulated and experimental results for spline tip	71
4.9	Simulated and experimental performance of the linear brass tip	72
4.10	The effect of rounding the outlet	75
4.11	Scan of holes using the linear tip	77
4.12	Scan of holes using the exponential tip	78
4.13	Scan of holes using the spline tip	79
4.14	Scan of holes using the shorter, brass linear tip	80
4.15	Testing transducers in open air	83
4.16	Transducer ringing	84
4.17	Plexiglas holes with 10MHz transducer	85
4.18	Plexiglas holes with 15MHz transducer	86
4.19	Plexiglas holes with second 15MHz transducer	87
4.20	Plexiglas holes with 20MHz transducer	88
5.1	Return signal from 3 mm pocket	92

5.2	Signal averages trace for 3 mm pocket	92
5.3	Return signal from 4 mm pocket	94
5.4	Signal averaged trace for 4 mm pocket	94
5.5	Return signal for 5 mm pocket	96
5.6	Signal averaged trace for 5 mm pocket	96
5.7	Tooth 4.7 cadaver scan	98
5.8	Scan with probe placed in a tub of water	99
5.9	A-scan view of cadaver tooth 4.7	101
5.10	Manual versus ultrasonographic probing depths	104
5.11	Comparison of original waveform to peak picking	107
5.12	B-mode image of tooth 3, mid-buccal position	108
5.13	Tooth 3, mid-buccal position, with peak picking	109
5.14	Mid-buccal scan of tooth 3 with peak picking and averaging .	110
5.15	Manual vs. ultrasonographic probing, after processing	112
6.1	Probes used during the clinical trials	114
6.2	Example A-scan trace from the clinical trials data	118
6.3	Example clinical trials data, after signal processing	119
6.4	Transitions in signal strength	120
6.5	Time gain amplification	121
6.6	Structure of the junctional epithelium	123
6.7	Smoothed data for automatic interpretation	126

6.8	Transition detection using derivatives	128
6.9	Difference plot comparison	131
6.10	Fitting a line using orthogonal regression	132
6.11	Orthogonal fit results (part 1)	134
6.12	Orthogonal fit results (part 2)	135
6.13	Orthogonal fit results (part 3)	136
6.14	One-way ANOVA results (part 1)	138
6.15	One-way ANOVA results (part 2)	139
6.16	One-way ANOVA results (part 3)	140
6.17	One-way ANOVA versus GI results (part 1)	142
6.18	One-way ANOVA versus GI results (part 2)	143
6.19	One-way ANOVA versus GI results (part 3)	144
6.20	Repeated measures analysis	146
7.1	Idealized periodontium used in this simulation	150
7.2	Axi-symmetric and Cartesian grids	155
7.3	Cylindrical to Cartesian coordinate conversion	156
7.4	CAFIT and EFIT trace comparison	158
7.5	CAFIT and EFIT wavefront comparison	159
7.6	Periodontium simulation with and without the probe	161
7.7	Trace for idealized periodontium	162
7.8	Trace for irregularity at 1 r.u.	162

7.9	Attenuation factor added to simulation	163
7.10	Irregularity at 1 r.u., plus attenuation	164
7.11	Irregularity at 1.7 r.u.	165
7.12	Irregularity at 3.1 r.u.	165
7.13	Irregularity at 1.7 r.u., junctional epithelium at 2.0 r.u.	166
7.14	Irregularities 0.05 r.u. wide	168
7.15	Irregularities 0.03 r.u. wide	169
8.1	Next-generation ultrasonographic probe	172

Abstract

Periodontal disease is one of the two major causes of tooth loss today, and has been associated with several systemic diseases, such as diabetes, cardiovascular disease, stroke, and adverse pregnancy outcomes. Unfortunately, the most widely used diagnostic tool for assessment of periodontal diseases, measurement of periodontal attachment loss with a manual probe, may overestimate attachment loss by as much as 2 mm in untreated sites, while underestimating attachment loss by an even greater margin following treatment. Manual probing is also invasive, which causes patient discomfort.

This work describes the development and testing of an ultrasonographic periodontal probe designed to replace manual probing. It uses a thin stream of water to project an ultrasonic beam into the periodontal pocket and then measures echoes off the periodontal ligament. Development issues addressed in this work included the proper design of the probe tip, which is needed to narrow the ultrasonic beam from a transducer with a 2 mm diameter active area to a 0.5 mm beam, which is the approximate width of the periodontal pocket at the gingival margin. The proper choice of transducer frequency, the proper method for controlling water flow from the probe, and the development of signal processing algorithms to aid in the interpretation of the echoes were also addressed.

To test the ultrasonographic probe, clinical trials were conducted on 12 patients in conjunction with the Old Dominion University School of Dental Hygiene. These tests indicate that probing depth measurements obtained through the ultrasonographic probe do not correlate with manual probing depths, since ultrasonographic probing measures echoes off specific anatomical features, while manual probing measures resistance to probing force. However, ultrasonographic probing did show promise as a diagnostic tool, as ultrasonic probing depth measurements correlated to overall gingival health, as measured by the Gingival Index of Loe and Silness. In addition, ultrasonographic probing, when combined with an automated feature recognition algorithm, showed better repeatability than manual and controlled-force probing.

**ULTRASONOGRAPHIC
MEASUREMENT OF
PERIODONTAL ATTACHMENT
LEVELS**

Chapter 1

Introduction

1.1 Periodontal Disease

Periodontal disease is one of the two major causes of tooth loss today, and is widely pervasive in older adults. Most adults have a mild form of periodontal disease, while over 20 percent of older Americans have severe periodontal disease [1, 2, 3]. A detailed analysis of the rate of periodontal disease infection for different age groups can be seen in figure 1.1, which is taken from *Oral Health in America: A Report to the Surgeon General*.

In addition to being a major cause of tooth loss, periodontal disease has recently been associated with several systemic diseases. Animal and population-based studies have demonstrated an association between periodontal disease and diabetes, cardiovascular disease, stroke, and adverse

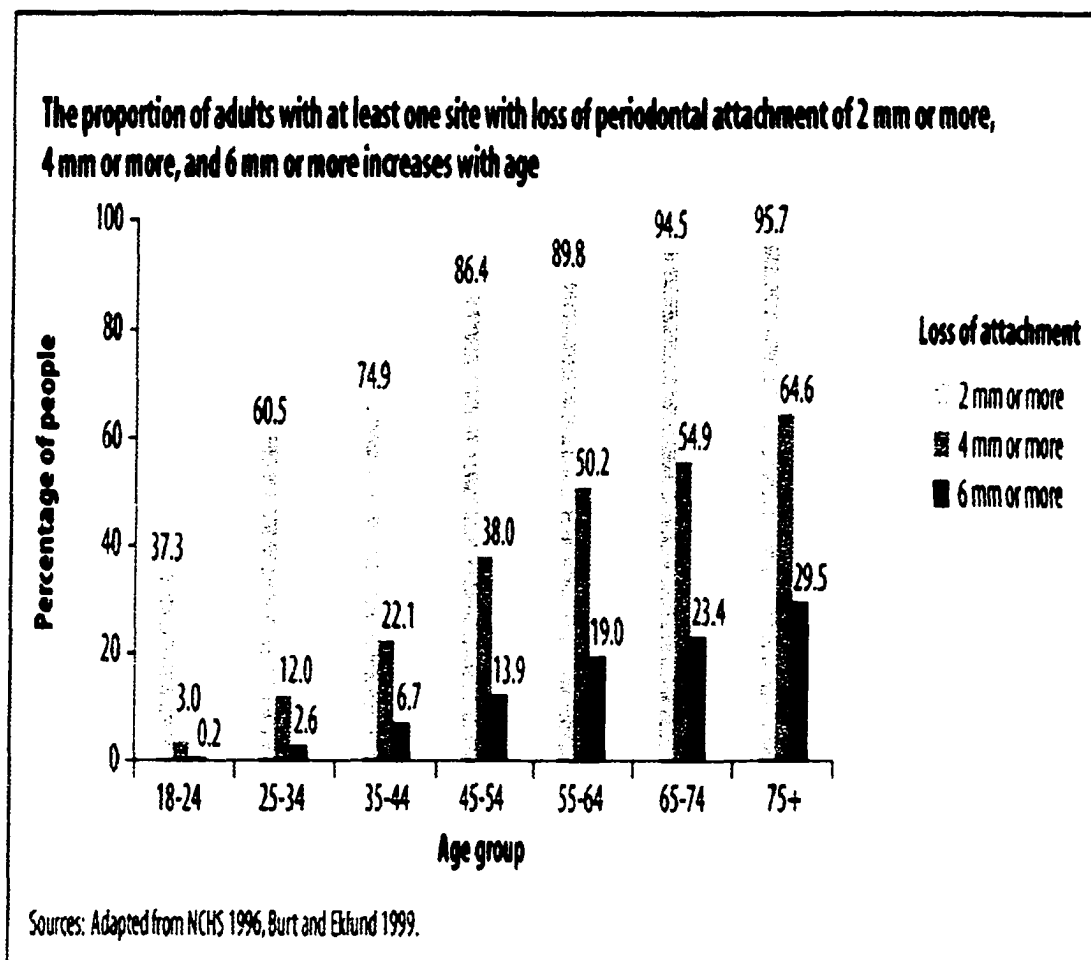


Figure 1.1: U.S. Periodontal Disease Infection Rate, as published in *Oral Health in America: A Report to the Surgeon General* [5].

pregnancy outcomes [4, 5]. Although the mechanisms that cause these associations are still not completely understood, more reliable detection of early stage periodontal disease could have widespread health benefits beyond the prevention of tooth loss.

Periodontal disease is the result of infections caused by bacteria in the plaque that form on oral surfaces. Symptomatically it begins as an inflammation of the gums characterized by a change in color from normal pink to red, with swelling, bleeding, and often sensitivity and tenderness. This early-stage periodontal disease is called gingivitis. More advanced periodontal disease (periodontitis) involves the loss of connective tissue attachment with subsequent destruction of alveolar (tooth-supporting) bone. If not treated, periodontitis can lead to the loss of teeth.

Destruction of connective tissue during periodontal disease results in the formation of periodontal pockets, which are defined anatomically as the region from gingival margin to the coronal (top) end of the junctional epithelium, as shown in figure 1.2 [6, 7]. In a healthy periodontium, this region is referred to as the sulcus, and is about 0.5 mm deep.

The region apical to (below) the sulcus is the junctional epithelium, a thin layer of skin-like tissue that is attached to the tooth surface. The junctional epithelium is about 0.15 mm wide subjacent to the sulcus bottom, and only a few cell layers thick at the bottom. In a healthy

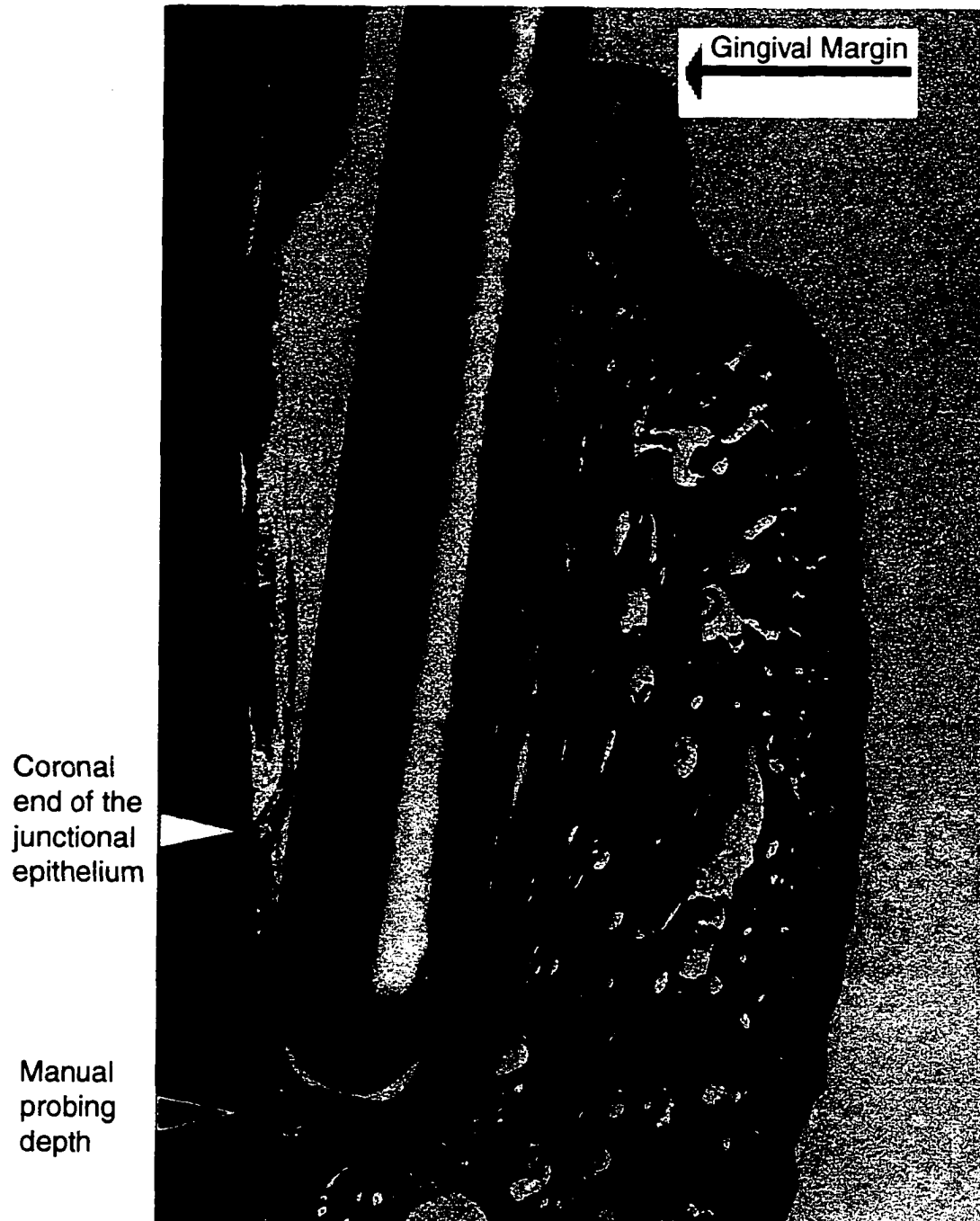


Figure 1.2: The periodontal pocket is defined anatomically as the region from the gingival margin to the coronal end of the junctional epithelium [8].

patient, the junctional epithelium is about 2 mm deep. In early gingivitis, a deeper sulcus can result from a small loss of junctional epithelium or from tissue inflammation and swelling. For patients with mild gingivitis, the sulcus may be a few millimeters deep, while it can be over 4 mm deep for patients with periodontitis.

As disease progresses to later stage gingivitis and then to periodontitis, the connective tissue and even alveolar bone will be lost to disease. However, since epithelial layers are continually replaced every 4-6 days, a small region of junctional epithelium will be present subjacent to the sulcus in all patients [8].

In a healthy patient, the junctional epithelium gives way to connective tissue at the cemento-enamel junction (CEJ). The first layer of connective tissue is the gingival fiber bundles, in which collagen fiber bundles are embedded in the gingiva and spread out in various directions to give the gingiva its stiffness. The gingival fiber bundles increase in density until they reach their highest density just above the alveolar bone. At the alveolar bone, the connective tissue is called the periodontal ligament, which attaches the root to the alveolar bone. Figure 1.3 shows the anatomic changes in the periodontium as periodontal disease progress from health to severe periodontitis.

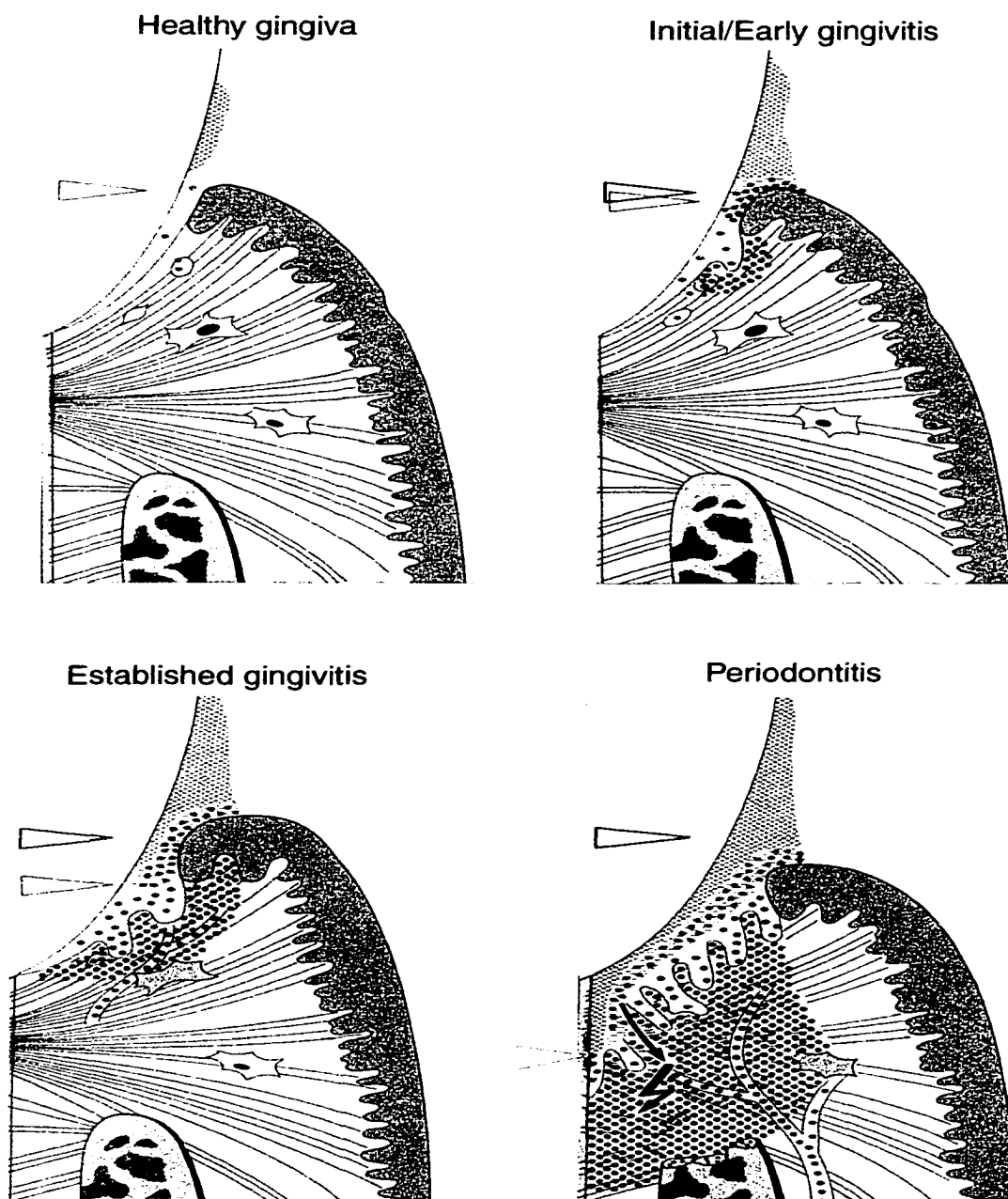


Figure 1.3: The stages of periodontal disease. The top-left drawing shows a healthy periodontium; the top-right early gingivitis, with a small pocket formed as indicated by the arrows; the bottom-left established gingivitis, with a deeper pocket; and the bottom-right periodontitis [8].

1.2 Current Diagnostic Techniques

Despite the widespread problem of periodontal disease today, currently available diagnostic tests are limited in their effectiveness. A summary of these tests is provided in figure 1.4. None of the tests are a completely reliable indicator of periodontal disease activity and the best available diagnostic aid, probing pocket depths, is only a retrospective analysis of attachment already lost [9, 10, 11, 12, 13, 14, 15]. In this technique, a probe such as the one shown in figure 1.5 is placed between the soft tissue of the gingival margin and the tooth. Using fixed markings on the probe, typically 1 or 2 mm apart, the depth of probe penetration is measured relative to a fixed point on the tooth such as the cemento-enamel junction (called the clinical attachment level). Alternatively, the depth is measured relative to the gingival margin (called the probing depth).

The first test outlined in figure 1.4, periodontal screening and recording, is a simplified method for probing pocket depths that allows quick diagnosis of patients. However, it does not provide a tooth-by-tooth assessment that allows for quantitative comparisons over time. Similarly, measures of gingival inflammation (listed third in figure 1.4) only provide a general indication of gingival health through the observation of gingival inflammation. The inability of both these diagnostic tools to provide a tooth-by-tooth assessment for later comparison is a major drawback, since

Test	Application	Strengths	Weaknesses
Periodontal screening and recording (PSR)	All patients in every practice	Cost-effective, quick, easy; detects patients with periodontal disease.	Does not provide a tooth-by-tooth assessment for later comparison during maintenance. A full periodontal examination is needed for this purpose.
Probing pocket depths	All patients	Shallow probing depths are associated with a lack of future disease progression.	Moderate to deep pockets in single probing depth examination will not distinguish with certainty which teeth will undergo progressive periodontal destruction
Gingival inflammation	Assessed in all patients	Absence of inflammation is associated with a lack of future progression. In treated patients, bleeding on probing is associated with an increased risk for progressive loss of attachment.	Presence of inflammation will not distinguish with certainty which teeth will undergo progressive periodontal destruction.
Radiographic evidence of bone loss	At risk patients as determined by PSR or periodontal examination	Absence of bone loss is associated with a lower risk of future progression.	Presence of bone loss on a single radiograph will not distinguish with certainty which teeth will undergo progressive periodontal destruction.
Microbial/plaque studies	High-risk or refractory studies	Absence of supragingival plaque is associated with lack of disease progression. In compromised or refractory patients, may be useful in determining the presence of pathogens.	At this time, routine testing offers limited benefit in adult periodontitis.
Biochemical profiles in gingival crevicular fluid	Not yet determined	A number of biochemical markers may identify individuals at risk.	At present, there are no specific biochemical profiles that characterize specific periodontal diseases.

Figure 1.4: Diagnostic tests for periodontal disease used today [64].



Figure 1.5: The standard tool used for manual probing of periodontal pocket depths [8].

disease activity occurs in periods of exacerbation and remission at specific but unpredictable locations. Therefore a quantitative diagnostic technique is needed that will allow site-by-site comparisons over time.

The second test listed in figure 1.4, probing of periodontal pocket depths, is the best diagnostic tool available today. Even so, numerous studies have questioned the ability of the periodontal probe to accurately measure the anatomic pocket depth [16, 17, 18, 19]. Instead, the periodontal probe measures the probing attachment level, which is defined as the distance from the cemento-enamel junction to the apical depth of periodontal probe tip penetration into the gingival crevice. The degree of probe tip penetration may be influenced by factors such as thickness of the probe, pressure applied, tooth contour, tooth position, presence of calculus, degree of periodontal inflammation, and the actual level of connective tissue fibers [20, 21, 22, 23, 24, 25].

As a result, probing measurements may overestimate attachment loss by as much as 2 mm in untreated sites, while underestimating attachment loss by an even greater margin following treatment [26, 27]. The development of automated, controlled force probes has reduced some of the operator-related error and subjectivity inherent in manual probing techniques [28, 29, 30, 31]. However, standardized probing forces do not address anatomic and inflammatory factors [32, 33, 34].

In addition, a computer-vision system that automates the reading of manual probe marking to the nearest 0.1 mm has been investigated to improve the accuracy of the depth readings [35, 36]. Once again, this technique only address one concern associated with manual probing—the inaccuracy in reading probing depths—while failing to address other sources of error.

Due to the inherent measurement error of routine manual probing, a 2 to 3 mm loss of probing attachment is required before a statistically significant loss of actual connective tissue can be identified [37, 38]. A manual probe cannot accurately detect small changes in attachment level until the cumulative loss reaches this threshold. The accuracy of research-oriented, computerized controlled force probes reduces this critical attachment loss threshold to a potential minimum of ± 1 mm [39].

Detection of bone loss through radiography, the fourth test outlined in figure 1.4, is another technique for the diagnosis of periodontal disease. However, to detect small changes in bone loss over time, subtraction radiography must be used. Even in this case, radiography cannot evaluate periodontal ligament attachment, and changes in bone have been shown to lag losses in connective tissue by several months [40, 41, 42, 43, 44]. This delay in diagnosis may reduce the effectiveness of interventional therapy. Finally, because serial radiography subjects patients to increasing amounts

of ionizing radiation, its use is limited to patients who have already been identified as at risk for periodontal disease.

Tests for the presence of periodontal disease-causing microbes in the subgingival plaque, listed fifth in figure 1.4, have also been developed. These tests are useful in formulating treatment programs for special patient populations and as a research tool. However, due to the limitations described below, routine testing is not usually necessary and indeed is not supported by the preponderance of the evidence [45, 46].

The traditional method for assessing the subgingival flora is by culturing samples extracted from the site of infection. Culturing allows the clinician to determine the antibiotic sensitivity of the organisms, but it is technique-sensitive: scrupulous care is required when sampling the periodontal pocket. This is especially true for microbes that are strict anaerobes, because they are killed by even brief exposure to air. The requirement that bacteria have time to grow also precludes chairside testing.

Bacterial species can also be identified by their DNA [47, 48, 49], or by unique antigenic components [50]. While the tests are quicker and more accurate than culturing, they do not indicate whether there is actual disease. Nor do the tests reveal anything about the antibiotic sensitivity of the detected bacteria.

Finally, biochemical profiles of the gingival crevical fluid (listed sixth

in figure 1.4) are now being investigated as a diagnostic tool. Once a periodontal infection is established, telltale metabolic changes occur in the body as a result of inflammation, injury, or death of tissue. A sample of fluid exudate from the gingiva in an affected pocket can be analyzed for these changes. They include elevated levels of prostaglandin E2 [51], interleukin 1 and interleukin 6 [52, 53, 54, 55], tumor necrosis factor [56], β -glucuronidase [57, 58], aspartate aminotransferase [59, 60], elastase [61, 62], and collagenase [63]. However, no scientific consensus has emerged to determine whether these metabolite measurements have the sensitivity and specificity to reliably detect disease [64].

1.3 New Diagnostic Tests

In addition to the diagnostic tests described in figure 1.4, several research projects have attempted to develop new diagnostic aids. Ultrasonographic and light-based imaging have both received some attention, although most of the research has been focused on the use of ultrasound because it has a greater penetration depth than light. One light-based technique called optical coherence tomography is under development that seeks to filter out backscattered light through the use of a Michelson interferometer, and thus allow imaging of internal structures 1-3 mm deep. While this technique has produced images of periodontal structure in *in vitro* porcine teeth, the

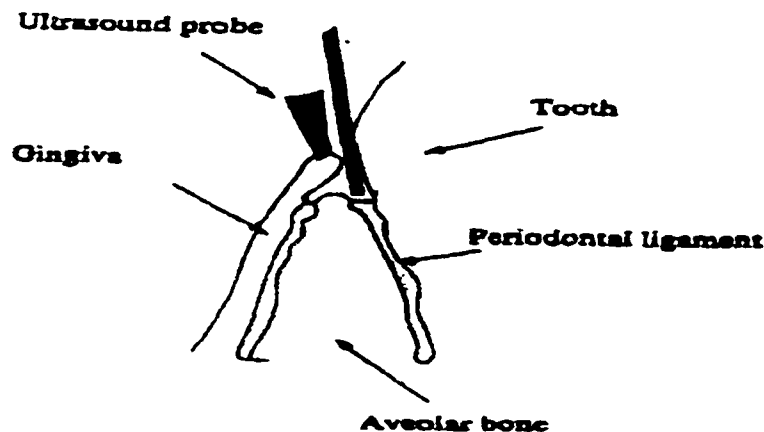


Figure 1.6: After earlier failures to image the periodontal pocket by aiming the ultrasonic probe through the gingival wall, recent research has been directed toward aiming the ultrasonic transducer apically into the periodontal pocket [70].

penetration depth is not yet great enough to reliably image through the gingival width of all teeth [65].

The first tests of ultrasonographic imaging of the periodontal space were designed to image the crest of the alveolar bone by aiming the ultrasound transducer perpendicular to the long axis of the tooth [66, 67, 68]. While these efforts proved the feasibility of ultrasonographic imaging, the techniques could not detect periodontal attachment loss. Instead, they could only detect echoes off the alveolar bone, and they never gained clinical acceptance.

More recently, alternative research has been conducted on the use of ultrasound to image the periodontal pocket space by aiming the transducer apically into the pocket from the gingival margin [69, 70, 71]. The major technical barrier to this approach is providing an efficient coupling medium for the ultrasonic wave into the thin (0.25-0.5mm) periodontal pocket. The method of Loker and Hagenbuch uses a metal delay line placed on the crest of the gingival tissue, so that the ultrasound wave travels through the gingiva. (Figure 1.6). As a result, this technique measures echoes off the alveolar bone rather than the periodontal ligament, since the bone is the only hard tissue coupled to the gingiva. Lassal and Payne investigated the use of a thin plate to serve as a Lamb-wave based waveguide. This research only reported on the laboratory testing such a waveguide, with no attempt made to image periodontal structures. However, since they envision coupling with the soft gingival tissue, they are likely to produce results similar to that of Loker and Hagenbuch.

The probe described by Hinders and Companion uses a thin stream of water to couple the ultrasound wave into the pocket space. (Figure 1.7). A tip placed over the transducer narrows the ultrasonic beam, so that the beam is approximately the same width as the opening into the sulcus at the gingival margin. Feasibility of the technique was demonstrated in the work of Hinders and Companion, but optimization of the probe design and

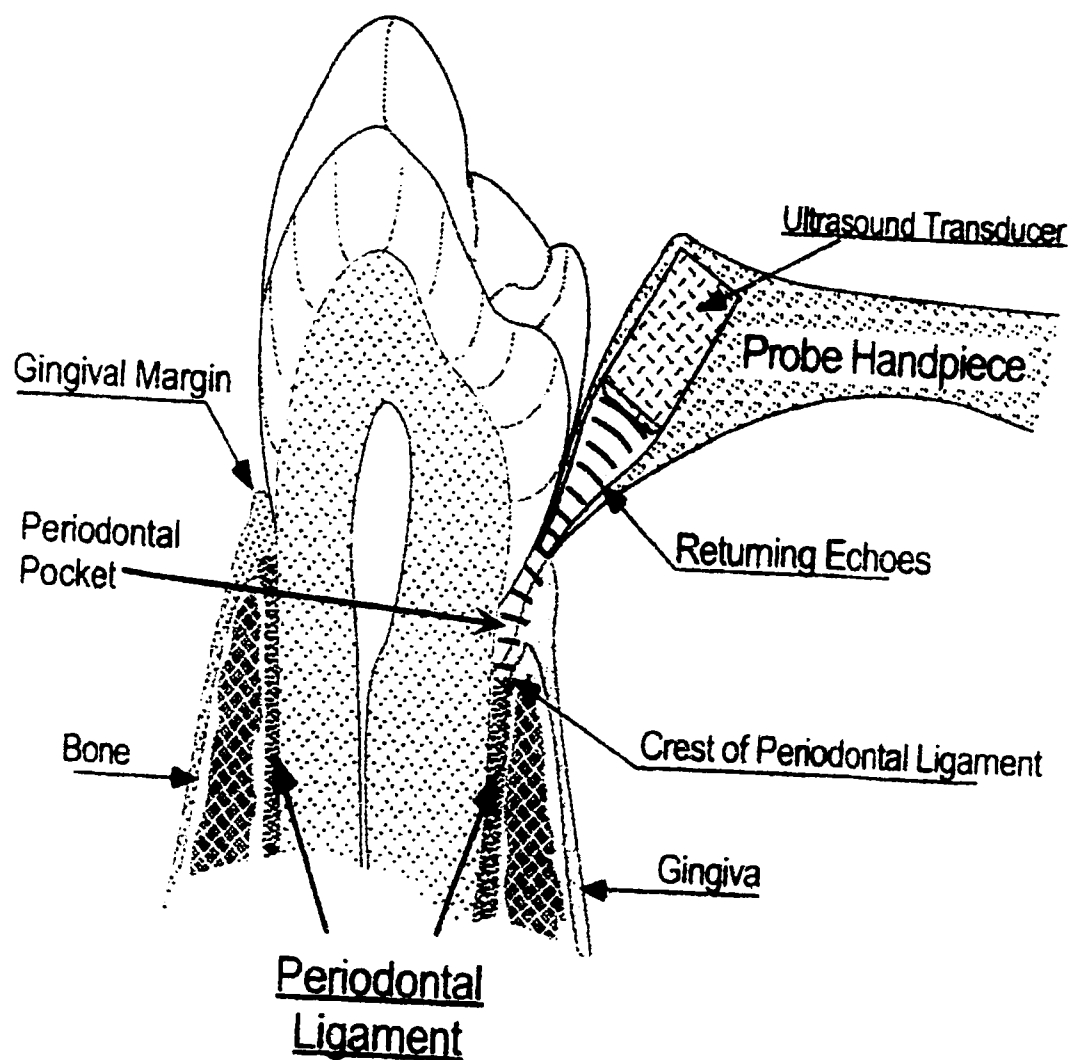


Figure 1.7: Periodontal probe described by Hinders and Companion.

clinical testing is required in order for this technique to gain widespread acceptance as a diagnostic tool in the dental community.

The aim of this work is to begin the optimization of the probe described by Hinders and Companion, and to conduct a first round of clinical testing. This testing will allow a thorough evaluation of the probe's performance, and the development of signal processing routines needed for simplified interpretation of the ultrasonic signal. These routines will be designed as a first step toward the development of artificial intelligence learning algorithms. It is anticipated that the complexity of the periodontal anatomy will require the use of automated feature recognition technology, so that the ultrasonic echoes can be translated into probing depth measurements in real-time. By doing so, dental examiners and patients will be able to easily interpret the results of the ultrasonic scan without needing a detailed understanding of how the ultrasonic technology works.

This dissertation is organized as follows. In chapter 2, a review of ultrasound technology, particularly as it relates to its use in medicine and dentistry is presented. Chapter 3 presents a computer simulation used to optimize the power transmitted through the tip of the ultrasonographic probe. Chapter 4 discusses engineering design issues related to the probe, while chapter 5 discusses the development of signal processing algorithms designed to aid data interpretation. Chapter 6 discusses the results of

clinical trials comparing the performance of the ultrasonographic probe with manual and controlled-force probing, while chapter 7 discusses a computer simulation designed to test a model proposed for interpreting the results of the clinical trials data. The dissertation concludes with a summary of the work completed and recommendations for future work.

Chapter 2

Introduction to Ultrasonography

Ultrasonography is a non-invasive imaging technique that uses ultrasonic energy to produce an acoustic map of a body. It is widely used in medicine for diagnostic imaging of anatomical structures and blood flow measurements, and in industry to detect hidden flaws in mechanical structures. This introduction to ultrasonography provides a concise description of the physics of ultrasound, its use in imaging, and a brief history of the use of ultrasound in medicine and dentistry.

2.1 The Physics of Ultrasound

Sound is mechanical energy that propagates through a continuous, elastic medium by the compression and rarefaction of the particles that comprise it. Compression occurs by a mechanical deformation induced by an external energy force that increases the pressure on the medium. Rarefaction occurs

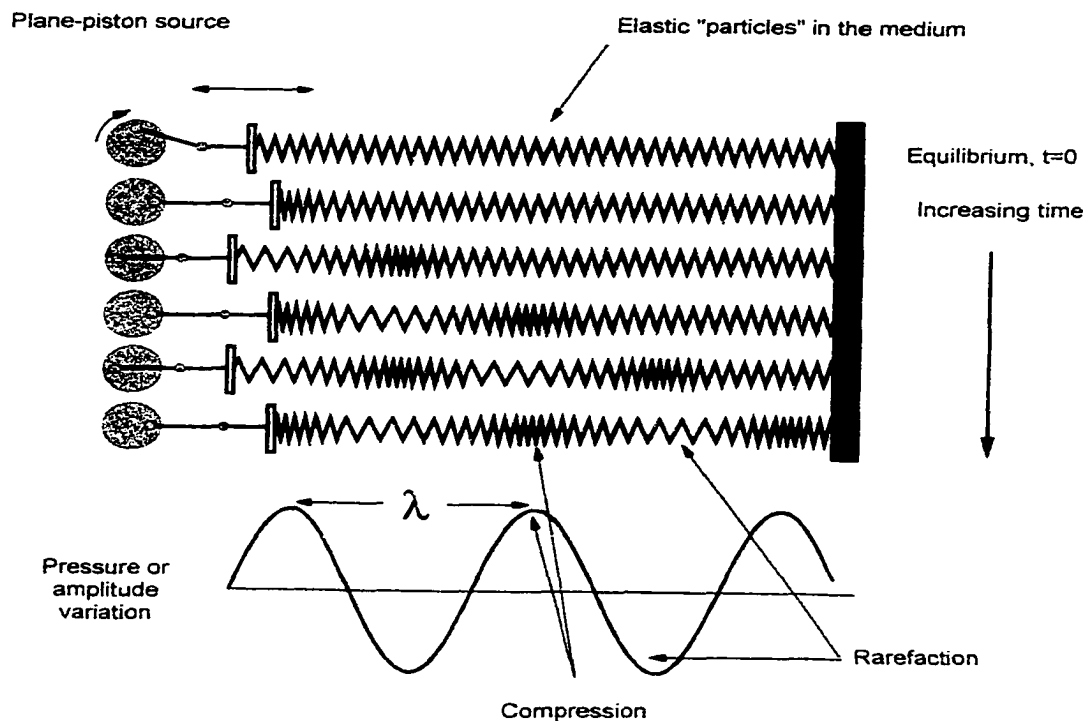


Figure 2.1: The compressions and rarefactions of a sound wave, as illustrated by the compressions and rarefactions of a spring [74].

in tandem with compression—as the force is removed, the compressed particles transfer their energy to adjacent particles with a subsequent reduction in pressure. (Figure 2.1). The series of compressions and rarefactions that propagates through the elastic medium is known as a sound wave.

The key parameters of the wave are its wavelength, frequency and velocity. The wavelength, λ , which refers to the distance between compressions or rarefactions, and is usually expressed in units of mm or μm . The frequency, ν , or number of times the sound wave repeats itself in one second, is usually expressed in units of Hertz (Hz), which equals one

wave cycle per second. The human ear is generally capable of detecting sound waves in the frequency range of 15Hz to 20kHz, and ultrasound refers to sound waves above this frequency range. The velocity of the sound wave, c , is related to λ and ν through the relationship $c = \lambda\nu$ and is dependent on the material through which the sound wave propagates. Generally, the stiffer the material, the faster the speed of sound in that material.

Mathematically, this compression and rarefaction of particles within a medium is described through the theory of elastodynamics. A simplified introduction to elastodynamics can be provided through two equations. The first equation is a derivation of Newton's second law of motion, $F = ma$ for the case of an elastic medium, which is expressed in the index notation for tensors as

$$\rho \partial_t^2 u_i - \partial_j \sigma_{ij} = 0, \quad (2.1)$$

where ρ is the mass density of the medium, u_i is the displacement vector of the particles within the medium, and σ_{ij} is the second rank stress tensor.

The second equation is the generalized Hooke's law

$$\sigma_{ij} = C_{ijkl} \epsilon_{kl}, \quad (2.2)$$

which states that the normalized deformation ϵ in a body is proportional to the stress placed on it. The proportionality constant C_{ijkl} in equation (2.2) is material dependent and, for the simple case of isotropic materials, is related to the Lamè constant λ^* and the shear modulus μ . The Lamè

constant λ can be described as a measure of a material's stiffness, while the shear modulus μ is a measure of a material's ability to propagate shear waves.

By substituting the strain displacement relation $\epsilon_{kl} = \frac{1}{2}(\partial_k u_l + \partial_l u_k)$ into equation (2.2) the elastodynamic wave equation can be derived, which is:

$$\rho \partial_t^2 u_i - \mu \partial^2 u_i + (\lambda + \mu) \partial_i (\partial_j u_j) = 0. \quad (2.3)$$

In the case of a fluid, which has a shear modulus approaching zero, the elastodynamic wave equation simplifies to:

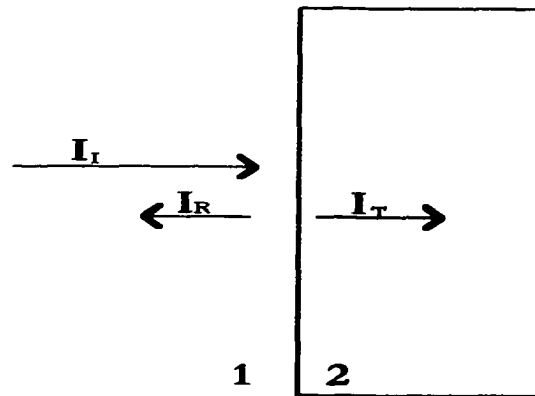
$$\rho \partial_t^2 u_i + \lambda \partial_j u_j = 0. \quad (2.4)$$

However, this simplification is usually expressed in terms of pressure, rather than the displacement vector u_i , because pressure is a scalar quantity defined as the perpendicular fluid force per unit area. With some mathematical manipulation, this simplification is:

$$(\nabla^2 + \frac{\omega^2}{c^2})p = 0, \quad (2.5)$$

where ω is $2\pi\nu$ and c is the speed of sound.

As a plane wave described by either equation (2.3) or (2.5) encounters an interface between two materials, it is divided into two components: some energy at the interface is reflected and some is transmitted. For the most simple case, in which the acoustic plane wave is



$$R_{12} = I_R / I_I = (Z_1 - Z_2) / (Z_1 + Z_2)$$

$$T_{12} = I_T / I_I = 2 Z_2 / (Z_1 + Z_2)$$

Where $Z = \rho c =$ acoustic impedance

Figure 2.2: Reflection and transmission of a sound wave incident normal to boundary between two materials [73].

incident normal to the material interface, the formula for computing the reflection and transmission factors is illustrated in figure 2.2.

In the more complicated case of a non-normal elastodynamic wave, the transmitted wave is refracted and divided into two components, a shear wave and a longitudinal wave, as shown in figure 2.3 [72, 73, 74].

2.2 Imaging with Ultrasound

In a typical set-up for ultrasonic imaging in medical applications, a transducer operates in pulse-echo mode (figure 2.4). That is, the piezoelectric transducer converts an electronic signal into an ultrasonic

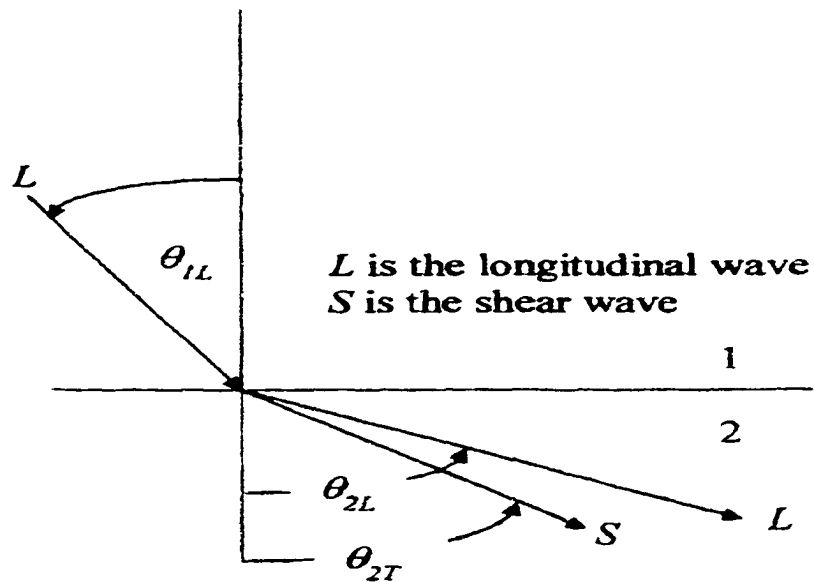


Figure 2.3: Transmission of an elastodynamic wave incident on a material boundary layer [73].

pulse, which propagates to tissue boundaries. At these boundaries, some of the incident wave energy is reflected, producing an echo. When this echo returns to the transducer, the wave's mechanical echo is converted to an electrical signal, which can be displayed as an A-mode image.

An A-mode image, or A-scan, displays the amplitude of the return echoes, as in figure 2.5. Each peak in the A-scan image represents a return echo, whose distance from the transducer can be determined by the equation

$$D = \frac{ct}{2}, \quad (2.6)$$

where D is distance, c is the speed of sound, t is the time of return echo

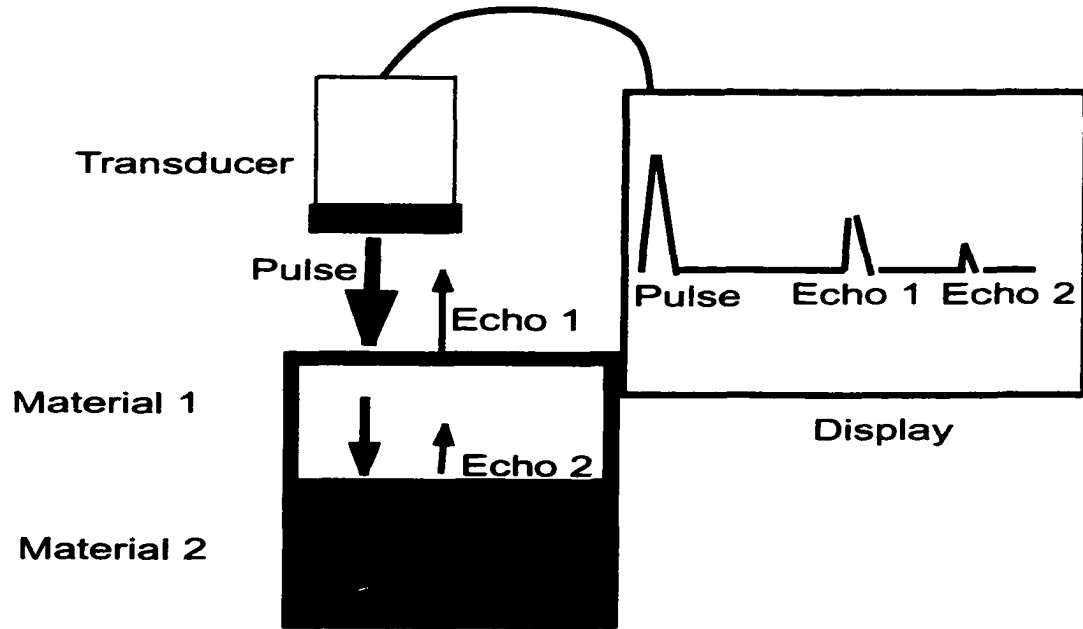


Figure 2.4: A pulse-echo setup used in ultrasonic imaging.

and the factor of 2 accounts for the fact that the echo must travel to the tissue interface and back to be detected by the transducer.

If the transducer scans from position to position, the series of A-mode images produced from the scanning can be added sequentially to produce a B-mode image, or B-scan, which converts the peak heights in the A-scan trace into a brightness value and assembles a series A-scan traces together to form a two-dimensional image (figure 2.6).

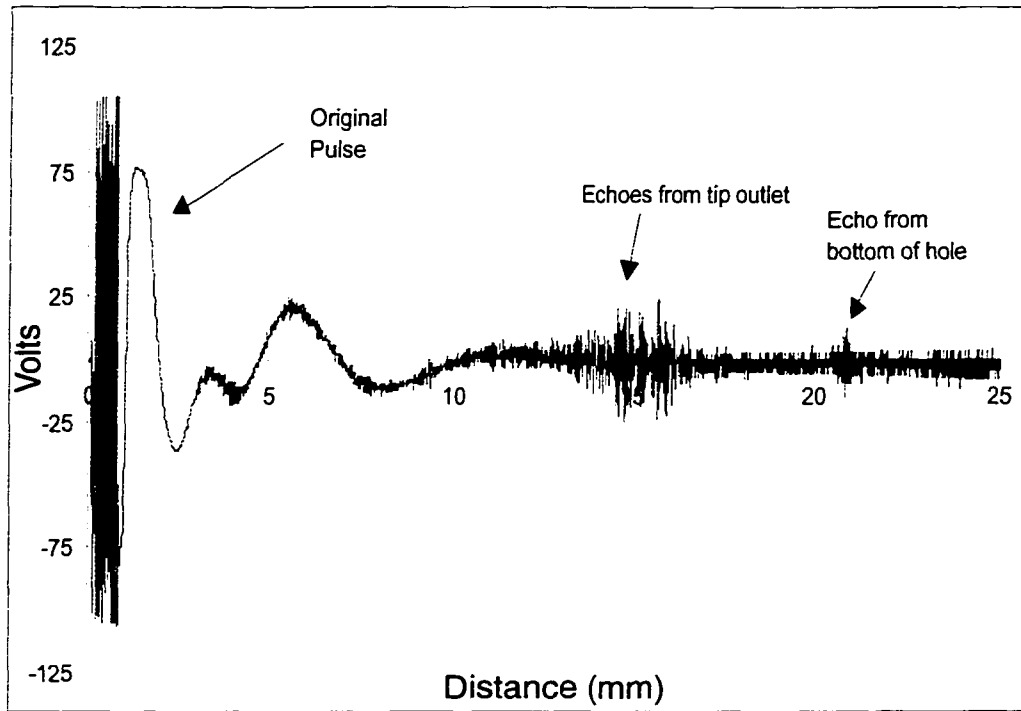


Figure 2.5: A representative A-scan image, taken with the ultrasonographic probe aimed at a 5mm-deep hole drilled in plexiglas. The peak heights represent the strength of the return echo.

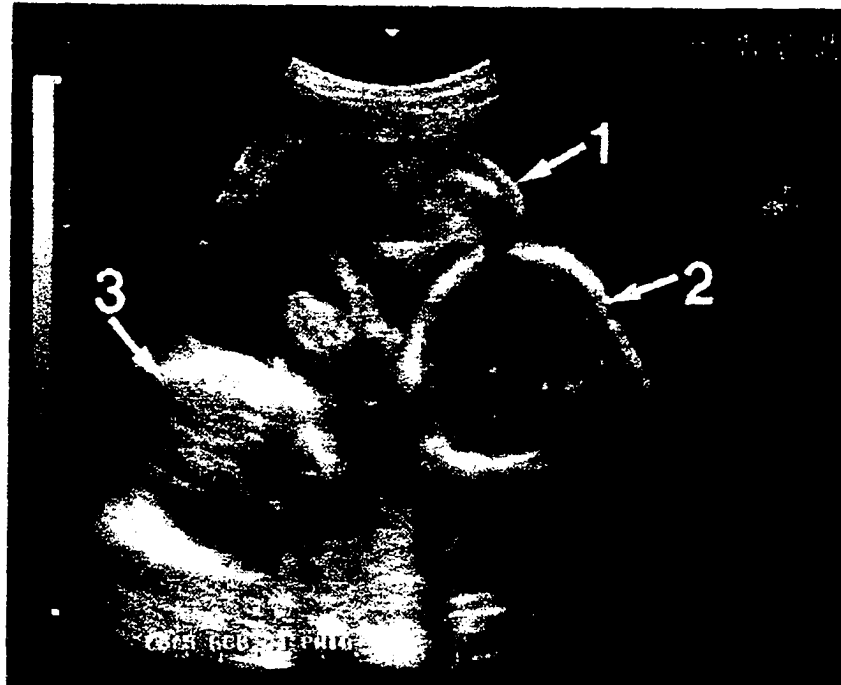


Figure 2.6: A representative B-scan image, where the brightness values of each pixel represent the strength of the return echo. The image is of triplets scanned using fetal ultrasound [77].

2.3 History of Ultrasound in Medicine and Dentistry

The first recorded use of sound-based imaging occurred in 1822, when Daniel Colladen used an underwater bell to calculate the speed of sound in the waters of Lake Geneva. However, this echo-sounding technique did not find widespread use until Pierre and Jacques Curie's 1880 discovery of the piezoelectric effect in certain crystals. This discovery made it possible to generate the ultrasonic waves needed to produce high-resolution images. A big push for the technology came during World War I, as underwater detection systems were needed for the navigation and remote detection of submarines.

Early use of ultrasonics in medicine, however, was largely confined to therapeutic applications, which utilized the heating effect from high-power, low-frequency ultrasound. It wasn't until after World War II that ultrasound received much attention for medical imaging. At this time, equipment capable of high-frequency and shorter pulse operation, and the availability of very high input impedance amplifiers, helped improve the resolution and sensitivity of ultrasonic imaging devices to make them attractive for medical applications.

Soon, many systems were developed that were capable of producing 2-D, accurate and reproducible images of the body organs. However, all of

these systems required the patient to be totally or partially immersed in water and remain motionless for extended periods. The development of smaller and better transducers made from barium titanate and lead zirconium-titanate ceramics improved the sensitivity and size of imaging equipment. These improvements allowed for the development of transducers placed in water bags, or those that only required a gel spread on the skin to couple the ultrasonic wave with the body.

The first commercial medical ultrasound system was the Diasonograph, which produced B-mode images by moving a probe across the abdomen using a motorized scanner. During the 1960's similar machines proliferated, until the development of phased- and linear-array transducers and real-time imaging in the late 1960's and early 1970's. These developments allowed B-scan images to be produced from a single probing position, thus eliminating the need for a motorized scanning arm. The result was the hand-held probe similar to what is used in the clinical ultrasound equipment today [75].

In dentistry, ultrasound is still primarily limited to therapeutic uses. The two main uses for ultrasonic instrumentation are the ultrasonic scaler and endodontic devices. The ultrasonic scaler operates at a frequency of 16-20kHz, and uses these high-frequency vibrations to mechanically remove plaque and calculus from the surface of the tooth. In endodontics, a

specially designed file is added to an ultrasonic scaler, which is then used to shape and clean root canals during root canal therapy [76].

Due to the widespread use of ultrasonic scalers in dentistry, the probe described in this work has been called a ultrasonographic periodontal probe to emphasize its use in diagnostic imaging, rather than therapy. Such a distinction is necessary, since ultrasonic imaging has only found a few specialized research uses in dentistry, most of which were highlighted in chapter 1. As a result, most practicing dental clinicians associate the term ultrasound with the relatively high-power, low-frequency devices that they use every day.

Chapter 3

Optimization of Probe Tip Geometry

3.1 The Cylindrical Acoustic Finite Integration Technique

The end of the ultrasonic periodontal probe handpiece has a funnel-shaped tip that houses the ultrasound transducer. This tip narrows the beam path of the ultrasound wave, thereby allowing it to enter the periodontal pocket without scattering. Because the tip alters the shape of the ultrasonic beam, the design of this tip has a large impact on the performance of the periodontal probe. The first task in optimizing the performance of the ultrasonographic probe was to determine the optimal shape of the probe tip.

To do so, a computer simulation of an ultrasonic wave traveling through a tip was developed. This simulation was designed to determine what tip shape produces the strongest and least-distorted return signal. It employed the cylindrical acoustic finite integration technique (CAFIT)

developed by Peiffer, et al [78], and a series of tests were run to narrow the range of shapes that needed to be produced for experimental testing.

The CAFIT algorithm is based on finite volume integration, a special formulation of the finite difference method of computing the solution to differential equations. Typically, finite difference schemes replace the differential $\frac{df(x)}{dx}$ with one of several different difference equations, such as the forward difference equation $\frac{f(x_{i+1})-f(x_i)}{\Delta x}$. The finite volume method produces a similar difference equation, but by starting with an integral equation. The process for turning the integral equation into a discrete difference equation involves the following three steps [79]:

- Dividing the space in which the governing equations operate into a lattice of finite control volumes and integrating the equations over these volumes.
- Substituting finite difference-type approximations into the integrated equations. This step converts the integral equations into a system of algebraic equations.
- Using a set of initial and boundary conditions, solving the algebraic equations for each spatial coordinate on the volume lattice. After solving for each spatial coordinate, the equations step forward in time and use the previous time step solution to solve for each spatial coordinate at the current time.

The accuracy of the numerical solution increases as the lattice and the time steps get smaller, although the size of those steps are limited in practice by computational speed and memory resources. Considerations of numerical accuracy (i.e., stability) also limit the size of the time steps compared to the spatial lattice divisions, or else the solution will diverge with time. For the finite volume method studied here, this is known as the Courant condition:

$$\Delta t \leq \frac{1}{\sqrt{\frac{1}{\Delta r^2} + \frac{1}{\Delta z^2}}}. \quad (3.1)$$

In this work, where $\Delta r = \Delta z$, the Courant condition is always met by setting $\Delta t = \frac{1}{2} \times \Delta r$, and so this relationship was used.

The governing equations of the CAFIT algorithm are the acoustic equivalents to the elastodynamic equations (2.1) and (2.2):

$$\rho_o \frac{\partial \vec{v}}{\partial t} = -\vec{\nabla} p, \quad (3.2)$$

and

$$\frac{\partial \rho}{\partial t} + \rho_o \vec{\nabla} \vec{v} = 0 \quad (3.3)$$

where ρ_o is the density of the medium that the ultrasound wave travels through, \vec{v} is the local velocity vector and p is the acoustic pressure.

Following the detailed derivation of Peiffer et al, these equations are converted into the following set of difference equations using the finite volume method described above, where p stands for pressure, u for the r-direction velocity vector component, and w the z-direction velocity vector

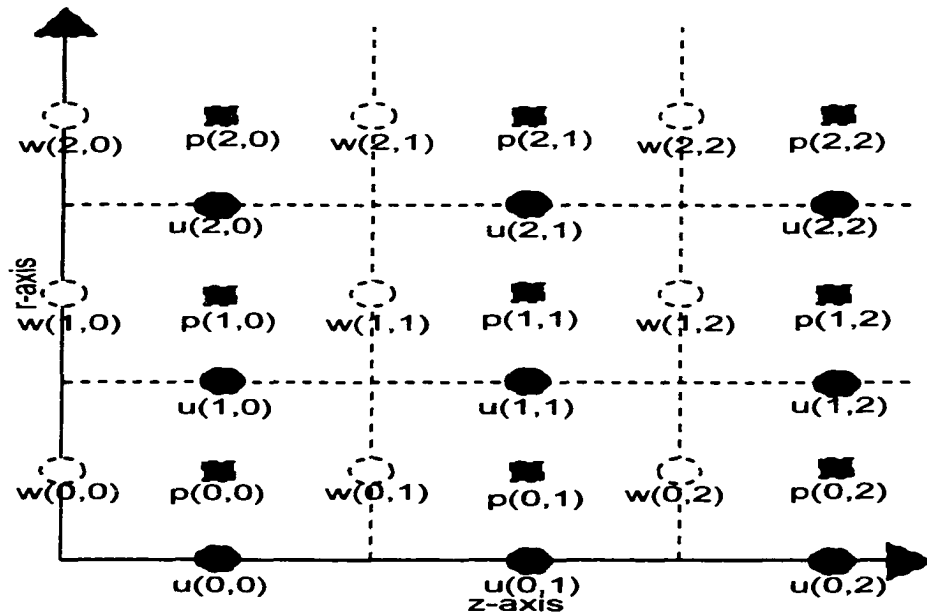


Figure 3.1: The staggered grid of the CAFIT algorithm, with the pressure elements a half-unit apart from the r- and z-direction velocity elements.

component:

$$p_{i,j}^t = p_{i,j}^{t-1} - \frac{\Delta t}{\Delta r} \left([u_{i,j}^{t-1} - u_{i-1,j}^{t-1}] - [w_{i,j}^{t-1} - w_{i,j-1}^{t-1}] - \frac{[u_{i,j}^{t-1} + u_{i-1,j}^{t-1}]}{2r} \right) \quad (3.4)$$

$$u_{i,j}^t = u_{i,j}^{t-1} - \frac{\Delta t}{\Delta r} [p_{i+1,j}^{t-1} - p_{i,j}^{t-1}] \quad (3.5)$$

$$w_{i,j}^t = w_{i,j}^{t-1} - \frac{\Delta t}{\Delta r} [p_{i,j+1}^{t-1} - p_{i,j}^{t-1}]. \quad (3.6)$$

The i, j subscripts represent the position of the variable on the lattice in the r- and z- directions, respectively, and the t superscript represents the number of time steps that the algorithm has gone through.

The CAFIT algorithm is employed on a staggered grid, with the pressure elements a half unit apart from the r-direction velocity elements $u_{i,j}$ and the z-direction velocity elements $w_{i,j}$, as shown in figure 3.1. This

staggered grid provides a better physical representation of the pressure field, since staggering gives a more accurate representation of non-uniform pressure gradients [79]. In addition, Peiffer, et al. claim that the staggered grid provides better accuracy with less calculation time than second-order finite difference techniques. A qualitative explanation for this claim is that the staggered grid effectively divides the spatial lattice in half, without requiring a corresponding halving of time steps to satisfy the Courant condition for numeric stability.

One other advantage of the staggered grid is that it is well-suited for solving problems in cylindrical geometries. Notice that there is a singularity at the axis ($r = 0$) in the first difference equation of the CAFIT algorithm. Because this method employs a staggered grid, the only elements that lie on the axis are the radial velocity elements $u_{0,j}$. If these elements vanish, the singularity will also vanish. This requirement is easily satisfied by setting the first difference equation equal to:

$$p_{i,j}^t = p_{i,j}^{t-1} - \frac{\Delta t}{\Delta r} (2u_{i,j}^{t-1} + [w_{i,j}^{t-1} - w_{i,j-1}^{t-1}]) \quad (3.7)$$

at the points beside the axis.

3.2 Parameter Testing

The CAFIT algorithm was first implemented for a cylindrical tip with walls sloping down to a narrow opening, 0.5 reduced units¹ in diameter. The top of the tip was 4.0 r.u. in diameter with a 2.0 r.u. diameter transducer placed in the middle of this area. The walls of the tip were assumed to be completely rigid, so the boundary conditions $u_{i_{max},j} = 0$ and $w_{i,j_{max}} = 0$ were used at the tip walls. Outside the tip, the vacuum boundary condition $p = 0$ was used at the air/water interface. Finally, the simulation was set up so that the probe was aimed at a metal reflector 20 mm from the transducer face, and an input wave pulse of the form $\sin(2\pi ft) * \sin(0.2\pi ft)$ that lasted 0.5 r.u. was sent down the tip.

Before comparing the performance of different tip geometries, the accuracy of the simulation at various step sizes and ultrasonic frequencies was studied. First, the simulation was run for a step size of $\Delta r = 0.05$ (and $\Delta t = 0.025$) at frequencies of 1, 10 and 15MHz. As can be see from figure 3.2, the numerical dispersion of the signal at 10 and 15MHz was too great to produce any kind of return signal. At 1MHz, numerical dispersion was not as much of a problem, but the wavelength of this signal was too large to accurately resolve the return signal off the reflector from the

¹ In this simulation, the reduced unit for distance is 1 r.u. = 1 mm and for time, 1 r.u. is the time it takes to move 1 r.u. of distance at the speed of sound in water.

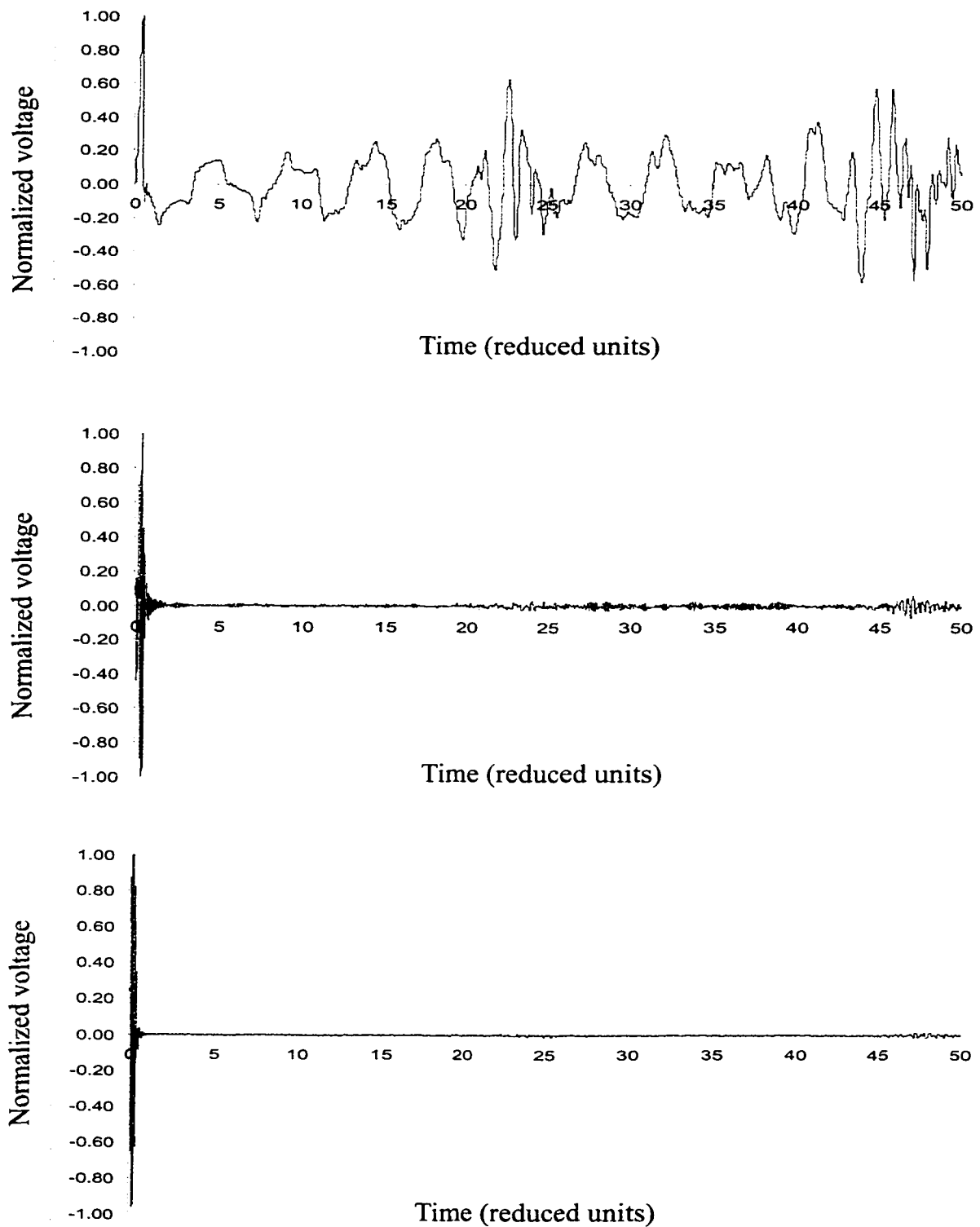


Figure 3.2: Traces for $\Delta r = 0.05$ reduced units with a 1MHz (top), 10MHz (middle), and 15MHz (bottom) signal.



Figure 3.3: A snapshot of the wavefront at $t = 10$ reduced units for a 1MHz (top), 10MHz (middle), and 15MHz (bottom) signal. The step size was $\Delta r = 0.05$ reduced units.

multiple reflections off the nozzle. Another view of the simulation results can be seen in figure 3.3, which provides a snapshot of the wavefront at 10 reduced time units.

Similar simulations were carried out for $\Delta r = 0.01, 0.005, 0.003$ and 0.001 , and the results of the first three sets of simulations are displayed in figures 3.4– 3.9. At $\Delta r = 0.001$ the simulation was too computationally intensive for the workstation computer used here.² However, the low numerical dispersion at frequencies above 10MHz for $\Delta r = 0.003$ and

² The workstation had dual Pentium III, 1 GHz processors with 1 GByte of RAM, and the Fortran code was compiled using Absoft's Pro FortranMP 7.0 compiler to take advantage of the dual processors.

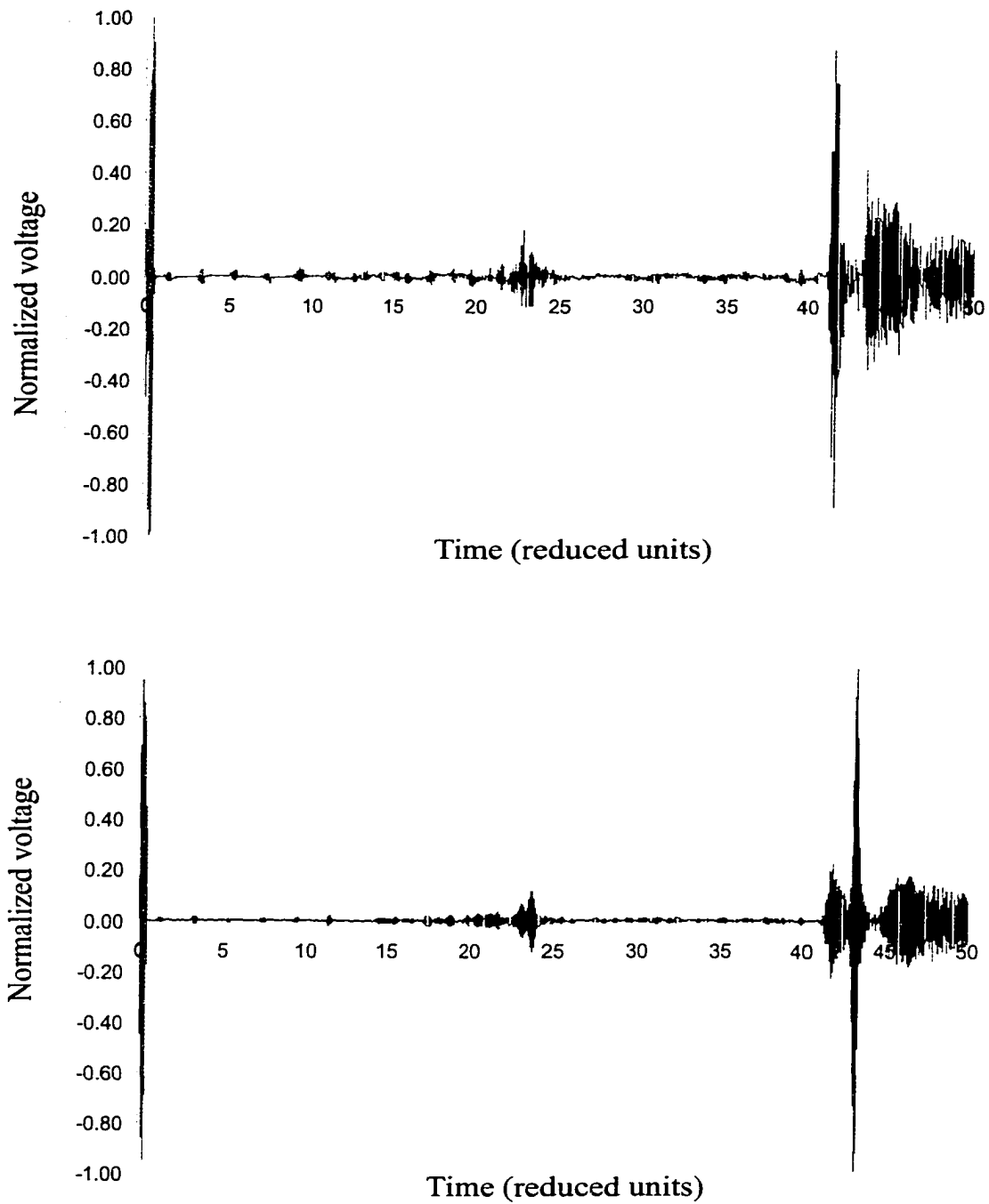


Figure 3.4: Traces for $\Delta r = 0.01$ reduced units with a 10MHz (top) and 15MHz (bottom) signal.



Figure 3.5: A snapshot of the wavefront at $t = 10$ reduced units for a 10MHz (top) and 15MHz (bottom) signal. The step size was $\Delta r = 0.01$ reduced units.

$\Delta r = 0.005$ indicate that running the simulation at smaller step sizes would not greatly increase the accuracy of the results.

As discussed by Peiffer et al, the CAFIT procedure produces accurate results only when $\Delta r \leq \frac{\lambda}{15}$. For a 10MHz ultrasound wave traveling in water, $\frac{\lambda}{15} = 0.01$ and for a 15MHz wave, $\frac{\lambda}{15} = 0.0067$. The results of these test simulations support Peiffer et al's conclusion, since adequate results were obtained at $\Delta r = 0.01$ and better results at $\Delta r \leq 0.005$. A more thorough comparison of the relationship between frequency and dispersion can be seen in figure 3.10, which shows processed waveforms as the frequency increase from 2 to 20MHz (and $\Delta r = 0.005$),

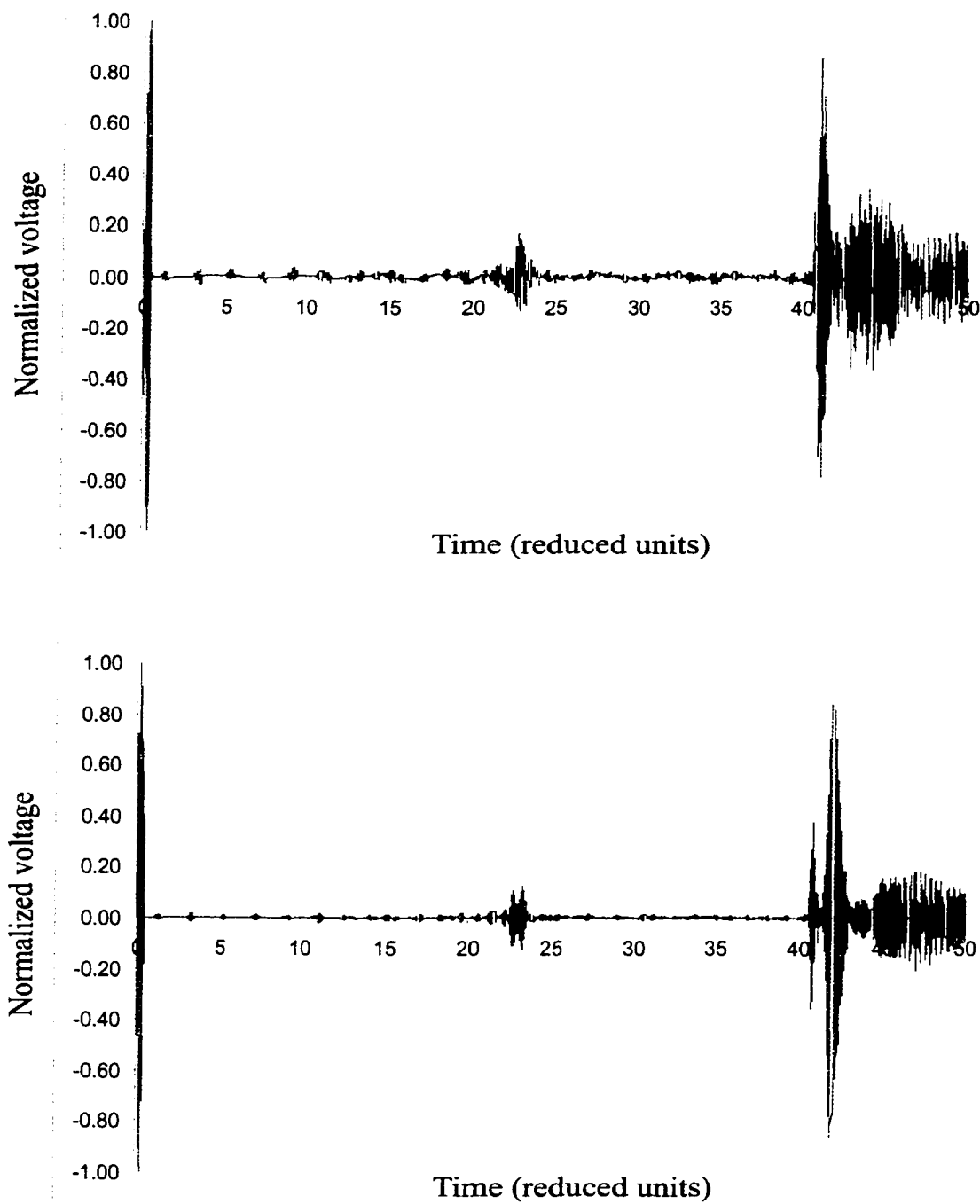


Figure 3.6: Traces for $\Delta r = 0.005$ reduced units with a 10MHz (top) and 15MHz (bottom) signal.



Figure 3.7: A snapshot of the wavefront at $t = 10$ reduced units for a 10MHz (top) and 15MHz (bottom) signal. The step size was $\Delta r = 0.005$ reduced units.

and in figure 3.11, which shows processed waveforms as the the step size increases from 0.005 to 0.05 r.u. (and the frequency is 15MHz).

After confirming the stability of this algorithm for $\Delta r \leq 0.005$, the simulation was run on a range of tip geometries to determine which would produce the strongest output signal for the periodontal probe. First, the angle θ of the tip walls was varied from 0 to 90° in 5° increments, while the length of the nozzle was held constant at 12 r.u. and the reflector was fixed at 20 r.u. from the transducer (see figure 3.12). In this simulation, the strongest return peak occurred for the 80° angle, although the 85° was almost as good (figure 3.13). These angles correspond to a smooth slope

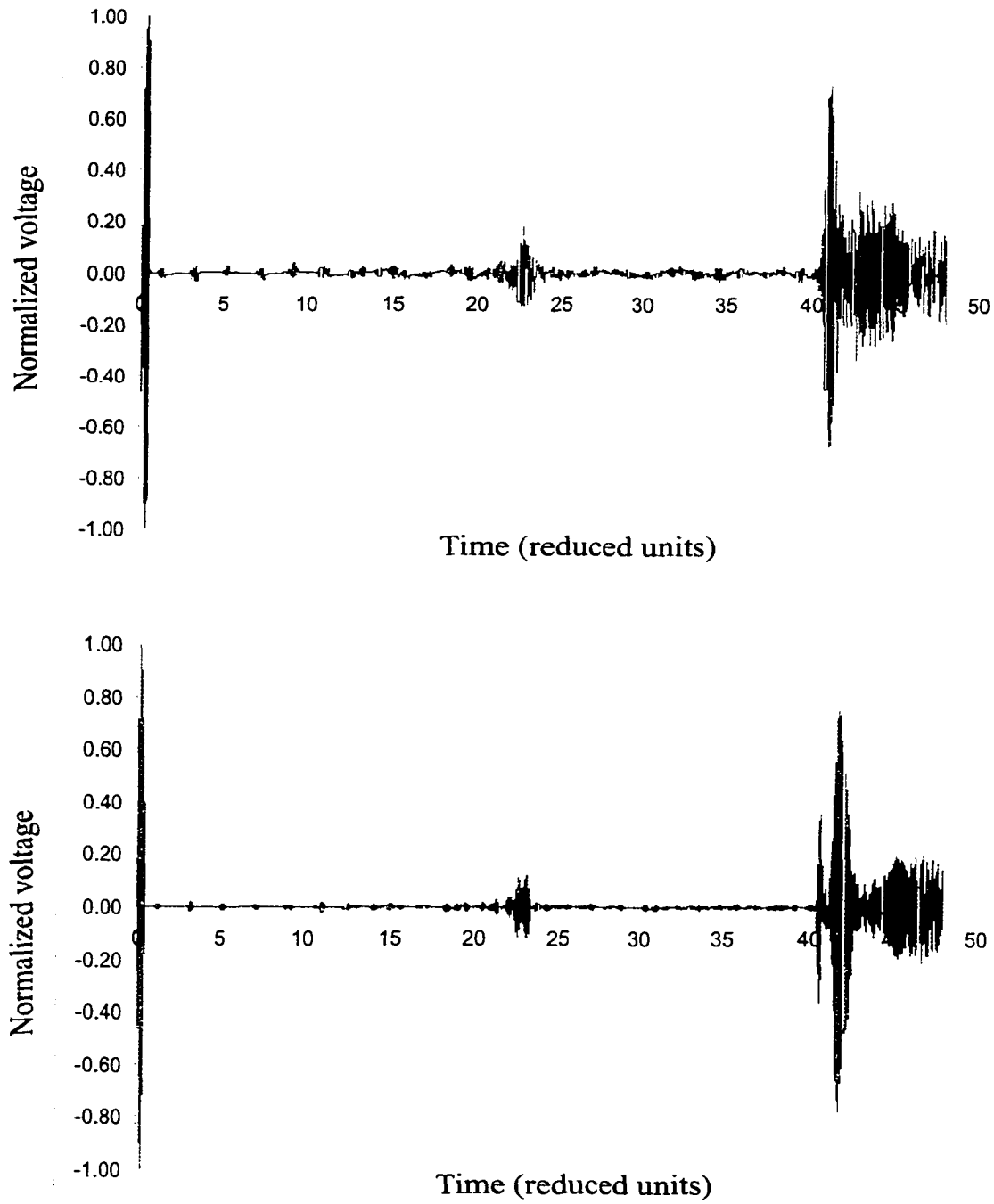


Figure 3.8: Traces for $\Delta r = 0.003$ reduced units with a 10MHz (top) and 15MHz (bottom) signal.



Figure 3.9: A snapshot of the wavefront at $t = 10$ reduced units for a 10MHz (top) and 15MHz (bottom) signal. The step size was $\Delta r = 0.003$ reduced units.

from the outer diameter at the top of the nozzle to the tip outlet at the bottom.

A similar variation of nozzle performance as the angle varies was tested, but with the position of the nozzle outlet varying with the angle, and the reflector position 5 r.u. from the outlet (see figure 3.14). Changing the nozzle length did not change the results much. Once again, the narrowest slope produced the best results ($\theta = 85^\circ$), as can be seen in figure 3.15.

Next, the diameter of the nozzle at the top was varied from 2 r.u. (the nozzle touching the edge of the transducer) to 6 r.u., with the length of the nozzle held constant at 12 r.u. and the walls always sloping evenly

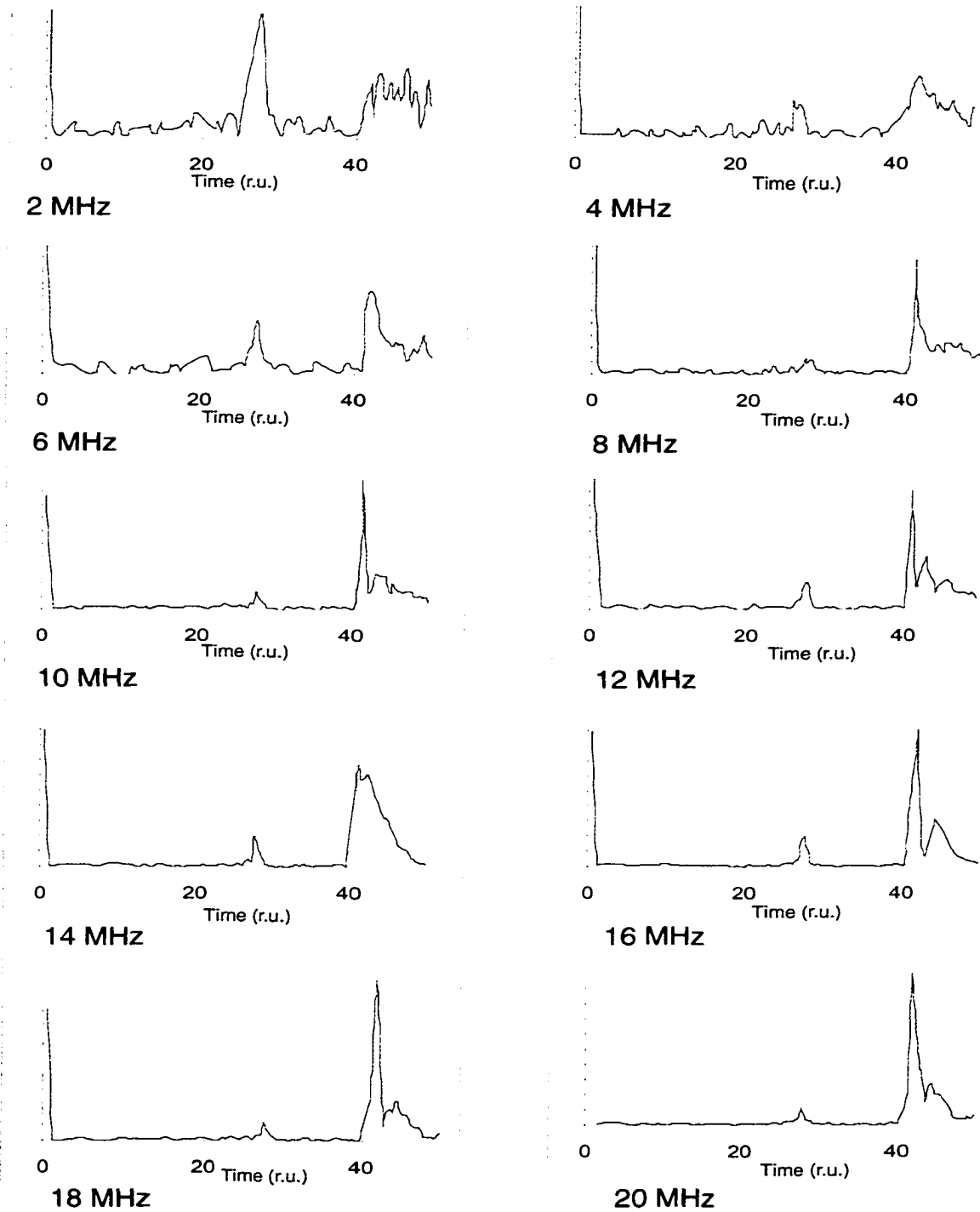


Figure 3.10: As the frequency increased from 2MHz (top right) to 20MHz (bottom left), the reflection off the plate (40 r.u.) gets sharper, while the reflection off the tip end (about 27 r.u.) gets smaller.

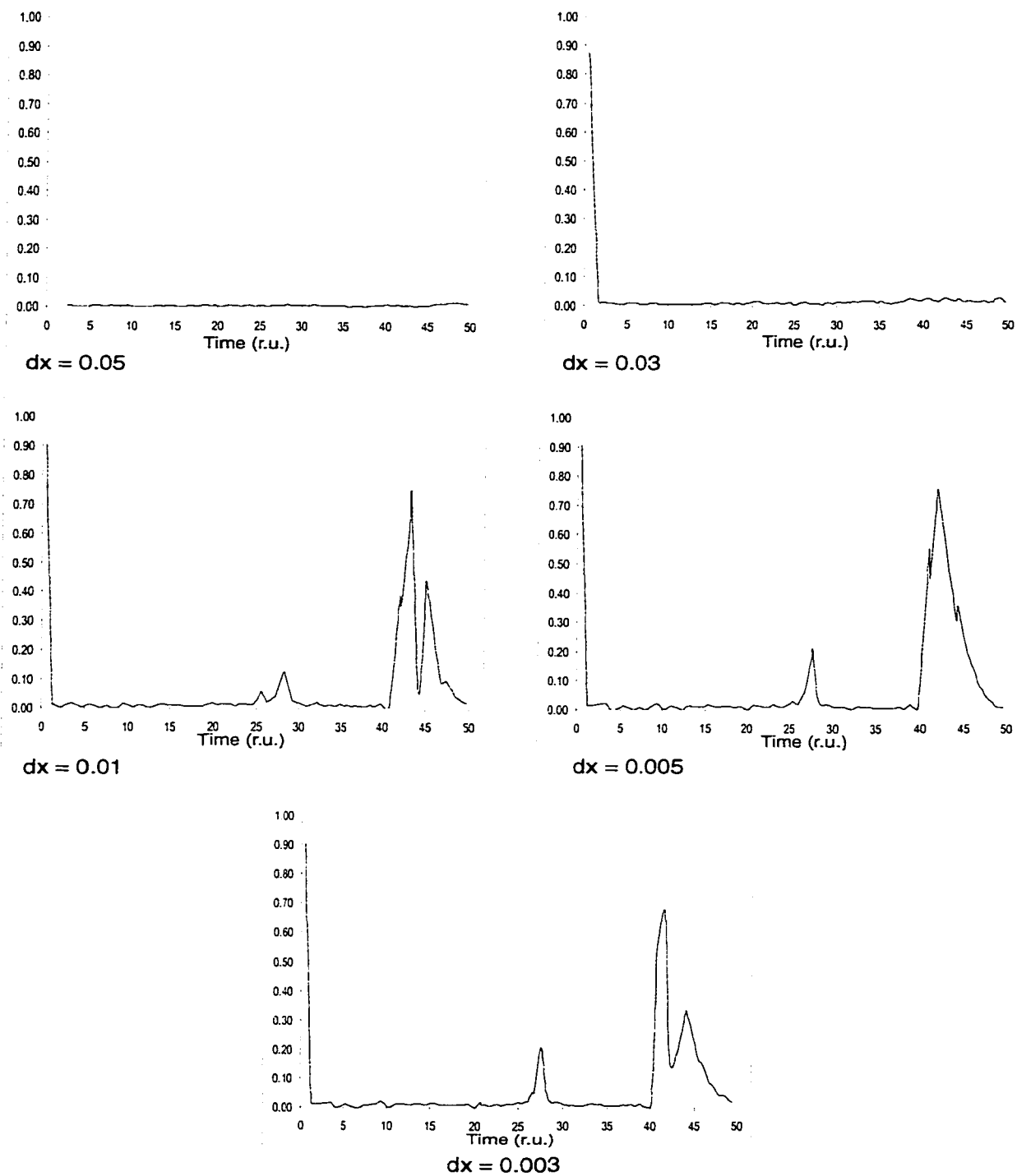


Figure 3.11: The graphs above show the change in return signal quality as the step size decreases. The largest possible step size to produce adequate results is 0.01 r.u.

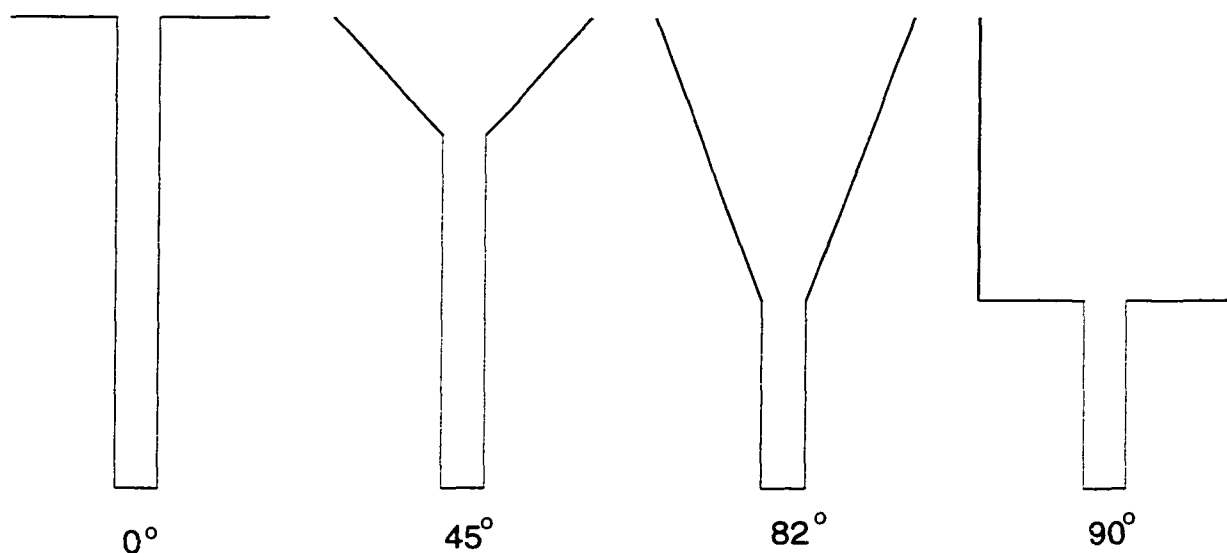


Figure 3.12: An illustration of how the tip shape changes as the wall angle varies from 5° to 90° .

down to the nozzle outlet (see figure 3.16). The strongest return peak occurred when the nozzle diameter was 2 r.u. and this peak decreased as the diameter increased (figure 3.17).

These three simulations indicate that to increase strength of the return signal, the tip's top diameter should conform as close as possible to the transducer diameter, while making it as long as possible so that the angle θ is as close to 90° as possible. Such a design minimizes the area of the tip wall perpendicular to the wavefront. This result coincides with those predicted by long-standing analytical treatments of acoustic horns, as highlighted in this discussion from Morse:

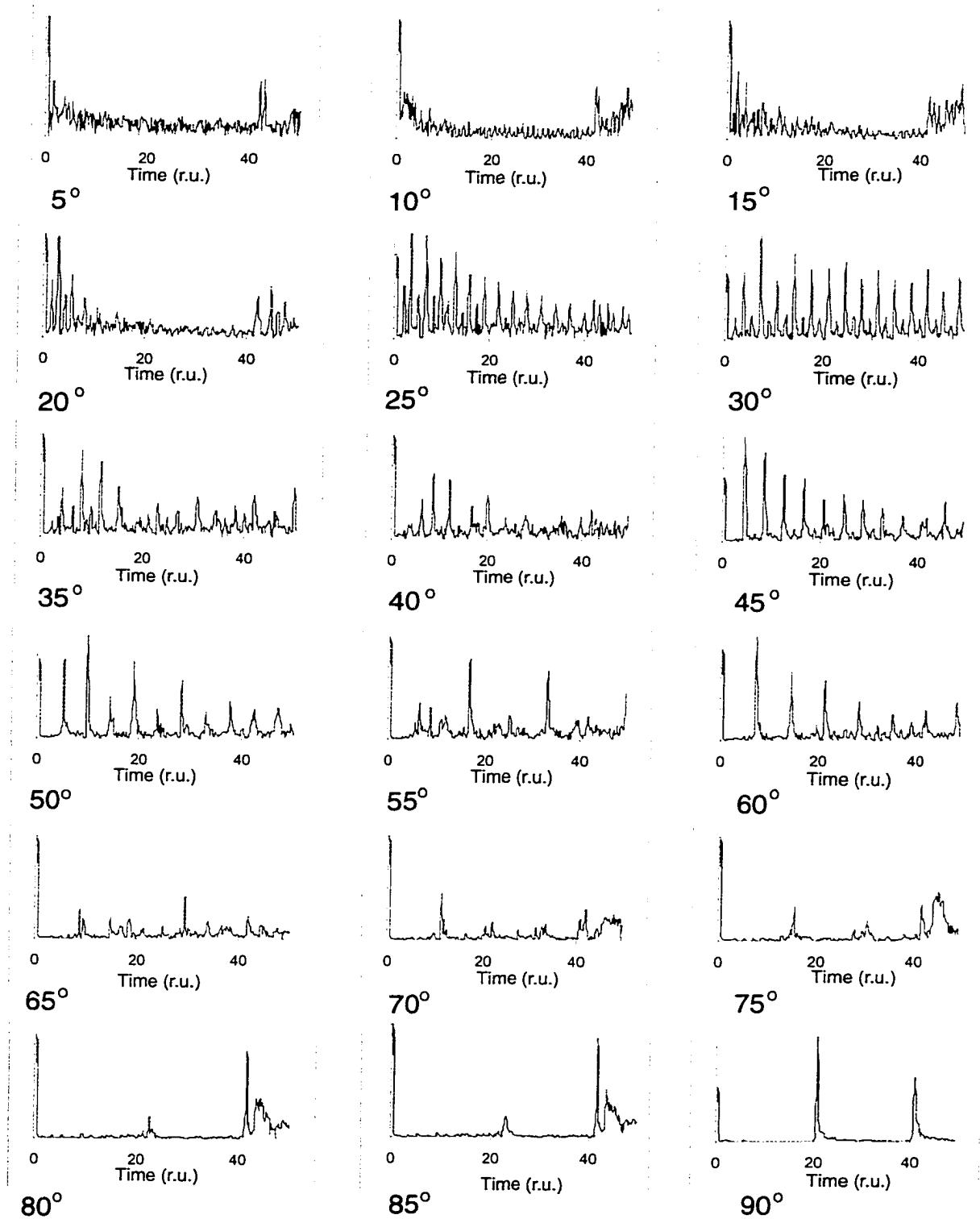


Figure 3.13: As the angle between the transducer face and the wall increases up to 85°, the signal reverberates less inside the tip. At 90° the flat walls at the outlet produce a large echo.

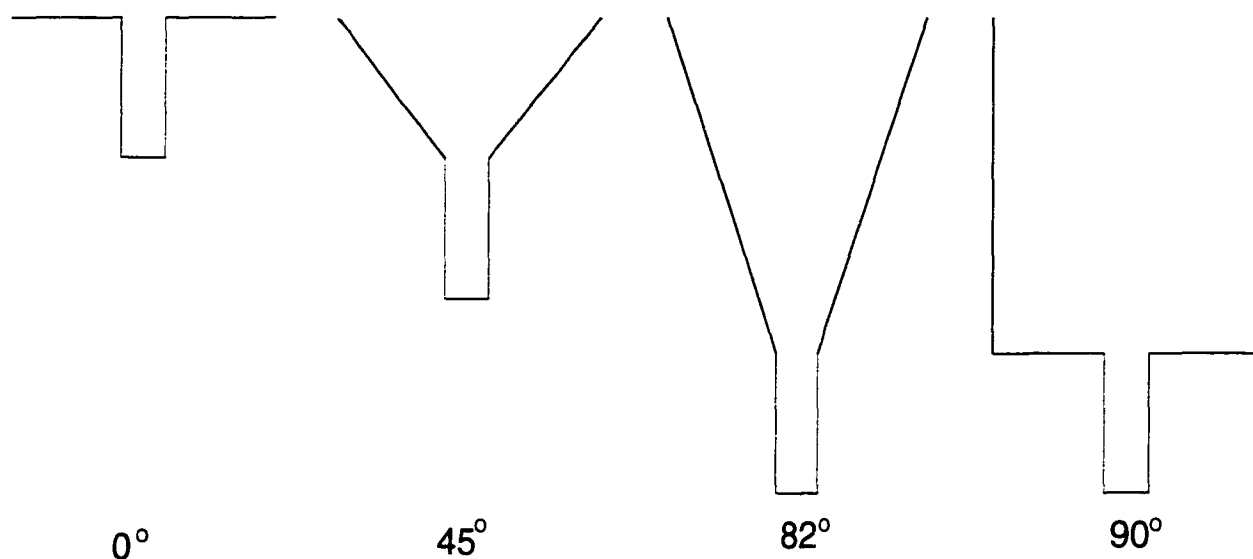


Figure 3.14: Tip shape as the wall angle varies from 5° to 90° , and the distance from the tip end to the reflector is held constant at 5 r.u.

When the coordinates [of the horn] do not have this property [matching the surfaces of constant wave phase], the particle velocity will not be parallel to the μ coordinate lines, and the wave will tend to reflect from the horn surface as it travels along, rather than moving parallel to it ... any reflection of the wave during its progress along a tube tends to trap some of the energy inside, causing resonance for some frequencies and poor transmission for others [80].

While minimizing the top diameter and maximizing the wall angle are useful guidelines for designing the tip, there are some practical

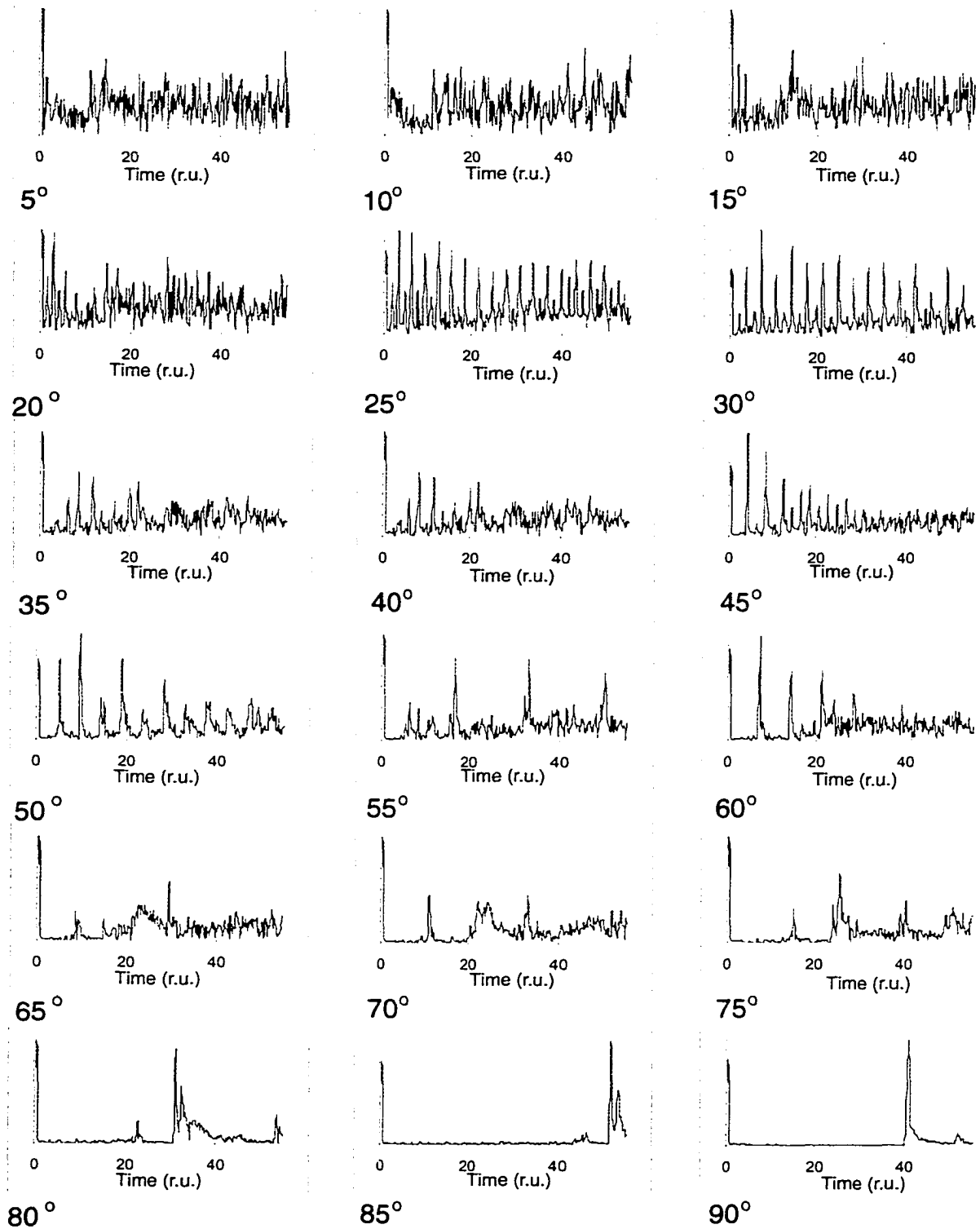


Figure 3.15: The effect of holding the distance from the tip end to the reflector constant is negligible, as the larger aspect ratio at smaller angles produces much stronger reverberations, negating the benefit of a shorter tip length.

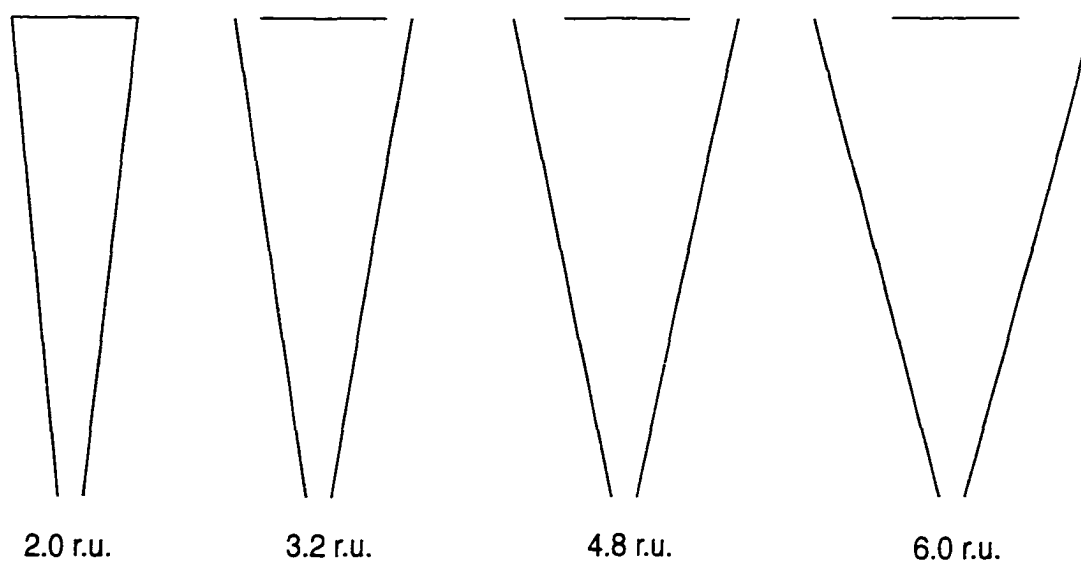


Figure 3.16: Tip shape as the tip diameter at the top varies from 2 reduced units to 6 reduced units.

limitations to these goals. First, the nozzle top needs to be a little wider than the transducer face to accommodate transducer packaging, and to allow adequate room for coupling water to flow into the tip. Second, the tip length cannot be too long, because it must fit comfortably in the patient's mouth. Finally, this simulation does not take into account the effects of signal attenuation, which could be significant if the tip were too long.

A final general question to be considered was whether there would be any significant change in results if the nozzle was aimed into a large bath of water instead of air (where the wave is confined to a narrow stream of water). Thus, the nozzle (4 r.u. top diameter, 12 r.u. long, smoothly sloping walls) was aimed into water baths of varying widths, from a 0.5 r.u.

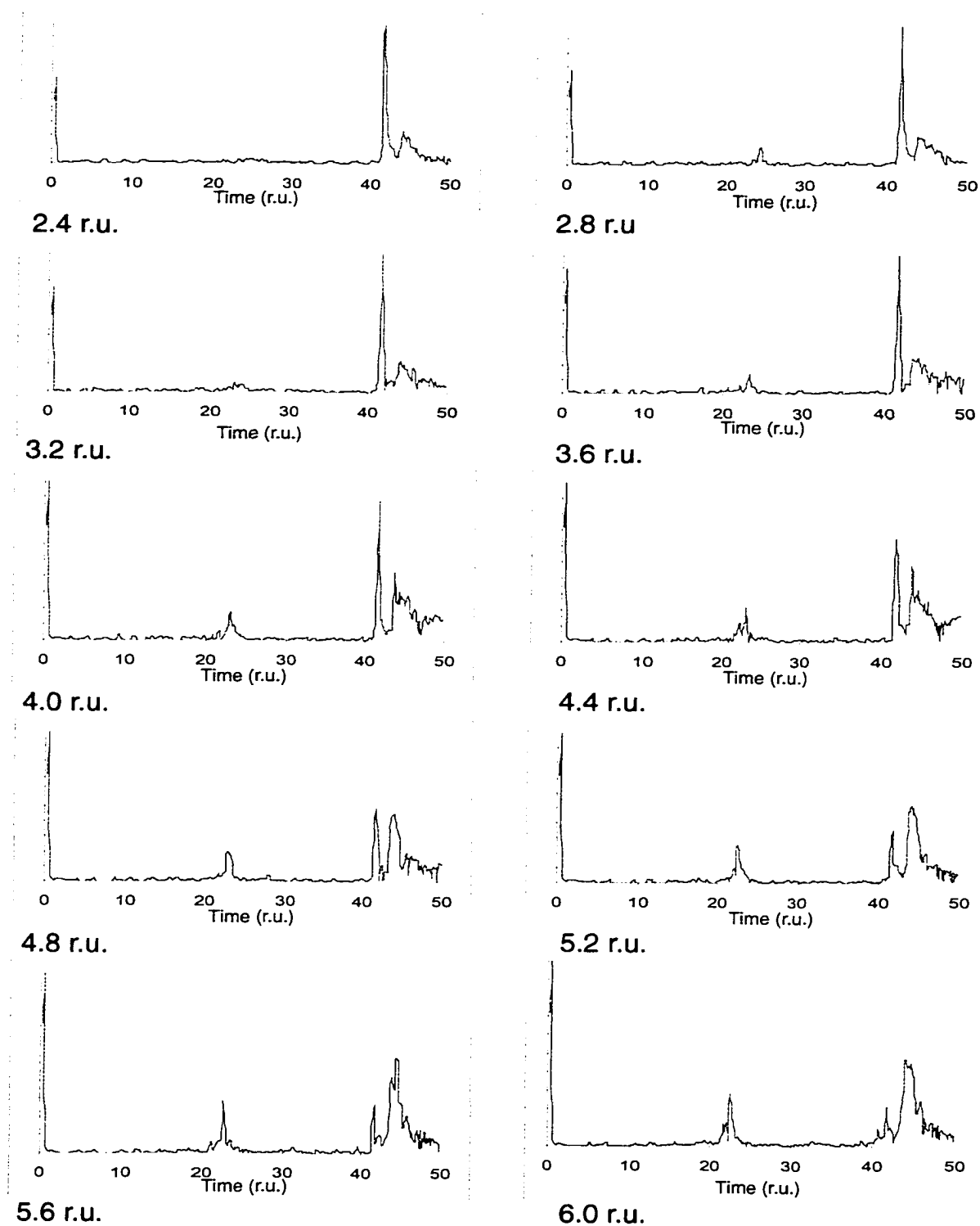


Figure 3.17: As the tip diameter at the top increases, the strength of the return signal decreases.

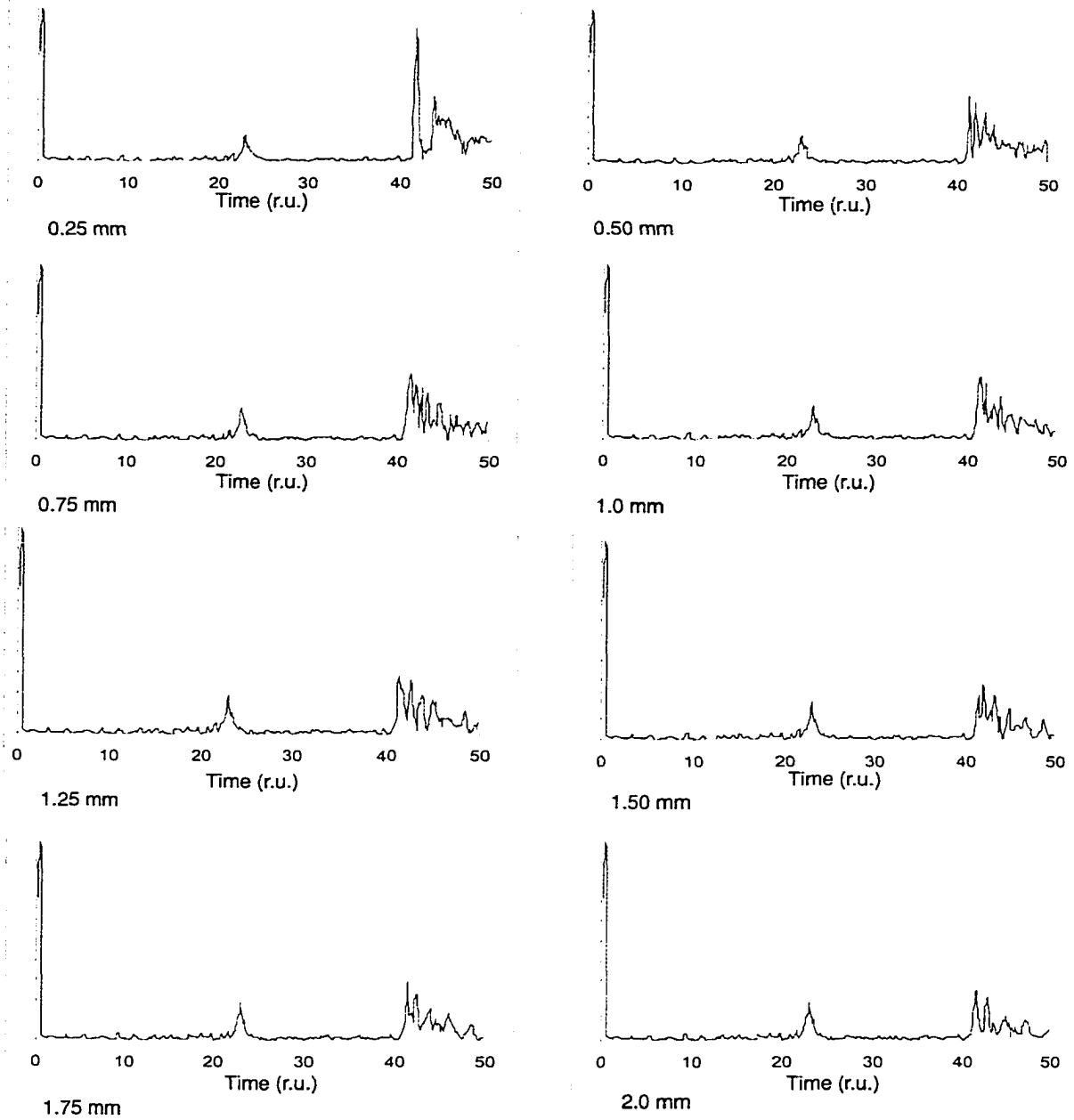


Figure 3.18: As the tip is aimed into increasingly large baths of water, the strength of the return signal decreases.

stream equal to the outlet width to a 4 r.u. bath. As can be seen from figure 3.18, the strength of the return signal decreases as the width of the water bath increases. The narrow stream forces the wavefront to continue moving parallel to the stream boundaries, while a larger bath allows the wavefront to spread out perpendicular to the air/water interface and reflect off it.

3.3 Shape Comparisons

After examining these general relationships, a few more specific shapes were considered, including:

- One where the radius of the tip walls varied linearly: $r = mz$.
- One where the radius of the tip walls varied exponentially: $r = r_i e^{-mz}$.
- One where the radius of the tip walls takes a parabolic shape:

$$z = (r - r_i)^2 + c^2.$$

- One where the radius of the tip walls takes an ellipsoid shape:

$$z^2 + (r - r_i)^2 = c^2.$$

Voltage traces for these simulations are shown in figures 3.19–3.22.

These results show that the exponential walls produced the strongest return signal, although only slightly better than the linear walls. The exponential

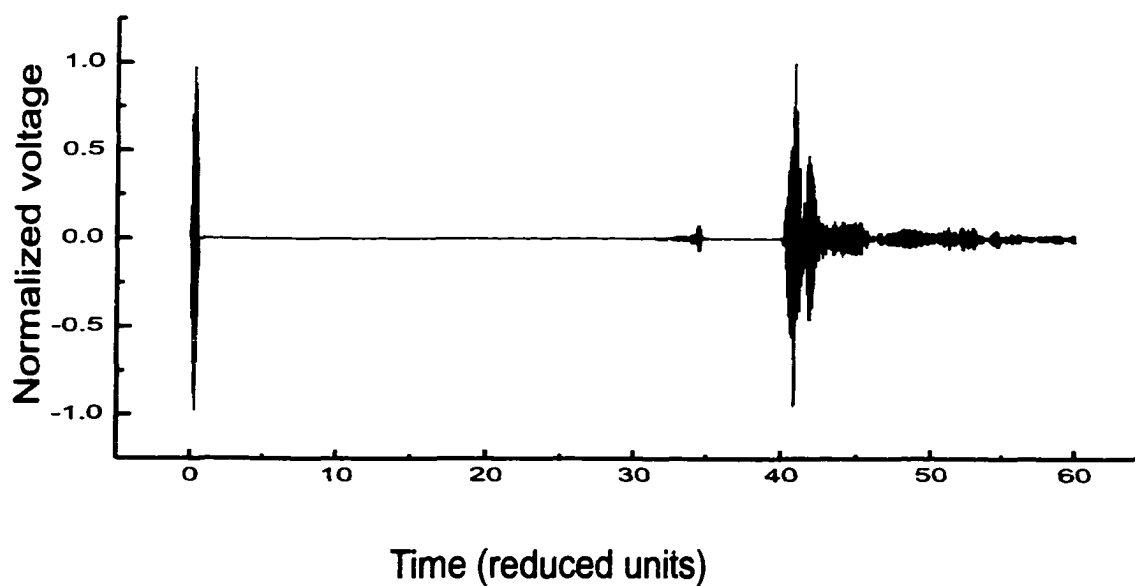


Figure 3.19: Return signal for the linear tip. The ratio of peak return signal to peak input signal was 1.02, with the return peak was found at 40.9 r.u.

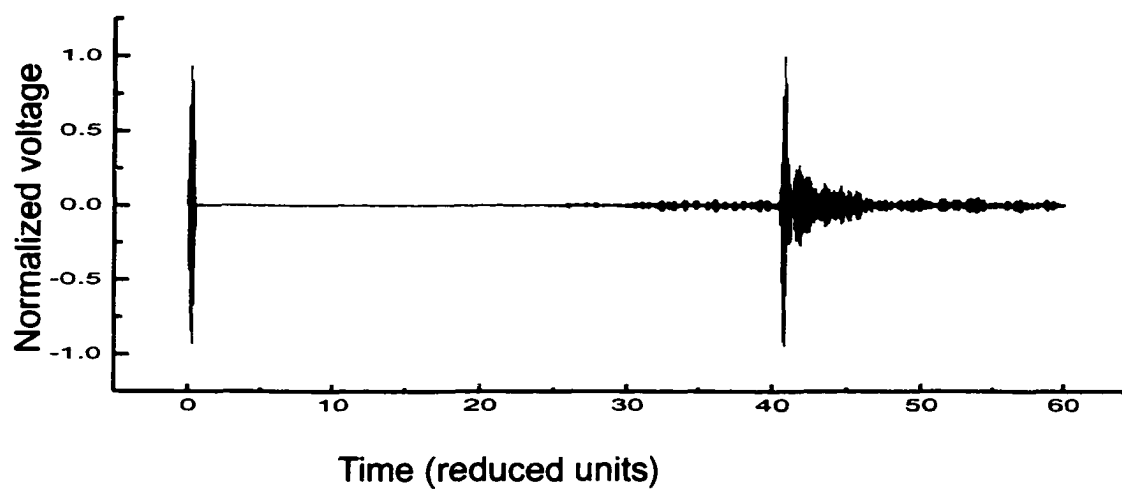


Figure 3.20: Return signal for the exponential tip. $\frac{peak_{out}}{peak_{in}} = 1.07$ and the return peak occurred at 40.8 r.u.

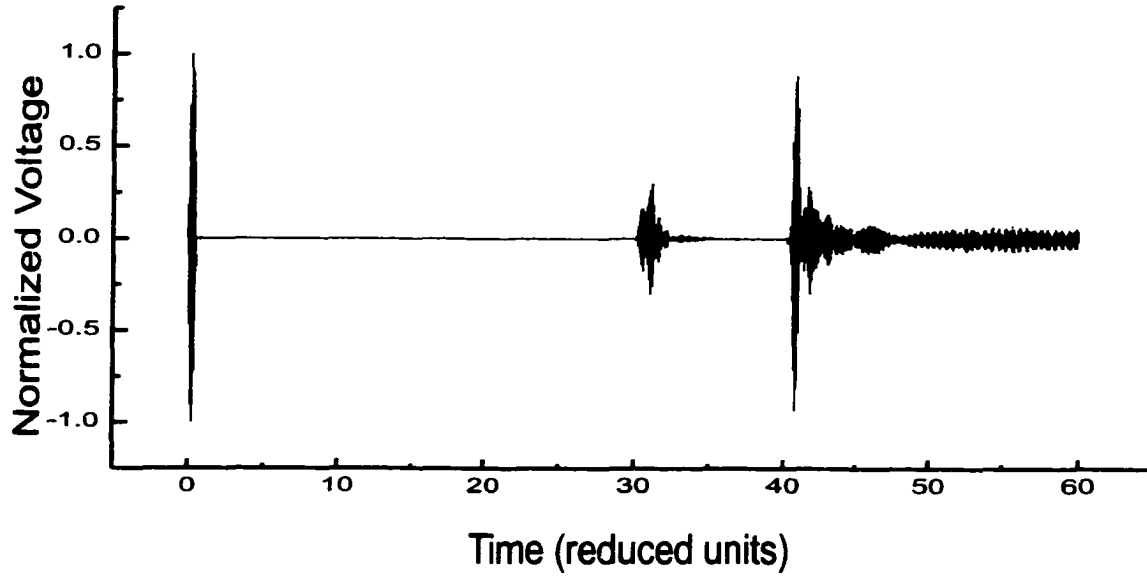


Figure 3.21: Return signal for the parabolic tip. $\frac{peak_{out}}{peak_{in}} = 0.89$ and the return peak occurred at 40.9 r.u.

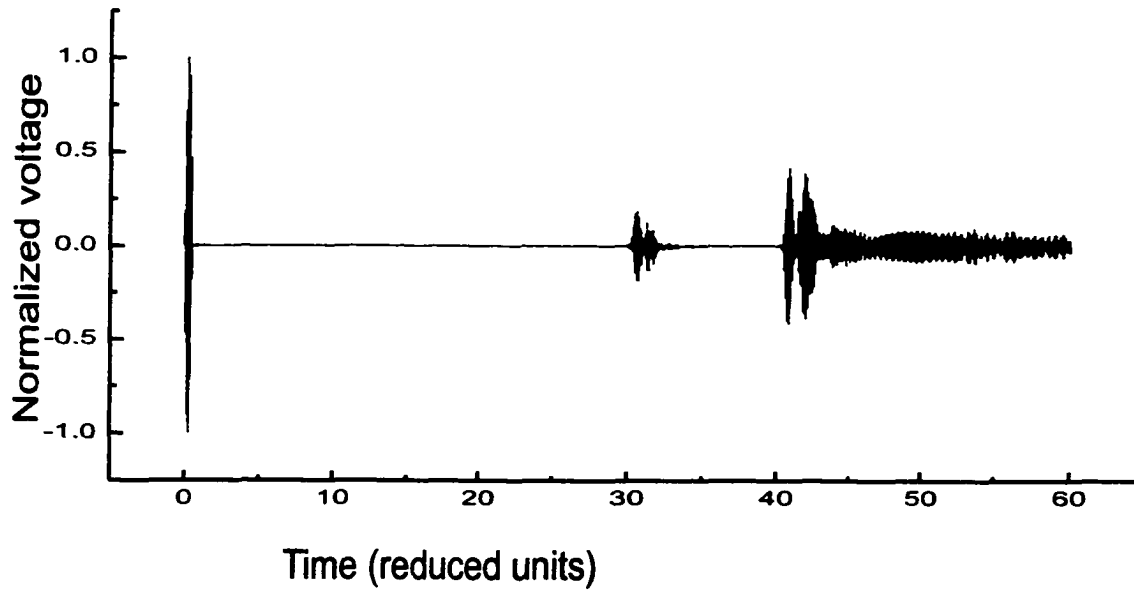


Figure 3.22: Return signal for the ellipsoid tip. $\frac{peak_{out}}{peak_{in}} = 0.42$ and the return peak occurred at 40.8 r.u.

walls performed slightly better because the top of the nozzle narrows more quickly to confine the waveform before it has time to spread out. However, once the walls match the width of the transducer, the exponential nozzle's walls narrow much more slowly, so that they do not have a significant area perpendicular to the wavefront that would cause internal reflections.

Based on these results, a linear tip that has a slight “nook” at the top was fabricated that incorporates the best features of the exponential and the linear tips. For the purposes of complete experimental validation, an exponential tip, a spline-shaped tip, and a linear tip without the “nook” were also fabricated.

Chapter 4

Development of the Probe

4.1 Probe System Setup

Building on the work of Hinders and Companion [69], a new ultrasonographic periodontal probe prototype was built according to the CAD drawings shown in figure 4.1. This probe was designed to have a removable tip, room for a 2mm-active area transducer housed at the base of this tip, a water line input running through the probe handle and emptying into a small open area around the transducer, and an electronics input-output cable also running through the base and connected to the transducer.

The transducer was driven using the Matec SR-9000 pulser-receiver card, which is a 8-bit plug-in card designed to connect to a 16-bit expansion

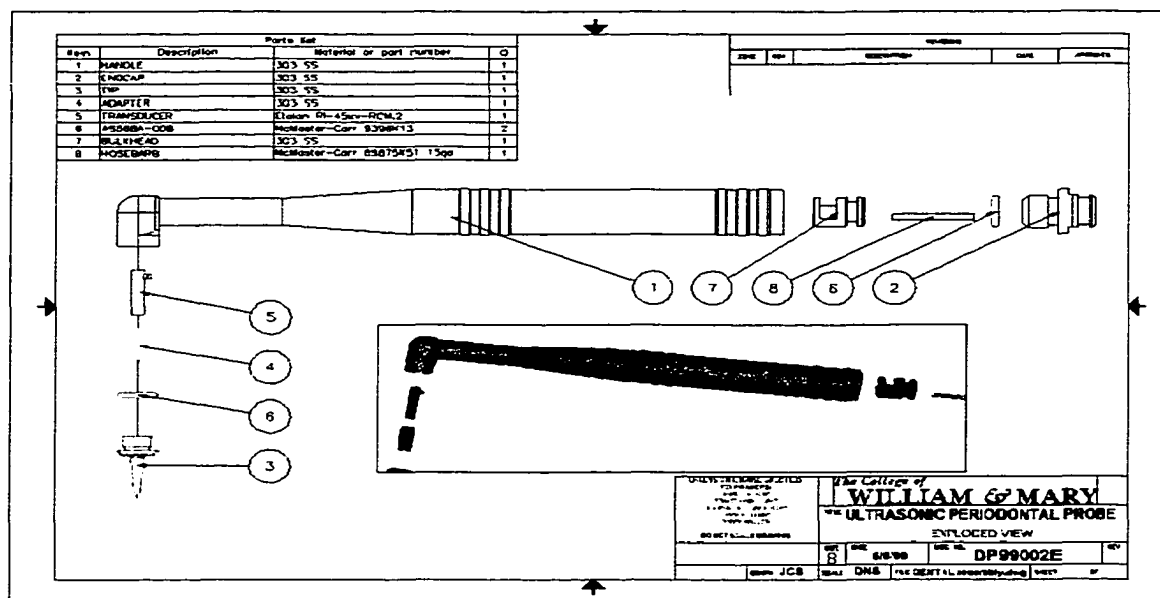


Figure 4.1: Design drawings for the prototype ultrasonographic periodontal probe.

slot in an IBM-compatible computer. The pulser produces a unipolar spike pulse with a voltage output of up to 300V and a rise time of less than 10ns into a 50ohm cable. The receiver offers 63.5dB of computer addressable gain in 0.5dB steps and has a bandwidth of 50MHz (with a low frequency end of 100kHz). In addition, the receiver has independently adjustable low-pass and high-pass filters. The low-pass filter settings ranged from 10MHz down to 550kHz, while the high-pass filter settings ranged from 800kHz to 10MHz. For this work, the low-pass filter was set to full band (since the transducers used in this work had a higher frequency range than the highest setting on the low-pass filter), while the high-pass filter was set

at 7MHz to filter out low frequency noise.

The receiver output was connected to a CompuScope 2125 analog-to-digital converter. The digitized signal was processed and saved using programs running LabView version 5.0. This system was run using a rackmount-type computer with a Pentium Pro processor contained in a ruggedized, portable case. (Figure 4.2).

Initial laboratory testing of the probe was designed to answer three questions:

- What is the optimal flow rate of the water to produce high-quality signals?
- Can the results of the computer simulations to determine the optimal tip shape be confirmed experimentally?
- What transducer provides the best combination of good signal strength and high resolution?

4.2 Determination of Optimal Water Flow

The first tests to determine optimal water flow were done using a gravity-fed water input and a small electronic pump. However, neither provided fine enough control over water flow to quantitatively determine what flow rate was required to obtain a high-quality return signal. Qualitatively, though, it was observed that a steady (laminar) flow

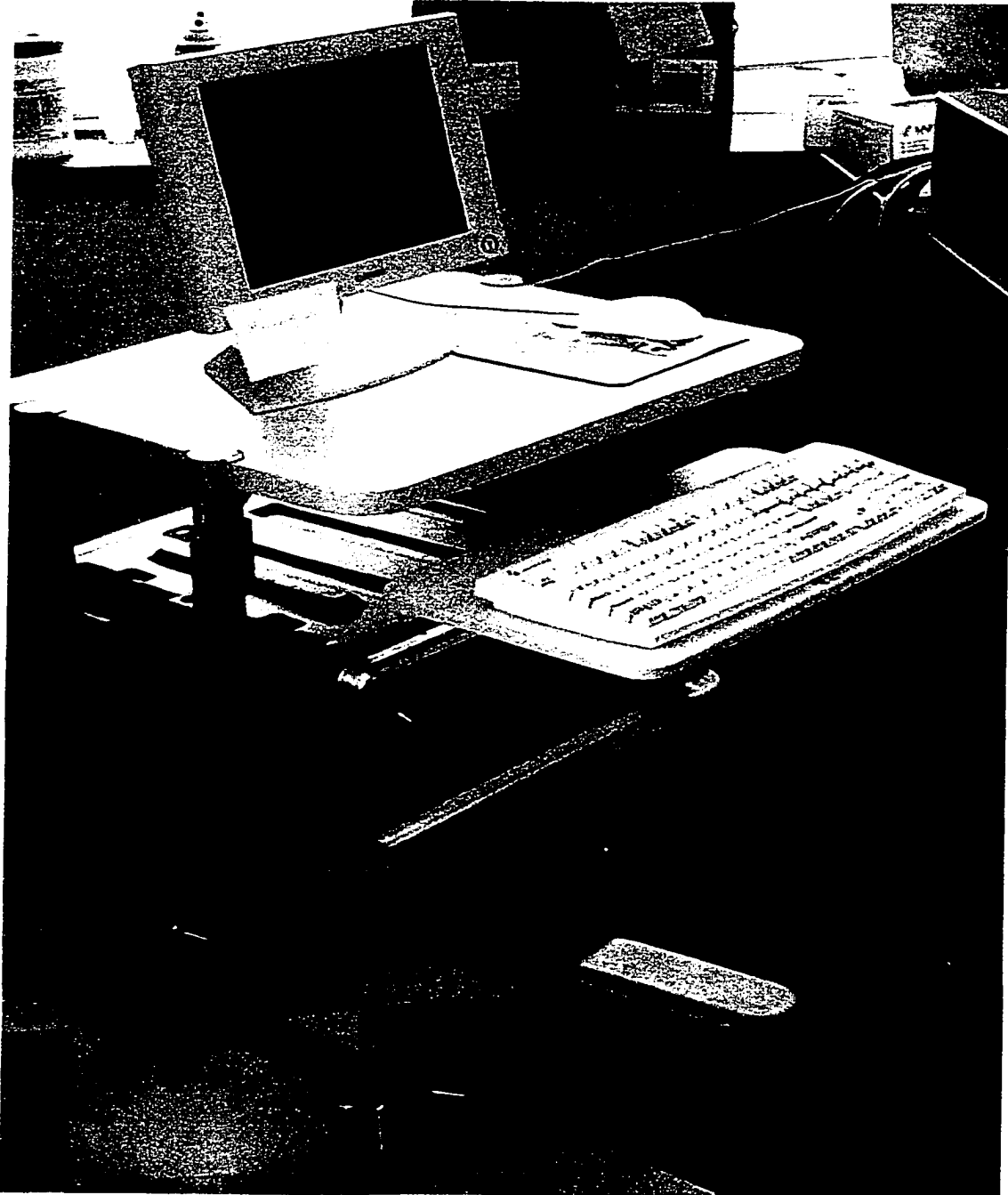


Figure 4.2: Rackmount computer system used to run the ultrasonographic periodontal probe.

produced the best returns. If the water pressure was too low, the water flow was interrupted and did not allow continuous transmission of the signal. However, if the pressure was too high, turbulent flow resulted, and once again transmission of the signal was broken up (Figure 4.3).

To develop a more quantitative understanding of this behavior, a low-pressure regulating valve equipped with a pressure gauge was inserted into the water line between the handpiece and the water source. This valve reduced the input water line pressure of up to 250 psi down to an adjustable range of 2-30 psi. This control allowed a detailed examination of the relationship between water flow, water line pressure, and the quality of the return signal.

This relationship can be expressed theoretically using the Reynolds number, Re . Re is a dimensionless parameter that quantifies the relationship between ρ , the density of a fluid flowing through a pipe, D , the internal diameter of the pipe that the fluid is flowing through, μ , the dynamic viscosity of the fluid, and V , the average velocity of the fluid in the pipe. This relationship is expressed as:

$$Re = \frac{\rho VD}{\mu} \quad (4.1)$$

Fluid flow through a pipe is normally laminar for $Re < 2000$ [81]. Thus, the critical velocity for determining laminar flow is given by the

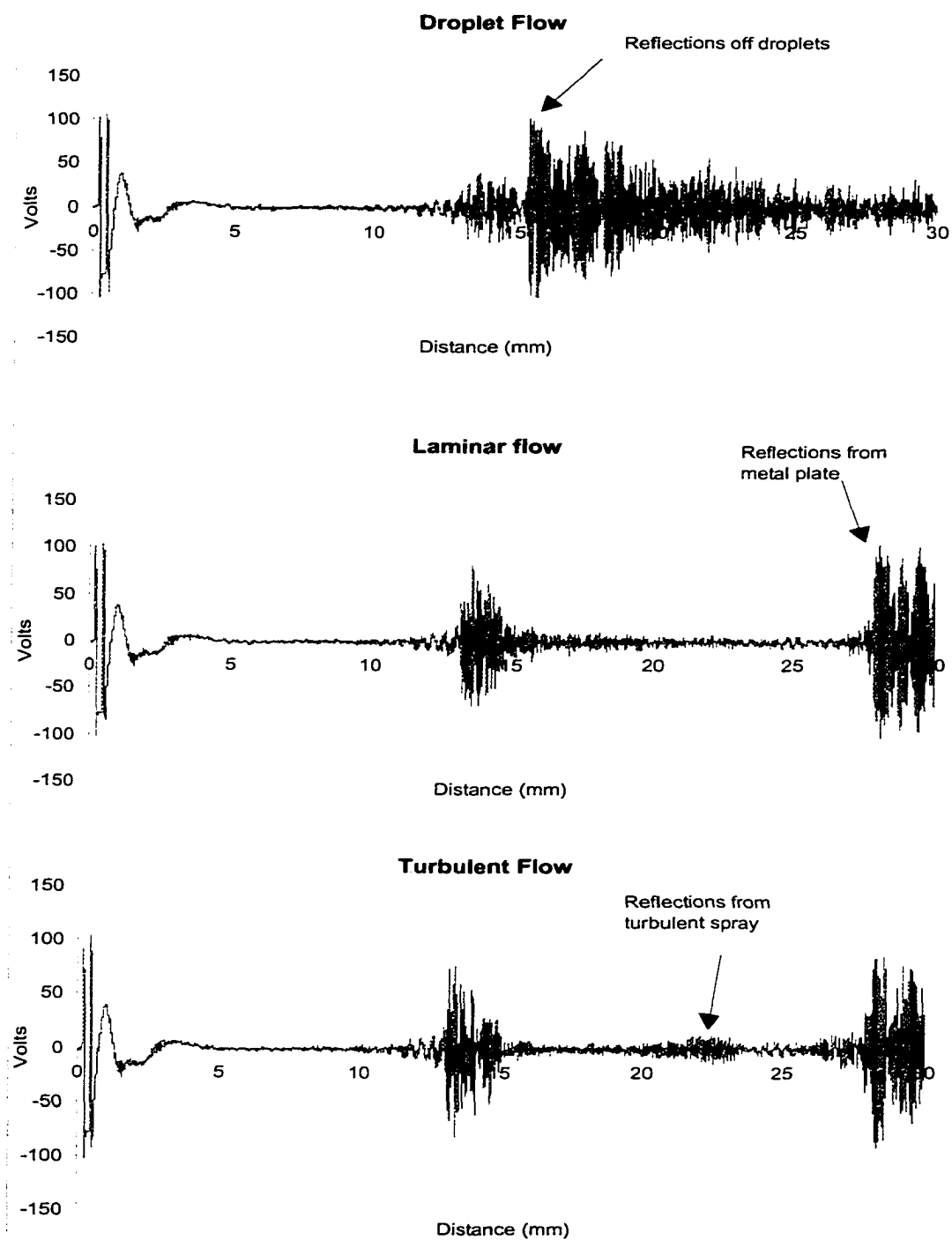


Figure 4.3: Signal for interrupted (top), laminar (middle), and turbulent (bottom) flow.

relationship

$$V_c = \frac{2000\mu}{\rho D}. \quad (4.2)$$

For water at room temperature, the kinematic viscosity $\nu = \frac{\mu}{\rho}$ is $1.11 \times 10^{-5} \frac{m^2}{s}$ [81] and for this probe, the 0.5mm-diameter tip outlet is the most narrow point in the “pipe,” so D is $5 \times 10^{-4}m$. Based on these values, $V_c = 4.43 \frac{m}{s}$.

Pressure (psi)	Flow rate ($\frac{m}{s}$)	Velocity ($\frac{m}{s}$)
2.5	0.6	3.0
5.0	0.8	4.0
7.5	1.0	5.0
10.0	1.1	5.5
12.5	1.3	6.5
15.0	1.5	7.5
17.5	1.7	8.4
20.0	1.8	9.0

Table 4.1: Water flow and velocity versus pressure values.

To determine the relationship between water line pressure and velocity, the flow rate for the probe was measured for pressures ranging from 2.5 to 20 psi. This was done by running the water output from the probe into a graduated cylinder for 1 minute, and then calculating the flow rate in $\frac{mL}{s}$ by dividing by $60 \frac{s}{m}$. Once the flow rate was obtained, the

average velocity of the water exiting the probe can be calculated using the relationship

$$V = \frac{\dot{Q}}{A}, \quad (4.3)$$

where \dot{Q} is flow rate, V is the average velocity of the water, and A is the area of the outlet. Table 4.1 shows the flow rate and average velocity of the water exiting the tip outlet at various pressure settings

Based on these results, the transition from laminar to turbulent flow should occur between 5.0 and 7.5 psi. Figure 4.4 shows signal readings off a metal plate at each of the pressures listed on the table. Note that traces become increasingly noisy starting at the 10 psi reading, which is the result of turbulence in the water flow. This turbulence could be seen visually as a spray. Although some spray is visible more than 20 mm from the outlet at low pressures, in the turbulent regime the spray began only a few millimeters from the outlet.

Although according to the theoretical calculations, this turbulence should have been visible starting at 7.5 psi, this was not the case. It is likely that a more accurate measurement of water flow, and a more accurate pressure gauge (the gauge used only had marking to the nearest 1 psi), would help resolve this discrepancy. However, for the purposes of this work, it is safe to conclude that a pressure setting below 5 psi provides the laminar flow needed for accurate imaging with the periodontal probe.

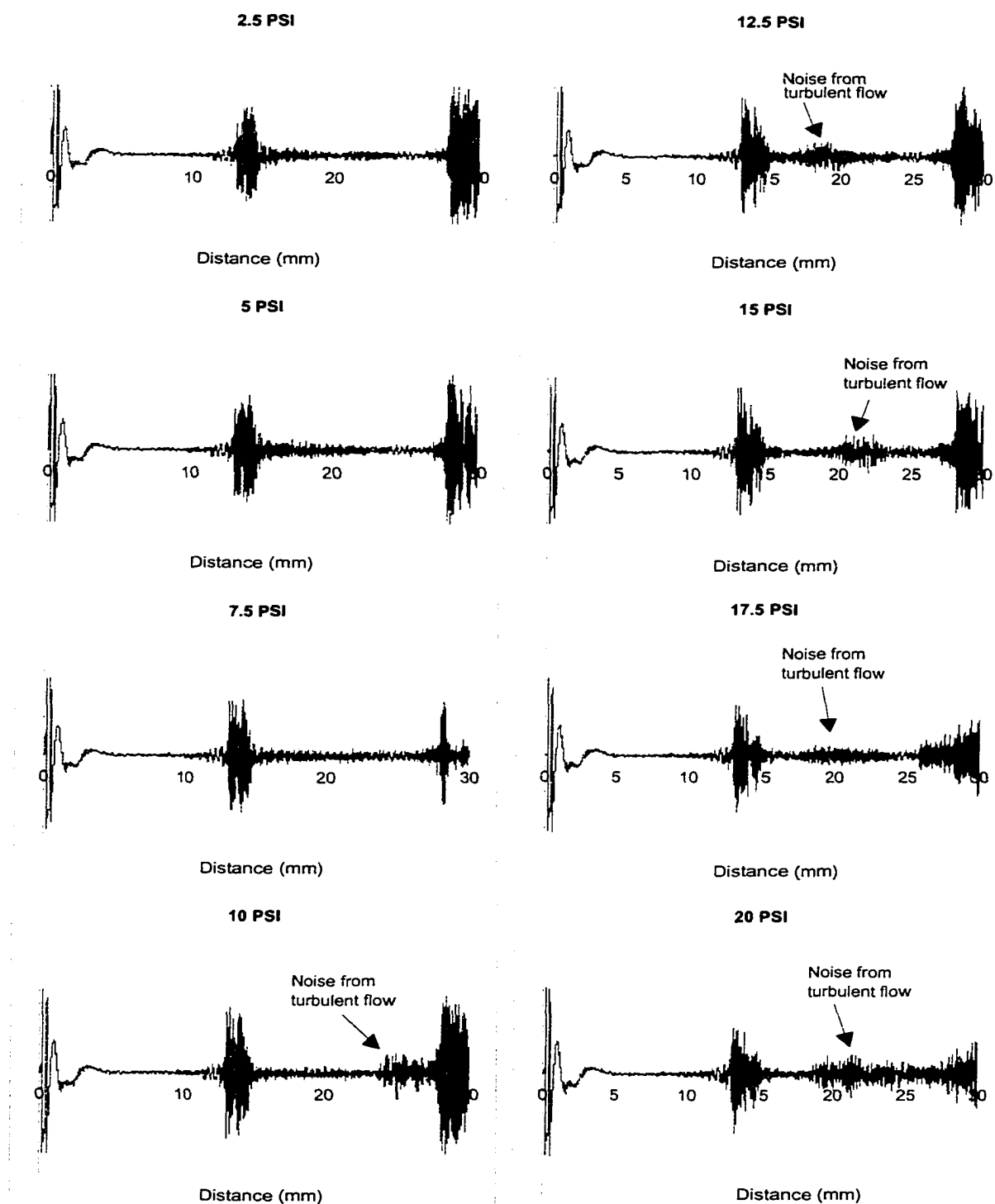


Figure 4.4: From this test of signal quality as the pressure is increased, noise from turbulent flow is not a problem below 7.5 psi. The values on the x-axis indicate distance from the transducer in mm.

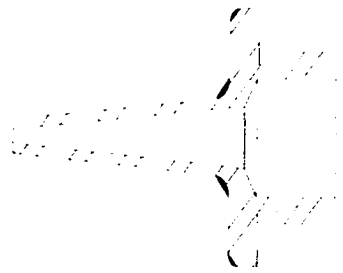
4.3 Experimental Validation of the Tip Shape Simulation

To test the validity of the CAFIT simulations of optimal tip shape described in chapter 2, four tips were machined (shown in figure 4.5) and their experimental performance was compared to a simulation.

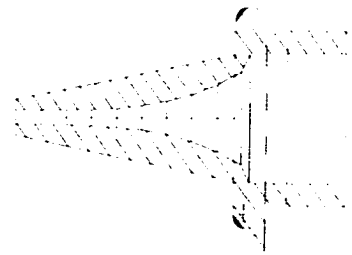
After making these tips, the periodontal probe was aimed at a flat metal target 20 mm away from the transducer face, thus recreating the conditions of the simulations. In figures 4.6–4.9, the experimental voltage traces are provided in a side-by-side comparison with computer simulation traces for tips of the same geometry. In these experiments, a custom 15MHz transducer manufactured by Valpey-Fisher was used in the periodontal probe.

From these comparisons, it is clear that the simulation only approximates the experimental results. In particular, the simulation does not take into account the effect of signal attenuation, the presence of noise or the fact that the return signal is electronically amplified in the real probe. As a result, backscatter appears much larger in the real signal than in the simulation. Also, because the real signal is amplified, direct comparisons of peak return sizes between the experimental results and the simulations are not meaningful.

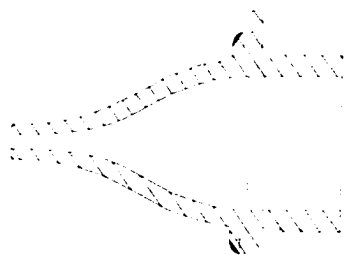
However, relative comparisons between the experimental results and



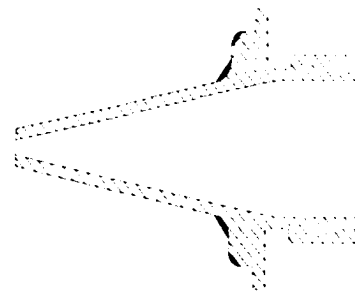
Linear-Shaped Walls



Exponential-Shaped Walls



Spline-Shaped Walls



Short, Linear-Shaped Walls

Figure 4.5: Shapes of the machined tips.

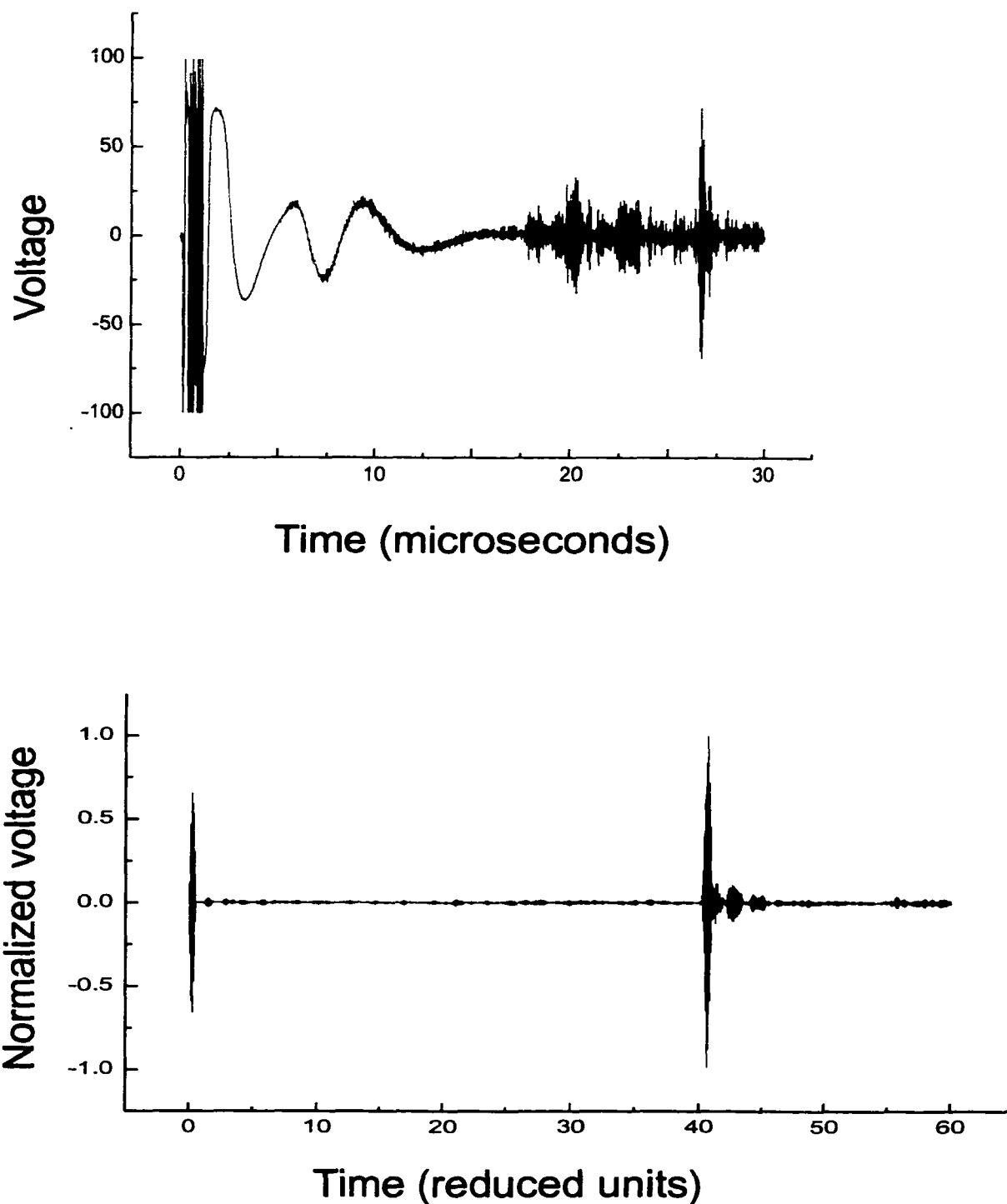


Figure 4.6: Experimental results (top) vs. simulation (bottom) for the linear tip. In the experiment, the peak return occurred at $26.7 \mu\text{s}$ with a peak value of 71.9 volts. In the simulation, the peak return occurred at 40.7 r.u. (which equals $27.1 \mu\text{s}$), with a peak value 1.52 times greater than the output signal.

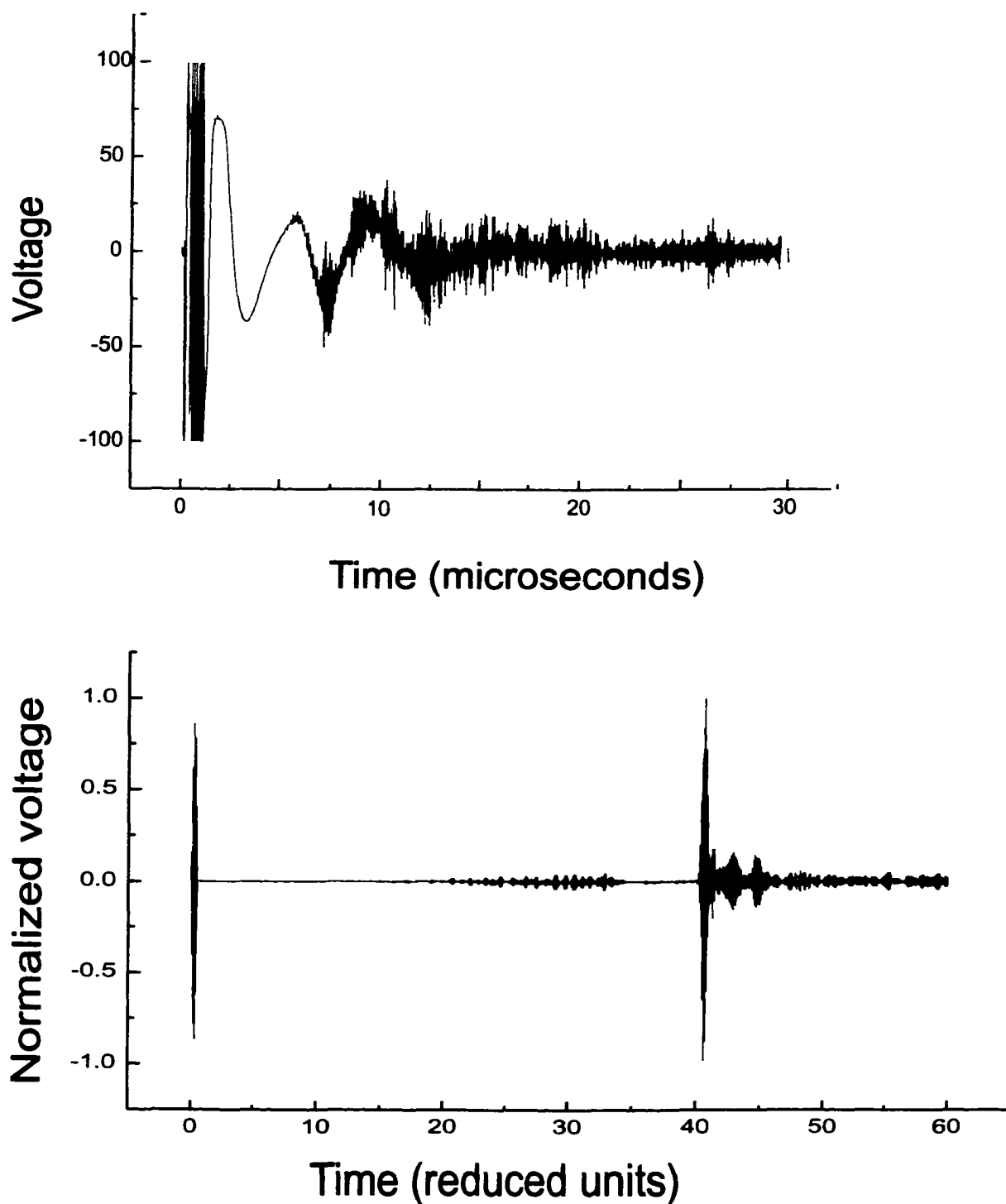


Figure 4.7: Experimental results (top) vs. simulation (bottom) for the exponential tip. In the experiment, the peak return occurred at $26.6 \mu\text{s}$ with a peak value of 18.0 volts. In the simulation, the return peak occurred at 40.7 r.u. (which equals $27.1 \mu\text{s}$) with a peak value 1.16 times the output signal.

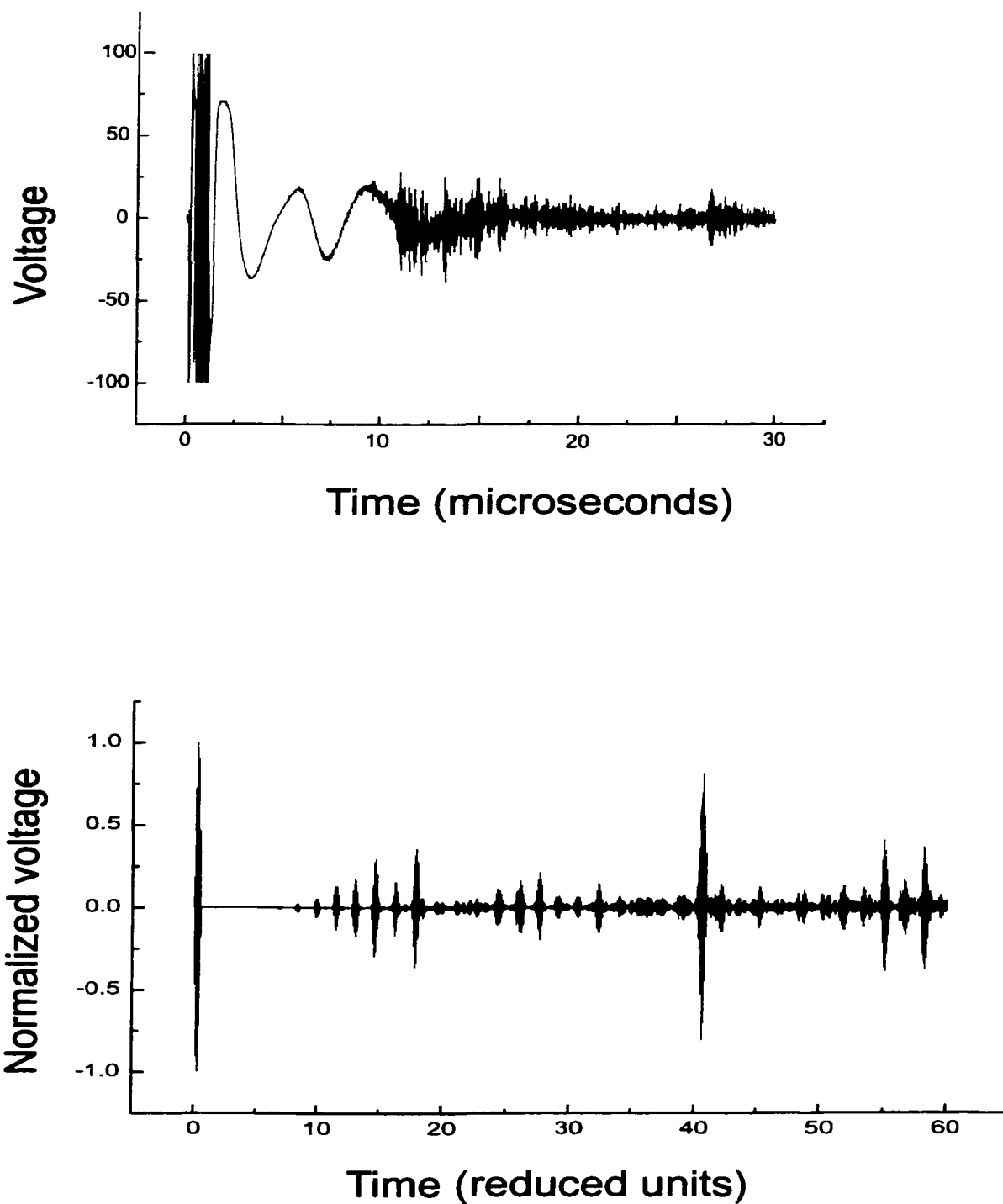


Figure 4.8: Experimental results (top) vs. simulation (bottom) for the spline tip. In the experiment, the peak return occurred at $26.7 \mu\text{s}$ with a peak value of 16.4 volts. In the simulation, the return peak occurred at 40.7 r.u. ($27.1 \mu\text{s}$) with a peak value 0.81 times the output signal.

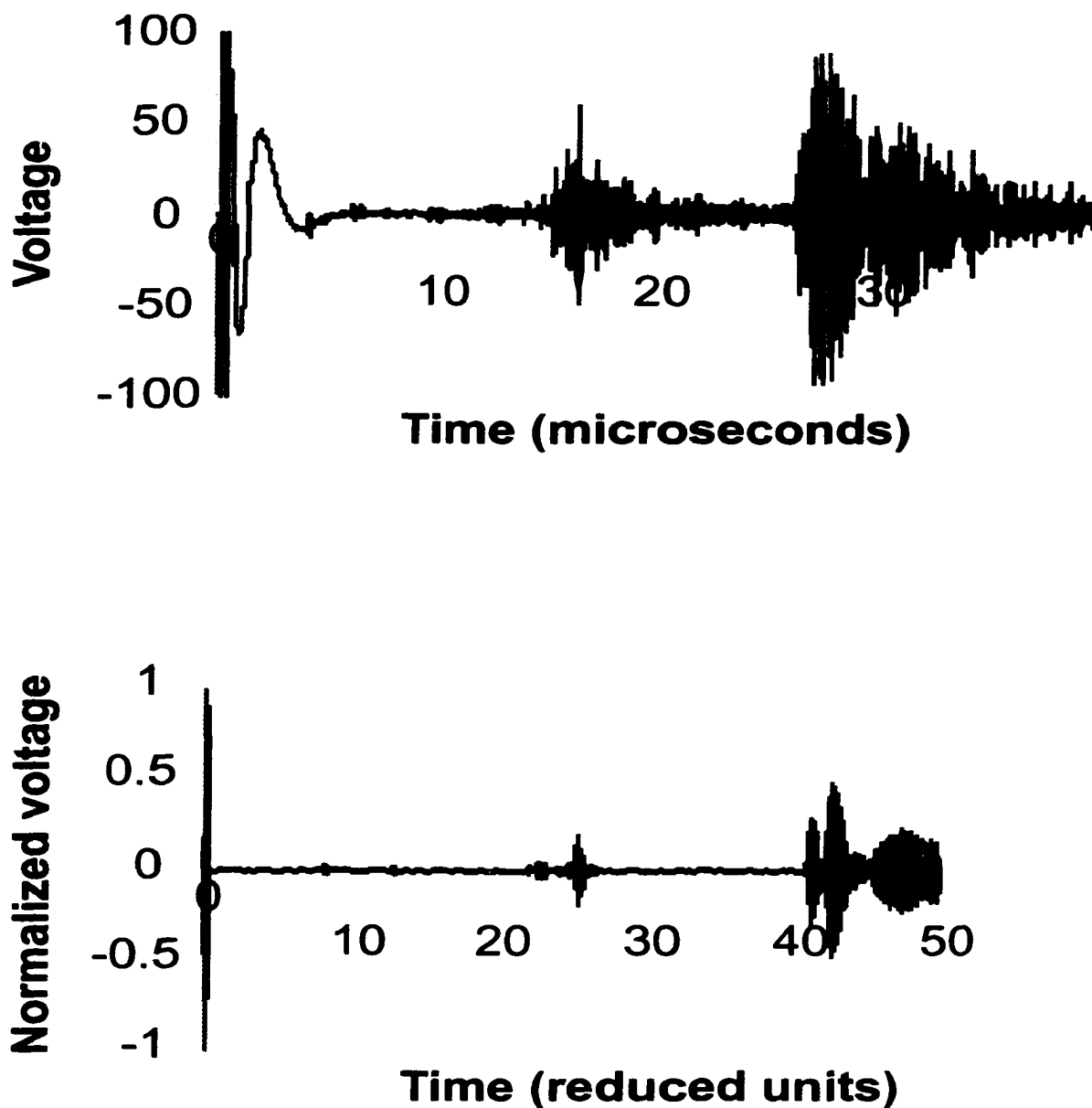


Figure 4.9: Experimental results (top) vs. simulation (bottom) for the shorter linear tip (made of brass). In the experiment, the largest return peak occurred at $27.9 \mu\text{s}$ with a peak value of 89 volts, while a smaller peak (46 volts) preceded this one at $27.2 \mu\text{s}$. In the simulation, the a large return peak occurred at 42.8 r.u. ($28.5 \mu\text{s}$) with a peak value 0.45 times the output signal, while a smaller peak (0.27 times the output signal) preceded that one at 42.5 r.u. ($28.3 \mu\text{s}$)

the simulations are useful. In the simulation, the long, thin linear tip (with the short nook at the top) produced the strongest return signal, followed by the exponential tip, the shorter linear tip, and then the spline-shaped tips walls. The experiment, however, showed that the two linear tips performed the best, while the exponential and spline-shaped tips hardly produced a return at all. A possible reason for the difference between the simulation predictions and the experimental results is that the exponential and spline-shaped tips were designed to move the backscatter up within the tip, so that there is less scattering around the tip outlet. However, because real signals attenuate, earlier scattering has a disproportionate affect on the size of the return signal.

One other factor for the difference may lie in the technique used to fabricate the tips. The first three tips (thin linear, exponential, and spline-shaped) were made by step-drilling a rough outline of the shape, followed by a finer cut using electro-discharge machining (EDM). The process was completed by polishing the inside with a fine grit. While this process produced tips of acceptable quality, it was very difficult to reproduce, primarily because it was difficult to center the EDM electrode with the step-drilled holes. And since the exponential and spline-shaped tips are more complicated shapes, possibly leading to significant manufacturing irregularities that are hard to inspect.

Due to these problems with EDM fabrication, a second manufacturing technique was also tested with the second, shorter linear tip. In this technique, a conical reamer was produced to drill out the hole of a linear sloping tip. The reamer can only produce very simple shapes, like the short, linear tip (which, in contrast to the longer linear tip, does not have a small nook at the top of the tip). This process produced perfectly aligned holes, but also left grooves along the walls as an artifact of the drilling. These grooves were too deep to remove through polishing, and they produced significant reflections that made these tips unuseable.

To remove these grooves, the same shape tips were made by this process out of brass rather than stainless steel, and the grooves were etched using a bath of nitric acid. This etching removed the grooves, resulting in the tips used in the comparisons above. However, it should be noted that the acid etching resulted in a wider tip outlet than in the other tips. To see how wider holes might affect tip performance, a final simulation was performed with the outlet rounded slightly out, so that it was 0.54 r.u. wide instead of 0.50 r.u. Results of this simulation, along with a picture of the tip boundary, are shown in figure 4.10. Surprisingly, the wider outlet actually reduces the performance of the tip, since the curving tip produces more perpendicular surface for the wave to reflect off of.

While comparison of returns off a flat metal plate helped test the

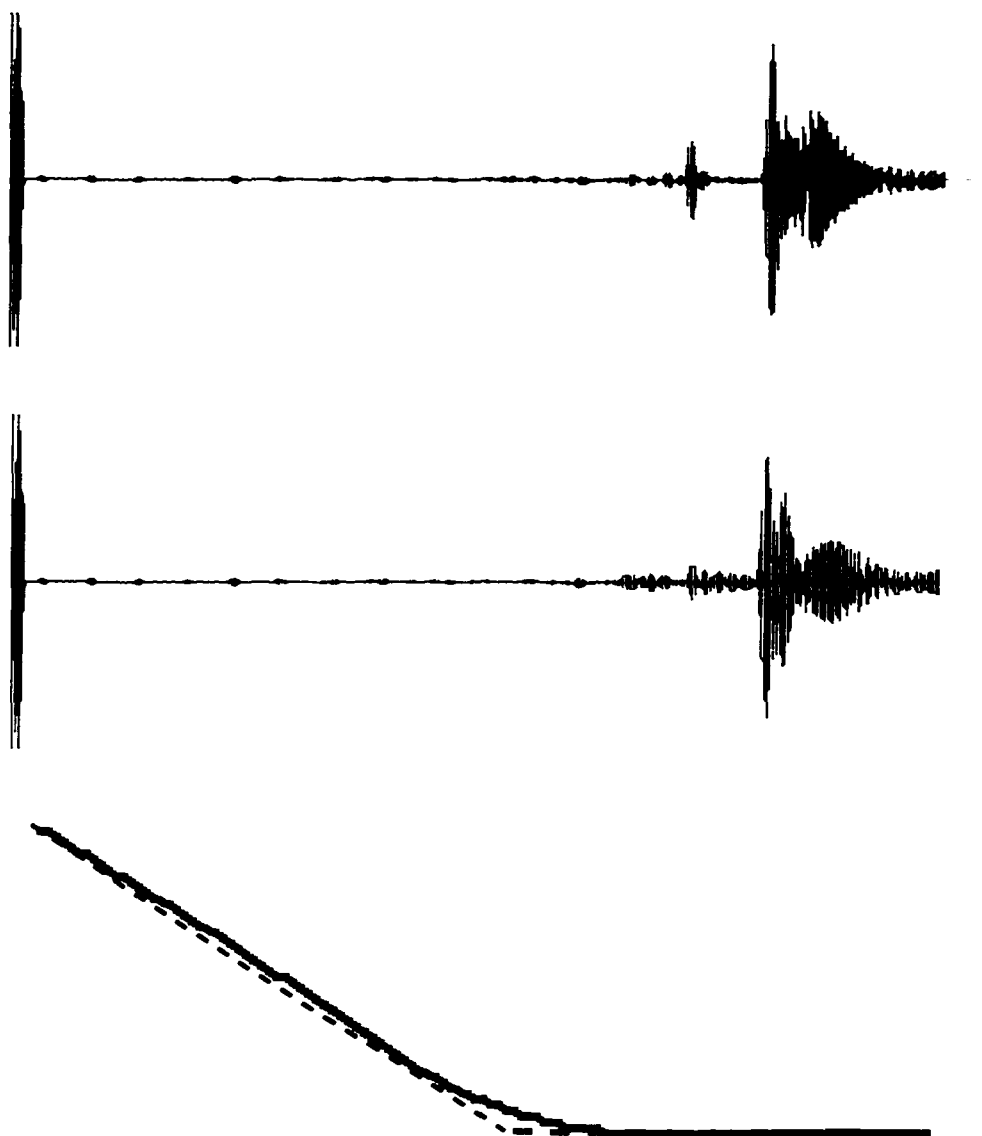


Figure 4.10: The effect of rounding the outlet. The top graph shows the voltage trace for a normal straight linear tip, while the middle graph shows the trace for the same tip, except that its outlet has been slightly rounded (the bottom figure shows the difference in the tips, with the dotted line representing the normal tip and the solid line representing the rounded tip). Notice that the normal tip has a more narrow reflection at the tip outlet than for the rounded tip. While it appears that this strong, narrow reflection would result in a weaker return signal, the opposite is true, as the return peak is slightly taller for the normal tip (0.82 vs. 0.79).

validity of the CAFIT simulation, a better test of the tip shapes comes from experiments conducted while imaging structures the size of a periodontal pocket. Therefore, further comparisons of tip performance were conducted while trying to image small holes, about 0.5 mm in diameter, drilled in a piece of plexiglas. The holes ranged in depth from 2-10mm. When imaging these holes, it is important to evacuate them of air, or else the ultrasonic wave will reflect off the air bubble and not the hole bottom, thus interfering with the depth measurement. To evacuate the hole, thin wire (close to 0.5 mm in diameter) was inserted in the hole to force out the air bubbles.

Hole	Man. Depth	Linear Tip	Exp. Tip	Spline Tip	Brass Tip
1	2 mm	2.2 mm	none	none	2.7 mm
2	5 mm	4.9 mm	none	none	4.9 mm
3	7 mm	7.3 mm	none	none	7.5 mm
4	10 mm	9.9 mm	none	none	none
5	9 mm	8.6 mm	none	none	9.0 mm
6	6 mm	5.9 mm	none	none	5.9 mm
7	4 mm	3.4 mm	none	none	3.5 mm

Table 4.2: A comparison of hole depth measurements using the ultrasonographic probe and a manual periodontal probe with 1 mm increments. The holes were drilled in a plexiglas phantom.)

Table 4.2 shows a comparison of the depth measurements recorded with a manual periodontal probe and the ultrasonic probe. The manual periodontal probe had markings every millimeter, and the standard dental practice of rounding up to the next visible marking was employed.

Figures 4.11– 4.14 show the ultrasound traces for each of the seven holes, plus one trace with the probe aimed at the top of the block. In each case,

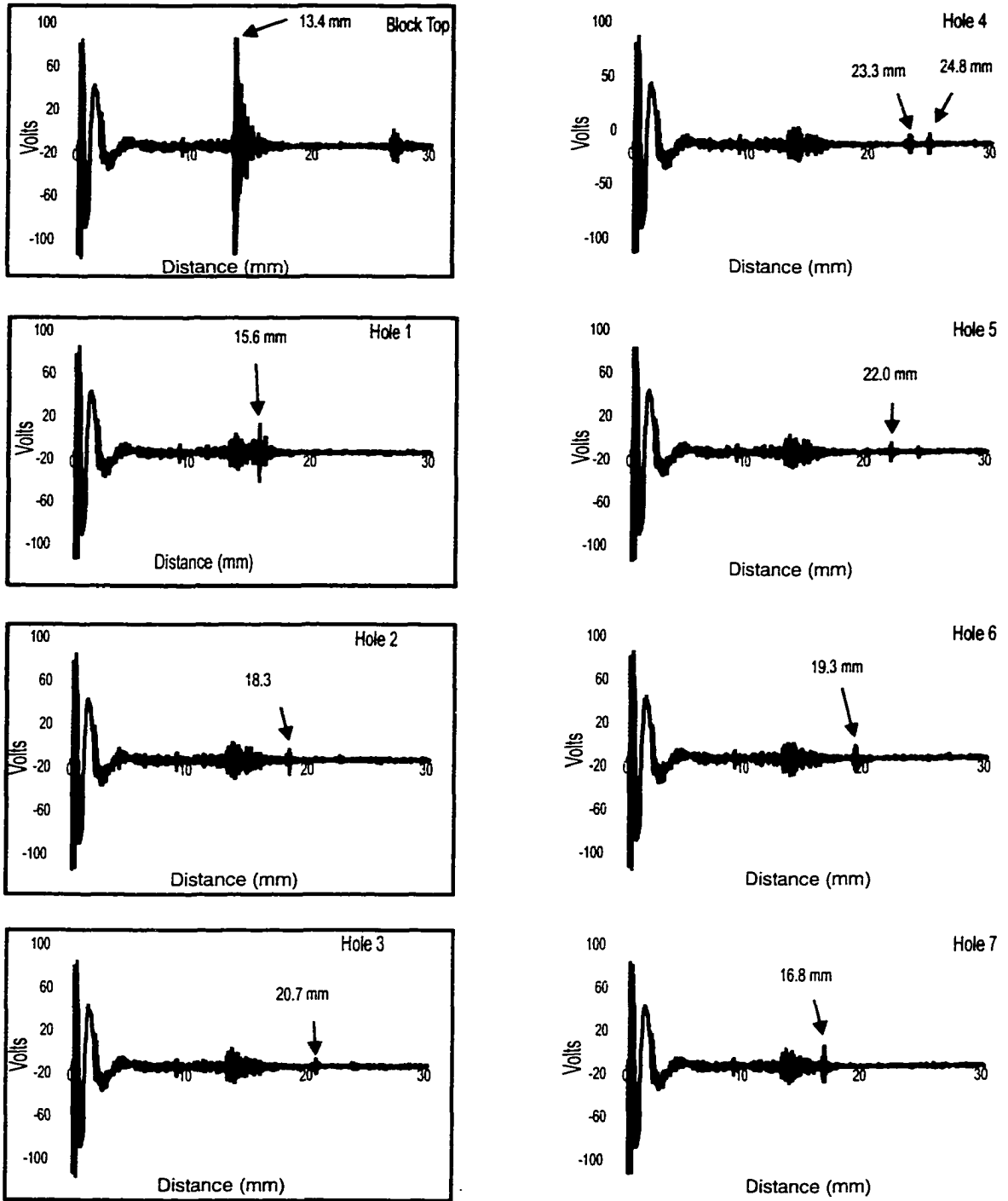


Figure 4.11: Scan of holes drilled in plexiglas block using the linear tip.

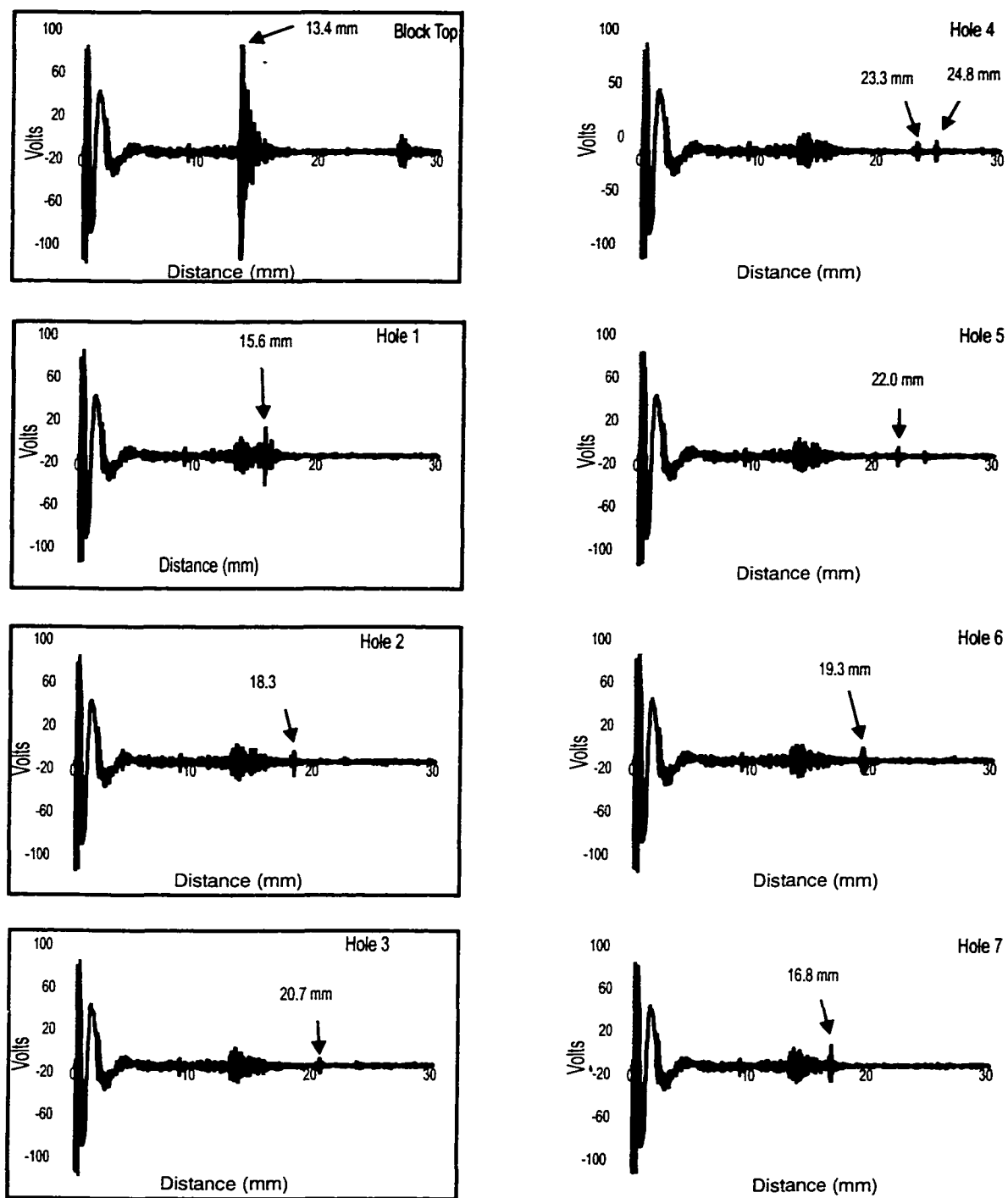


Figure 4.12: Scan of holes drilled in plexiglas block using the exponential tip.

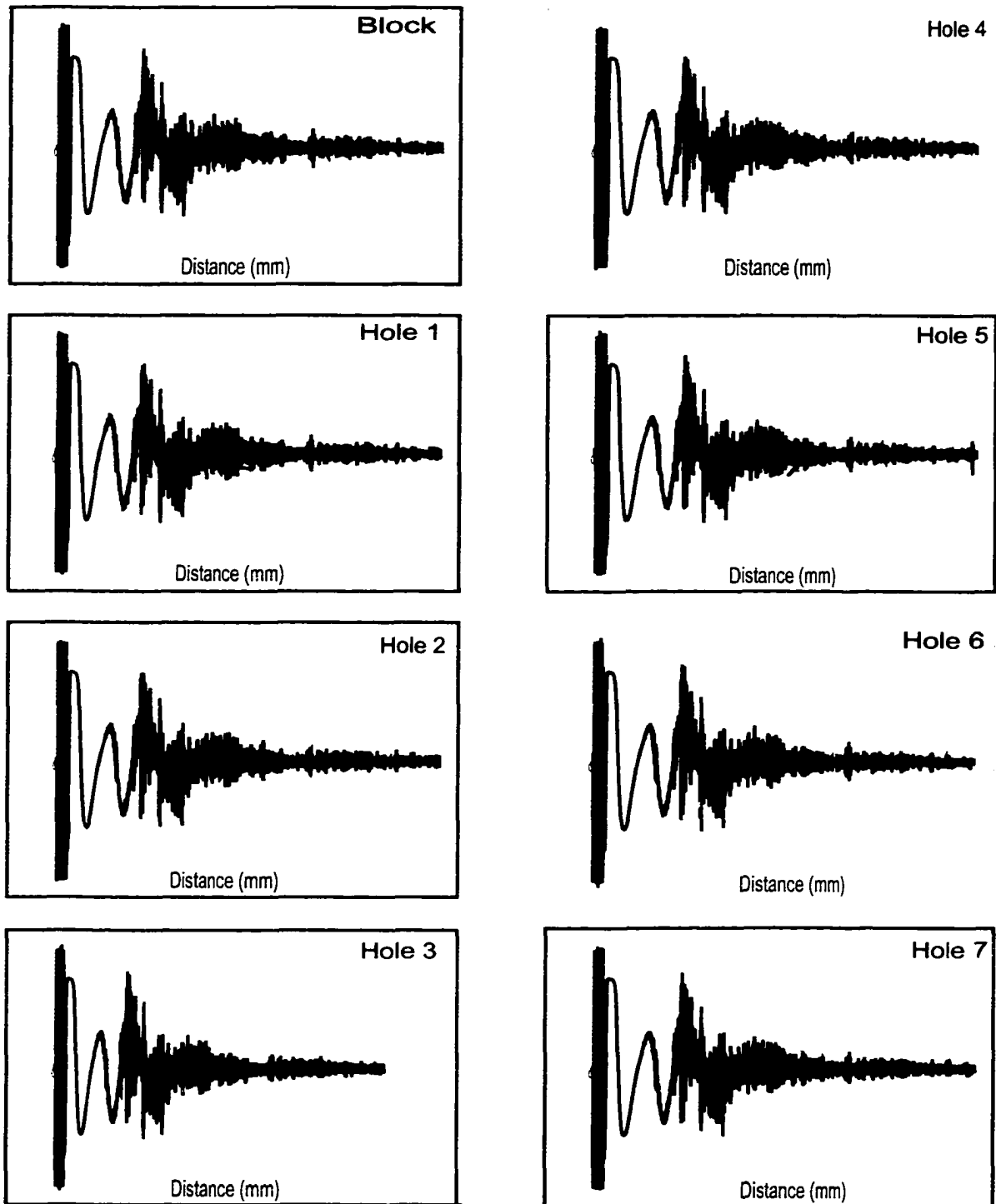


Figure 4.13: Scan of holes drilled in plexiglas block using the spline-shaped tip.

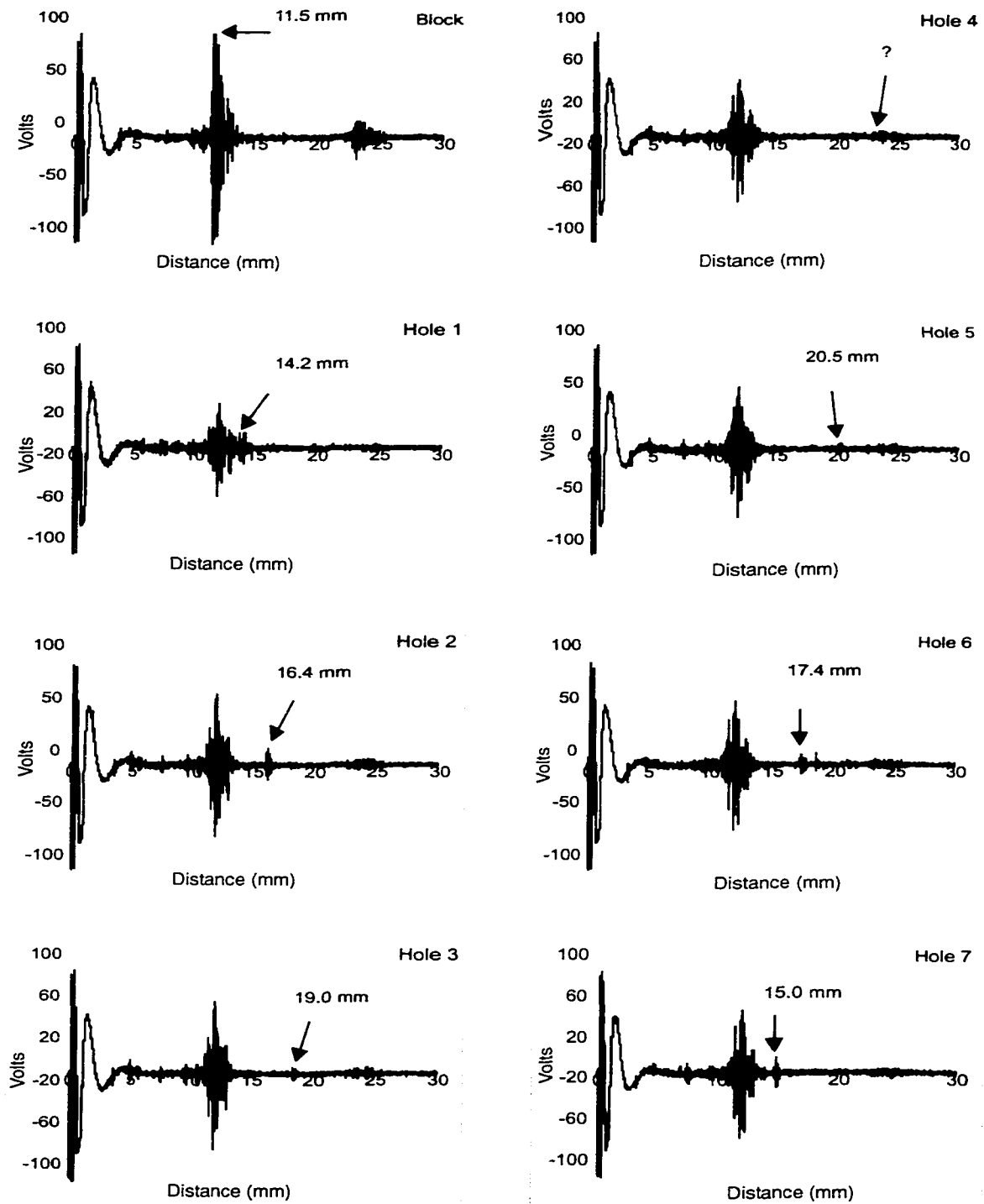


Figure 4.14: Scan of holes drilled in plexiglass block using the second, shorter linear tip.

the 15MHz Valpey-Fisher transducer was used in the probe.

In figure 4.11, where the linear tip was used, the returns off the bottom of the hole were always visible. In figures 4.12 and 4.13, though, where the exponential and spline tips were used, there was too much signal clutter to distinguish reverberations from inside the tip from reflections off the hole. Figure 4.14 shows the results for the short linear tip, which was able to image all the holes except for the deepest middle hole.

Therefore, both the CAFIT simulation and the experimental evidence indicate that linear tip walls sloping down to a narrow outlet reduces the ultrasonic beam profile with the least scattering. In addition, a sharper slope early on (before the wave has spread out too much to reflect off these sharply sloping walls) can produce more narrow walls, resulting in some improvement in the signal output. While refinements to the CAFIT simulation that account for signal attenuation, transducer gain, and turbulence in the water flow may produce more accurate simulations, the technique still provides a useful figure of merit to determine which tip geometries scatter ultrasound the least. Such a figure of merit allows for efficient testing of many tip geometries without an expensive process of manufacturing and testing different shapes by trial and error.

4.4 Transducer Testing

The final question addressed was the best choice of transducer for this probe. A range of custom transducers with a 2mm-diameter active area, a center frequency ranging from 10-25MHz, and -6dB bandwidth of between 5 and 8MHz, were produced by Valpey-Fisher, Inc.

Each of the transducers were first tested outside of the probe by imaging a flat metal plate approximately 20 mm from the transducer. As can be seen from figure 4.15, one of the 20MHz transducers produced an extremely weak return signal, while the 25MHz transducer produced spurious return signals that were the result of using a very high internal gain to compensate for the weak return signal. As a general rule, the higher frequency transducers required more damping to eliminate ringing in the signal (see figure 4.16). So although higher frequency signals are theoretically capable of greater resolution, this ringing reduced the resolution. If the ringing was eliminated through greater damping, signal strength was sacrificed. This is what happened with the 20 and 25MHz transducers that performed poorly [82].

After the initial test, those transducers that produced acceptable returns off the metal plate were tested by imaging the 0.5 mm diameter holes drilled in a plexiglas block.

Figures 4.17– 4.20 provide the results for each of the transducers

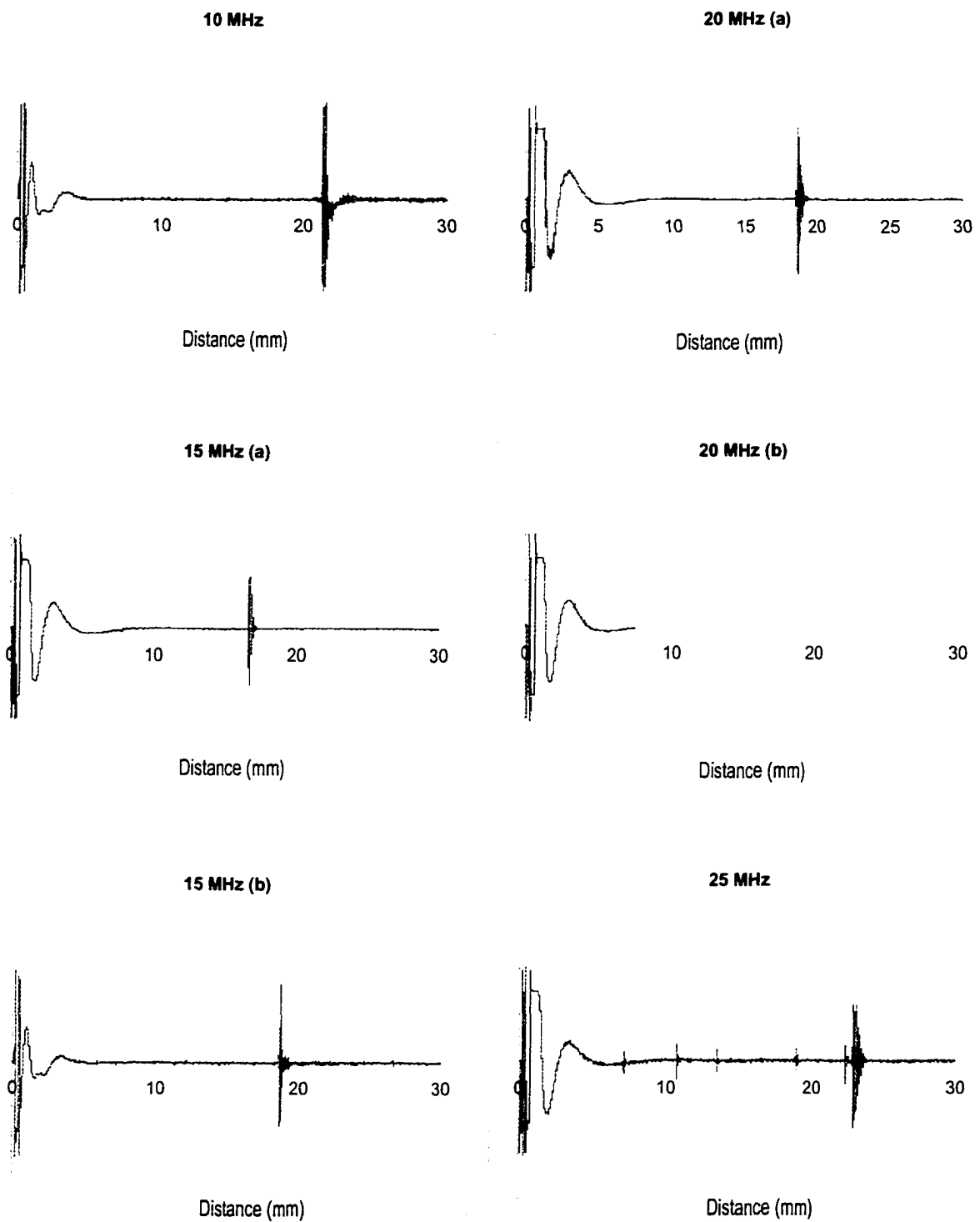


Figure 4.15: Testing of the transducers in open air.

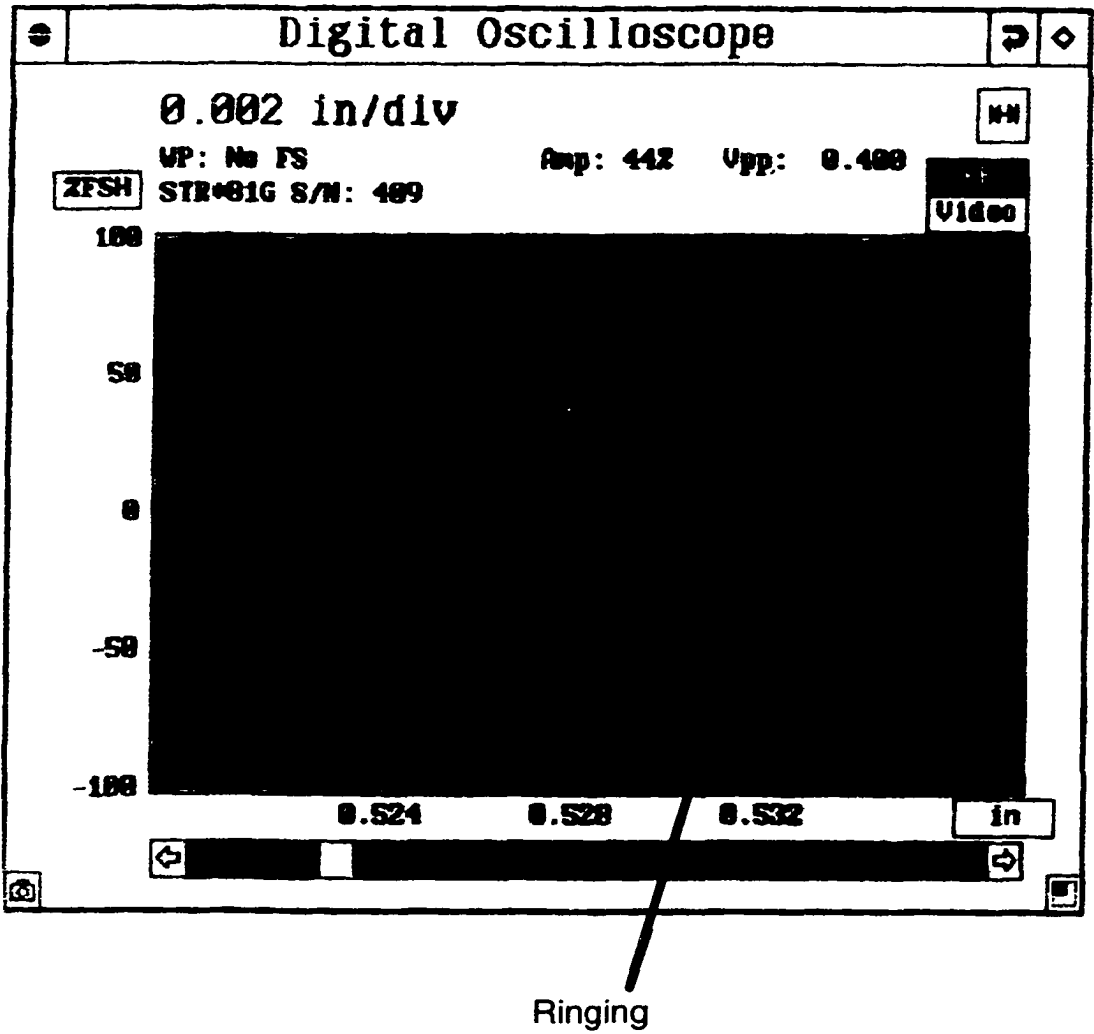


Figure 4.16: Example of a transducer exhibiting “ringing.”

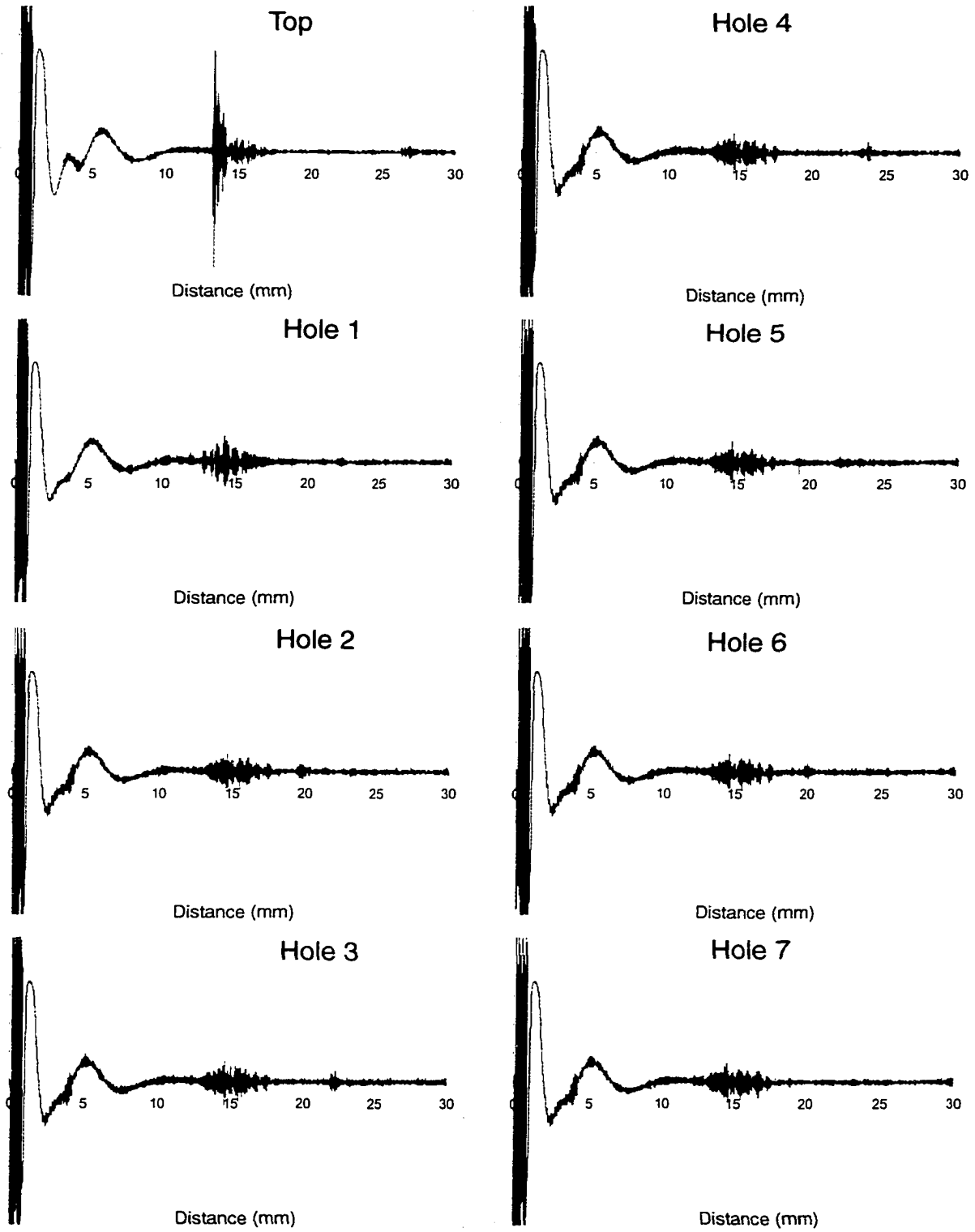


Figure 4.17: Imaging holes in plexiglas with the 10MHz transducer.

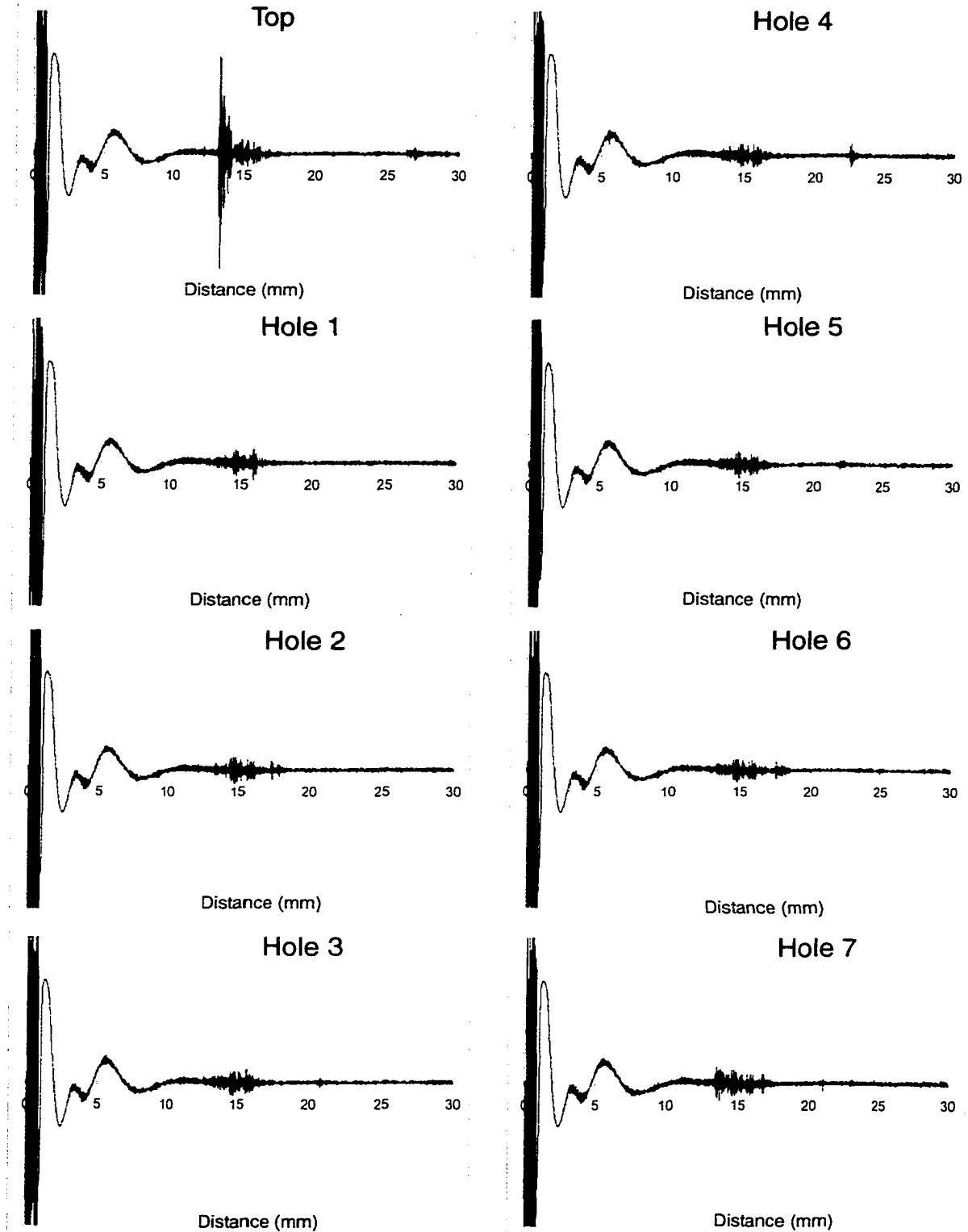


Figure 4.18: Imaging holes in plexiglas with the first 15MHz transducer.

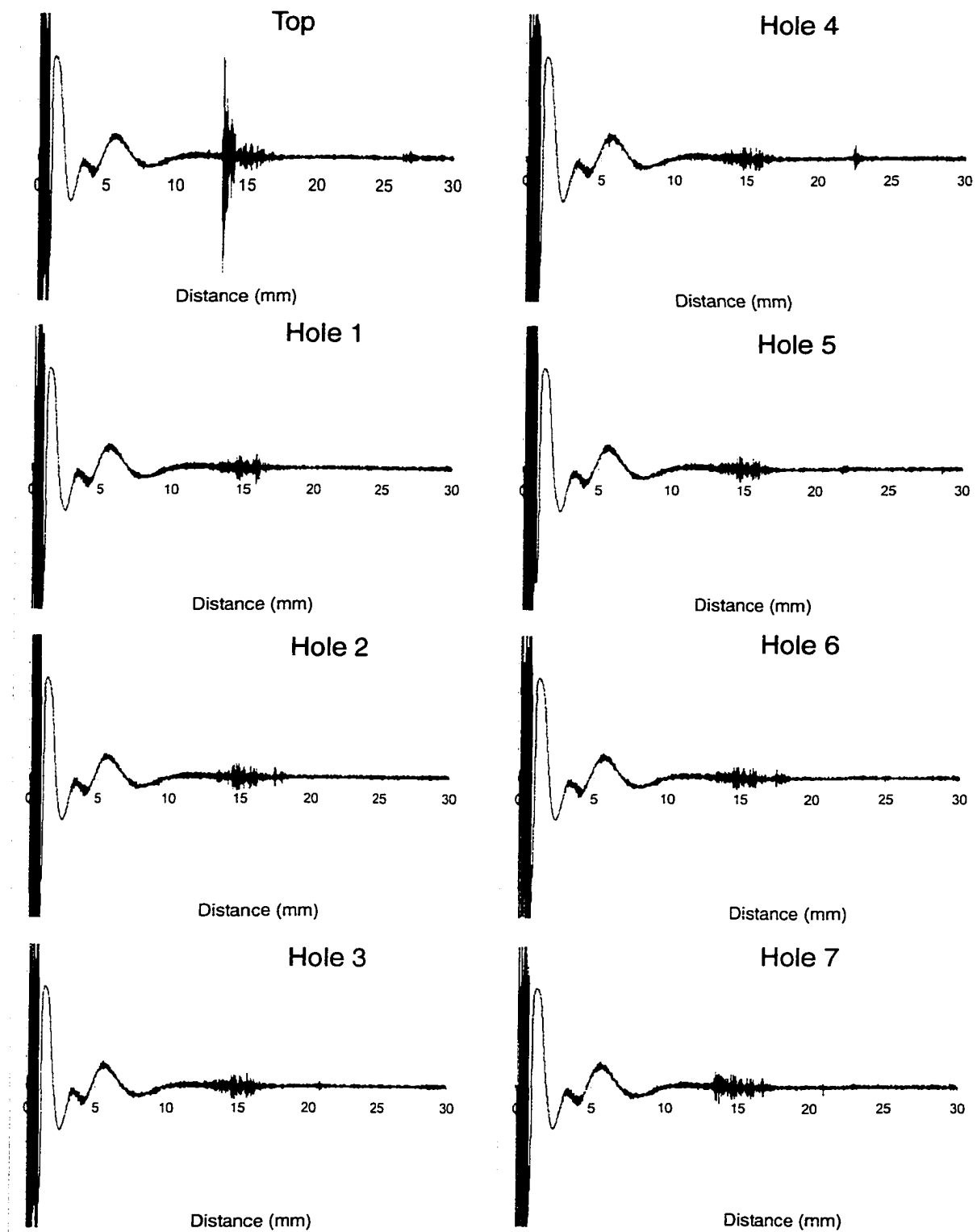


Figure 4.19: Imaging holes in plexiglas with the second 15MHz transducer.

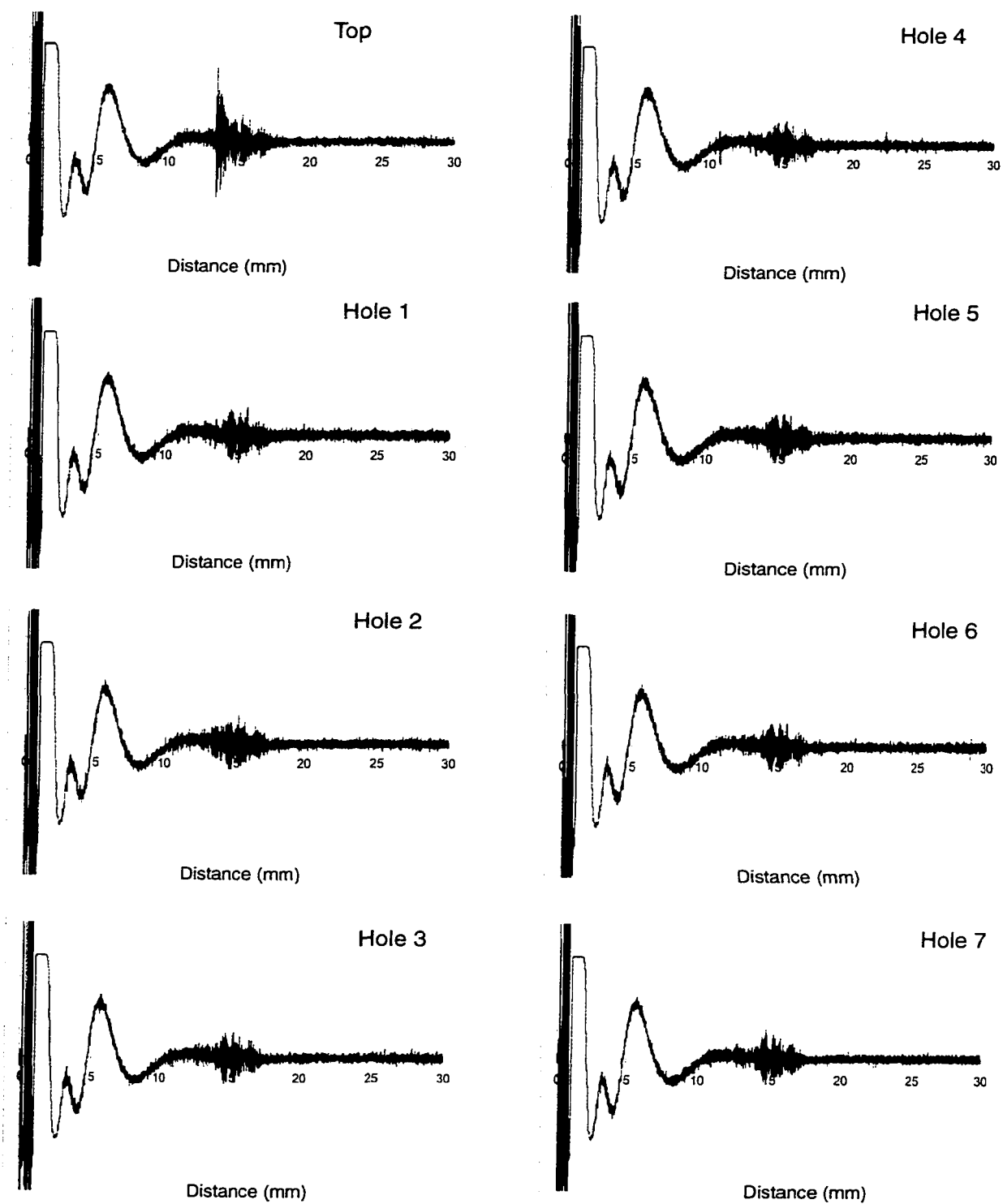


Figure 4.20: Imaging holes in plexiglas with the 20MHz transducer.

described above. The 20MHz transducer did not provide enough signal strength to image these holes, while both 10 and 15MHz transducers provided comparable resolution and signal strength. In addition, two other manufacturers provided custom transducers that did not perform well enough to use in this comparison study, much less in a clinical probe. Therefore, based on these results, 10MHz transducers were used in the tests that follow. Although the 15MHz transducers performed equally well in the study, the 10MHz transducers are easier to obtain, since 2mm-diameter transducers that operate above 10MHz are difficult to produce.

Thus, based on these results, all subsequent tests were performed with a pressure setting in the 5 psi range. In addition, the probe was equipped with the 10MHz Valpey-Fisher transducer, and the tip with long, thin linear walls and a slight “nook” at the top.

Chapter 5

Development of Signal Processing Algorithms

5.1 Preliminary Tests

After the prototype ultrasonic periodontal probe was completed, a series of tests were conducted to determine how effective the probe was at measuring the depth of periodontal pockets, and to begin developing methods for automating the analysis of the return signals.

The first test was conducted on a human subject, in which a single A-scan image of the periodontal pocket was saved. In this setup, a dental hygienist held the probe while an operator viewed the oscilloscope trace on the LabView data acquisition software's graphical user interface. As the hygienist pivoted the probe through various angles, the operator viewed which trace provided the best return signals and told the hygienist to hold the probe in place when the return signal was strongest. At that point, the

oscilloscope trace was saved.

This process was repeated on three different pockets chosen for their pocket depths as measured with a manual periodontal probe. One pocket was 3 mm, one 4 mm and one 5 mm. For each pocket, two sets of ultrasonic probing measurements were taken, once of a single trace and once of a trace averaged from 50 continuously acquired signals.

This process proved to be cumbersome, since the return signal would fade as the probe angle changed slightly due to hand jiggle, or as variations in water flow slightly changed the return signal. When the operator told the hygienist to stop moving the probe, the time lag between making the instruction and saving the trace was often long enough for the signal to fade out. This time lag made it difficult to obtain good data, and to correlate the strength of the signal with the position of the probe.

Figures 5.1 and 5.2 show the single trace and the signal averaged trace for the 3 mm pocket. Both traces show a first large peak at about 13 mm, which is approximately the distance from the transducer face to the end of the tip.

Both traces also show multiple return signals in the region from 13 mm to 17 mm. At this point, it was not clear what was causing these early returns (features inside the periodontal pocket or artifacts from the tip). However, the final return was assumed to be the bottom of the periodontal

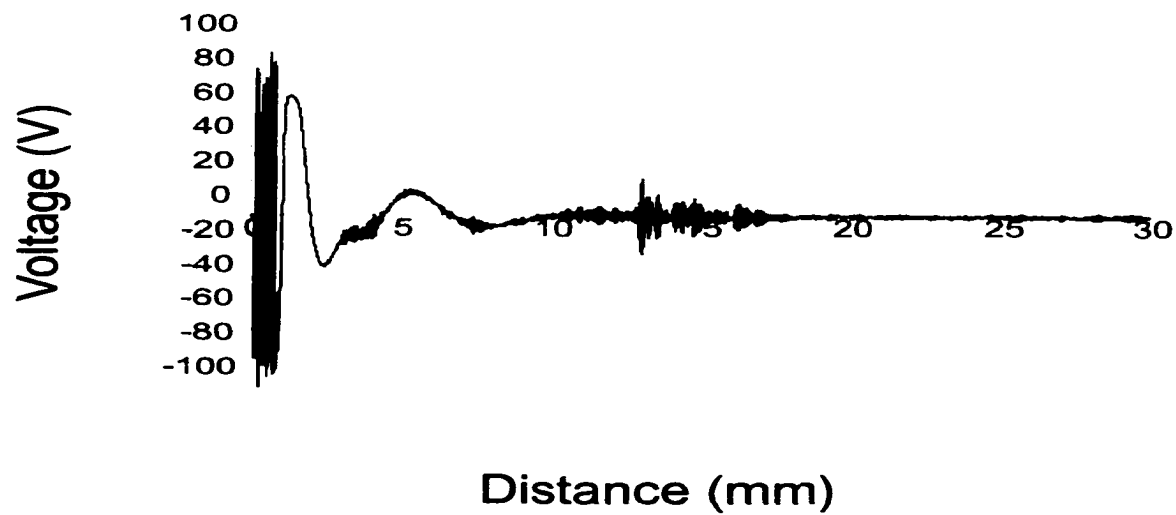


Figure 5.1: The return signal acquired from the 3 mm pocket.

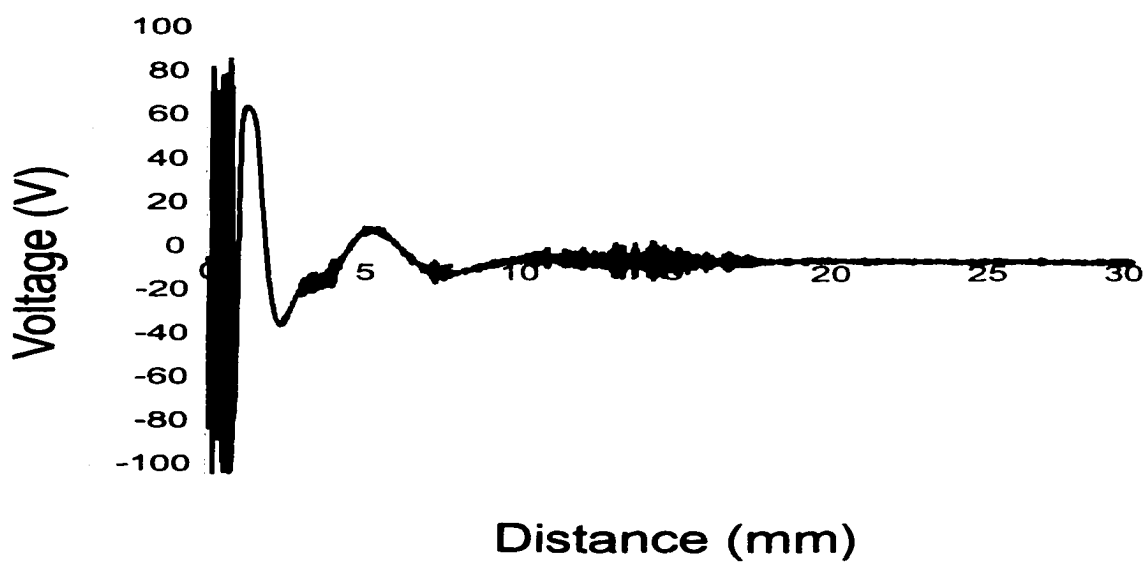


Figure 5.2: The signal averaged trace for the 3 mm pocket.

pocket, which occurs at 17.1mm. Measured from the first peak, which is a reasonable marker for the top of the pocket (it is either the end of the tip or reflections off the tooth surface), this results in a pocket depth of 4.0 mm for the single trace and 3.6 mm for the signal averaged trace. This value is within the 1 mm measurement error that is considered acceptable for a trained dental hygienist making pocket depth measurements with a manual periodontal probe. However, the difficulty in coordinating the acquisition of the signal with the positioning of the probe makes validity of these measurements somewhat questionable.

In comparing the traces in figure 5.1 and 5.2, the blurring of the return signal during averaging is the most noticeable feature. This blurring is evidence that the signal is not stationary but evolves over time, making the A-scan data acquisition mode a poor method to obtain data in the periodontal pocket. Assuming that the variations in signal strength and position are due to effects that can be considered random, such as variations in water flow, signal averaging may be a useful method for eliminating these variations. However, the noise in these traces has a large component that is not random, but rather is due to signal inductance from the analog-to-digital converter or from the coaxial cable. As a result, signal averaging does not improve the signal-to-noise ratio, as one would expect.

Figures 5.3 and 5.4 show similar results for the 4 mm pocket as for

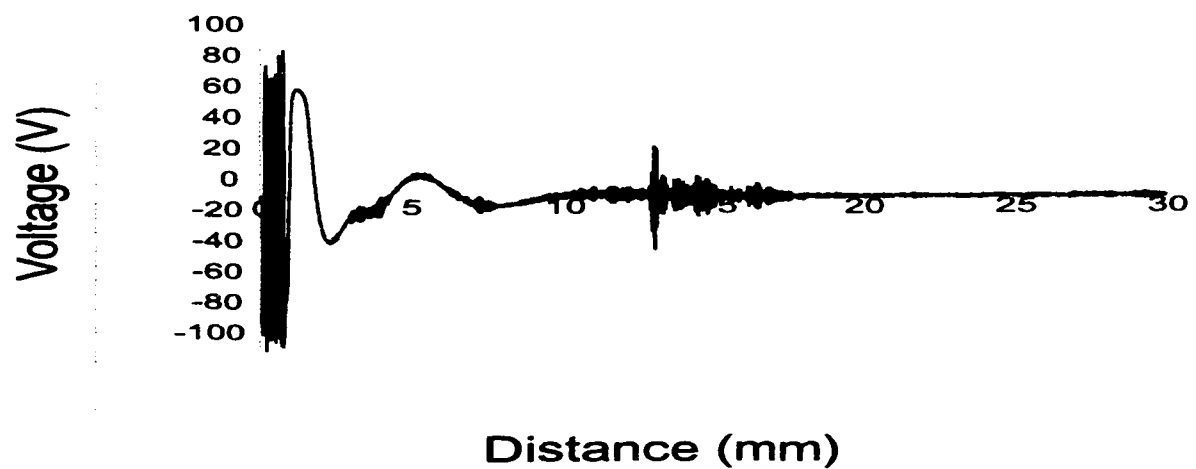


Figure 5.3: The return signal acquired from the 4 mm pocket.



Figure 5.4: The signal averaged trace for the 4 mm pocket.

the 3 mm pocket, with the ultrasonic pocket depths about 3.9 mm for both the single trace and the signal averaged trace (the blurring due to signal averaging makes it difficult to determine the exact position of the bottom of the pocket in figure 5.4).

For the 5 mm pocket (figures 5.5 and 5.6), the results are also similar, although the bottom of the pocket as measured by the ultrasonic probe does appear to be a little deeper: 4.5 mm for the single trace and either 4.0 mm or 4.8 mm for the averaged trace (the peak at 4.8 mm is very small, and could be noise).

To eliminate the coordination problems between saving a trace and properly orienting the probe, the LabView data acquisition software was modified to continuously save a series of scans as the hygienist aimed the probe in the sulcus.

This new data acquisition mode was first tested on cadaver jaw specimens obtained from the Periodontics Department of the Naval Postgraduate Dental School in Bethesda, Maryland. Cadaver jaws provide a useful phantom to test the probe because they accurately reproduce the geometry of the periodontal pocket, but are easier to work with during the initial test since there are no concerns of patient discomfort during extended examinations.

The jaw specimens were preserved in formalin, and unfortunately

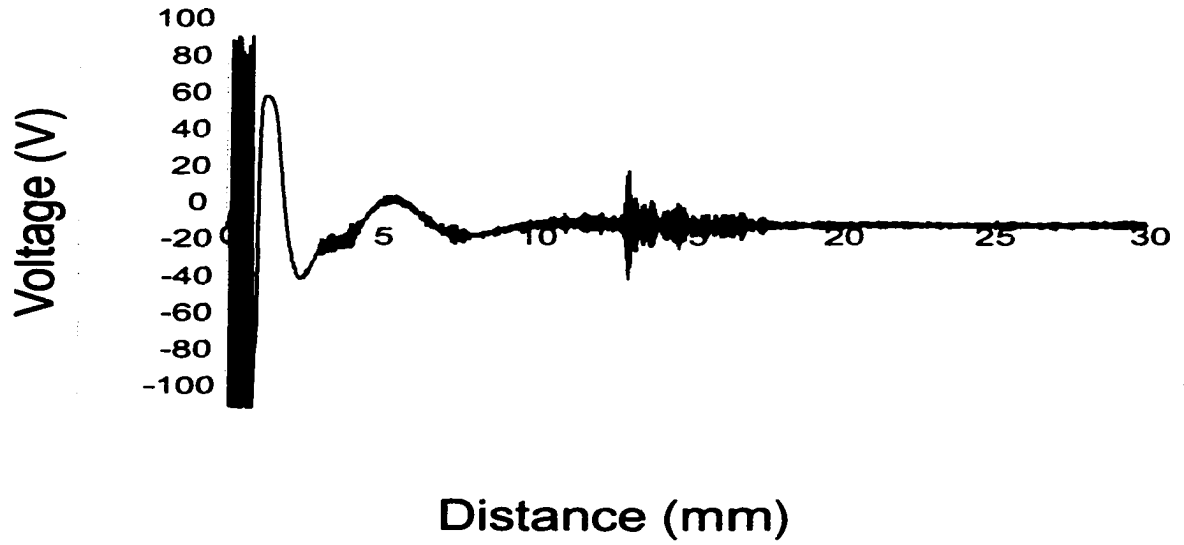


Figure 5.5: The return signal acquired from the 5 mm pocket.

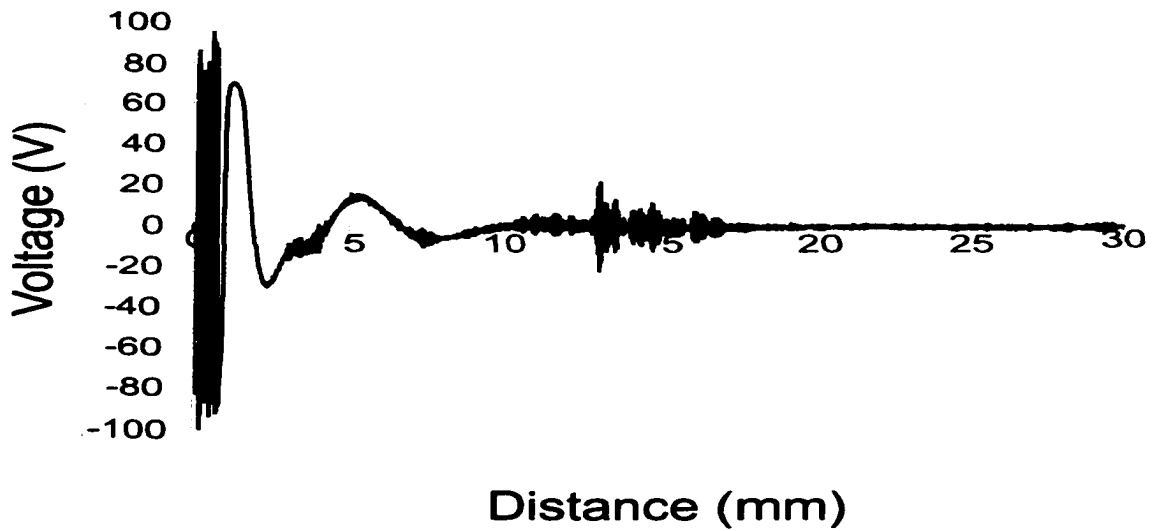


Figure 5.6: The signal averaged trace for the 5 mm pocket.

the periodontal tissue had hardened and tightened around the tooth, so that no periodontal pocket remained. To form a periodontal pocket that could be analyzed with the ultrasonic probe, surgical incisions (about 1 mm wide) were made along the gingival line, forming a series of pockets that ranged from 6 to 8 mm deep. While these incisions produced a pocket that could be probed, the ultrasonic properties of the tissue were still significantly different from those of living tissue. In addition, the pocket was larger than a pocket would be in a live patient (1 mm wide versus 0.25-0.5 mm wide), which could affect the nature of the return signal.

Of the three cadaver specimens, the first section had seven teeth on it. Two surgical incisions were made, one at the lingual mesial position of tooth 4 and one at the lingual position of tooth 7. The pocket depth on the tooth 4 incision, as manually measured using a probe with markings every 2 mm, was 8mm. To determine the pocket depth from the ultrasonic periodontal probe, the A-scan ran while trying to orient the probe to get the strongest return signal. These A-scan traces were added up sequentially to form a two-dimensional B-mode image, as shown in figure 5.7. This figure has the points within each A-scan trace on the y-axis, with the voltage levels indicated by greyscale pixels, while each trace is added along the x-axis. From visual inspection of this image, the line at point 1750

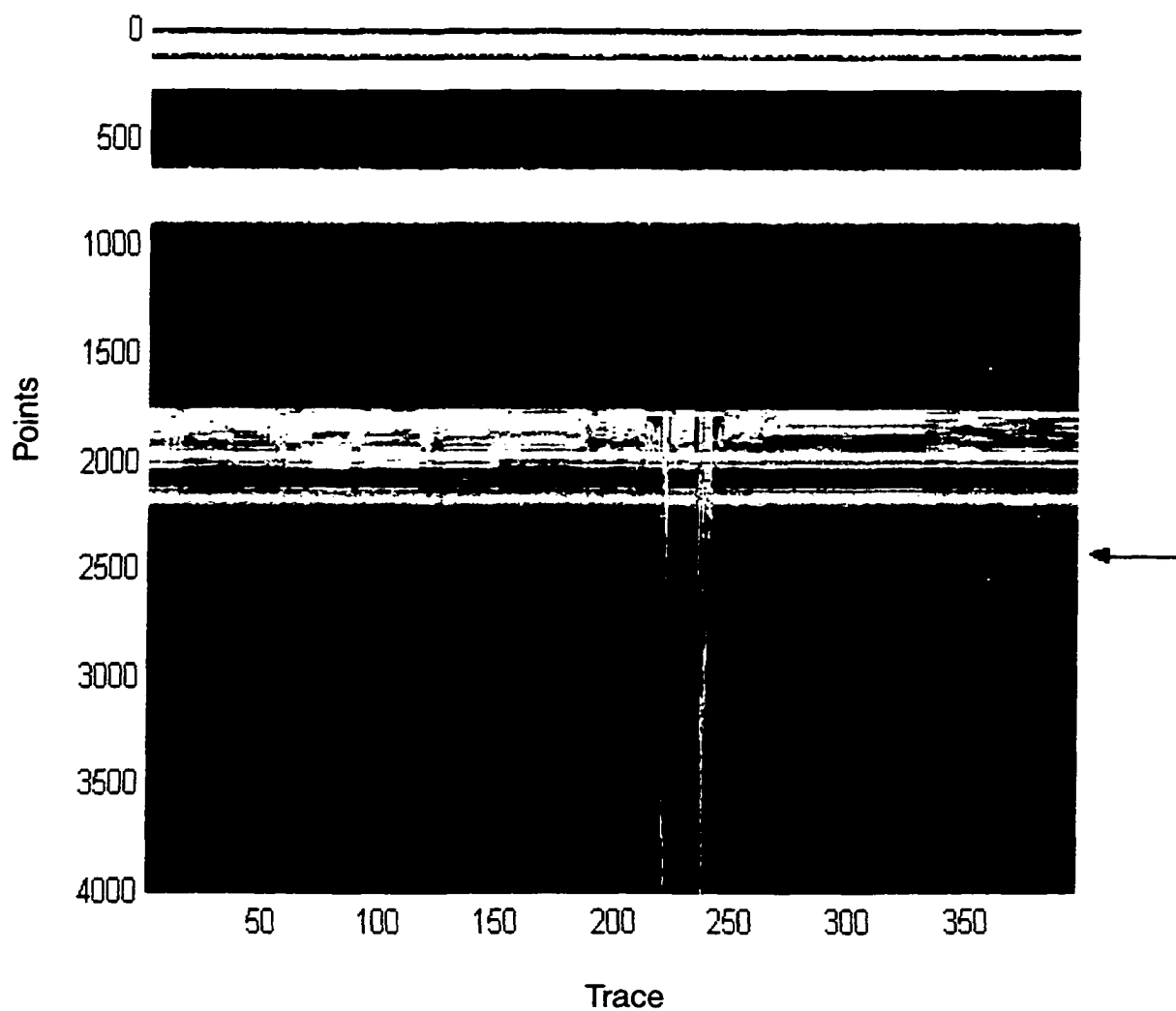


Figure 5.7: The first scan of tooth 4 on the 7-tooth cadaver jaw segment. The arrow points to the feature of interest at point 2450, which became visible after moving the probe orientation in the pocket until a strong return appeared. The white line in the middle of the scan occurred when the probe was moved away from the pocket for a moment.

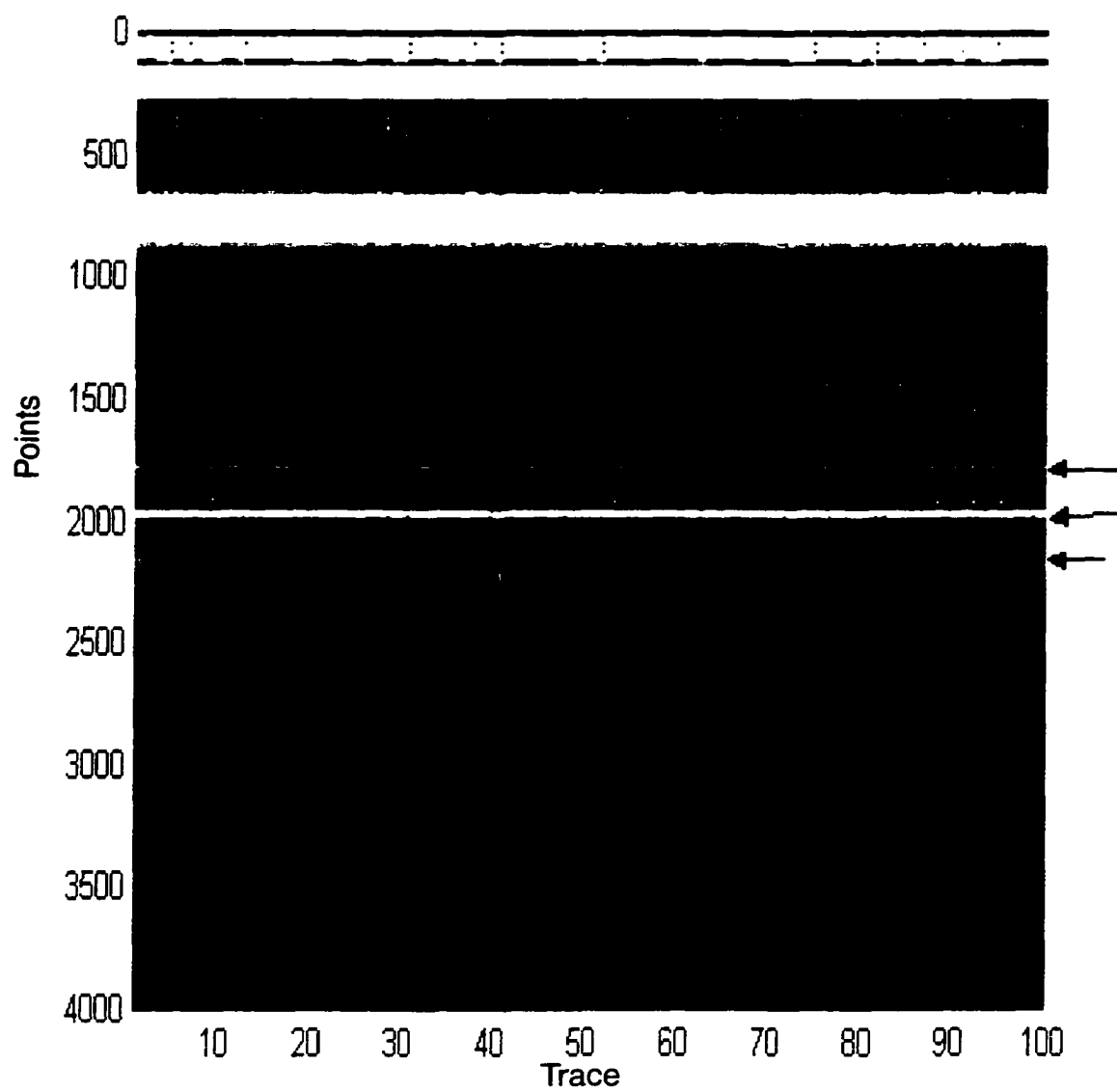


Figure 5.8: Scan taken while the probe was placed in a tub of water with no reflectors nearby. Note the three return lines at 1750, 1950 and 2150, which also appear in all the scans of the cadaver jaws.

Jaw	Tooth	Manual	1st Ultrasound	2nd Ultrasound
1	lingual mesial 4	8 mm	5.3 mm	4.5 mm
1	lingual 7	6 mm	13.9 mm	13.9 mm
2	distal buccal 2	6 mm	4.5 mm	4.5 mm
3	distal 2	8 mm	3.8 mm	4.5 mm

Table 5.1: Pocket depths in cadaver jaw specimens.

corresponds to the end of the probe tip, which is 13.1 mm long.¹ Two other prominent lines are at 1950 and 2150, but these lines are considered artifacts of the tip, since they show up on every cadaver jaw scan, and on a scan taken while the probe was sitting in a jar of water with no reflectors nearby (figure 5.8). The fourth line, which only appears towards the end of the scan in figure 5.7, is the feature considered most likely to be the bottom of the periodontal pocket. Since it is at 2450, this translates to a pocket depth of 5.3 mm, assuming that this feature is truly at the bottom of the pocket so that the ultrasound wave travels at the speed of sound in water, $1500 \frac{m}{s}$, for the whole trip.

The scan can also be analyzed by looking at any one of the traces in the 2-D image shown in figure 5.7. Figure 5.9 shows the 255th trace acquired from the image in figure 5.7, which shows more clearly the four feature lines described earlier.

The other pockets in the cadaver jaw specimens were measured in the same way, and the results of these measurements are shown in table 5.1.

¹ $Dis. = \frac{point}{sam.rate} * \frac{velocity}{2}$. In this case, $dis. = \frac{1750}{100MHz} * \frac{1500 \frac{m}{s}}{2} * 1000 \frac{mm}{m} = 13.1$ mm, since the sample rate was 100MHz and the speed of sound in water is $1500 \frac{m}{s}$.

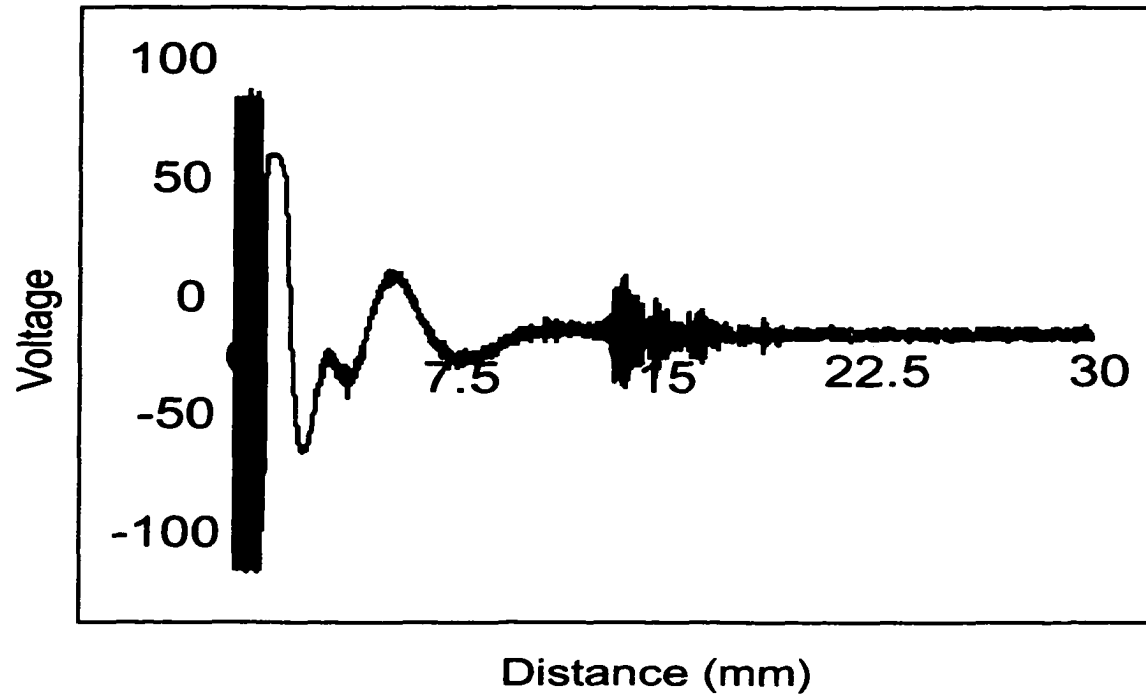


Figure 5.9: An A-scan like view of the 255th trace in figure 5.7. The peaks at about 13 mm, just under 15 mm, and just above 15 mm correspond to the feature lines at 1750, 1950 and 2150 in figure 5.7, while the smaller peak at about 18 mm corresponds to the feature line at 2450.

Because the return signals were so difficult to acquire during the first set of measurements, the measurements were repeated to see if the same pocket depth measurements would be acquired a second time. As can be seen from the table, there is almost no correlation between the manual probing depths and the ultrasonic probing depths, and the repeatability of the measurements was not very good either. However, it is not clear whether these poor results are due a problem with the ultrasonic probe, or to the poor quality of the cadaver specimens.

Rather than continue to investigate why the cadaver specimens did not produce good data, another test was conducted on a live patient. Such a test, using the new data acquisition program that allows for better analysis of the data, could determine whether more cadaver studies were necessary, or if tests on live patients would be a better use of available resources.

For this test, a patient with healthy teeth (pocket depths as measured with a manual probe ranged from 1 to 4 mm deep) volunteered to be examined with the ultrasonic probe. Manual and ultrasonic pocket depth measurements were taken on the first quadrant of teeth, plus a few extra teeth in the fourth quadrant that had 4mm-deep pockets.

During this test, the probe started out in a vertical position, nearly parallel to the tooth face (figure 1.7). From this position, hygienist slightly

moved the probe about its vertical axis to see if slight changes in probe position would provide a stronger return signal. However, after looking at a few teeth, the strongest signal always came from the starting position, and so the hygienist was instructed not to move the probe from that position.

5.2 Signal Processing

After obtaining this data, the scans were visually inspected to determine pockets depths and these measurements were compared to the pocket depths measured with the manual probe. Figure 5.10 summarizes the results of this visual inspection, by comparing the manual pocket depth measurements with the ultrasonic pocket depth measurements (as determined by visual inspection of the trace images).

Because the ultrasonic scans produce such a cluttered signal, a visual examination is a laborious and subjective measurement. The eye must pick out which peak among many is the feature of interest, and visually determine its position. Training a dental hygienist to make such a complicated interpretation of the data in a clinical setting is highly unrealistic, so any practical tool for measuring periodontal pockets depths must be able to automatically determine pocket depths.

The first step in automating this data analysis is to simplify the trace and extract only the features of interest. To this end, an automated

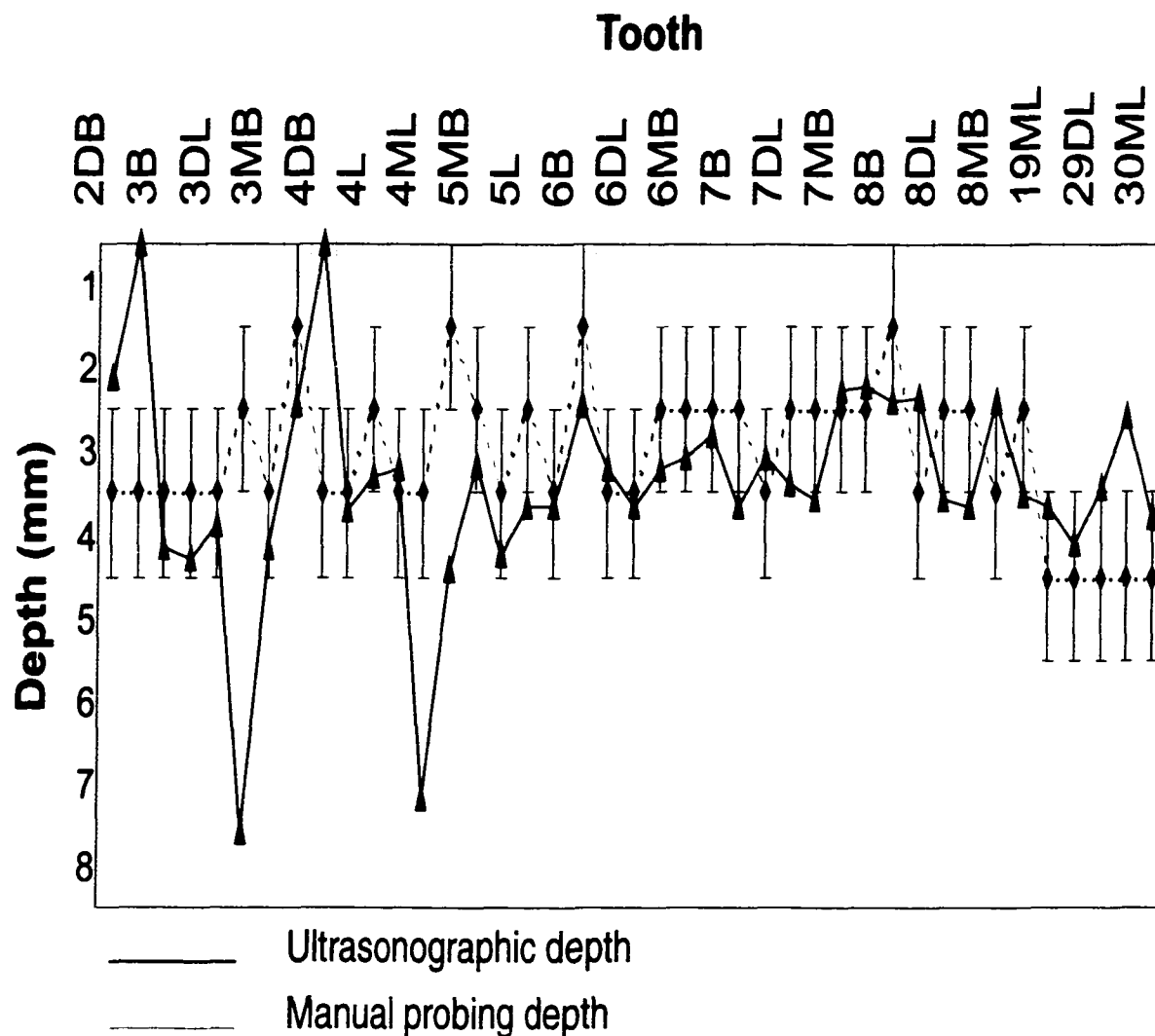


Figure 5.10: A comparison of manual probing depths (dotted line with error bars) with pocket depth measurements obtained from the ultrasonic periodontal probe. Of the 42 measurements obtained on this patient, 8 of the depth measurements were not within the ± 1 mm error considered acceptable for a trained dental hygienist making pocket depth measurements with a manual probe. However, the ultrasonic return signals were too difficult to accurately interpret at two positions (2 mesial buccal and 4 distal buccal).

pick peaking algorithm widely used in making spectrographic measurements was adapted for this analysis. Peak picking is most commonly accomplished through slope detection or polynomial curve fitting [83, 84, 85, 86, 87], although some work on the use of wavelet transforms has also been undertaken [88]. Slope detection, while providing better resolution than the other techniques, is more computationally costly. However, in this case, the computational complexity of the problem is greatly reduced by the fact that only the peak position must be detected, and not the peak shape, as is required in spectrographic measurements to determine the concentration of a chemical element along with its identity. Thus, the conceptually simple slope detection was employed.

The slope detection algorithm used in this project was modified from a commercial routine freely available from Galactic Industries Corporation [89]. In this algorithm, the first derivative of the discrete waveform is taken using a central difference approximation, and the average value of the first derivative is computed. Next, the local maxima are found wherever the derivative changes sign from positive to negative. If the slope just before this point is greater than the average slope, the original value of that data point is retained. All other points are set to zero.

The next step is to smooth the data by taking the maximum value within each block of 10 data points. Data smoothing reduces resolution

between scan points from 0.0075 mm to 0.075 mm, which is still smaller than the fundamental resolution limit for a 10MHz transducer.

At this point, the original waveform has been simplified greatly, as can be seen from the comparison of the original waveform obtained from a measurement of tooth 3 at the buccal position and the waveform after the peak picking algorithm has been applied (figure 5.11). However, as these A-scan waveforms are compiled into a 2-D B-mode image, certain features appear transient, while others remain fairly constant (they may fluctuate about some central value), as can be seen in figures 5.12 and 5.13. To eliminate the transient features and the fluctuations about a central value, signal averaging was applied after the peak picking algorithm.

Signal averaging is useful now, after the peak picking algorithm has been employed, because peak picking eliminates small variations in the signal due to movement of the probe, changes in water flow, or other factors. In the original waveform, the signal is not constant, so averaging blurred the signals and failed to eliminate the noise. In addition, the noise was not completely random in the original waveform, but was induced from signals nearby the analog-to-digital converter or the coaxial cables.

However, while the frequency of the noise in the raw waveform was not random, the amplitude was. Only a small percentage of the noisy signals were strong enough to produce a local maximum whose peak is

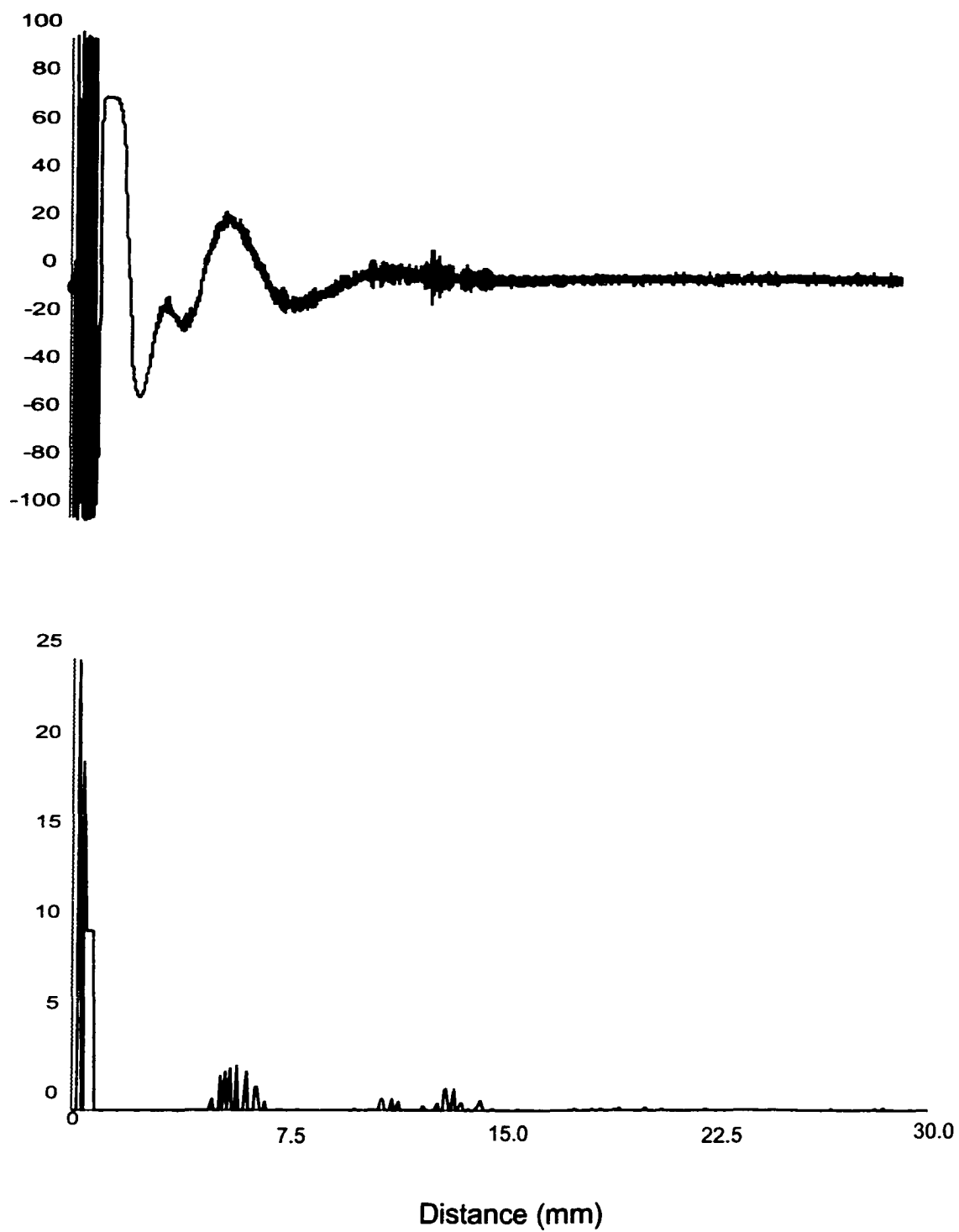


Figure 5.11: A comparison of the original waveform, and the waveform after the peak picking algorithm has been applied.

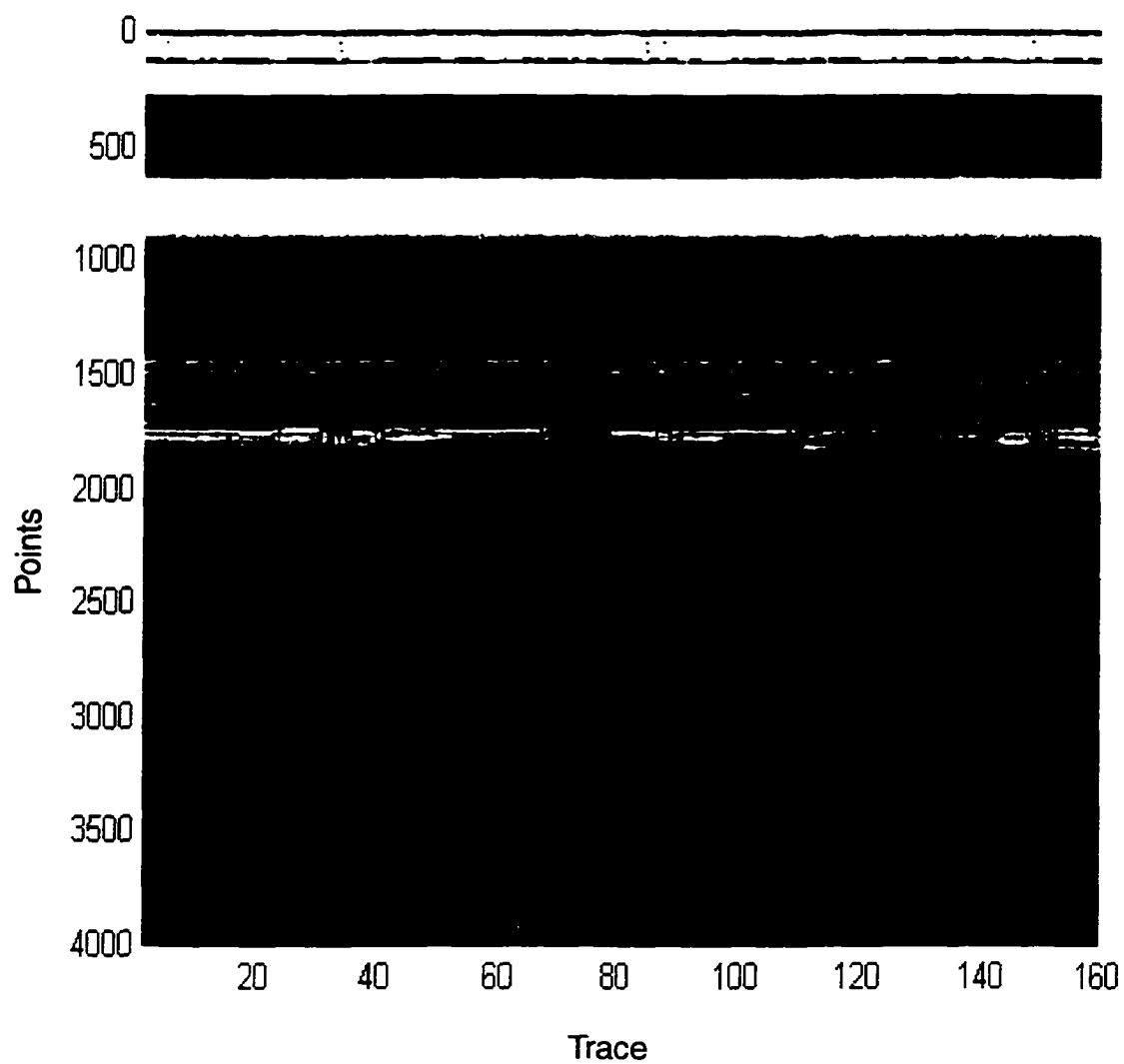


Figure 5.12: The B-mode image of the original waveforms compiled while the probe examined tooth 3 at the buccal position of the first volunteer.

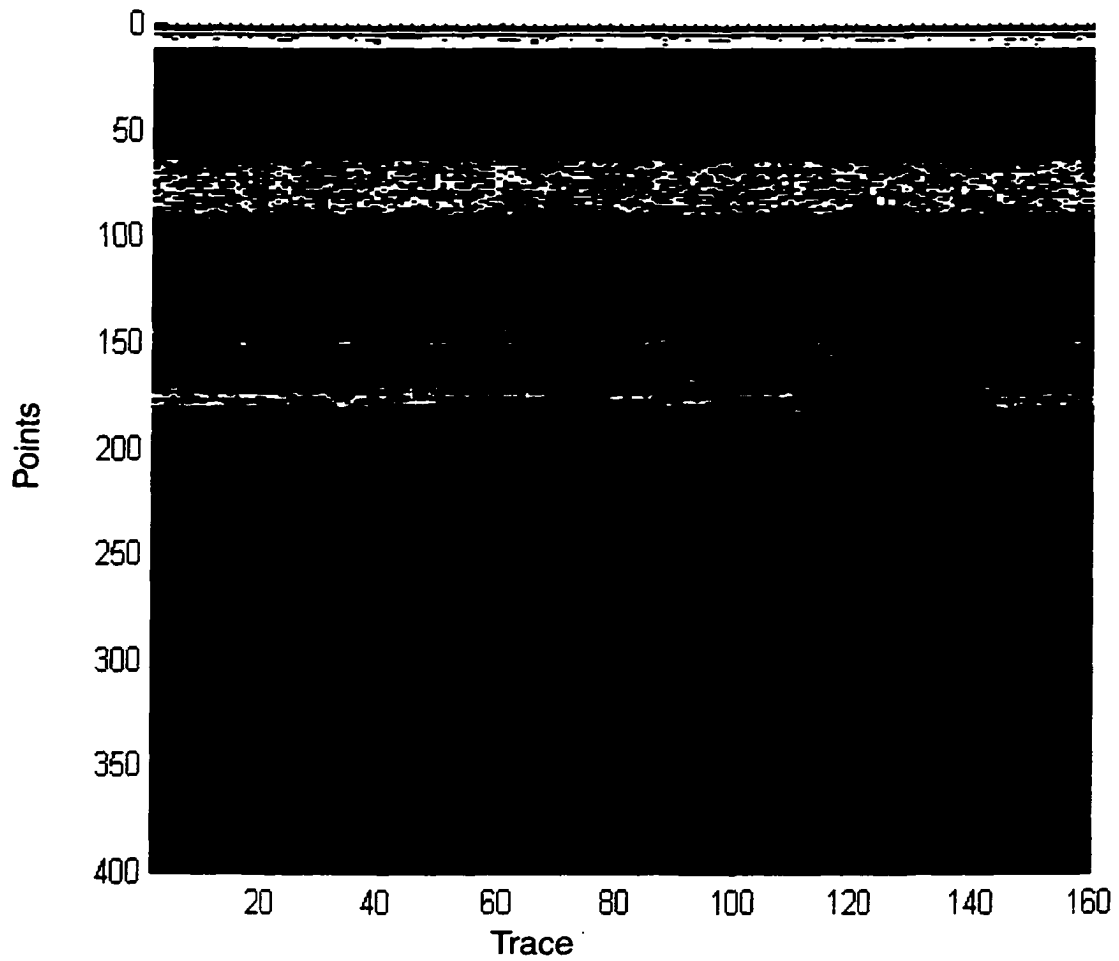


Figure 5.13: The B-mode image of the same tooth as in figure 5.12, except that peak picking has been applied to the image. Notice that while there is some variation in the signal from trace to trace, certain features stand out when looking at the image as a whole.

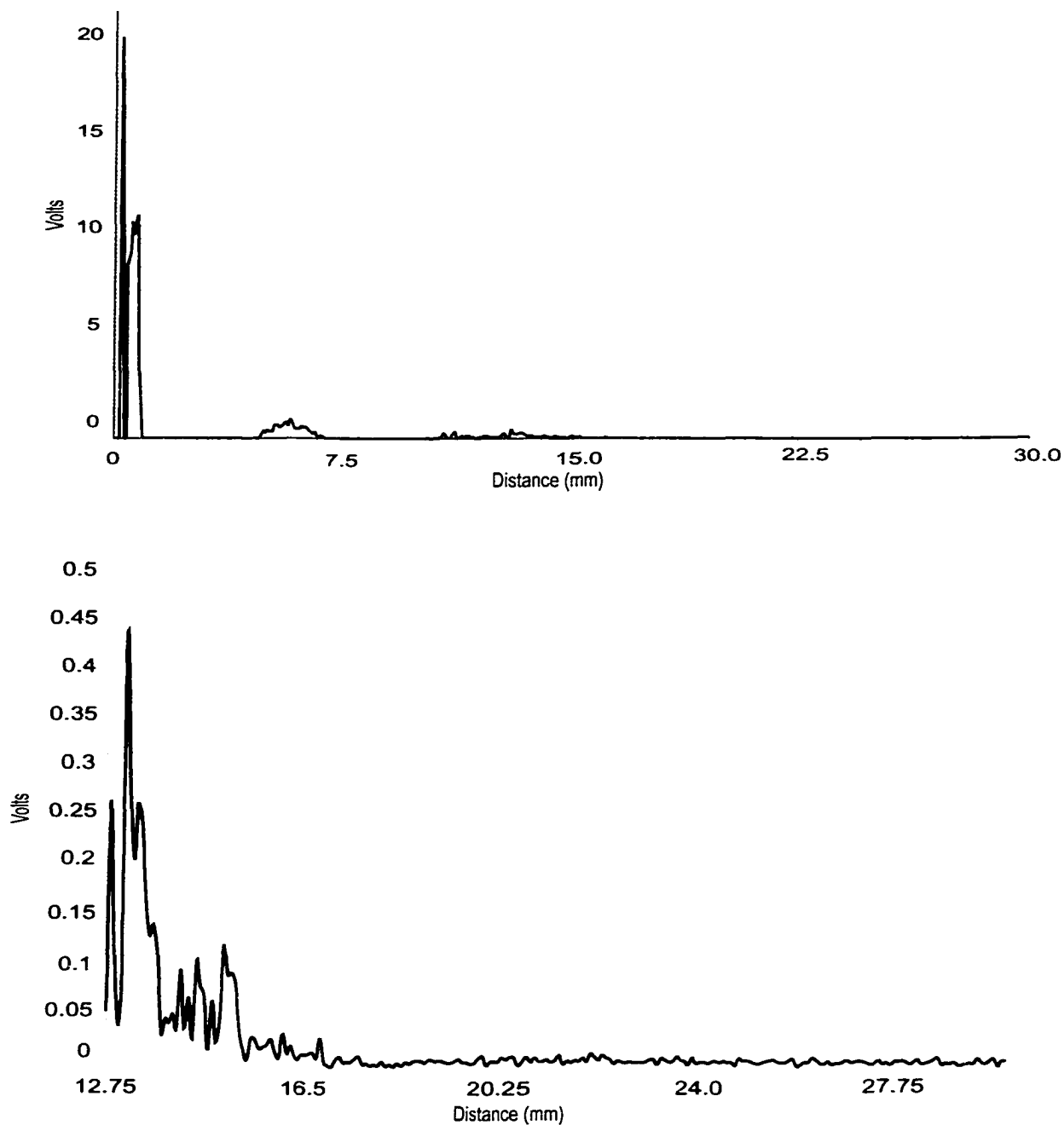


Figure 5.14: The waveform that results when signal averaging is applied to the image in figure 5.13. The bottom graph zooms in on the region of interest just after the tip. The first peak, at 13.1 mm is either a reflection as the ultrasound wave leaves the tip or a feature on the tooth, such as the cemento-enamel junction. The last significant peak, at 15.0 mm, is considered the bottom of the periodontal pocket, leading to a pocket depth measurement of 1.9 mm.

higher than the average peak, and the position of these peaks is essentially random. So, if signal averaging is applied after peak detection, the peaks from noise will be averaged out. The results of applying signal averaging after peak picking can be seen in figure 5.14.

With the aid of the peak detection algorithm and signal averaging, it is now easier to identify the weak signals that return from the bottom of the periodontal pocket. Therefore, the analysis of the data in figure 5.10 was repeated. Figure 5.15 summarizes this analysis, comparing the pocket depth measurements as measured by the manual probe with the pocket depth measurements made from inspection of the ultrasonic signal after peak picking and signal averaging had been applied to the raw signal.

Because the waveform has been greatly simplified and peaks due to noise were eliminated, it is much easier to distinguish peaks in the processed data. As a result, this analysis gave more accurate results than the analysis of the raw data. (If accuracy is defined as correlation with the manual probing depths.)

While peak detection followed by signal averaging simplifies the waveform and improves pocket depth measurement accuracy, some human interpretation of the data is still required. However, with more clinical data, it is hoped that the peak picking algorithm can be combined with a fully automated signal interpretation algorithm.

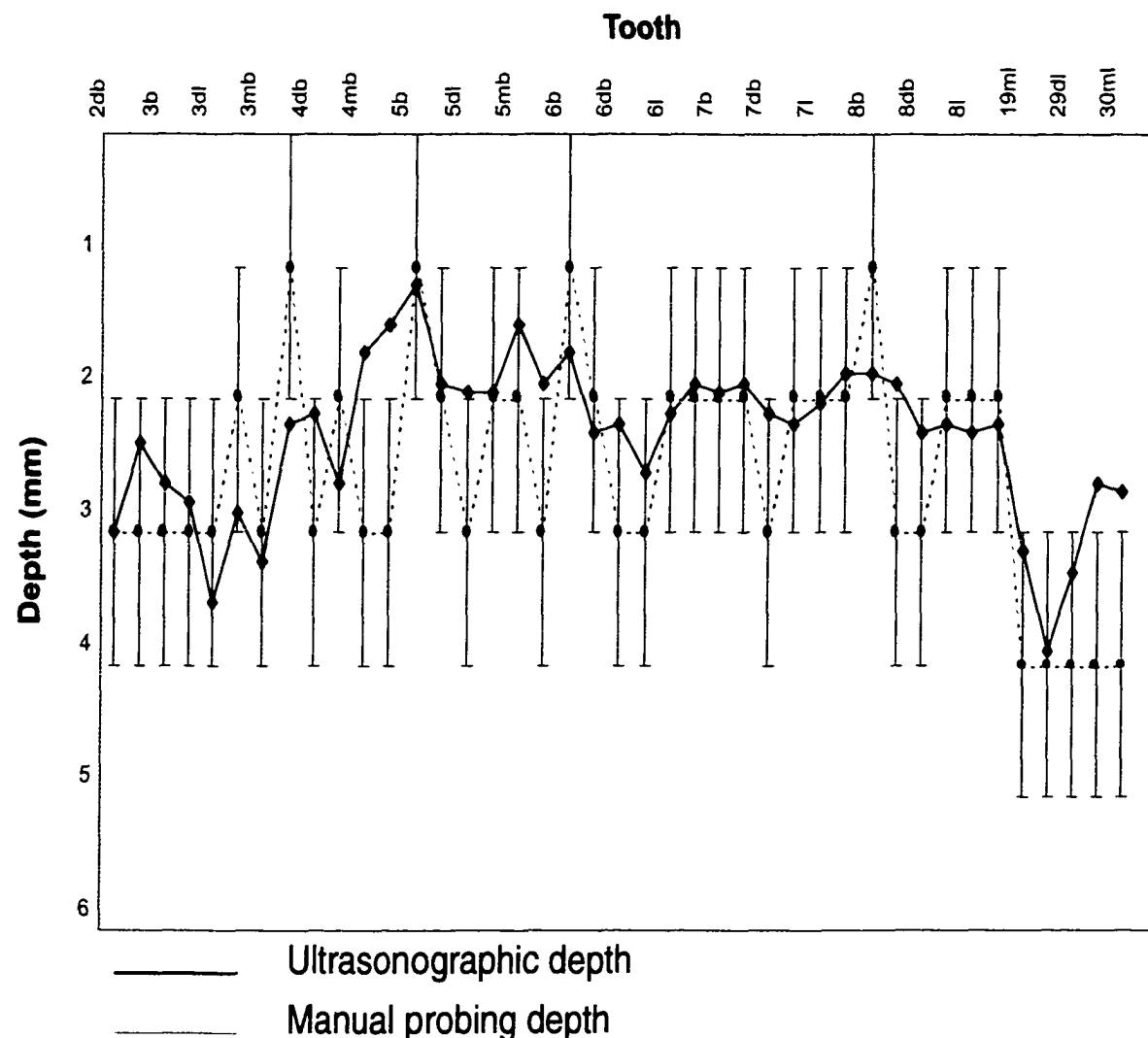


Figure 5.15: Comparison of the manual probing measurements with measurements obtained from inspection of the processed ultrasonic return signals. The combination of peak detection and signal averaging produced a greatly simplified waveform for analysis, which resulted in more accurate depth measurements than were made from inspecting the raw waveform (figure 5.10). In this plot, only 5 of the pocket depth measurements were not in the ± 1 mm error considered acceptable for a trained dental hygienist making pocket depth measurements with a manual periodontal probe. What's more, the furthest any of these 5 data points came from the error bar was 0.5 mm, while the furthest any of the 8 data points in figure 11 that were outside the ± 1 mm error bar came was 4 mm.

Chapter 6

Clinical Trials

6.1 The Study Protocol

From September to November 2000, a clinical study of the ultrasonographic periodontal probe was conducted at the Old Dominion University dental hygiene clinic. The study protocol was approved by the Institutional Review Board of Old Dominion University. Twelve subjects enrolled into the study presented with at least 24 teeth and varying levels of periodontal disease. 162 teeth provided 972 independent measurements. Health histories were reviewed, and subjects enrolled did not require antibiotic premedication before dental treatment.

The study involved one patient visit in which two periodontal examinations were performed 1 hour apart. The appointment scheduling

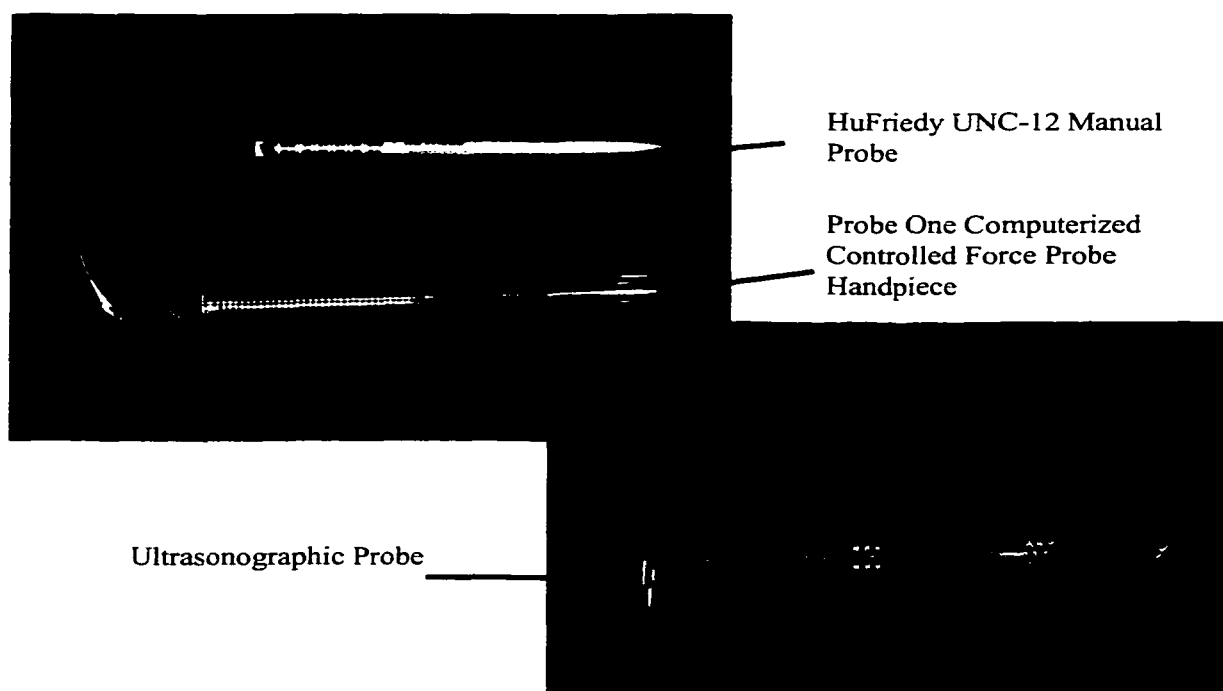


Figure 6.1: Manual and controlled force probes (top left), and the prototype ultrasonographic probe (bottom right), used in the clinical trials.

was long enough apart so that the operator could not recall probing measurements, but short enough to avoid tissue changes between visits.

To reduce intra-examiner variability, a single practicing dental hygienist with over 30 years of experience was used. To avoid examiner bias, the examiner was not permitted to view pocket depth recordings on the computer screen for either mechanical probe. The examiner was previously trained and calibrated with the manual probe to simulate pressure in the range of 20-30 grams.

Quadrants to be treated were randomly assigned. Three probing methods were evaluated: the ultrasonographic probe, computerized

controlled-force probe, and manual probe. (See figure 6.1.) The order of the probing method and quadrant to be treated were randomly assigned using simple randomization. Periodontal measurements were performed at six sites per tooth: disto-buccal, mid-buccal, mesio-buccal, disto-lingual, mid-lingual and mesio-lingual.

The comparison probes used in this study were a computerized controlled-force probe and the UNC-12 manual probe. The computerized probe system (Probe One - American Dental Technologies, Inc., Corpus Christi, TX) is a constant force automated probing system. The system includes a control unit, 2 memory cards, handpiece, printer, footswitch, and disposable probe tips. The controlled-force probe uses a plastic filament, with a rounded tip diameter of 0.54 mm, to probe the pocket. The probe measures depths from 0.0 mm to 10.0 mm in 0.5 mm increments, with approximately 30 grams of force. To operate the computerized probe, a flexible filament fiber was inserted between the gingiva and the tooth surface. The probe filament was gently depressed until the tip reached the base of the periodontal pocket. At the point of contact, the footpedal was depressed to capture the data.

Manual probing measurements were determined with new, same batch UNC-12 probes (HuFriedy, Chicago, IL) with a tip diameter of 0.45 mm and calibrated markings every millimeter for 12 mm with colored

reference points at 5 and 10 mm.

The Gingival Index (GI) of Loe and Silness [90] was used at the beginning of the appointment to assess the severity of gingival tissues adjacent to selected teeth. A score from 0-3 was assigned using the following criteria:

- 0:** Absence of inflammation
- 1:** Presence of mild inflammation, slight color change, slight edema, and no bleeding on probing
- 2:** Presence of moderate inflammation, moderate redness, and edema with bleeding on probing
- 3:** Presence of severe inflammation, marked redness and edema, and tendency toward spontaneous bleeding

Bleeding indices were not captured since bleeding would not be a comparable indicator with the non-invasive ultrasonographic probe.

The ultrasonographic probe was equipped as described in chapter 3 and the gain on the pulser/receiver was set very high (45 dB) in order to adequately amplify the small signals that return off the bottom of the periodontal pocket. Finally, during the first 6 examinations, water flow in the ultrasonographic probe was controlled through a pressure gauge that was set just below 5 psi. For the last 6 examinations, a foot pedal was

incorporated into the probing apparatus that allowed the hygienist to control the flow of water and the computer interface (which previously was controlled by an examination assistant) as she moved the probe from position to position. As a result, the foot pedal shortened examination time and improved patient comfort.

During the exam, the ultrasonographic probe was held in a vertical position, almost parallel to the tooth face. In addition, the hygienist looked for two visual clues to determine if the probe tip was in the right position: a slight blanching of the gum tissue and complete coupling of water into the periodontal pocket (no water squirted back out of the pocket during probing). Under these conditions, a high-quality signal was almost always acquired. In the few cases where a poor-quality signal was obtained—usually due to poor water flow—the hygienist was instructed to repeat the measurement at that site.

Once the proper probing position was found, the ultrasonographic probe was held in place for a few seconds until a series of A-scan traces could be acquired by the LabView data acquisition software. For the first patient, the amount of time the probe was held in place was determined by trial and error. In most cases, a few seconds was enough to acquire 30-40 A-scan traces. For the second patient, the LabView software was reprogrammed to acquire 100 traces. While this improved the quality of the

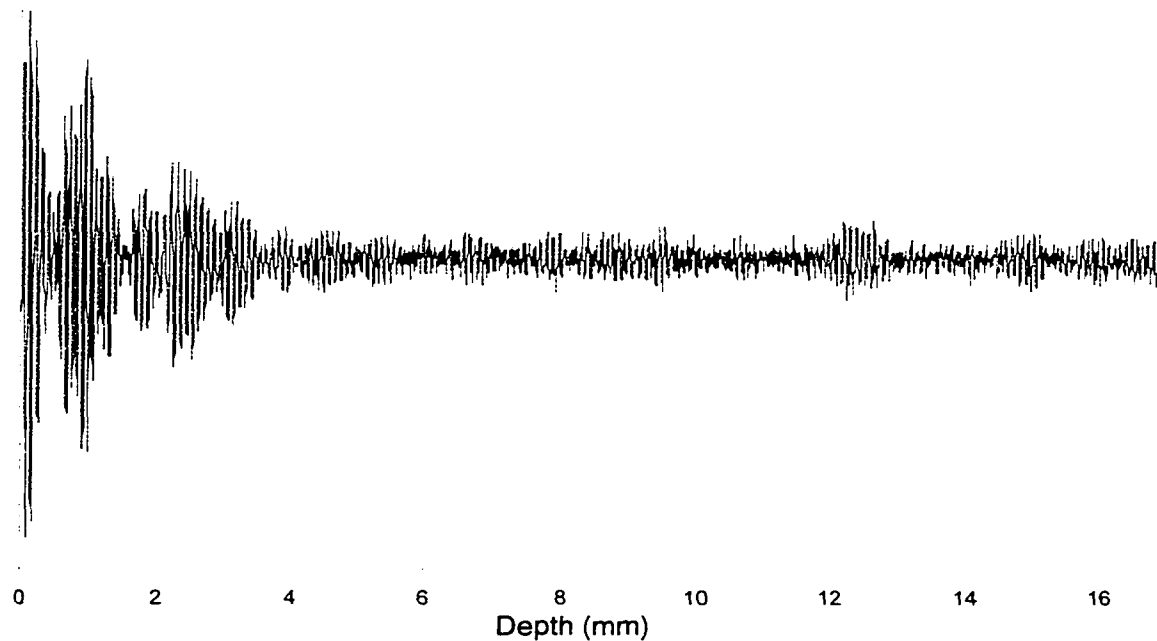


Figure 6.2: An example of an A-mode trace obtained from scanning a periodontal pocket.

processed signal somewhat, the extra time needed to acquire the signal led to operator fatigue and patient discomfort. Thus, for all subsequent examinations, the LabView software was set to acquire 36 A-Scan traces. (For the sake of consistency, all the results described below are based on averaging only the first 36 traces, no matter how many were acquired during the exam.) During the exam, the raw data was saved on the computer hard drive so that it could be processed later in the lab. An example trace is shown in figure 6.2.

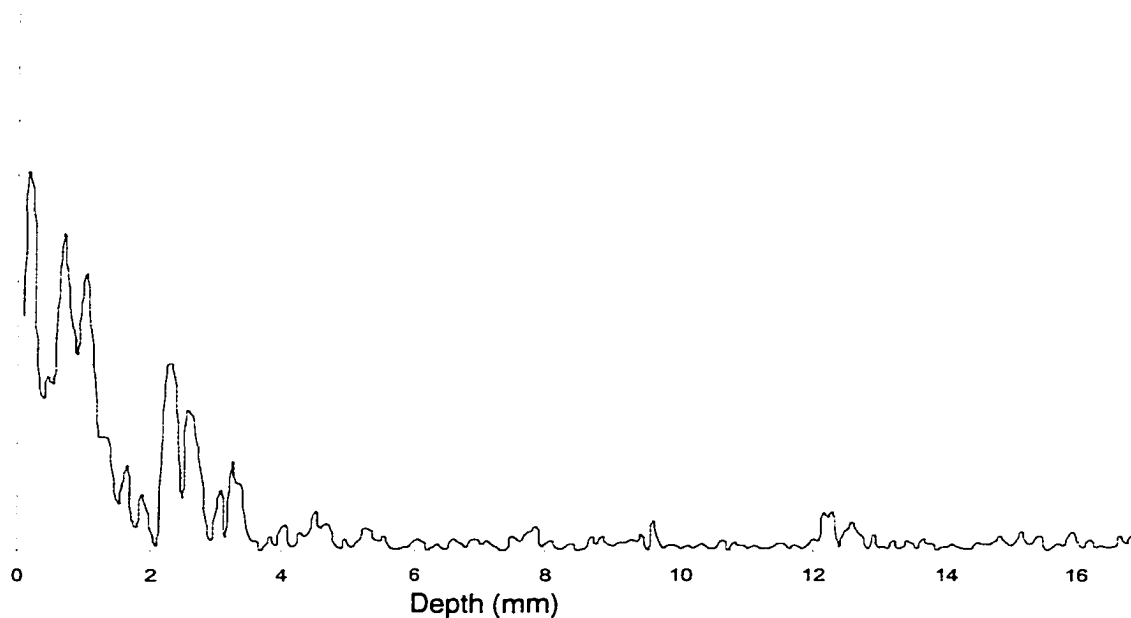


Figure 6.3: The same A-scan trace shown in figure 6.2, after signal processing has been applied.

6.2 Data Processing Techniques

This raw data was processed using the same techniques—peak picking followed by smoothing and averaging—that were described in chapter 4.

This processing resulted in signals like those shown in figure 6.3.

Based on two observations made during these examinations, the signals appeared to be the result of returns off the tooth surface. First of all, one of the patients (Patient 4) had very smooth teeth, due to a loss of enamel. As a result, the ultrasonographic return signals were very weak. Second, whenever a particularly strong signal was encountered, and the hygienist was asked why, she would say that the patient had “a lot of tooth

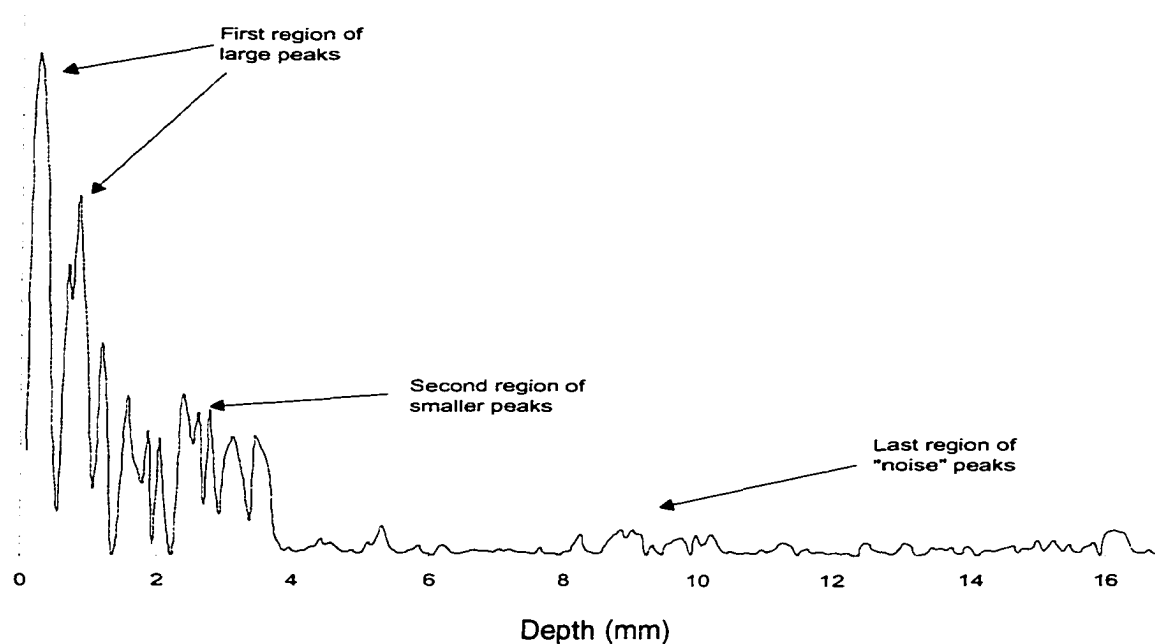


Figure 6.4: Transitions in signal strength in an example trace. The larger peaks are likely due to echoes from exposed tooth surfaces, while the smaller peaks are the result of echoes from tooth surfaces covered with soft tissue.

anatomy,” which means that the tooth had a lot of surface irregularities that produced ultrasonic returns.

After all the raw data was processed, it was examined to find any trends in the returns. After a general examination, no attempt was made to match individual peaks to a particular pocket feature, since the peaks were too numerous to make such a match. Instead, it appeared that the heights of the peaks often underwent two transitions in amplitude: first from very large to medium height, and then another transition from medium to very small. In many cases, these transitions are quite abrupt, while in others they are gradual, but in all cases the decrease in peak height was too great

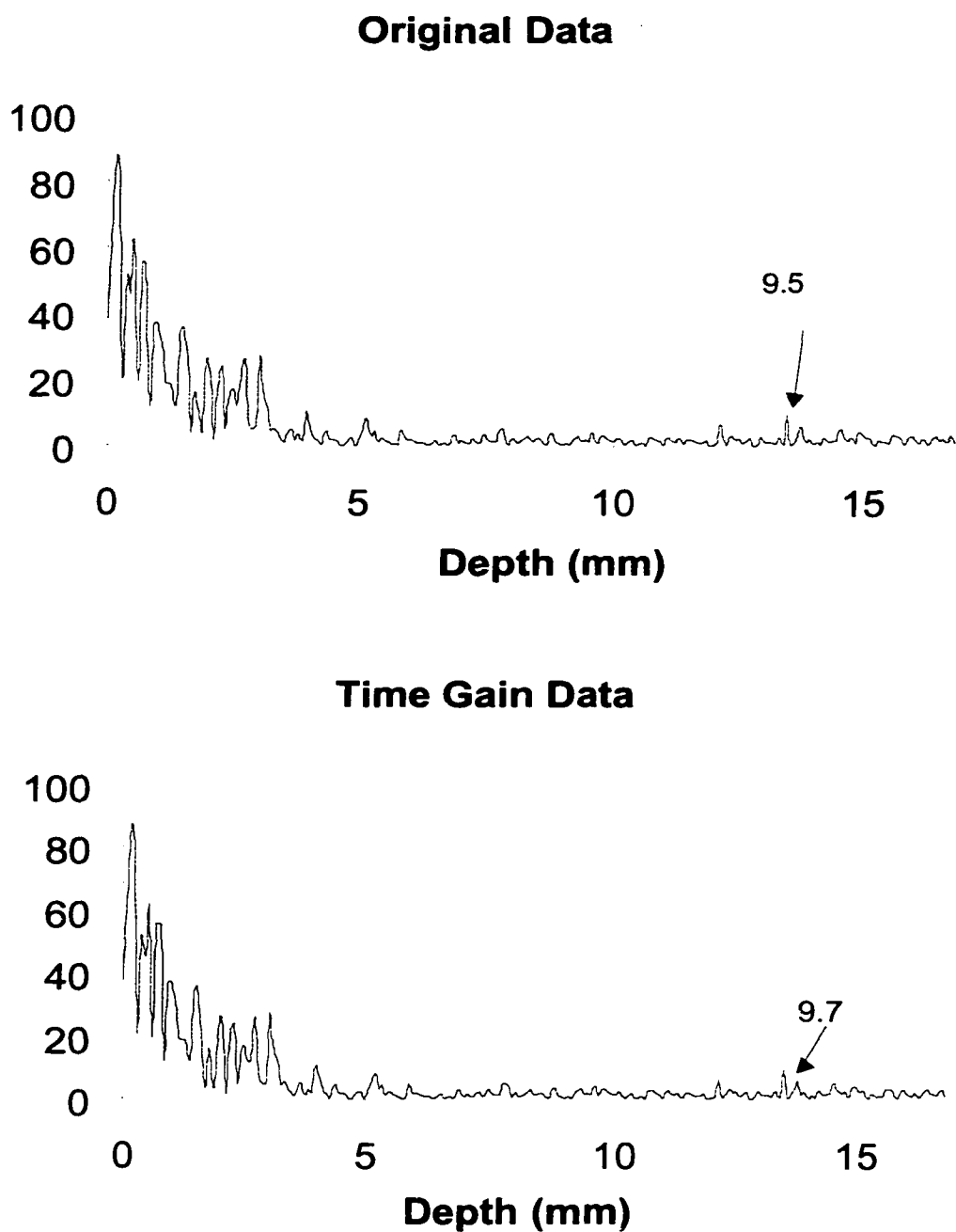


Figure 6.5: Original waveform (top) compared to a waveform with time gain amplification applied (bottom). The amplification factor was determined using a reference signal in water. As can be seen from these graphs, the attenuation of the reference signal in water is negligible. Therefore the attenuation of the signal early on is likely due to other factors.

to be accounted for by attenuation alone. An example trace highlighting these transitions is shown in figure 6.4, while figure 6.5 compares a signal with time gain amplification (to compensate for signal attenuation in water) with a raw signal. (The time gain was computed by comparing reflections off a metal plate at 10 mm and 30 mm from the transducer, and multiplying data points by an exponential function designed to make the two reflections equal in size.)

One possible explanation for these transitions is based on the fact that the region of the periodontium immediately adjacent to the tooth consists of three sections: the sulcus, the junctional epithelium, and the connective tissue, as shown in figure 6.6. In a healthy tooth, the sulcus is about 0.5 mm deep, but may be a few millimeters deep for patients with mild gingivitis, to over 4 mm deep for patients with periodontitis. In the sulcus, there is no tissue immediately adjacent to the tooth, so the return signals are not attenuated. Therefore, the first large peaks may correspond to this region of the periodontal pocket.

From the sulcus, the wave enters the junctional epithelium, a thin layer of skin-like tissue that is attached to the tooth surface. The junctional epithelium is about 0.15 mm wide subjacent to the sulcus bottom, and only a few cell layers thick at the bottom. In a healthy patient, the junctional epithelium is about 2 mm deep. In early gingivitis, some of the junctional

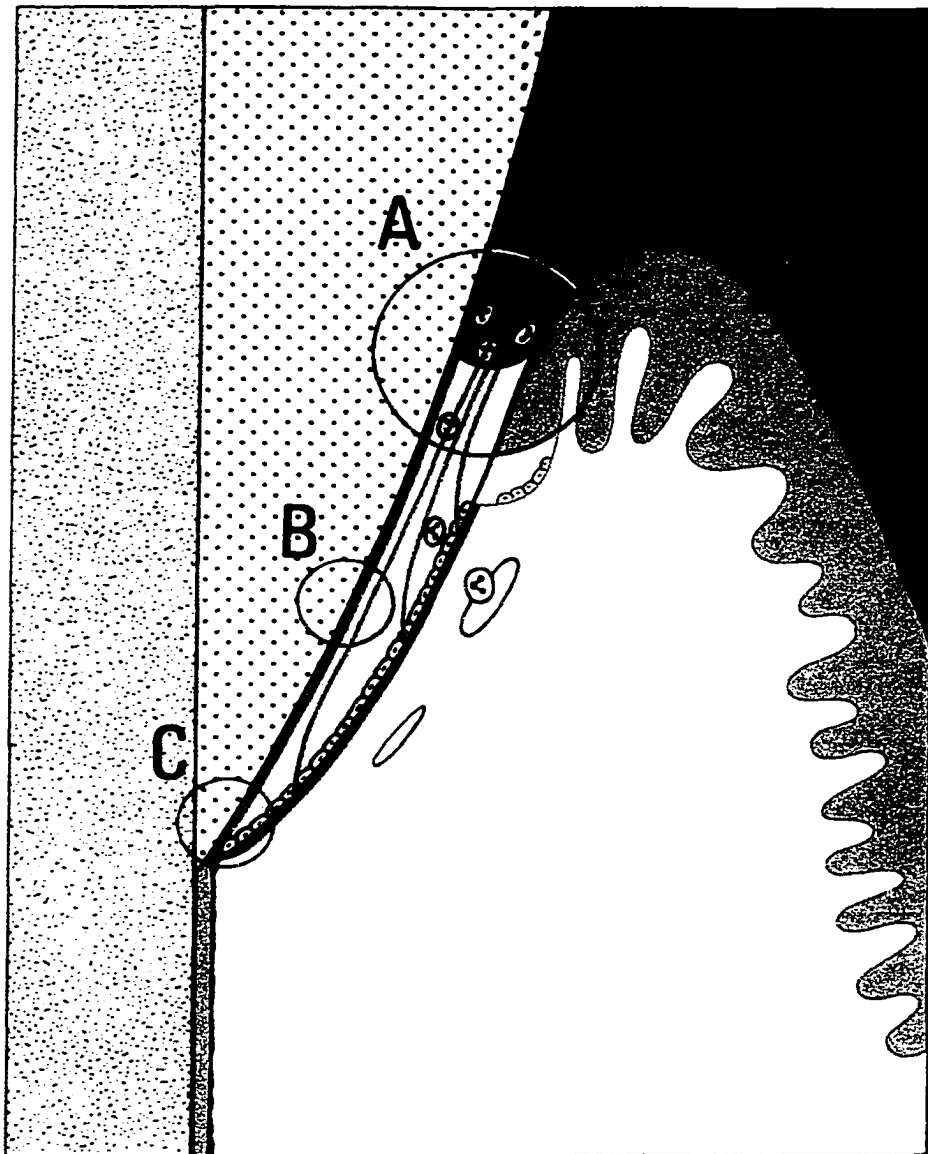


Figure 6.6: Structure of the junctional epithelium. The area in pink is the junctional epithelium, while the arrows and cell-like structures at the edges shows that the junctional epithelium continually replaces lost tissue [8].

epithelium is lost, leading to a deeper sulcus. As disease progresses to later stage gingivitis and then to periodontitis, the connective tissue and even alveolar bone will be lost to disease. However, since epithelial layers are continually replaced every 4-6 days, a small region of junctional epithelium will be present subjacent to the sulcus in all patients. The medium-sized peaks may correspond to reflections in this region, because junctional epithelium attached to the tooth surface attenuates reflections off the tooth [8].

In a healthy patient, the junctional epithelium gives way to connective tissue at the cemento-enamel junction (CEJ). The first layer of connective tissue is the gingival fiber bundles, in which collagen fiber bundles are embedded in the gingiva and spread out in various directions to give the gingiva its stiffness. The gingival fiber bundles increase in density until they reach their highest density just above the alveolar bone. At the alveolar bone, the connective tissue is called the periodontal ligament, which attaches the root to the alveolar bone.

Connective tissue is attached to the tooth surface, which means it is unlikely that an ultrasound wave will reflect off the tooth surface in this region. Thus, the very weak signals toward the tail end of the signal—most of which are indistinguishable from noise—may correspond to the third region of connective tissue.

Using this model as a guide, five people experienced in ultrasound signal analysis were asked to examine the processed data and identify the two transition points of the signal: the bottom of the sulcus, which corresponds to the position of last large peak, and the bottom of the junctional epithelium, which corresponds to the position of the last medium peak.

Several examiners were used to determine how consistently different people could identify features from these signals, and if experienced people would be more effective at picking out these features than an automated feature recognition algorithm. Before running this comparison, however, three different approaches to automated feature recognition were investigated. In each case, the algorithm was designed for the limited goal of identifying the second transition from medium-sized peaks to very small peaks, since this transition is more likely to correspond to a fixed anatomical point.

The first algorithm employed a simple thresholding test in which the very small peaks were considered noise. Thus, the threshold was set by the average noise value. Assuming that on average there are many more "noise" points than "signal" points in the trace, the noise value can be determined by taking the average value of the entire trace, and setting the threshold for the transition between periodontal pocket to connective tissue

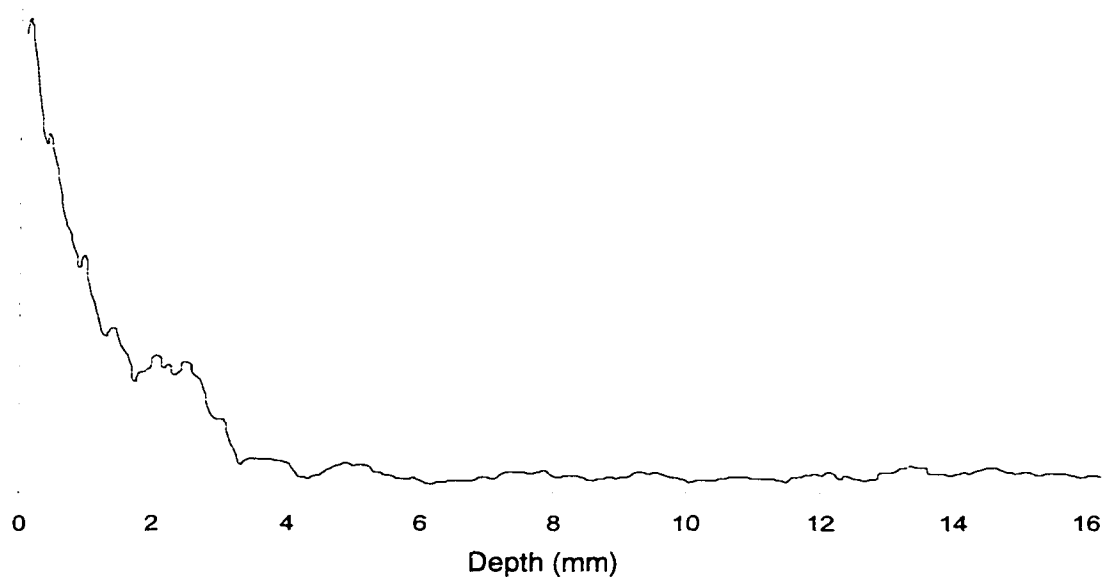


Figure 6.7: Data smoothed by averaging the 10 nearest-neighbor points on the trace, for the purpose of automatic interpretation.

at that level. Alternatively, since most of the signal in these traces is concentrated at the beginning of the trace, the threshold can be set by taking the average of the last 175 points of the trace (of 225 total), so that the threshold is a little lower.

However, this thresholding test must be accompanied by a smoothing algorithm that eliminates the severe peaks and valleys within the signal region, so that an early valley is not mistaken for a transition from signal to noise. Nearest neighbors averaging, in which each point was adjusted to equal the average of a specified number of its nearest neighbors, was used to smooth the the signal trace. Figure 6.7 illustrates a signal

Smoothing Parameter	Threshold	1st Der.	2nd Der.
1	1.65	0	0.19
10	3.17	0	0.13
20	3.18	1.66	0.16
30	3.05	0	0.17
40	2.98	3.56	0.13
50	2.82	3.63	0.14
60	2.79	3.56	0.15
70	2.93	3.53	0.14
80	2.79	3.51	0.15
90	2.95	5.29	0.14
100	2.77	2.02	0.14

Table 6.1: Feature depths for three different algorithms.

processed using this combination of smoothing and thresholding.

An alternative approach involves smoothing the signal and then taking the first derivative of the signal. Because the smoothed signal has a global minimum near the transition region, taking the first derivative may be used to find that minimum. Similarly, this transition could be found by taking the second derivative of the smoothed signal and finding the point where the second derivative changes from negative to positive. Figure 6.8 shows examples of traces processed using the first and second derivative.

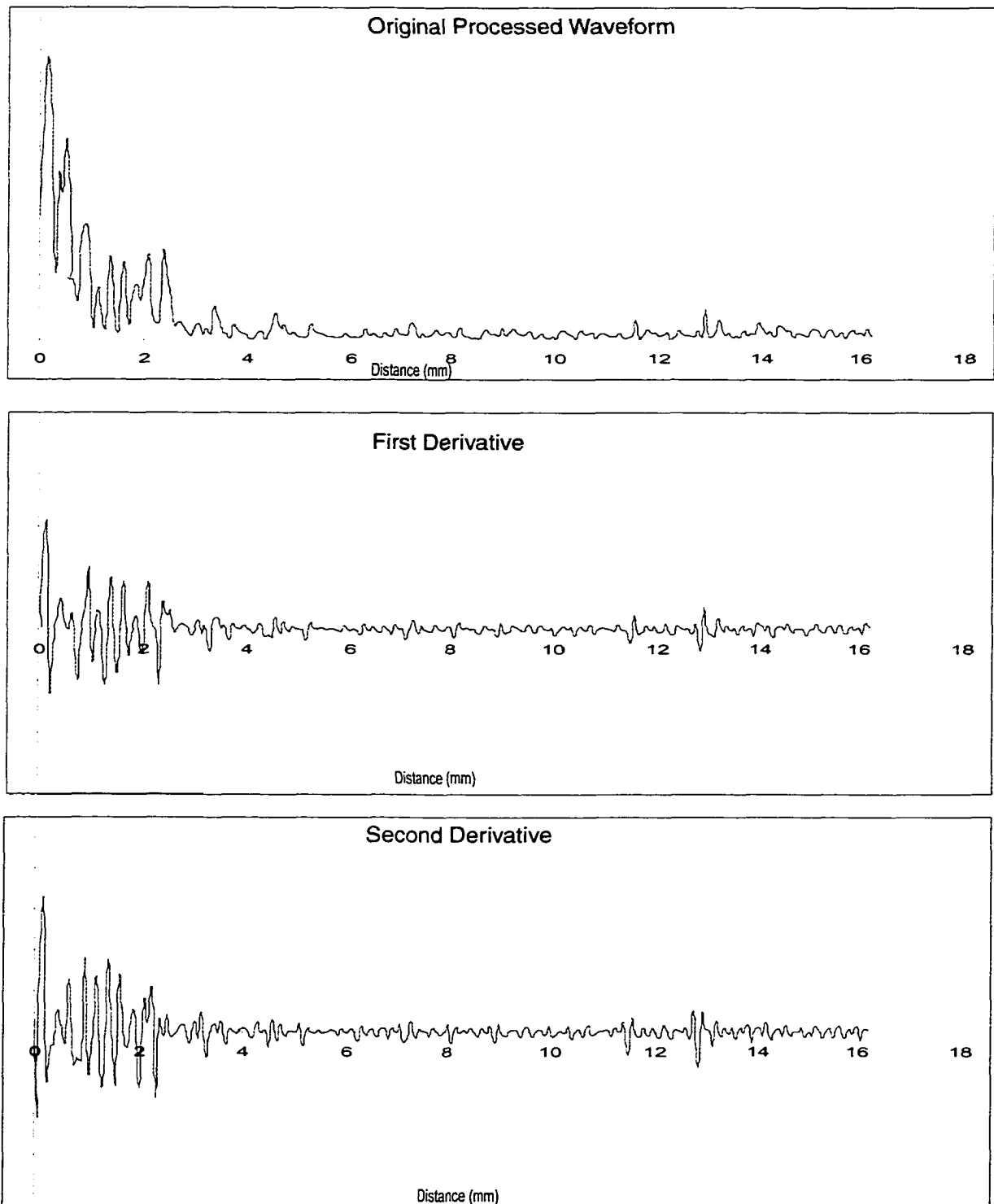


Figure 6.8: Transition detection using derivatives.

Table 6.1 shows the feature depths obtained from applying these three algorithms at various smoothing parameters for patient 3's 10th tooth at the mid-buccal position. (The most common depth obtained by visual inspection was 3.2mm)

From this test, it appears that the thresholding algorithm is the most promising candidate for comparison to visual inspection. The derivatives did not work as well because they use difference equations that amplify small variations in the signal. This amplification negates the effect of the smoothing algorithm, so that valleys within the signal region can be mistaken for the transition from signal to noise.

As a result, the thresholding test was applied to all the clinical trials data using three different smoothing parameters (averaging the 10, 30 and 50 nearest neighbors) and two different thresholds (finding the noise value from the average of the all the points, and finding the noise value by averaging the last 175 of the 225 points in the trace).

6.3 Statistical Analysis of the Probing Depth Measurements

Signal analysis of the ultrasonographic data yielded 16 values for each probing site: two features (the bottom of the sulcus and the bottom of the junctional epithelium) as identified by 5 examiners (for a total of 10 values), plus six values for the bottom of the junctional epithelium as identified by

the automated feature recognition algorithm set at different parameters.

These data were statistically compared to the manual probing depths, the controlled force probing depths, and the gingival index ratings to answer two questions:

1. How well did the ultrasonographic data correspond to the other probing techniques, or to other measures of gingival health?
2. Which type of probing measurement was the most repeatable?

To compare the ultrasonographic data to the manual probing data, the measurements were first presented in the graphical form proposed by Altman and Bland [91], which was developed in response to criticisms of the most common practices used in comparison studies (correlation, paired t , and regression). In this graphical form, the difference between two corresponding measurements is plotted against their mean value. This plotting scheme amplifies small differences in the measurements, and allows one to see trends in how the differences change as the size of the measurements increase.

Four plots using Altman and Bland's scheme are shown in figure 6.9, in which the manual probing data is plotted against one observer's values for two transition regions (the bottom of the sulcus and the bottom junctional epithelium), one automated determination of the second transition region (set with a smoothing parameter of 10 nearest neighbor

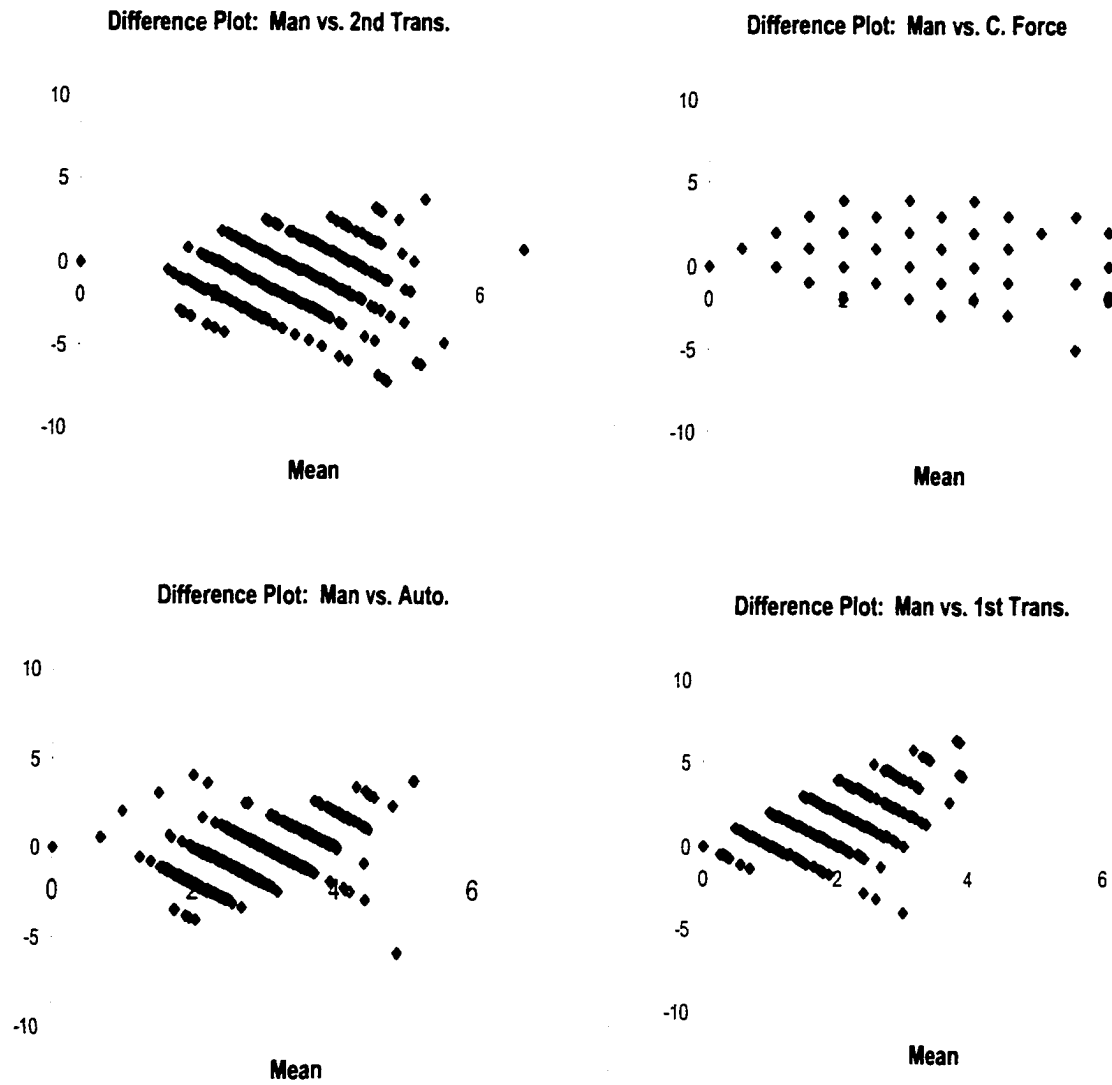


Figure 6.9: Comparison of probing measurements using a difference plot.

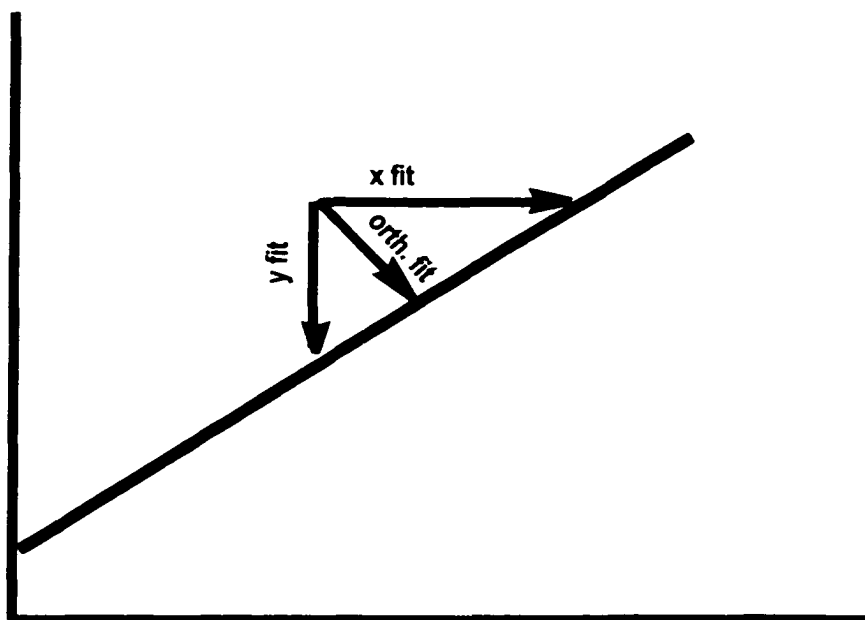


Figure 6.10: In orthogonal regression, a line of best fit is found by minimizing the distance perpendicular to each point, rather than the x- or y-direction distance.

averaging and the higher threshold value), and the controlled-force probe measurements. In these plots, two measurement methods with 1:1 correspondence would have a cluster of points close to the line $y=0$. Of the plots shown, the controlled force probe and the automated algorithm come the closest to fulfilling this goal, although in both cases there many points with significant differences (greater than 3mm). The two plots that use data from the observer do not match up nearly as well.

A more rigorous comparison technique, described by Tan and Iglewicz [92], is provided by orthogonal regression. Orthogonal regression finds the line of best fit through an x-y scatterplot of the comparison data.

However, unlike traditional linear regression, the y-variable is not treated as a dependent variable, with the line of best fit drawn to minimize the error in the y-direction. Instead, orthogonal regression assumes that there is error in both variables, and finds the line of best fit by minimizing the error in a direction orthogonal to the points in the scatterplot, as shown in figure 6.10. (Note, however, that the scaling of the perpendicular is reserved as a statistical issue, which depends on the ratio of variance between the two data sets, rather than a purely geometric issue.) [93]

Figures 6.11 to 6.13 show the results of the orthogonal fit to the scatterplot data for each measurement technique. The plots show three lines of fit: first, a standard linear fit; second, an orthogonal fit that is based on a ratio of the total variance in each data set (variance due to random error, plus subject-to-subject variance); and third, a fit assuming equal variances.

In these plots, the controlled force probe measurements, plus some of techniques used to find the second transition region, produced orthogonal fits that were close to one. The measurements of the first transition region (the bottom of the sulcus), however, did not correspond well to the manual probing depths, and tended to have a negative relationship (the sulcus depth got more shallow as the manual probing depths increased).

Of the measurements that produced an orthogonal fit line with a slope close to one, only the controlled-force probe's line had a y-intercept

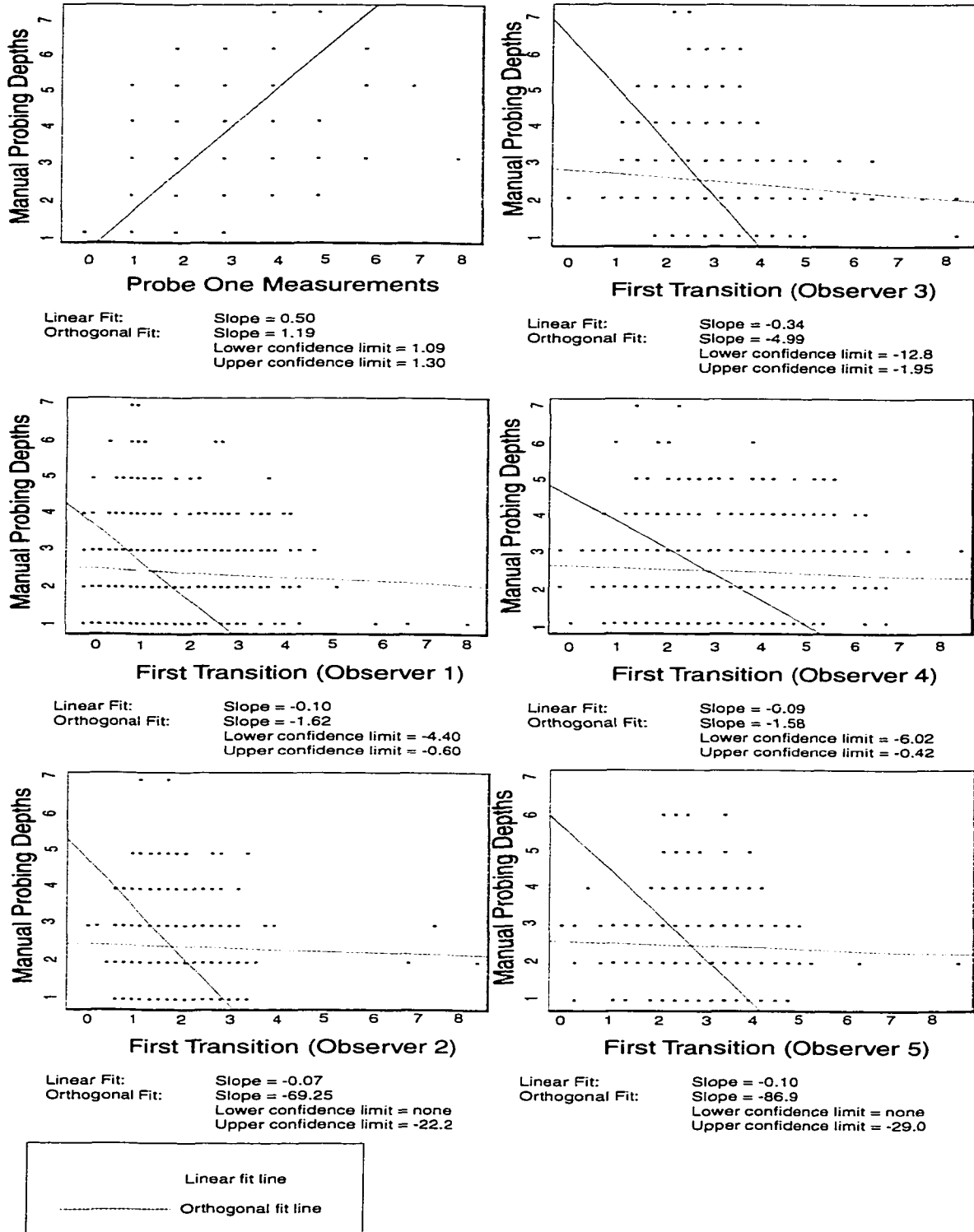


Figure 6.11: Orthogonal fit results for the Probe One and 1st transition measurements.

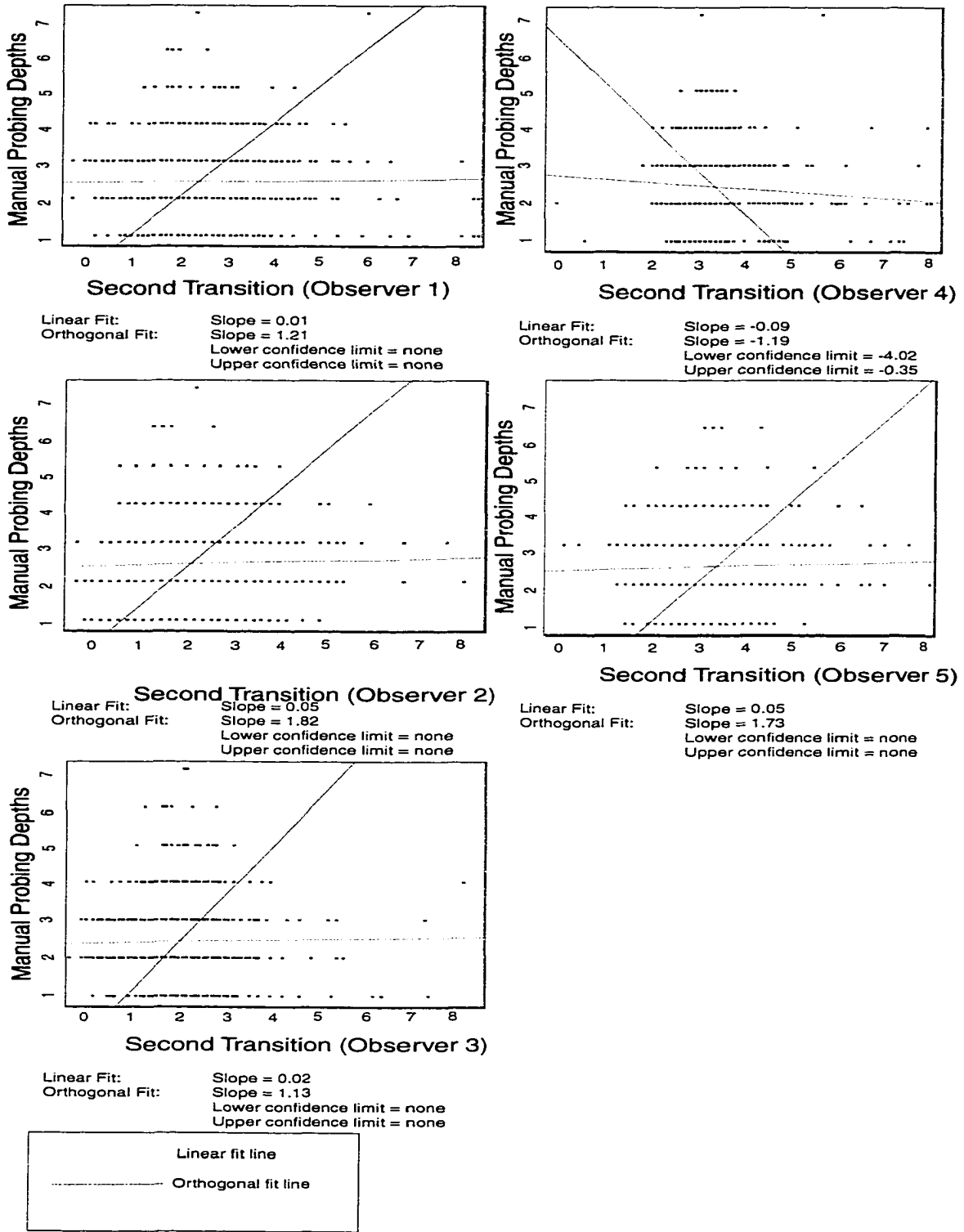


Figure 6.12: Orthogonal fit results for the 2nd transition measurements.

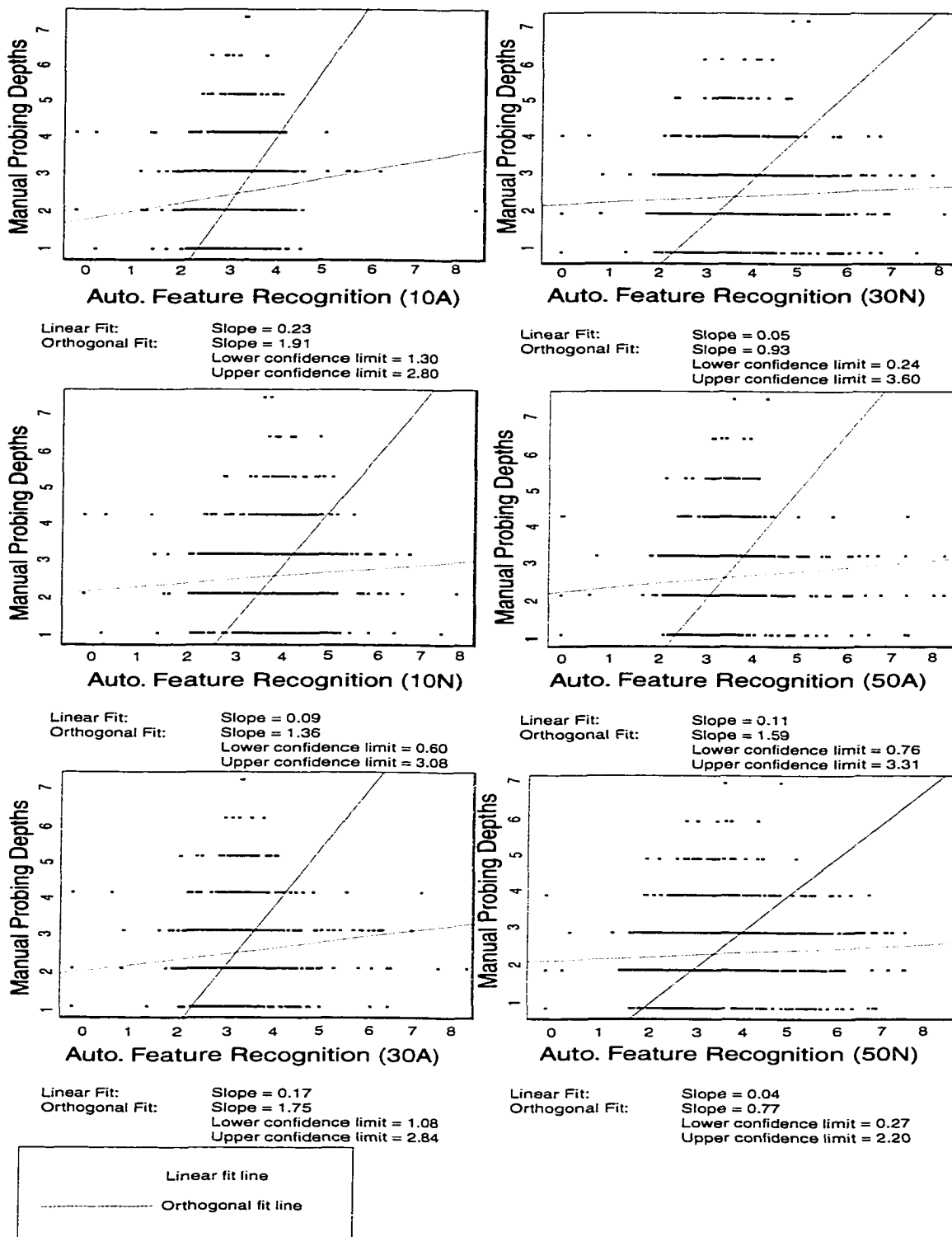


Figure 6.13: Orthogonal fit results for the automatic feature recognition measurements.

less than 1 mm. The techniques used to estimate the depth of the junctional epithelium produced y-intercepts ranging from -1 to -3, which means that the manual probing data tended to be a few millimeters lower than these estimates.

From this analysis, it appears that the measures of the second transition region offer some promise as a clinical marker of pocket depths. However, because the human examiners could not consistently identify this transition region (some of the orthogonal fits came close to a slope of 1, but others did not), an automated feature recognition algorithm appears better suited for extracting this data.

However, this orthogonal fit was not conclusive, so a second analysis was attempted in which the manual probing data were treated as an ordinal variable rather than a continuous variable. This treatment is possible because the manual probing data is obtained on a gross scale (1 mm increments from over a range from 1 to 7mm) as compared to the ultrasonographic data (0.1 mm increments over the same range).

By treating the manual probing data as an ordinal variable, comparisons across a group—all ultrasonographic measurements taken at sites with a particular manual probing values [1,2,3,etc.]—are possible. Using this technique, a one-way analysis of variance was performed that grouped the manual probing values with the 16 ultrasonographic measurements and

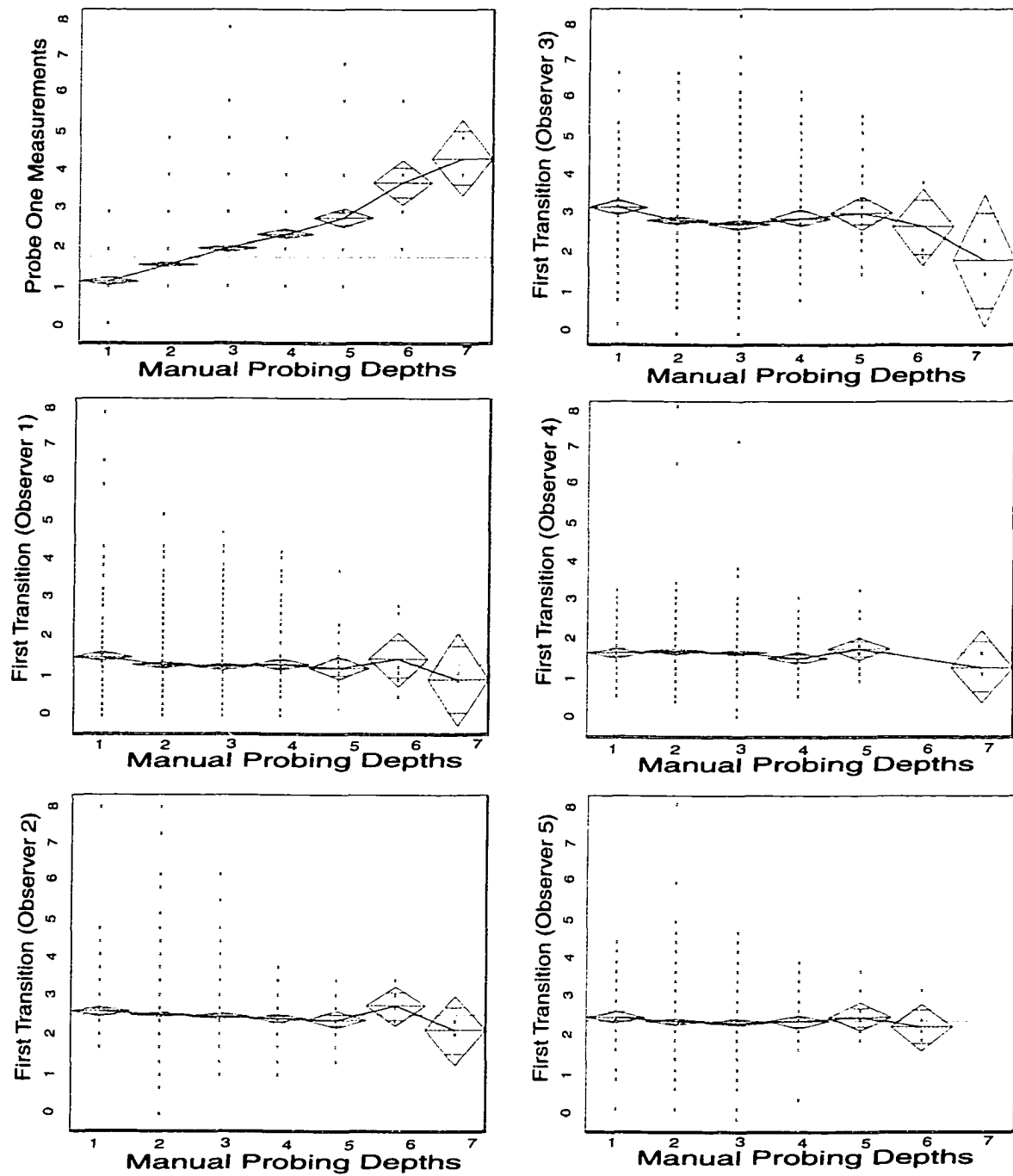


Figure 6.14: Results of the one-way ANOVA for the Probe One and 1st transition measurements.

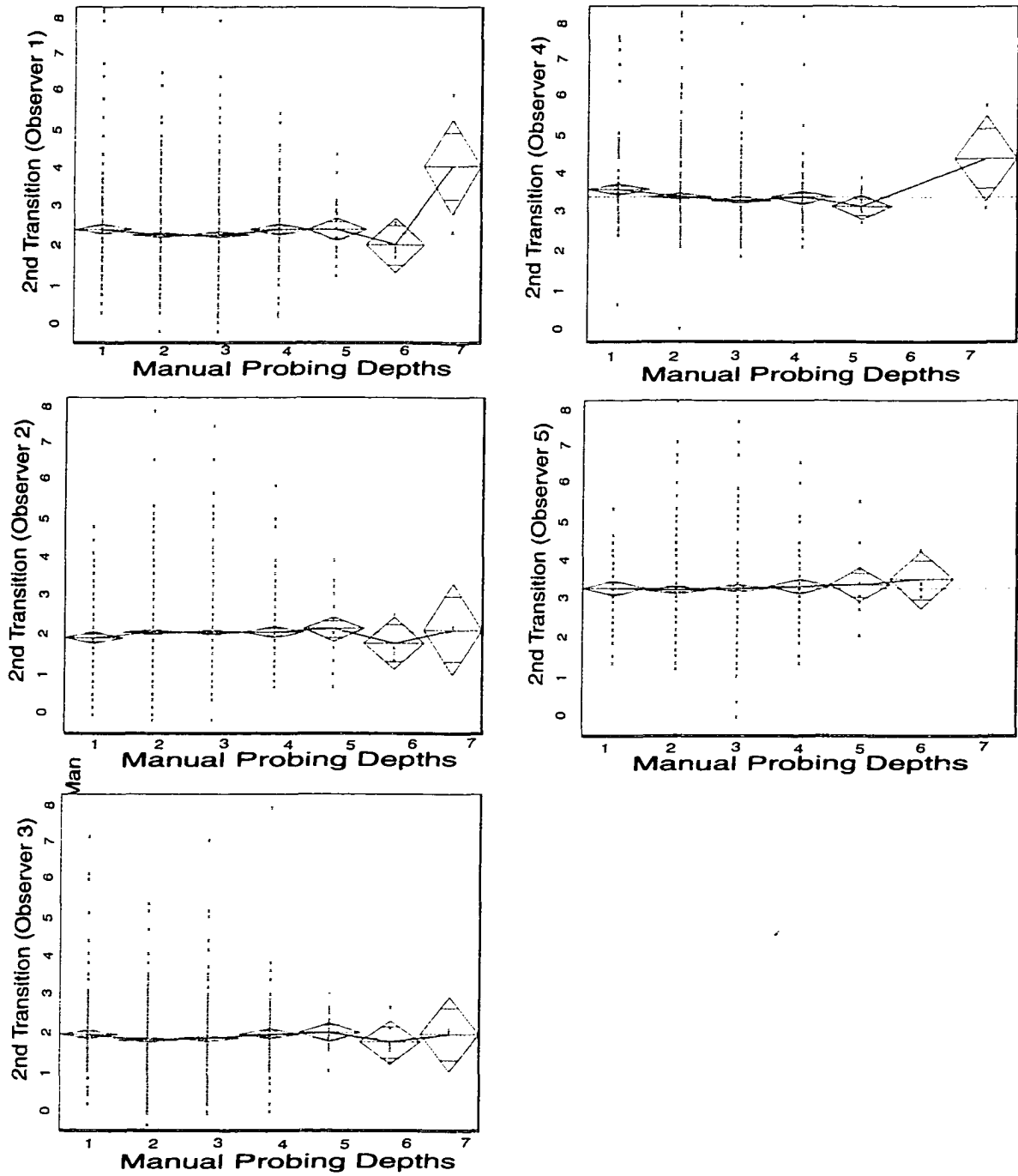


Figure 6.15: Results of the one-way ANOVA for 2nd transition measurements.

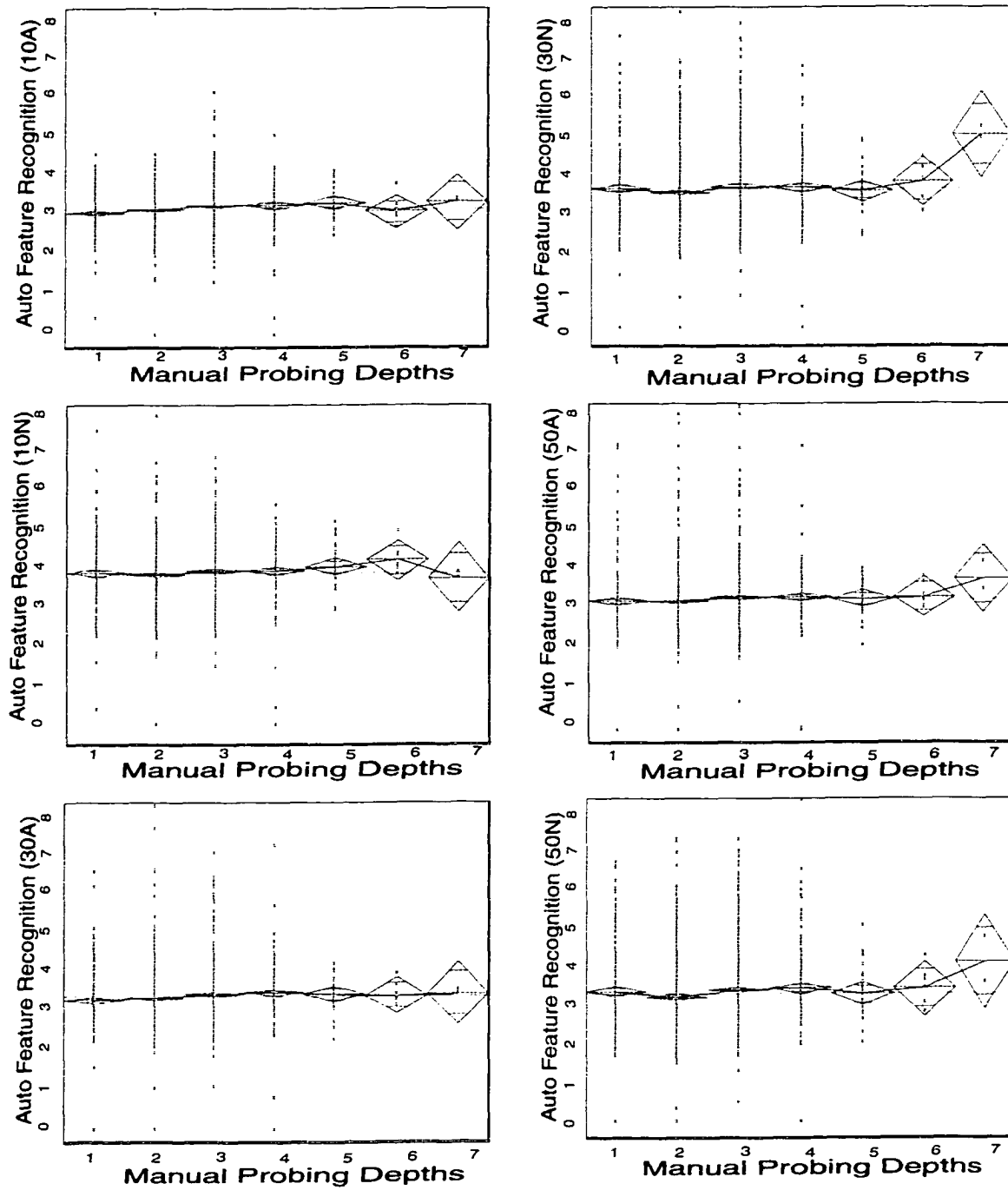


Figure 6.16: Results of the one-way ANOVA for the automatic feature recognition measurements.

the Probe One measurements. The results of this analysis are shown in figures 6.14-6.16. As can be seen from these results, the Probe One data showed some increase in the group means as the manual probing data values increased. For the 16 sets of ultrasonographic data, however, the group means showed no significant variation from the grand mean.

Due to the significant difference between the probing depth and the true pocket depth, manual and controlled force probing measurements are not likely to correspond to anatomical features, as the ultrasonographic probe should do. As can be seen in figure 1.2, manual probing measurements will usually fall somewhere between the bottom of the sulcus and the bottom of the junctional epithelium. For more severe cases of periodontitis, the anatomy becomes more complicated and manual probing is even less likely to match a specific anatomical feature.

Even though the ultrasonographic data cannot be directly compared to manual probing measurements, ultrasonographic probe should correspond to some measure of gingival health. The only such measure obtained during these clinical trials came from the gingival index (GI). As a result, a one-way analysis of variance was performed on the gingival index data against the manual probing data, the controlled-force data, and the 16 different ultrasonic data values. The results of this analysis are shown in figures 6.17-6.19.

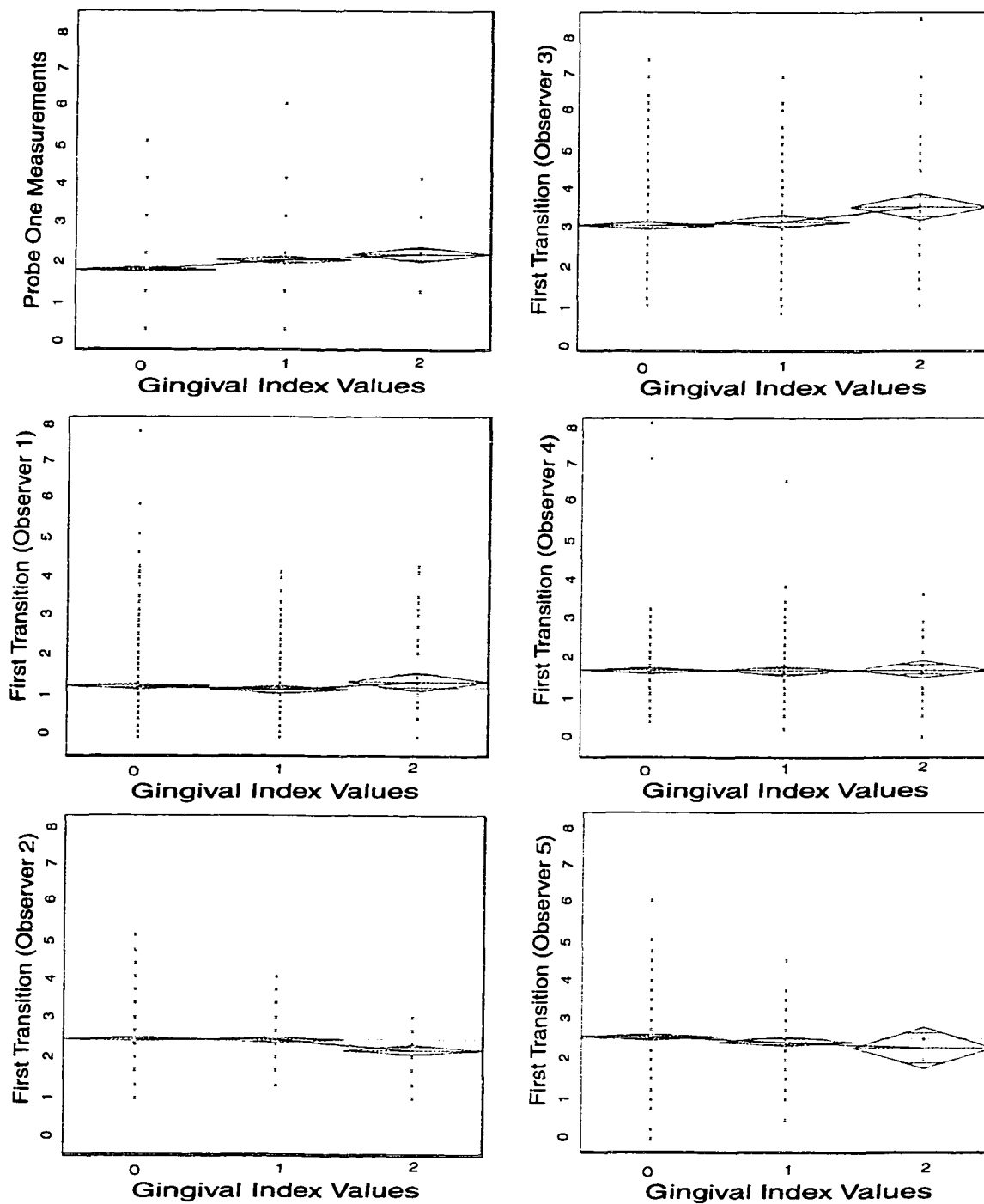


Figure 6.17: Results for one-way ANOVA compared to GI (Part 1).

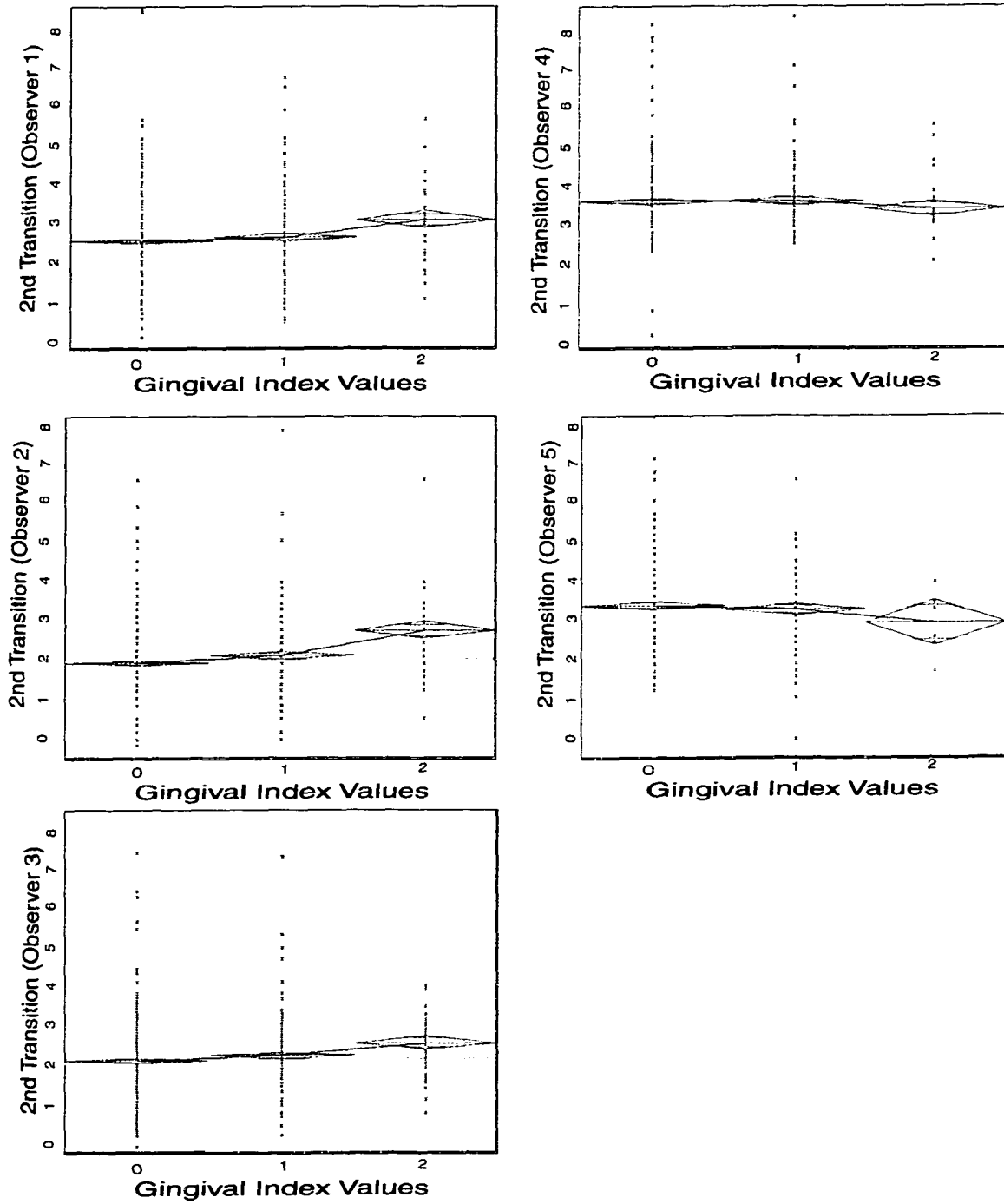


Figure 6.18: Results for one-way ANOVA compared to GI (Part 2).

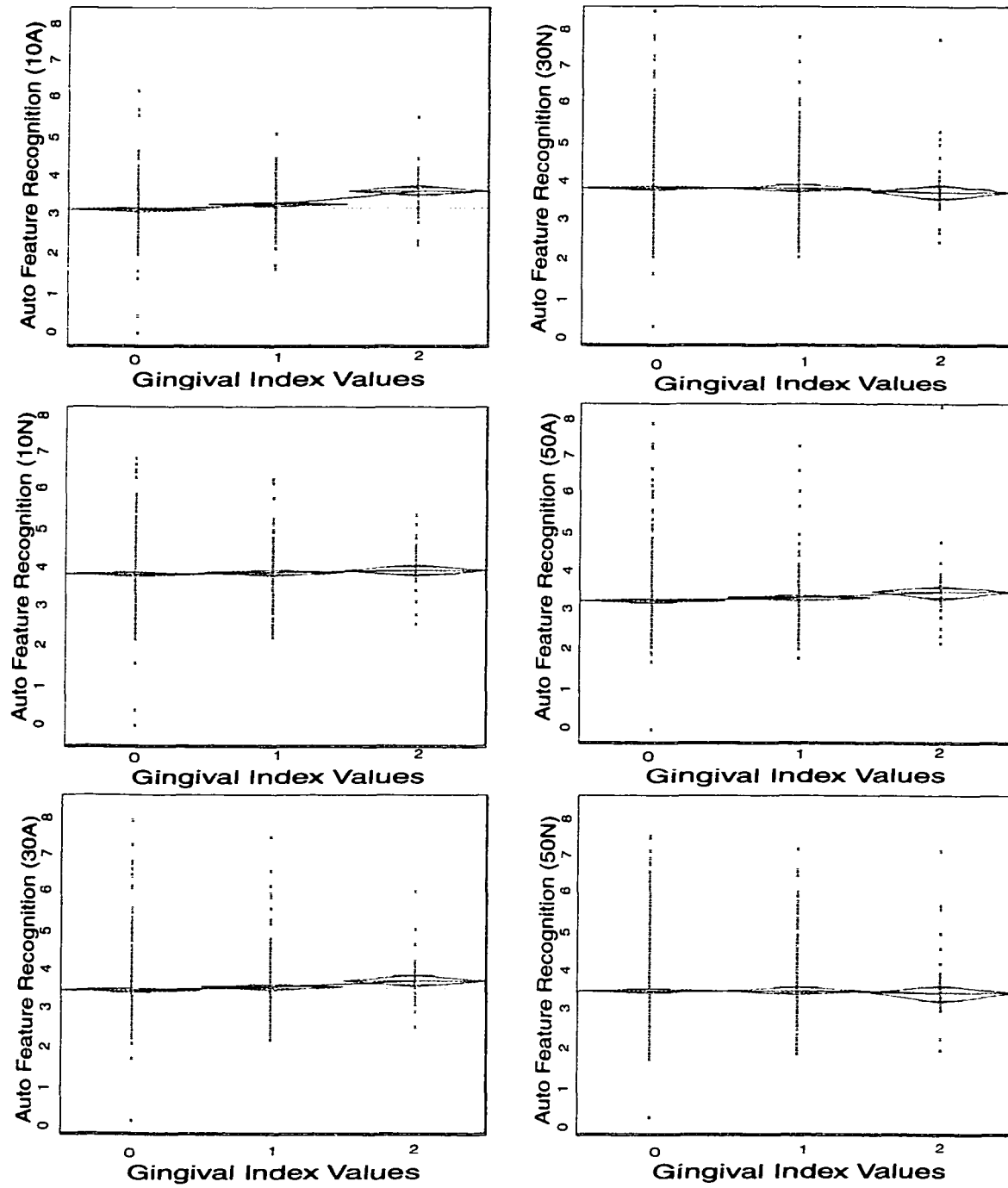


Figure 6.19: Results for one-way ANOVA compared to GI (Part 3).

Because the patients examined during this trial generally exhibited good gingival health, few of the sites had GI rankings of 2, and none had GI rankings of 3. Despite this limited sample range, there is some indication that the second transition region (the bottom of the junctional epithelium) gets deeper as the GI scale gets higher, and that it does so just as well as the manual probing data (and much better than the controlled-force probing data) . However, this trend was only true for 3 of the 5 observers, plus for the automated feature algorithms at 3 of the 6 parameter settings. Also, there was no indication that the first transition region, as identified by all 5 observers, got deeper as the GI ranking got higher.

In addition to the comparison of the measurement techniques, the clinical trials data were analyzed to assess the repeatability of the measurement techniques. To do so, each of the data sets were modeled to separate out variation due to error (the variation that would occur if the same measurement were repeated again under the exact same conditions) from variation due to other factors. These factors included variation across patients, tooth numbers, probing locations and observers (for the ultrasonographic data only). However, for the purposes of simplicity, only some of the ultrasonographic data was analyzed with this model. Since the earlier results indicated that the first transition region did not correspond to any measure of gingival health, those points were not considered in this

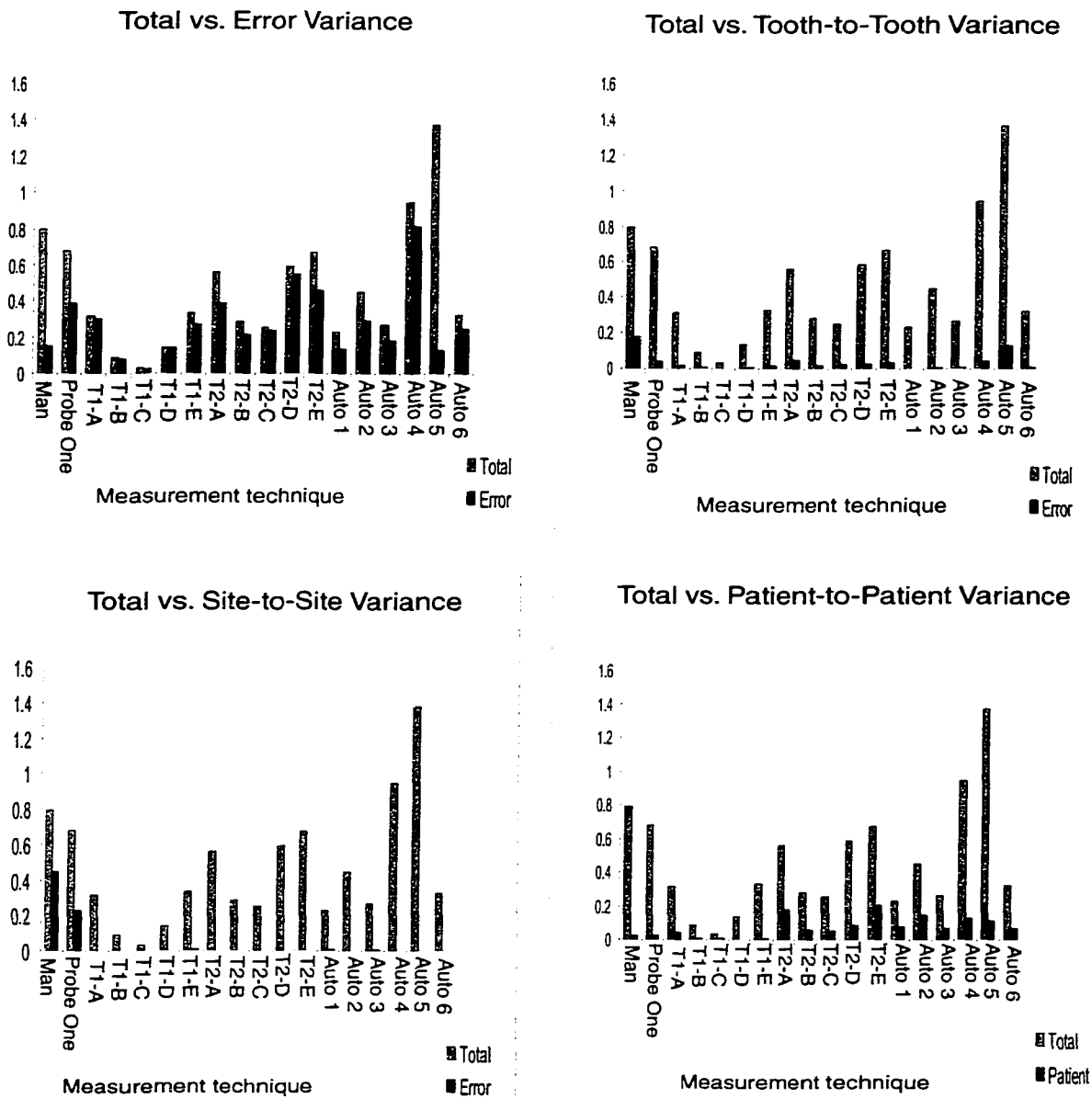


Figure 6.20: Repeated measures analysis.

model. In addition, the automated feature recognition corresponded best to GI rankings and manual probing depths when the smoothing parameter was set for 10 nearest neighbor averaging and the lower threshold setting, so only results using those parameter settings were used for this analysis.

As can be seen from figure 6.20, the repeatability of manual probing and ultrasonographic probing with automated feature recognition is comparable (as indicated by their similar values for variance due to error). However, manual probing has a much larger total variance, because manual probing has much larger site-to-site and tooth-to-tooth variance components. This either indicates a bias in manual probing (perhaps due to a site- or tooth-specific change in angulation or probing pressure) or a failure to detect important variations in probing depth on the part of ultrasonographic probing. Two observations, however, point to a bias in manual probing. First, ultrasonographic probing has a larger patient-to-patient variance, where one would expect variance due to differences in overall gingival health. Second, controlled-force probing, which is designed to eliminate variations in probing force, also has lower site-to-site and tooth-to-tooth variance than manual probing.

Chapter 7

Elastodynamic Simulation of the Periodontium

7.1 Simulation Development

In Chapter 5, a model of the behavior of the ultrasonic signal within the periodontium was proposed to help interpret the data obtained during the clinical trials. Two key observations made while conducting the clinical trials were used to help formulate this model. First, one patient had very smooth teeth due to a loss of enamel, which led to weak ultrasonographic return signals. Second, probing sites with unusually strong signals had teeth with “a lot of anatomy,” or surface irregularities that produced ultrasonic returns. Thus, the first assumption of the model is the signals analyzed using the probe are composed entirely of echoes off of hard tissue within the periodontium.

Although the signal is composed from echoes off of hard tissues, this

data can be used to infer the depth of the periodontal pocket. Within the pocket, the surface of the tooth is exposed, and ultrasonic signals can echo directly off the tooth surface. However, if the tooth surface is covered with tissue, the echo will be attenuated. Because the junctional epithelium is softer than the connective tissue, it is reasonable to assume that it will attenuate the signal less than the connective tissue. This leads to the three regions of the signal discussed in Chapter 5: First there is the region of very strong returns, in which the ultrasonic wave passes through water (from the probe) to echo off the tooth surface. Second, there is the region of slightly attenuated returns, in which the ultrasonic wave must pass through junctional epithelium layers before echoing off the tooth surface. Finally, there is the region with no detectable returns, in which connective tissue completely scatters the ultrasonic wave and no echoes from the tooth can be detected.

Using this model as guide, an idealized periodontium was developed for use in a computer simulation designed to test this model. This idealized periodontium, shown in figure 7.1, consists of three regions. The first region is the periodontal pocket, which is filled with water from the ultrasonographic probe. The second region is junctional epithelium, and the rest of the periodontium is gingiva. The inner surface is an interface with the tooth, and so for this boundary the rigid body boundary condition

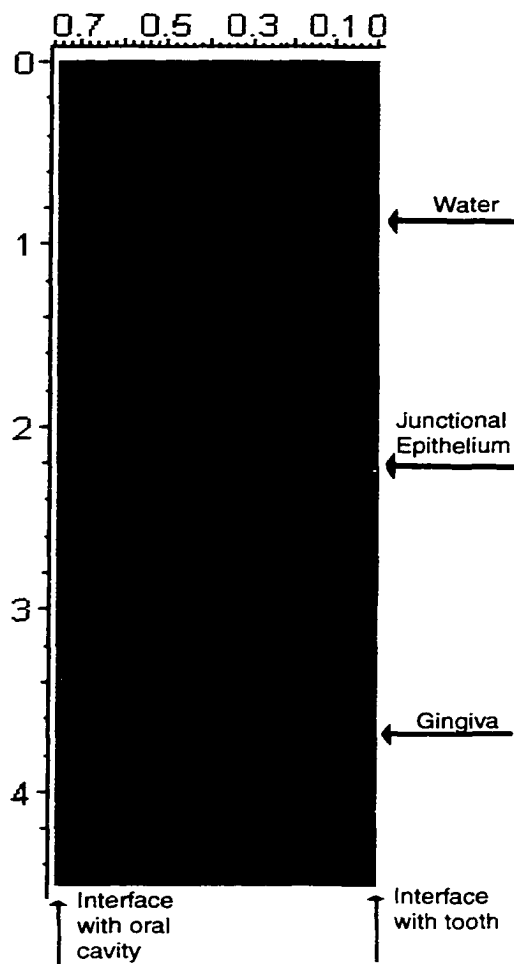


Figure 7.1: Idealized periodontium. The pink region represents the portion of the pocket filled with water from the probe, the blue region represents junctional epithelium, and the red region represents gingiva. The left border is tooth, and is assumed to be a completely rigid structure, while the right border is air and is assumed to be a vacuum interface.

$v_{ij} = 0$ was used. The outer surface is an interface between gingiva and the oral cavity (air), and so for this boundary the vacuum boundary condition $\sigma_{ij} = 0$ was used.

In addition, the ultrasonic parameters of the gingiva and the junctional epithelium needed to be defined. Values for the Lamé parameters λ and μ were not available in the literature, nor were they for the density ρ . However, because the gingiva contains fiber bundles that give it some stiffness (like muscle), while the junctional epithelium is softer and more skin-like, the ultrasonic properties of muscle and skin, respectively, were used for this simulation. For muscle, the values $\lambda = 2.46 \times 10^9$ Pa, $\mu = 0.25 \times 10^6$ Pa, and $\rho = 1.08 \times 10^3 \frac{kg}{m^3}$ were used, and for skin, $\lambda = 2.30 \times 10^9$ Pa, $\mu = 0.19 \times 10^6$ Pa, and $\rho = 1.02 \times 10^3 \frac{kg}{m^3}$ were used [95, 96]. In the simulations that follow, it should be kept in mind that muscle and skin are probably more dense than gingiva and the junctional epithelium, respectively, since gingiva is softer than muscle and junctional epithelium mixes with crevicular fluid to make it more liquid-like than skin.

The simulation was designed using the elastodynamic variation of the CAFIT algorithm discussed in Chapter 3, called the elastodynamic finite integration technique (EFIT) of Fellingner, et al [94]. This algorithm is derived the elastodynamic equations (2.1) and (2.2) using the same finite volume discretization technique outline in Chapter 3.

Following the detailed derivation of Fellingner et al, results in in the following discrete equations:

$$v_i^{(t)} = v_i^{(t-1)} + \dot{v}_i^{(t-\frac{1}{2})} \Delta t, \quad (7.1)$$

and

$$\sigma_{ij}^{(t+\frac{1}{2})} = \sigma_{ij}^{(t-\frac{1}{2})} + \dot{\sigma}_{ij}^t \Delta t. \quad (7.2)$$

In equation (7.1),

$$\dot{v}_i^{(n)} = \frac{1}{\Delta x} \frac{2}{\rho_o^{(n)} + \rho_o^{(n+M_i)}} \times [\sigma_{ii}^{(n+M_i)} - \sigma_{ii}^{(n)} + \sigma_{i,i+1}^{(n)} - \sigma_{i,i+1}^{(n+M_i+1)} + \sigma_{i,i+2}^{(n)} - \sigma_{i,i+2}^{(n-M_2)}], \quad (7.3)$$

where the n superscript denotes a node position on the grid and the M_i superscript denotes the number of nodes away from n in the i direction. In equation 7.2

$$\dot{\sigma}_{ii}^{(n)} = \frac{1}{\Delta x} \{ (\lambda^{*(n)} + 2\mu^{(n)}) [v_i^{(n)} - v_i^{(n-M_1)}] + \lambda^{*(n)} [v_{i+1}^{(n)} - v_{i+1}^{(n+M_i+1)} + v_{i+2}^{(n)} - v_{i+2}^{(n-M_i+2)}] \} \quad (7.4)$$

and

$$\dot{\sigma}_{ij}^{(n)} = \frac{1}{\Delta x} \frac{4}{\mu^{(n)} + \mu^{(n+M_i)} + \mu^{(n+M_j)} + \mu^{(n+M_i+M_j)}} \times [v_i^{n+M_j} - v_i^{(n)} + v_j^{(n+M_i)} - v_j^{(n)}], \quad (7.5)$$

where λ^* and μ are the two independent Lamé constants given by the relationship

$$c^{(n)} = \lambda^{(n)} + 2\mu^{(n)}, \quad (7.6)$$

where $c^{(n)}$ is the speed of sound at node n .

7.2 Simulation Testing

In setting up these equations to simulate ultrasonic wave behavior in the periodontium, one complication comes from the fact that the probe tip has cylindrical symmetry but the periodontium does not. If it were computationally possible to run the simulation for a full three-dimensional space on a workstation, this problem could easily be overcome by converting cylindrical coordinates to Cartesian coordinates. The limiting factor in performing a full 3-D simulation is RAM storage space, since all the data within the spatial grid must be saved after each time step to compute the values at the next time step. For this simulation, 3-D grid has on the order of 10^8 points (for a $1 \times 1 \times 20$ r.u. simulation space and steps sizes of 0.005 r.u.). Each point has 8 values associated with it (three for stress, two for velocity, and three for the ultrasonic material parameters). At double precision storage (16 bits per value), this adds up to 13GBytes of memory that must be stored from one time step to the next. The high-end workstation used for this simulation had 1GByte of RAM, so a 3-D simulation is not possible on this workstation. However, reducing the grid to two dimensions reduces the number of grid point to about 10^5 points, leading to a memory requirement of 13MBytes, well within the capabilities

of the workstation.

In simplifying to two dimensions, the conversion from cylindrical to Cartesian coordinates is not as easy, since the cylindrical system assumes symmetry about the r -axis, while the Cartesian system does not. In the first attempt at simplifying to two dimensions, wave propagation was simulated within the tip in cylindrical coordinates, and the wavefront values were saved as the wave left the tip. These values were then converted to 2-D Cartesian grid, and a simulation was run with the wavefront propagating through the periodontium. Finally, as the wavefront echoes reached the periodontal pocket opening, these values were saved.

However, it was not possible to convert the wavefront in Cartesian coordinates back to cylindrical coordinates without losing some information about the wave, since the 2-D axisymmetric grid has fewer points than the Cartesian grid. (Figure 7.2). This loss of information led to a weak return signal that was difficult to interpret. (Figure 7.3).

Because converting from a axi-symmetric space to a Cartesian space did not produce satisfactory results, another approach was attempted. In this approach, two simple simulations of the probe aimed at a flat metal plate 17 mm from the transducer were performed. First the probe was assumed to be cylindrical (using the CAFIT algorithm described in Chapter 2) and then it was assumed to be rectangular with sloping walls

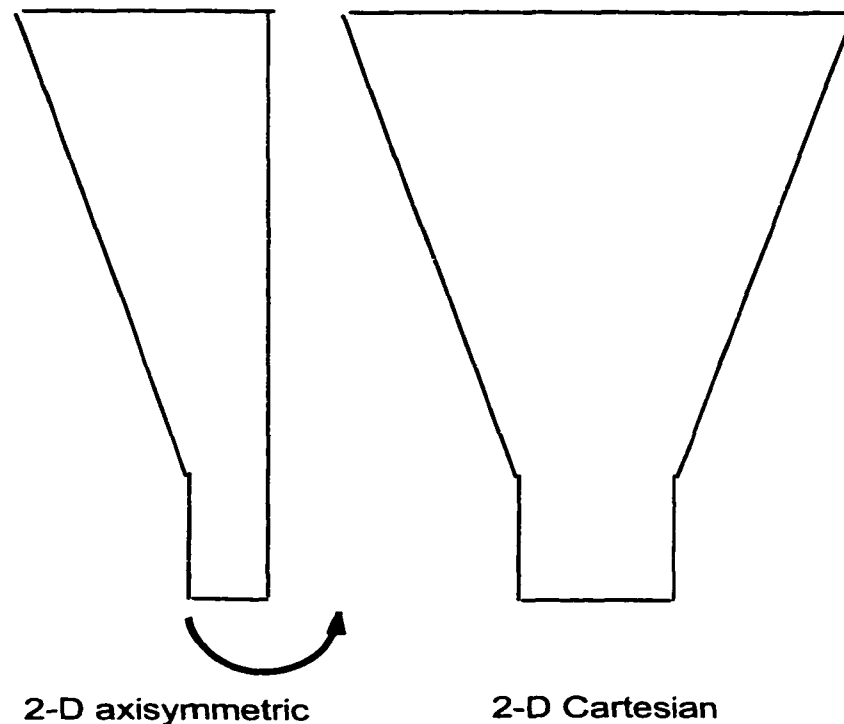


Figure 7.2: The assumption of symmetry about the r -axis cuts the number of grid-points in half for the simulation in the cylindrical coordinate system.

(using a 2-D version of the EFIT algorithm). The results of this comparison are shown in figures 7.4 and 7.5. In both cases, Δx was 0.005 reduced units (1 r.u. = 1mm) and Δt was 0.0025 r.u.

The results of this comparison indicate that the 2-D Cartesian simulation exaggerates scattering within the tip. Echoes originating outside the tip were much smaller than corresponding echoes from the simulation using cylindrical coordinates, while echoes originating within the tip were larger. The cylindrical geometry produces less scattering in the tip because the geometry tends to concentrate wave energy toward the center of the tip space (due to the $\frac{1}{r}$ term in equation (3.4)), while in the Cartesian

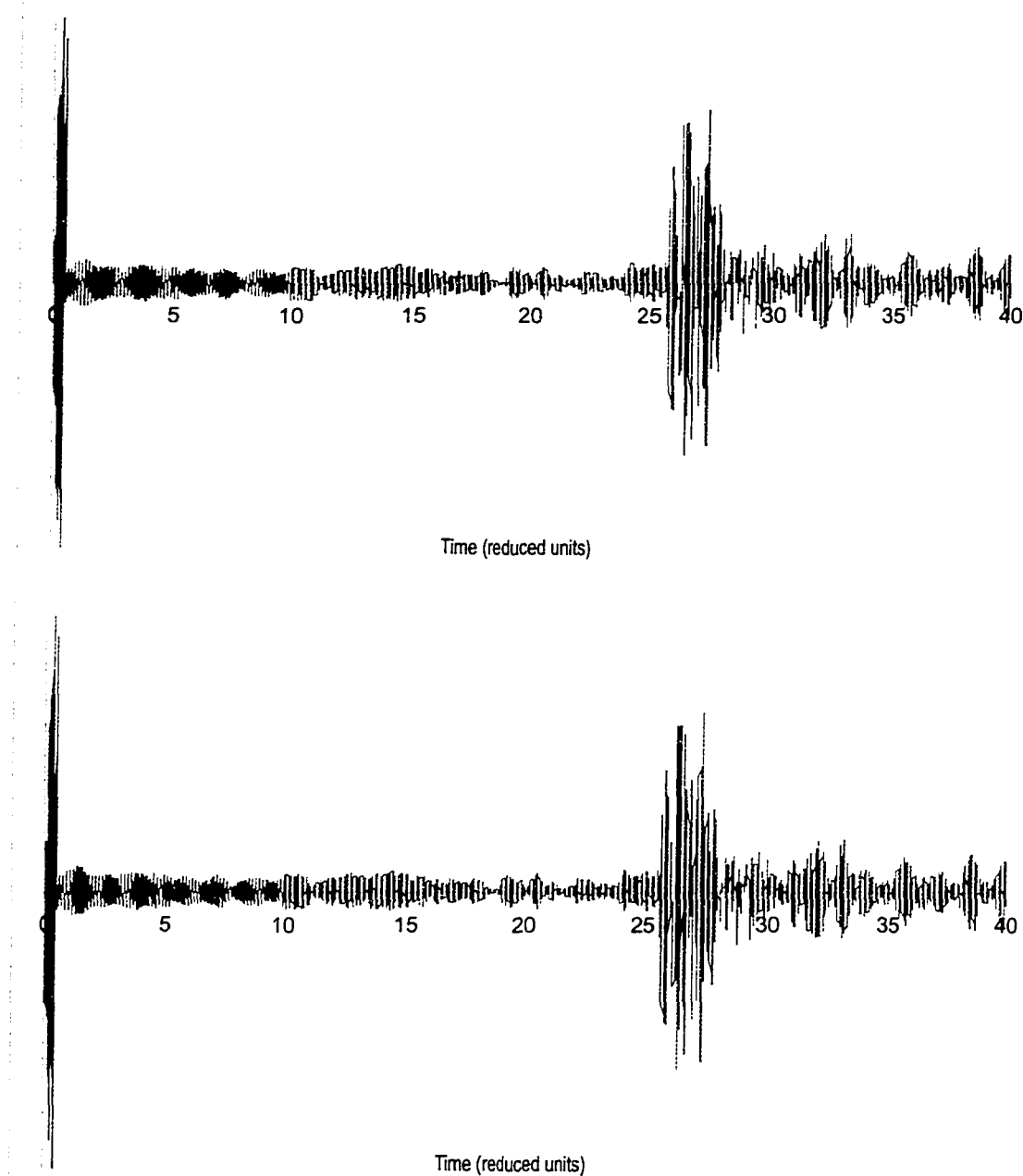


Figure 7.3: The cluttered return signal shown above occurred as a result of converting the wavefront in a Cartesian grid to a 2-D axi-symmetric cylindrical grid. The conversion overemphasized scattering at the tip, to the point the echoes outside the tip are impossible to identify. The top return was for a simulation with a smooth tooth, while the bottom was for a simulation with a large surface irregularity placed on the tooth 1 r.u. from the tip outlet.

geometry the wavefront is evenly distributed along the y-coordinate plane.

Despite the differences in signal strength between the simulations run in a 2-D Cartesian space and a 2-D axisymmetric cylindrical space, the phase of the returning echoes is the same for both geometries. Thus, information about the time delay of the return signal can still be used in simulations performed in a Cartesian space even though the actual probe tip has a cylindrical geometry.

During this comparison, the EFIT-based simulation took several days to run, while the CAFIT-based simulation took less than a day. The EFIT simulation took much longer due to the added complexity of storing and recalling the material properties λ , μ , and ρ at each step of the simulation. As a result, another simplification to the simulation was considered, in which the probe tip was eliminated by placing an idealized transducer at the opening to the periodontal pocket. This simplification would make testing a wide range of model parameters more practical.

Before making this simplification, though, another test was run to see how well the results from this simulation compared to the results from the simulation with the probe tip placed at the opening to the periodontal pocket. Figure 7.6 shows a comparison of the results for the shortened simulation using the idealized transducer, and for the longer simulation that included the probe. Like the earlier comparison of the cylindrical

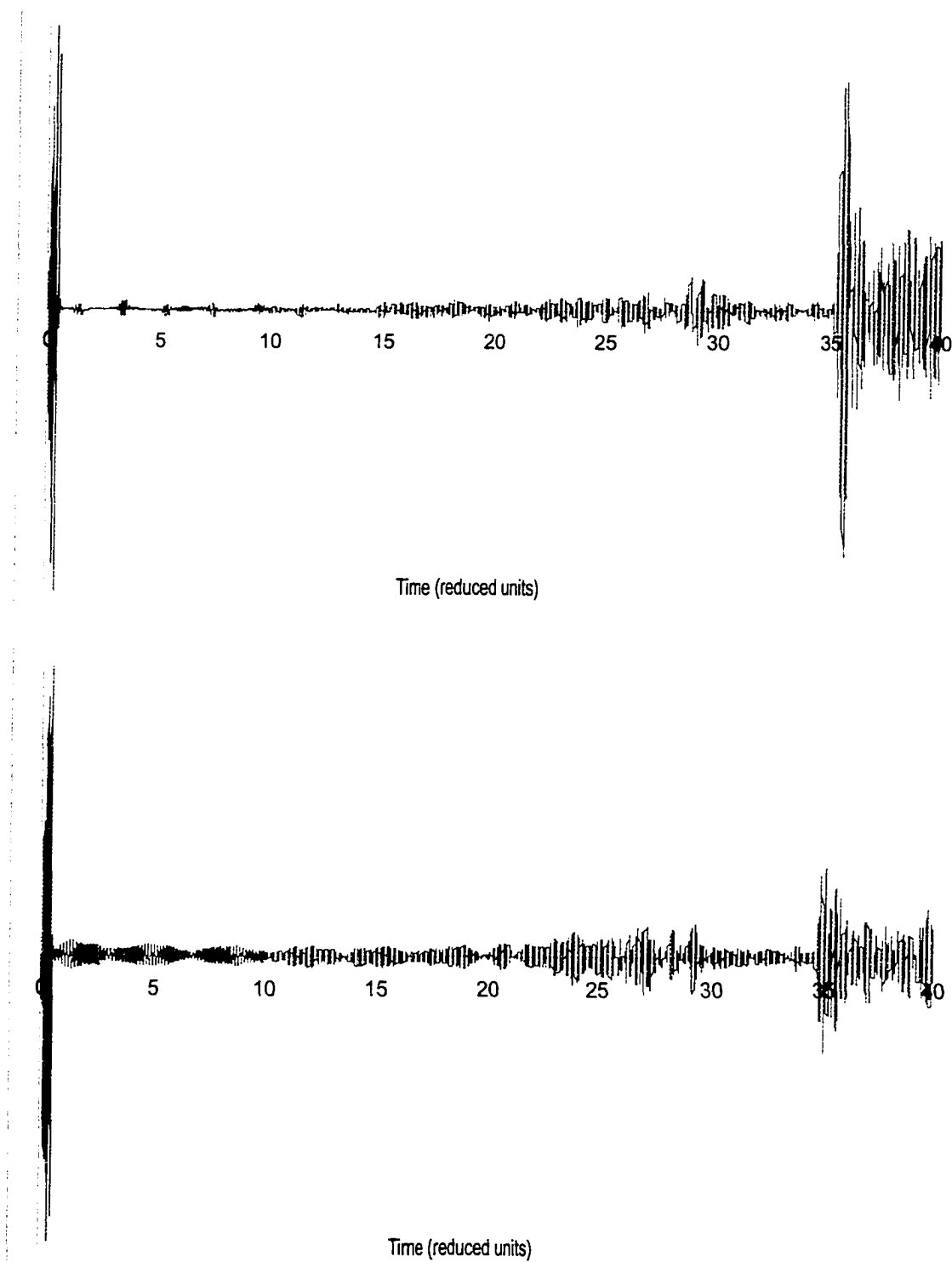
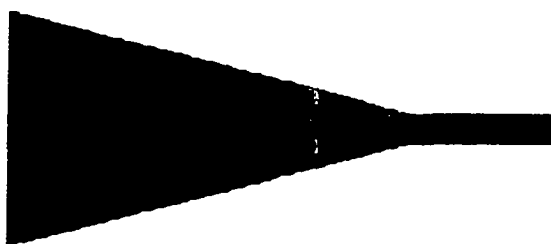


Figure 7.4: Comparison of traces from the CAFIT and EFIT algorithms



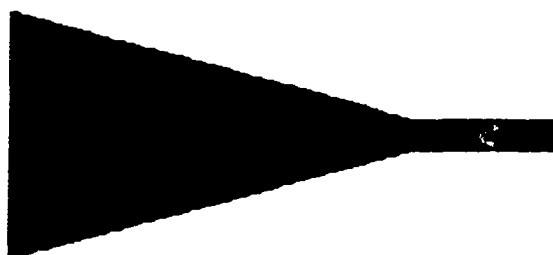
CAFIT simulation at 10 r.u.



EFIT simulation at 10 r.u.



CAFIT simulation at 20 r.u.



EFIT simulation at 20 r.u.

Figure 7.5: Comparison of wavefronts at $t = 10$ r.u. and 20 r.u. for the CAFIT and EFIT algorithms

versus the rectangular tip, this simplification preserves phase information but destroys information about the amplitude of the return signal.

7.3 Simulation Results

Once it was determined that a shorter simulation using the idealized transducer would still provide useful information on the phase of the return signal, this simulation was run for the periodontium model shown in figure 7.1. For this simulation, the only return is from the bottom of the simulation space at 8 reduced time units, which corresponds to a feature at 4 reduced distance units. (Figure 7.7.)

Next, a surface irregularity 0.15 r.u. wide was added to the tooth 1 r.u. down from the top of the periodontium. (Figure 7.8.) In this case, a strong primary echo occurs at 2 r.u. (time), with weaker secondary echoes at 4 and 6 r.u. The large echo at 8 r.u. is from the bottom of the simulation space.

After completing these initial simulations, another level of complexity was added by accounting for attenuation within the different materials. For the purposes of this simulation, it is assumed water does not attenuate the signal at all, while the junctional epithelium has a small attenuation factor of 0.999 per simulation step, and gingiva attenuates signals more strongly (due to the presence of collagen fibers) at 0.98 per

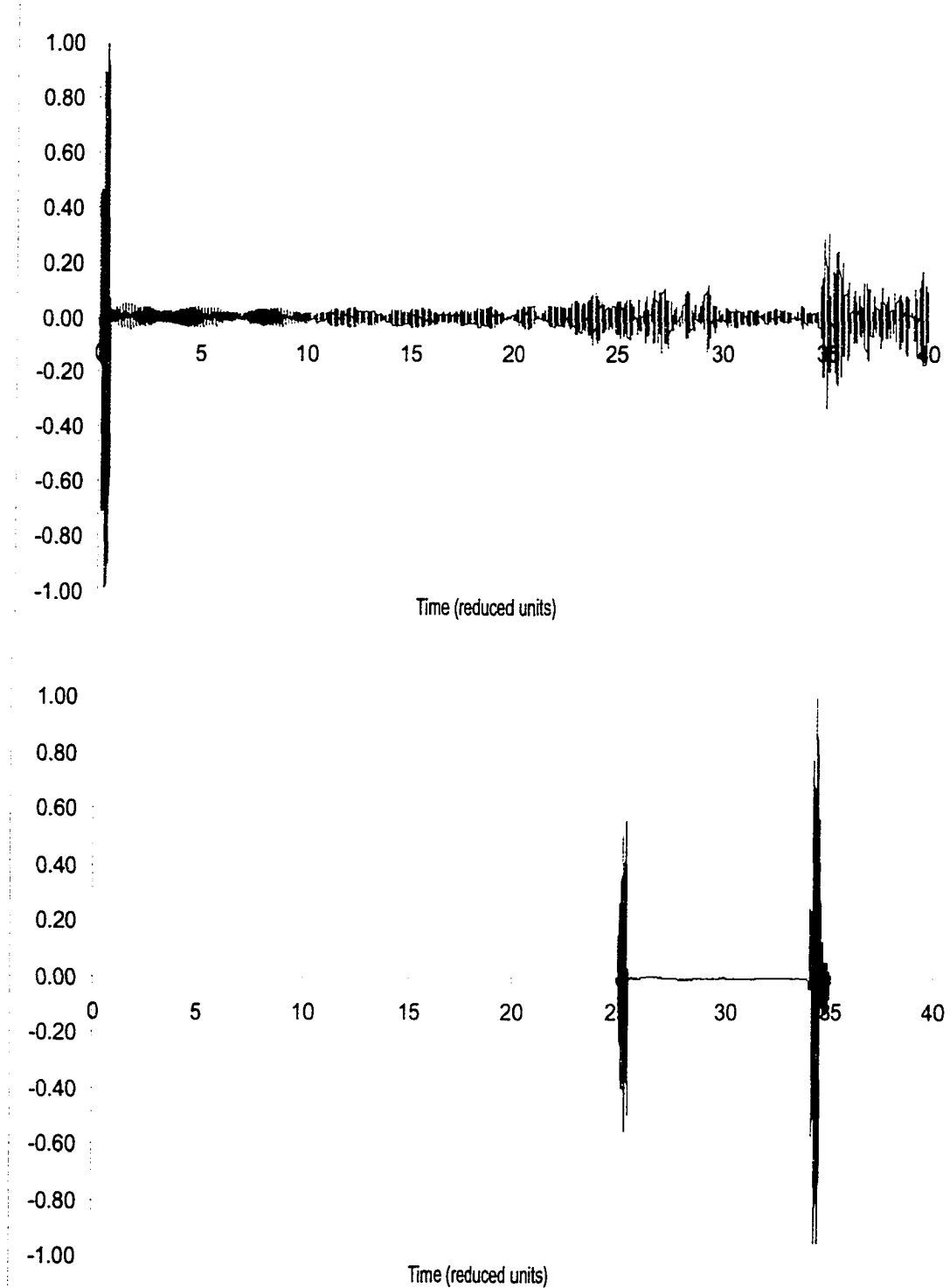


Figure 7.6: Comparison of traces for the simulation for the probe plus periodontium, and for the periodontium only.

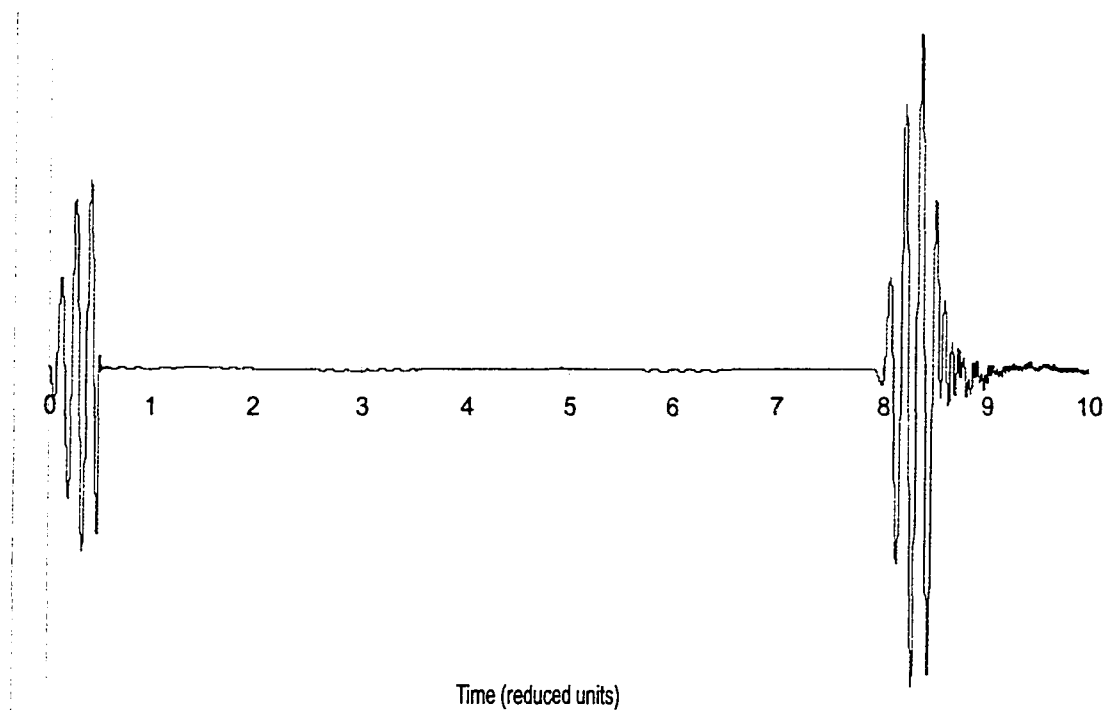


Figure 7.7: Trace for simulation of the idealized periodontium of figure 7.1.



Figure 7.8: Trace for simulation with a surface irregularity at 1 r.u. (distance).

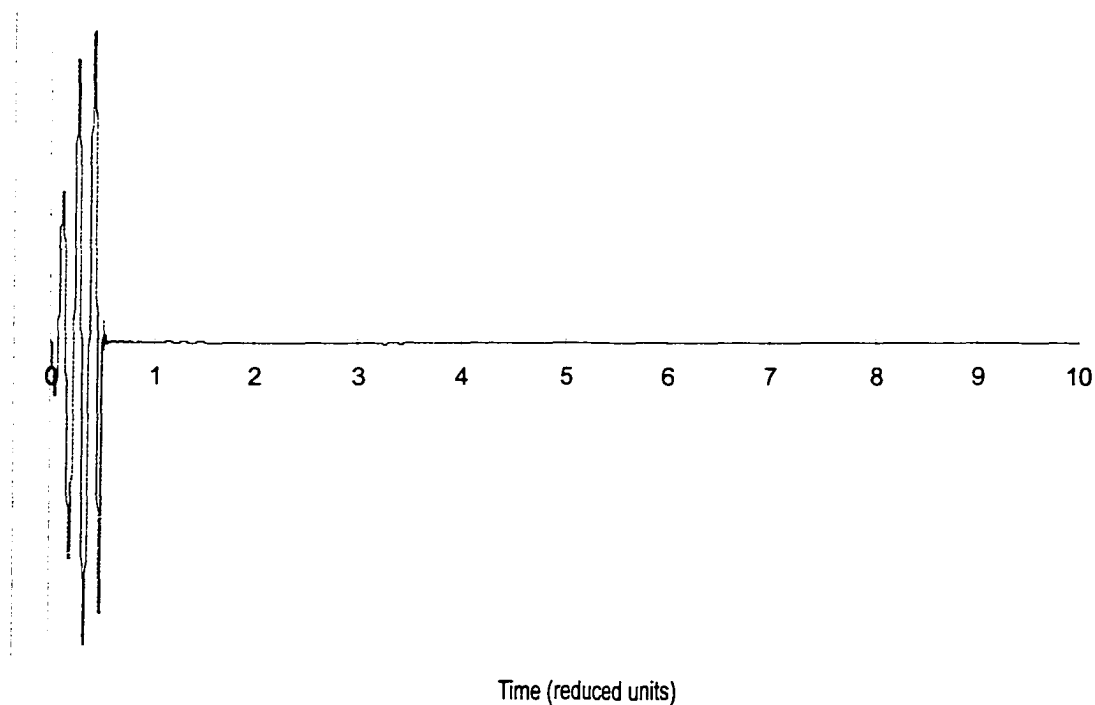


Figure 7.9: As a result of attenuation in the junctional epithelium and the gingiva, there are no echoes evident in this simulation for a smooth tooth surface.

simulation step.

The trace in figure 7.9 shows the results for a simulation of the same space as if figure 7.7, except that the attenuation factors have been added in. As a result, the wavefront does not reach the end of the simulation space, and no echoes are recorded.

When the 0.15 r.u. wide surface irregularity is added to the tooth surface at 1 r.u. (before the wave enters the junctional epithelium), the primary and secondary echoes from this irregularity are evident once again (figure 7.10). In addition, if the surface feature is moved beneath the junctional epithelium to 1.7 r.u., the echoes are still evident (figure 7.11).

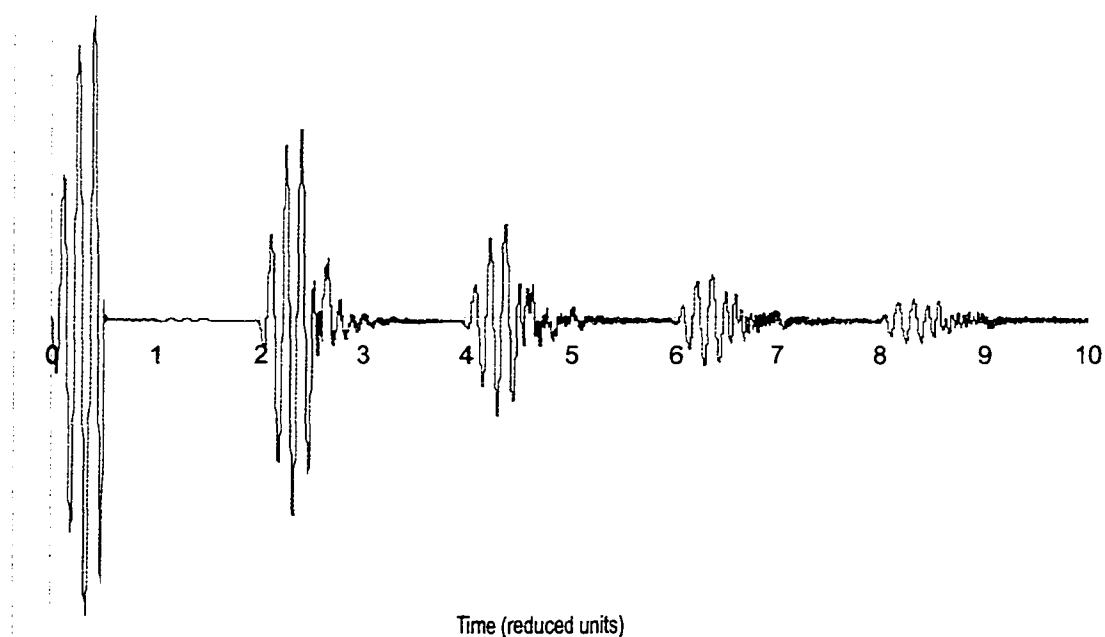


Figure 7.10: Echoes off a surface feature on the tooth 1 r.u. (distance) from the gingival margin.

However, if the surface feature is moved into the connective tissue of the gingiva, attenuation of the signal is too great for an echo to return to the transducer (figure 7.12).

To compare the effect on signal amplitude when an echo originates in the junctional epithelium versus the periodontal pocket, a simulation was run where the surface feature was at 1.7 r.u., but the junctional epithelium was moved from 1.5 r.u. to 2.0 r.u. Thus, the irregularity is at the same depth as in figure 7.11, but no longer covered by tissue. As a result, the signal amplitude is higher, as can be seen in figure 7.13.

Finally, because the surface irregularity was nearly as wide as the

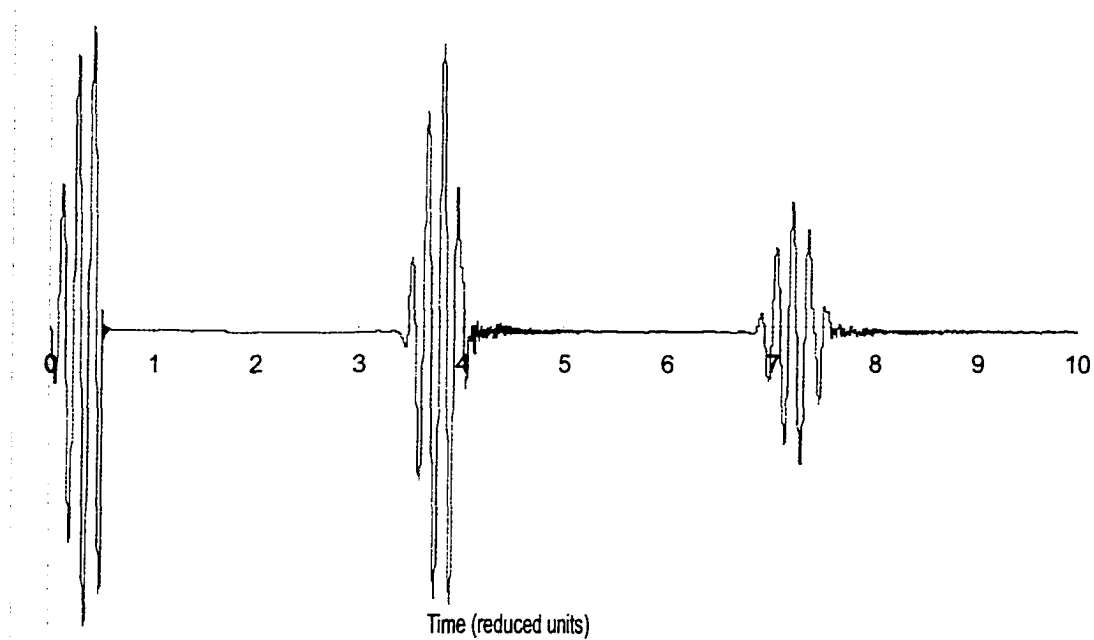


Figure 7.11: Echoes off a surface feature on the tooth 1.7 r.u. (distance) from the gingival margin.

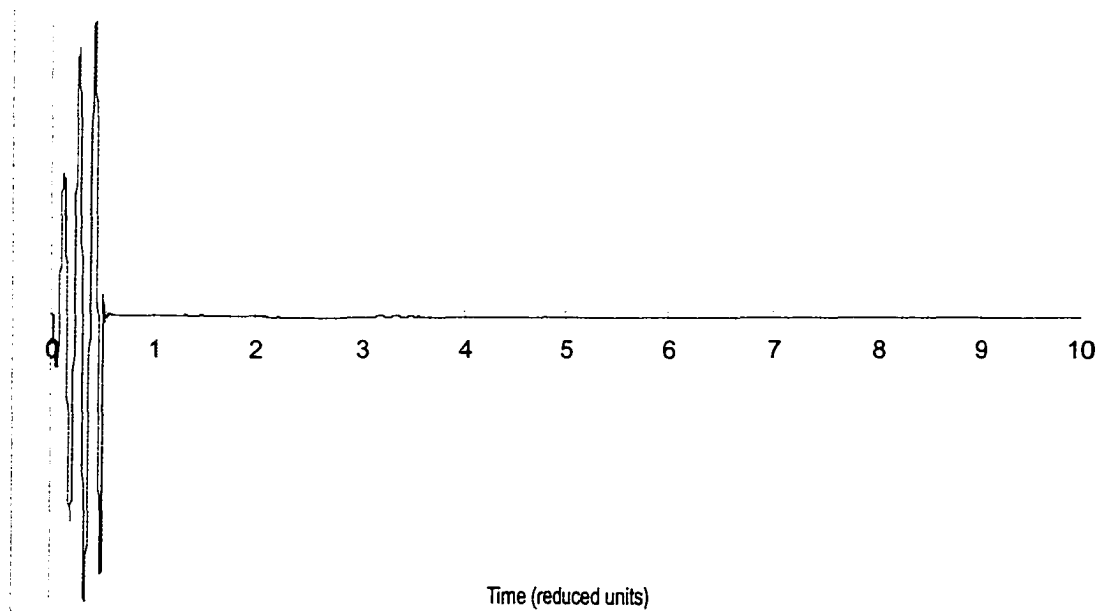


Figure 7.12: Return signal when a surface feature is on the tooth 3.1 r.u. (distance) from the gingival margin.

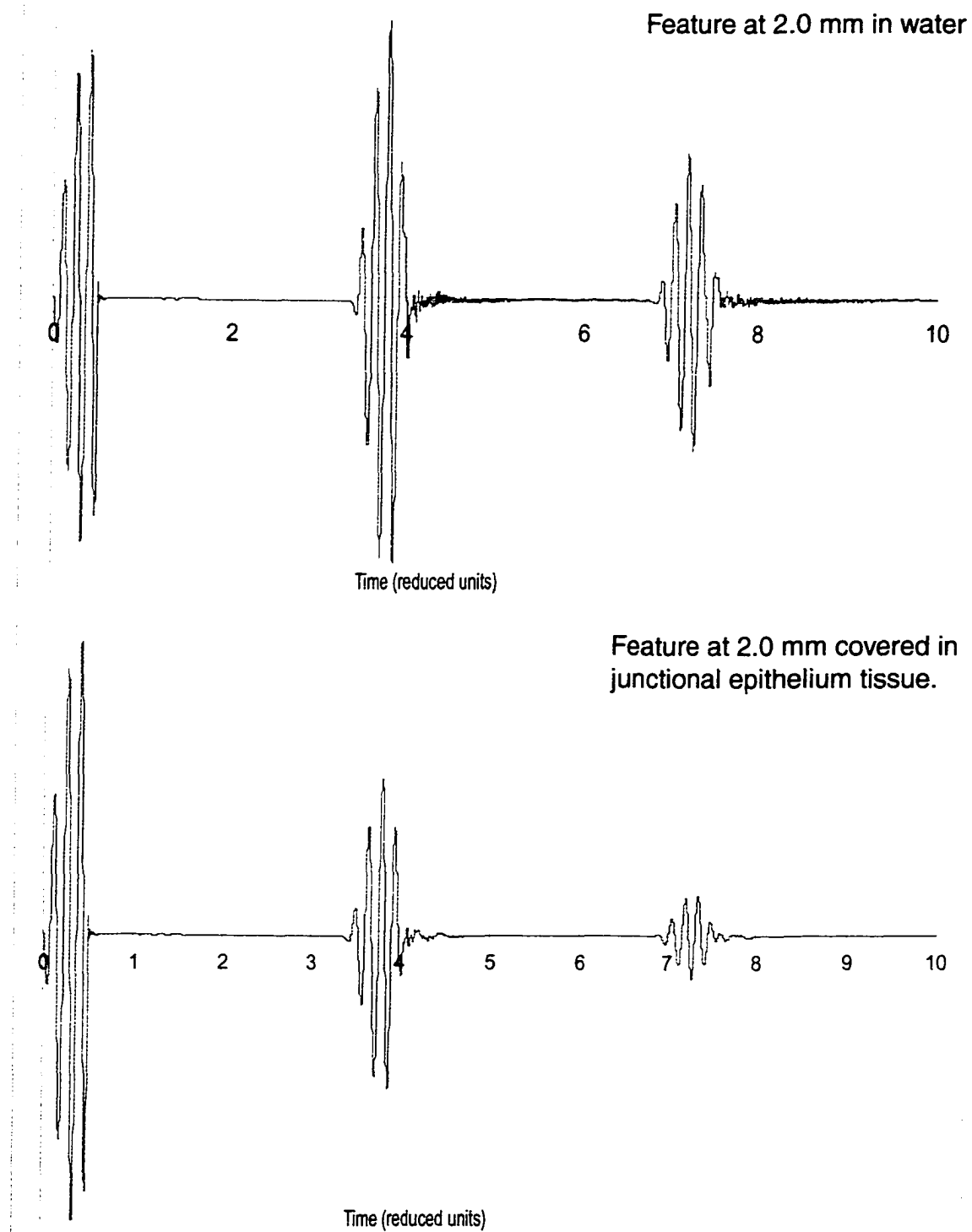


Figure 7.13: When the a surface feature is no longer covered by epithelial tissue, the return signal is stronger.

periodontal pocket (at least toward the middle of the pocket), another series of simulations was conducted to see how thin an irregularity must be before echoes are detectable on the signal trace. As can be seen in figure 7.14, a 0.05 r.u. irregularity produces an echo, although it is much smaller than that from a 0.15 r.u. irregularity. If the irregularity is further reduced to 0.03 r.u. wide, no echoes are evident (figure 7.15.)

From this series of simulations, it appears plausible that return signals in the clinical data are solely the result of echoes from the tooth surface. Since the material properties of the junctional epithelium and the gingiva are not known, it is still possible that ultrasonic echoes could result from interactions with these structures, even though the simulation did not produce such echoes. However, since muscle and skin are most likely more dense than gingiva and junctional epithelium, and therefore more likely to produce echoes, this possibility does not seem likely.

In addition, from this simulation it appears that the transitions in return signal strength observed in the clinical trials data could result from attenuation of the signal. In the simulations, echoes from the tooth surface were stronger if they originated in the open pocket versus the junctional epithelium, and undetectable if they originated from the connective tissue region of the gingiva. Therefore, this simulation supports the two hypotheses of the model used to interpret the clinical trials data.

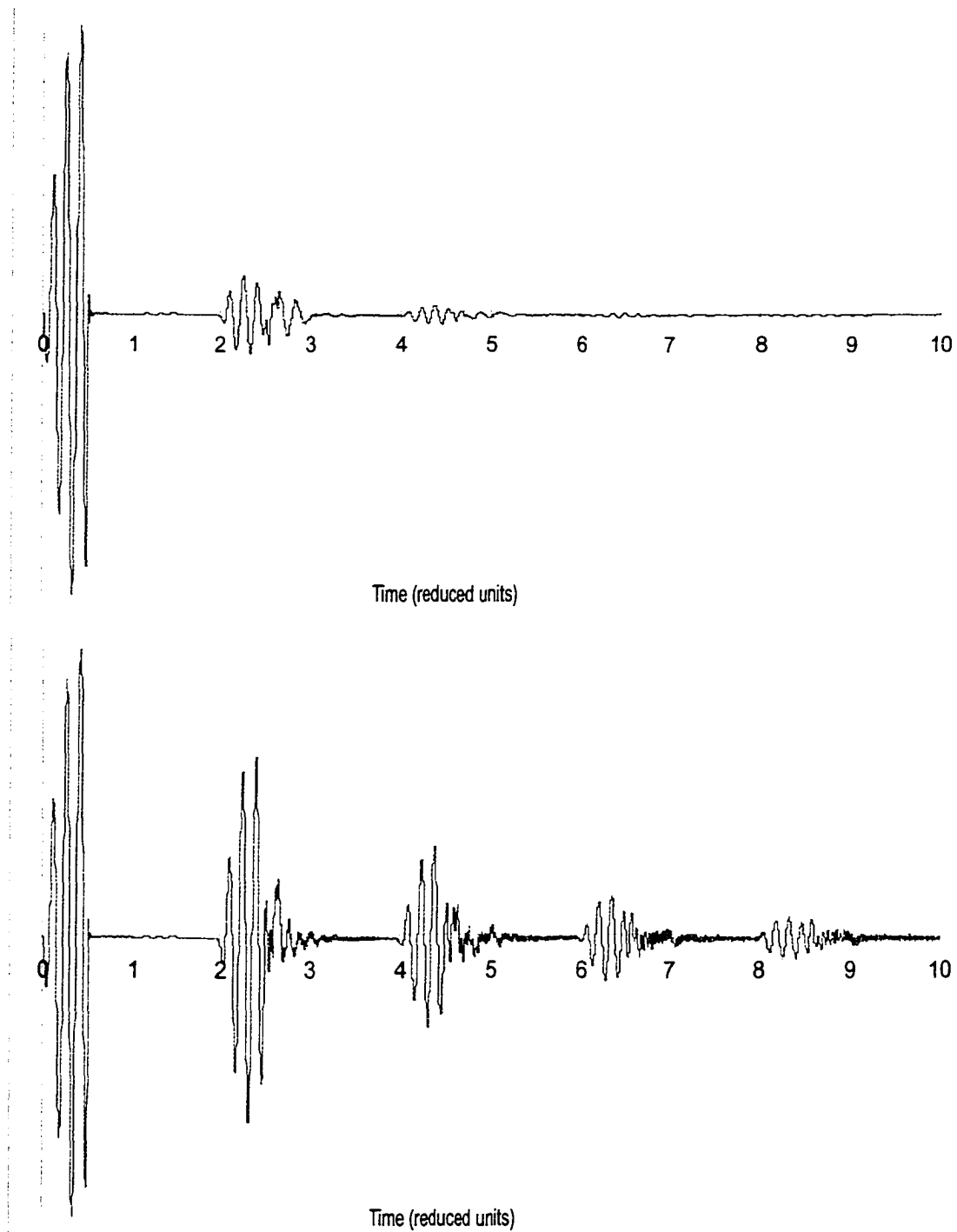


Figure 7.14: Irregularities 0.05 r.u. wide produce smaller returns than 0.15 r.u. irregularities.

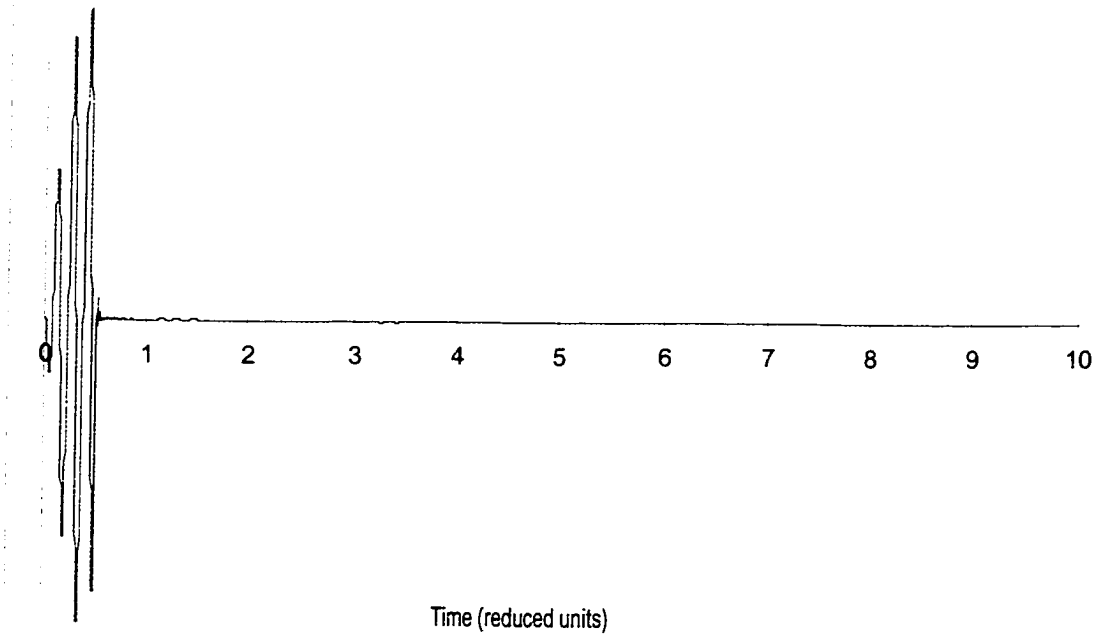


Figure 7.15: Irregularities 0.03 r.u. wide do not produce echoes at all.

Chapter 8

Conclusion and Recommendations for Future Work

The work performed in this dissertation can be divided into three categories: engineering of the ultrasonographic probe, development of signal processing algorithms needed to help interpret the data obtained with this probe, and testing of the probe in a clinical setting. This chapter highlights the achievements within each category and outlines future work needed for successful development of the ultrasonographic probe.

8.1 Engineering of the Probe

During this work, an ultrasonographic probe prototype was demonstrated that provides a strong signal when used to acquire data within the periodontal pocket. The biggest challenge in the development of this prototype was producing a tip/transducer combination that maximized the

return signal while minimizing clutter caused by echoes off the tip walls. The computer simulation and subsequent experimental testing determined that a conical tip with straight walls minimizes echoes from the tip walls, while a small nook around the transducer provides enough space for water to enter the tip but quickly narrows the space in which the wavefront can spread out laterally. By minimizing lateral spreading, the wavefront energy is directed out of the tip nozzle, rather than toward the tip walls, which produces echoes that distort the signal.

In addition, a pressure regulator was integrated into the probe to provide fine control of the water flow, and it was determined that a pressure setting below 5 psi provided the non-turbulent flow needed to acquire useful data. Finally, during the clinical trials, the hygienists using the probe provided some useful feedback on how a next-generation handpiece should be constructed. In particular, they wanted a contra-angled barrel to make it easier to position the probe within the mouth, and a shorter, lighter handpiece that would make the probe easier to handle over a long time. As a result of this work, a next-generation probe was recently completed, and will be used in future tests of the device. This prototype is shown in figure 8.1.

The major engineering task still pending is to add the ability to scan the probe along the gingival margin. Right now, the probe can only acquire

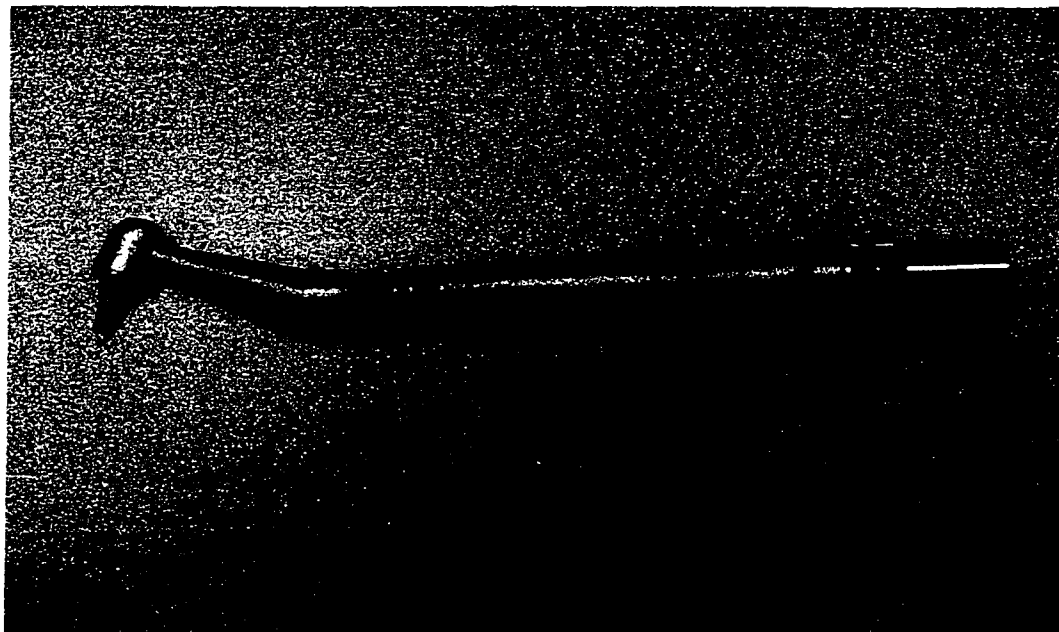


Figure 8.1: The next-generation ultrasonographic probe arising from this work.

data point-by-point, because an operator must manually record the position of the probe prior to taking data. The use of a foot pedal and an improved software interface has made the process of manually recording the position information as fast as possible, but it still limits the clinician to acquiring 6 to 12 data points per tooth, which makes it possible to miss small pockets of disease activity between data points. A full scanning capability, in contrast, would allow the clinician to quickly acquire a full-mouth view of the periodontal anatomy, thus providing a more accurate diagnosis.

To develop full scanning capability, however, the probe must acquire data that provides information about the position of probe within the mouth. Although it is hoped that some anatomical marker could be found

within the ultrasonic A-scan traces that would provide this information, the clinical trials performed in this work did not provide any such marker.

Although future trials may provide new insight into the probing data, and allow for the identification of such an anatomical marker, future work should also concentrate on integrating a second sensor into the probe that provides position data during scanning. Toward that end, a miniBird magnetic tracking sensor was acquired from Ascension Technology Corporation. This sensor uses pulsed DC magnetic field to detect the position and orientation of a magnet housed within the probe with six degrees of freedom. (By using a pulsed DC magnetic field, rather than an AC magnetic field, the sensor eliminates interference from metal objects caused by the formation of eddy currents.) This sensor will enable future research to be conducted on producing a probe with full scanning capability.

8.2 Signal Processing

The signal processing algorithms described in this work were designed to measure periodontal attachment levels for comparison to manual probing depth measurements. As a result, the peak picking and smoothing algorithms described here sacrificed resolution for ease of interpretation. If this pocket depth measurement is all the ultrasonographic probe needs to provide, than the algorithms described here may be sufficient.

However, after more clinical trials are conducted, it may be possible to begin more sophisticated interpretation of the signals to detect the presence of calculus or plaque, or to find the position of the cemento-enamel junction. If so, new algorithms would have to be developed preserve the frequency content of the signal, so that more sophisticated waveform analysis can be conducted.

8.3 Clinical Trials

The methodology of the clinical trials described in this work were designed to provide comparison to manual and controlled-force probing depth measurements. However, it is clear from this work that such a comparison will not provide the information needed to make the ultrasonographic probe a clinically accepted method for monitoring the progression of periodontal disease.

In future work, clinical trials are needed to cover patients exhibiting a wider range of disease activity. In addition, further clinical trials are needed that will provide better understanding of which anatomical features produce ultrasonic echoes from the probe. This data could be used to help develop more sophisticated signal processing routines for identifying more features than is now possible.

In addition, this understanding may help develop automated

routines for interpretation ultrasonic return signals. While the automated feature recognition algorithm discussed in this work appears promising for identifying pocket depths, an adaptive thresholding algorithm in which artificial intelligence techniques are used to determine the optimal smoothing and thresholding parameters for each trace may significantly improve the accuracy of the algorithm. Alternatively, completely new routines could be developed that complement new signal processing routines developed to identify additional features in the periodontal pocket.

As a result, the following types of studies have been proposed in future work: flap surgery, en bloc, extracted teeth, fresh cadaver, and comparison to mechanical probing.

8.3.1 Flap Surgery

A study that seems quite promising is to ultrasonically scan human patient volunteers immediately prior to gum flap surgery. After scanning a site, the gum line on the tooth is marked and the pocket is stained prior to surgery, and then a digital photograph is taken after the tissues are exposed. This will allow mapping of the gingival margin, the cemento-enamel junction (CEJ), and the bottom of the pocket, which can be compared to echoes from the ultrasonic scan. These tri-contour data sets will be especially valuable in identifying the CEJ echoes in the ultrasonic data, so that

attachment level can be determined, rather than just pocket depth.

Because flap surgery is performed on patients with periodontal disease, the data obtained from these studies is likely to have a high proportion of diseased sites. Because periodontal disease is site-specific, the flap surgery will also provide some scans of healthy sites. However, these studies will need to be coordinated with others performed on patients with a higher proportion of healthy sites, particularly if the data obtained from these studies will be used to develop automated feature recognition algorithms.

8.3.2 En Bloc Studies

Another quite promising type of study is to scan patients just prior to en bloc procedures where a “block” of teeth, bone and soft tissues is excised due to cancer in the jaw (or for other reasons). Although the number of these procedures is fairly small, they can each be expected to be quite rich in data. This is because the periodontal tissues will be relatively undisturbed, and histology can be subsequently performed on the block. If the block is finely sectioned and the histological slides are digitally photographed with the resulting images segmented, then the 3-D anatomy of interest can be reconstructed in the computer. Although flap surgery will allow mapping of three contours (gum line, CEJ, pocket) it can't give the

3D mapping that this study can. Since ultrasound is sensitive to the 3D anatomy, this “visible human” type of representation would be very valuable.

Since the cancer is likely uncorrelated to periodontal disease, en bloc studies should provide more variety in periodontal disease status than for the flap surgery studies.

8.3.3 Extracted Teeth Studies

In teeth due to be extracted, the gum line can be marked on the teeth prior to extraction, and afterwards it may be possible to measure the ligament attachment level relative to gum line and the CEJ. It’s not clear how visible these remnants of attachment will be, but it may be that suitable staining can be found to enable it. The tooth could be histologically sectioned as in the en bloc studies or photographed as in the flap surgery studies. If the study include teeth extracted for orthodontic reasons, the full range of periodontal disease activity should be present in these teeth.

8.3.4 Fresh Cadaver Studies

As discussed in Chapter 5, fixed cadaver studies aren’t especially useful because the ultrasonic properties of the fixed soft tissues are changed rather dramatically, and the anatomy is badly distorted when the soft tissue

shrinks during fixation.

Fresh cadavers would minimize these problems, and if histology is subsequently done fresh cadaver studies could provide the type of 3-D data expected from the en bloc studies. Indeed, if en bloc samples are scanned before and after surgery, it may be possible to use this data to help adjust for varying cadaver responses as tissue status changes.

8.3.5 Comparison Studies

Finally, because the current “gold standard” in the diagnosis of periodontal disease is mechanical probing, further comparison studies will need to be conducted between ultrasound, manual and controlled-force probing.

Because the first set of clinical trials were conducted on generally healthy patients, it did not represent a thorough comparison needed to allow ultrasonic probing to replace manual probing as a new gold standard. In addition, a comparison study may be a useful complement to the slower procedures described above, since extremely large data sets will be needed to accurately train an automated feature recognition algorithm.

Bibliography

- [1] C.W. Douglas et al. National trends in the prevalence and severity of the periodontal diseases. *J. Am. Dental Assoc.*; 107(403-411), 1983.
- [2] E.P. Barrington and M. Nevins. Diagnosing periodontal diseases. *J. Am. Dental Assoc.*; 121(460-464), 1990.
- [3] R.C. Page. Critical issues in periodontal research. *J. Dental Res.*; 74(1118-1128), 1995.
- [4] E.B. Fowler. Periodontal disease and its association with systemic disease. *Military Medicine*; 166(85-89), 2001.
- [5] National Institute of Dental and Craniofacial Research. Chapter 5: Linkages with general health. In *Oral Health in America: A Report of the Surgeon General*; <http://www.nidcr.nih.gov/sg/sgrohweb/chap5.htm>, 2000.
- [6] M.A. Listgarten. Normal development, structure, physiology, and repair of the gingival epithelium. *Oral Sci. Rev.*; 1(3), 1972.
- [7] F.A. Carranza and M.G. Newman. *Clinical Periodontology*; 8th edition, W.B. Saunders Company, Philadelphia, 1996.
- [8] K.H. Rateitschak. *Color Atlas of Dental Medicine: Vol. 1 Periodontology*; ed. K.H. and E.M. Rateitschak, H.F. Wolf and T.M. Hassell. 2nd edition, Thieme Medical Publishing, Inc. 1989.
- [9] A.D. Haffajee et al. Clinical parameters as predictors of destructive periodontal disease activity. *J. Clinical Periodontology*; 10(257), 1982.

- [10] J.F. Tessier et al. Probing velocity: novel approach for assessment of inflamed periodontal attachment. *J. Periodontology*; 65(103-108) 1994.
- [11] P.S. Hull, V. Clerehugh and A. Ghassemi-Aval. An assessment of the validity of a constant force electronic probe in measuring probing depths. *J. Periodontology*; 66(848-851), 1995.
- [12] T.E. Rams and J. Slots. Comparison of two pressure-sensitive periodontal probes and a manual probe in shallow and deep pockets. *Int. J. of Periodontics & Restorative Dentistry*; 13(521-529), 1993.
- [13] N.P. Lang and E.F. Corbet. Diagnostic procedures in daily practice. *Int. Dental J.*; 45(5-15), 1995.
- [14] G. Greenstein and I. Lamster. Understanding diagnostic testing for periodontal diseases. *J. Periodontology*; 66(659-666), 1995.
- [15] M.A. Listgarten. Periodontal probing: What does it mean? *J. Clin Periodontology*; 7(165), 1980.
- [16] L. Tupta-Veselicky, P. Famili, F.J. Ceravolo and T. Zullo. A clinical study of an electronic constant force periodontal probe. *J. Periodontology*; 65(616-622), 1994.
- [17] M.E. Palou, M.J. McQuade and J.A. Rossman. The use of ultrasound for the determination of periodontal bone morphology. *J. Periodontology*; 58(262-265), 1987.
- [18] F. Hunter. Periodontal probes and probing. *Int. Dental J.*; 44(557-583), 1994.
- [19] L. Mayfield, G. Bratthall and R. Attstrom. Periodontal probe precision using 4 different periodontal probes. *J. Clin. Periodontology*; 23(76-82), 1996.
- [20] M.K. Jeffcoat. Machines in periodontics. *Scientific*; 84(18-22), 1991.
- [21] M. Quiryen, A. Callens, D. van Steenberghe, and M. Nys. Clinical evaluation of a constant force electronic probe. *J. Periodontology*; 64(35-39), 1993.
- [22] M. Cattabriga. Future diagnostic possibilities in periodontology. *Int. Dental J.*; 43(109-115), 1993.
- [23] S.G. Grossl, R.G. Dunford, H.A. Koch, E.E. Machtei, R.J. Genco. Sources of error in periodontal probing

- measurements. *J. Periodontal Research* 31(330-336), 1996.
- [24] D.S. Barendregt, U. van der Velden, J. Relker and B.G. Loos. Clinical evaluation of tine shape of 3 periodontal probes using 2 probing forces. *J. Clin. Periodontology*; 23(397-402), 1996.
- [25] J.J. Garnick and L. Silverstein. Periodontal probing: probe tip diameter. *J. Periodontology*; 71(96-103), 2000.
- [26] S.F. Wang, et al. Reproducibility of periodontal probing using a conventional manual and an automated force-controlled electronic probe. *J. Periodontology*; 66(38-46), 1995.
- [27] J.F. Tessier, et al. Relationship between periodontal probing velocity and gingival inflammation in human subjects. *J. Clin. Periodontology*; 20(41-48), 1993.
- [28] L. Tupta-Veselicky, et al. A clinical study of an electronic constant force periodontal probe. *J. Periodontology*; 65(616-622), 1994.
- [29] M. Cattabriga. Future diagnostic possibilities in periodontology. *Int. Dental J.*; 43(109-115), 1993.
- [30] M.C.K. Yang, et al. Reproducibility of an electronic probe in relative attachment level measurements. *J. Clin. Periodontology*; 19(306-311), 1992.
- [31] N. Ahmed, T.L.P. Watts, and R.F. Wilson. An investigation of the validity of attachment level measurements with an automated periodontal probe. *J. Clin. Periodontology*; 23(452-455), 1996.
- [32] A. Agüero, et al. Histological location of a standardized periodontal probe in man. *J. Periodontology*; 66(184-190), 1995.
- [33] J.F. Tessier, et al. Relationship between periodontal probing velocity and gingival inflammation in human subject. *J. Clin. Periodontology*; 18(548-653), 1993.
- [34] J.G. Keagle, et al. Effect of gingival wall on resistance to probing forces. *J. Clin. Periodontology*; 22(953-957), 1995.
- [35] S. Albalat, et al. Automated system for periodontal disease diagnosis. in *Medical Imaging 1997: Image Processing*,

- Kenneth M. Hanson, editor, Proceedings of SPIE vol. 3034, 106-112, 1997.
- [36] M.C. Juan, et al. Computer-aided periodontal disease diagnosis using computer vision. *Computerized Medical Imaging and Graphics*; 23(209-217), 1999.
- [37] A.D. Hafajee, S.S. Socransky, and J.M. Goodson. Comparison of different data analyses for detecting changes in attachment level. *J. Clin. Periodontology*; 10(298), 1983.
- [38] W.P. Dreyer. Technological advances in the clinical diagnosis of periodontal diseases. *Int. Dental J.*; 43(557-566), 1993.
- [39] C.H. Gibbs, J.W. Hirschfeld, and J.G. Lee. Description and clinical evaluation of a new computerized periodontal probe: the Florida Probe. *J. Clin. Periodontology*; 15(137), 1988.
- [40] P.F. van der Stelt. Modern radiographic methods in the diagnosis of periodontal disease. *Adv. Dental Res.*; 7(158-162), 1993.
- [41] M.K. Jeffcoat. Radiographic methods for the detection of progressive alveolar bone loss. *J. Periodontology*; 63(367-372), 1993.
- [42] E. Hausmann. Studies on the relationship between changes in radiographic bone height and probing attachment. *J. Clin. Periodontology*; 21(128-132), 1994.
- [43] M.J. Goodson. Patterns of progression and regression of advanced destructive periodontal diseases. *J. Clin. Periodontology*; 9(472), 1982.
- [44] E. Hausmann. Radiographic and digital imaging in periodontal practice. *J. Periodontology* 71(497-503), 2000.
- [45] G.C. Armitage. Periodontal diseases: diagnosis. *Ann. Periodontology*; 1(37-215), 1996.
- [46] American Academy of Periodontology (AAP). World Workshop on Clinical Periodontitis Consensus Report. *Ann. Periodontology*; (1)926-32, 1996.
- [47] B.J. Moncla, et al. The use of whole-cell DNA probes for the identification of *Bacteroides intermedius* isolates in a dot blot assay. *J. Dent. Res.*; 67(1267-70), 1988.

- [48] E.D. Savitt, et al. Comparison of cultural methods and DNA probe analyses for detection of *Actinobacillus actinomycetemcomitans*, *Bacteroides gingivalis*, and *Bacteroides intermedius* in subgingival plaque samples. *J. Periodontology*; 59(431-8), 1988.
- [49] E.D. Savitt, M.W. Keville, and W.J. Peros. DNA probes in the diagnosis of periodontal microorganisms. *Archives Oral Biology* 35(153S-9S), 1990.
- [50] J.J. Zambon, V. Bochacki, and R.J. Genco. Immunological assays for putative periodontal pathogens. *Oral Microbiology Immunology*; 1(39-44), 1986.
- [51] P.F. Cavanaugh, et al. Coordinate production of PGE2 and IL-1 in the gingival crevicular fluid of adults with periodontitis: its relationship to alveolar bone loss and disruption by twice daily treatment with ketorolac tromethamine oral rinse. *J. Periodontal Res* 33(75-82), 1998.
- [52] S. Offenbacher, B.M. Odle, T.E. Van Dyke. The use of crevicular fluid prostaglandin E2 levels as a predictor of periodontal attachment loss. *J. Periodontal Res*; 21(101-12), 1986.
- [53] M. Geivelis, et al. Measurements of interleukin-6 in gingival crevicular fluid from adults with destructive periodontal disease. *J Periodontology*; 64(980-3), 1993.
- [54] M.P. Masada, et al. Measurement of interleukin-1 alpha and -1 beta in gingival crevicular fluid: implications for the pathogenesis of periodontal disease. *J. Periodontal Res*; 25(156-63), 1990.
- [55] C.C. Tsai, Y.P. Ho, C.C. Chen. Levels of interleukin-1 and interleukin-8 in gingival crevicular fluids in adult periodontitis. *J Periodontology*; 66(852-9), 1995.
- [56] E.F. Rossomando, J.E. Kennedy, and J. Hadjimichael. Tumour necrosis factor alpha in gingival crevicular fluid as a possible indicator of periodontal disease in humans. *Archives Oral Biology*; 35(431-4), 1990.
- [57] I.B. Lamster, et al. Development of a risk profile for periodontal disease: microbial and host response factors. *J Periodontology*; 65(511-20), 1994.

- [58] I.B. Lamster, et al. The relationship of β -glucuronidase activity in crevicular fluid to probing attachment loss in patients with adult periodontitis: findings from a multicenter study. *J Clin Periodontology*; 22(1):36-44, 1995.
- [59] D.A. Chambers, et al. A longitudinal study of aspartate aminotransferase in human gingival crevicular fluid. *J Periodontal Res*; 26(65-74), 1991.
- [60] G.R. Persson and R.C. Page. Diagnostic characteristics of crevicular fluid aspartate aminotransferase (AST) levels associated with periodontal disease activity. *J. Clin. Periodontology*; 19(43-8), 1992.
- [61] G.C. Armitage, et al. Longitudinal evaluation of elastase as a marker for the progression of periodontitis. *J. Periodontology*; 65(120-8), 1994.
- [62] K.G. Palcanis, et al. Elastase as an indicator of periodontal disease progression. *J. Periodontology*; 63(237-42), 1992.
- [63] W. Lee, et al. Evidence of a direct relationship between neutrophil collagenase activity and periodontal tissue destruction in vivo: role of active enzyme in human periodontitis. *J. Periodontal Research*; 30(1):23-33, 1995.
- [64] National Institute of Dental and Craniofacial Research. Chapter 8: Personal and provider approaches to oral health. In *Oral Health in America: A Report of the Surgeon General*; <http://www.nidcr.nih.gov/sgr/sgrohweb/chap8.htm>, 2000.
- [65] B.W. Colston, et al. Imaging of hard- and soft-tissue structure in the oral cavity by optical coherence tomography. *Applied Optics*; 37(3582-5), 1998.
- [66] H. Fukukita, et al. Development and application of an ultrasonic imaging system for dental diagnosis. *J. Clin. Ultrasound*; 13(597-600), 1985.
- [67] C. Lost, K.M. Irion, and W. Nussle. Periodontal ultrasonic diagnosis: experiments on thin bony platelets and on a simulated periodontal ligament space. *J. Periodontal Res*; 23(347-351), 1988.

- [68] M.E. Palou, M.J. McQuade, and J.A. Rossman. The use of ultrasound for the determination of periodontal bone morphology. *J. Periodontology*; 58(262-5), 1986.
- [69] M.K. Hinders and J.C. Companion. Ultrasonic periodontal probe. In D.E. Chimenti and D.O. Thompson, editors, *Review of Progress in Quantitative Nondestructive Evaluation*; volume 18, pages 1609-15. Kluwer Academic/Plenum Publishers, 1999.
- [70] D.R. Loker and K. Hagenbuch. Ultrasonic periodontal diagnostic instrumentation system with clinical results. *Measurement*; 23(125-9), 1998.
- [71] A.C. Lassal and P.A. Payne. Scanning and imaging using lamb waves. *Acoustical Imaging*; 23(355-61), 1997.
- [72] M.K. Hinders. Lecture notes: APSC 722 Quantitative Non-Destructive Evaluation I, Lecture No. 2. Spring 1999.
- [73] J.L. Rose. *Ultrasonic Waves in Solid Media*. Cambridge University Press, 1999.
- [74] J.T. Bushberg, J.A. Seibert, E.M. Leidholdt, J.M. Boone. *The Essential Physics of Medical Imaging*. Williams and Wilkins, 1994.
- [75] J. Woo. A short history of the developments of ultrasound in obstetrics and gynecology. <http://www.ob-ultrasound.net/history.html>, 2001.
- [76] A.D. Walmsey, W.R.E. Laird, and P.J. Lumley. Ultrasound in dentistry. Part 2—periodontology and endontics. *J. Dent.*; 16(11-17), 1991.
- [77] F.W. Kremkau. *Diagnostic Ultrasound*, 5th edition. W.B. Saunders Company, 1998.
- [78] A. Peiffer, B. Kohler, and S. Petzold. The acoustic finite integration technique for waves of cylindrical symmetry (CAFIT). *J. Acoust. Soc. Am.*; 102(697-706), 1997.
- [79] H.K. Versteeg. *An Introduction to Computational Fluid Dynamics: The Finite Volume Method*. Longman Scientific and Technical, 1995.
- [80] P.M. Morse. *Vibration and Sound*, 4th edition. The Acoustical Society of America, 1981.

- [81] R.C. Binder. *Fluid Mechanics*, 5th edition. Prentice-Hall, Inc., 1973.
- [82] D. Garland, Valpey-Fisher, Inc. Phone conversation, June 2000.
- [83] E. Reh. An algorithm for peak shape analysis for differentiating unresolved peaks in chromatography. *Trends in Analytical Chemistry*; 12(192-4), 1993.
- [84] M.D. Judd. A simple, low-computation peak detection algorithm for the angle-of-arrival spectrum for signal subspace models. *IEEE Transactions on Aerospace and Electronic Systems*; 28(1158-63), 1992.
- [85] M.I. Sezan. A peak detection algorithm and its application to histogram-based image data reduction. *Computer Vision, Graphics and Image Processing*; 49(36-51), 1990.
- [86] M. Blaauw. Statistical properties of a peak-search algorithm for gamma-ray spectrometry as related to Currie's detection limits. *Nuclear Instruments and Methods in Physics Research A*; 336(273-277), 1993.
- [87] D.M. Howard. Peak-picking fundamental period estimation for hearing prostheses. *J. Acoust. Soc. Am.* 86(902-10), 1989.
- [88] D.A. Sadler, et al. Tutorial guide to the use of wavelet transforms to determine peak shape parameters for interference detection in graphite furnace absorption spectroscopy. *Spectrochimica Acta Part B* 53(821-35), 1998.
- [89] Galactic Industries Corporation. Peak picking. http://www.galactic.com/Algorithms/peak_picking.htm. 2000.
- [90] H. Le and J. Silness. Periodontal disease in pregnancy: Correlation between oral hygiene and periodontal conditions. *Acta Odontol Scand*; 22(121-135), 1964.
- [91] D.G. Altman and J.M. Bland. Measurement in medicine: the analysis of method comparison studies. *The Statistician*; 32(307-317), 1983.
- [92] C.Y. Tan and B. Iglewicz. Measurement-methods comparisons and linear statistical relationship. *Technometrics*; 41(192-201), 1999.

- [93] SAS Institute. *JMP Statistical Discovery Software User's Manual* January 2000.
- [94] P. Fellingner, R. Marklein, K.J. Langenberg, S. Klaholz. Numerical modeling of elastic wave propagation and scattering with EFIT-elastic dynamic finite integration technique. *Wave Motion*; 21(47-66), 1995.
- [95] E.L. Madsen, H.J. Sathoff, J.A. Zagzebski. Ultrasonic shear wave properties of soft tissues and tissue-like materials. *J. Acoust. Soc. Am.* 74(1346-55), 1983.
- [96] S.A. Goss, R.L. Johnston, F. Dunn. Comprehensive compilation of empirical ultrasonic properties of mammalian tissues. *J. Acoust. Soc. Am.* 64(423-56), 1978.

Vita

John Edward Lynch

Ted was born in Boulder, Colorado on February 9, 1969. He graduated from Webster High School (Webster, New York) in 1987, and received a Bachelor of Arts degree in English from the College of William and Mary (Williamsburg, Virginia) in 1990. He then moved to Arlington, Virginia and worked as a science writer with the National Technology Transfer Center until 1996. In 1996 he received a Masters of Science degree in physics from George Mason University (Fairfax, Virginia), and spent two years teaching at Menyamya High School in Papua New Guinea for the U.S. Peace Corps. Upon returning from Peace Corps service, Ted entered the doctoral program at the College of William and Mary's Department of Applied Science. While pursuing his doctoral degree, he returned to the National Technology Transfer Center, where he helps small firms to commercialize their government-funded research. He currently lives in Williamsburg, Virginia with his wife Mary and his son Evan.